Dynamics of layered Jahn–Teller crystals of rare-earth compounds (Review)

V. I. Kut'ko*

B. Verkin Institute for Low Temperature Physics and Engineering, National Academy of Sciences of Ukraine, pr. Lenina 47, Kharkov 61103, Ukraine

(Submitted January 28, 2004; revised July 9, 2004)
Fiz. Nizk. Temp. **31**, 3–42 (January 2005)

Spectroscopic data on crystals of rare-earth compounds having structural instability due to the cooperative Jahn–Teller effect are reviewed. Based on an analysis of these data, it is inferred that the dynamic coupling of low-frequency electronic excitations of the rare-earth ions with crystal lattice vibrations plays an essential role in the formation of the low-energy spectra of layered crystals. The role of this coupling in the formation of anomalies of various physical properties of crystals of rare-earth compounds with highly anisotropic structure is examined. © *2005 American Institute of Physics.* [DOI: 10.1063/1.1820349]

INTRODUCTION

Anharmonicity and the phase transitions brought about by the electron–phonon interaction are problems of particular interest in the study of the dynamic properties of solids. Usually a phenomenological approach is used in the analysis of structural phase transitions in solids. The primary reason for this is that in most cases there is no known description on the microscopic level for the mechanisms causing the change in structure of a substance upon a change of the external parameters. However, there is a wide class of materials in which structural phase transitions are due to the microscopic mechanism known as the cooperative Jahn–Teller effect (CJTE). A special place among the crystals with the CJTE is held by rare-earth compounds. Because of the strong localization of the electrons of the $4f$ shell in them, the structural phase transitions due to the CJTE occur at low temperature. Consequently, the molecular fields governing the Jahn–Teller ordering are insignificant. Therefore the structure of the orbital ordering established as a result of the CJTE can be altered by relatively weak external influences.

Historically the first experimental studies of the cooperative Jahn–Teller effect in rare-earth compounds were done on highly symmetric, weakly anisotropic crystals, and theoretical models of the CJTE were constructed on the basis of those experiments.[1–4] The small value of the dynamic coupling of low-energy excitations of rare-earth ions with crystal lattice vibrations simplifies the theoretical approach to the description of the CJTE in weakly anisotropic crystals. In such materials the Debye temperature is much greater than the temperature of the structural phase transitions, and the rare-earth ion electronic levels active in the phase transitions cross the acoustic vibrational branch in the region where the density of states is insignificant (see Fig. 1a), which makes for a low value of the dynamic coupling.

In highly anisotropic crystals the situation is qualitatively different. According to theory (see, e.g., Refs. 5–10), low-frequency vibrational spectrum of such crystals should exhibit features of the density of states in the form sharp spikes. This can lead to a significant increase in the dynamic coupling of the low-energy electronic excitations of the rare-earth ions with lattice vibrations.

At a crossing of electronic levels with the corresponding low-frequency vibrational branches in the region where the density of states is maximal (see Fig. 1b) a dynamic enhancement of the coupling of the electronic and ionic subsystems occurs on account of the pronounced resonance character of the interaction of the excitations.

It is of interest to elucidate the role of the dynamic coupling of the electronic and ionic subsystems in the formation of the low-energy spectra of excitations of highly anisotropic Jahn–Teller crystals and to establish the features of their physical properties that result from this coupling. Model objects for highly anisotropic Jahn–Teller systems are layered crystals in which the Jahn–Teller ions are ions of the rare-earth metals (Dy, Er, Tm,...). The most completely and systematically studied of the rare-earth compounds with a layered structure are the alkali–rare-earth double molybdates (ARDMs). Therefore, in this review we use the experimental results obtained on those materials. These compounds, with the general formula $AR(MoO_4)_2$ where A is an alkali metal ion and R is a rare-earth metal ion, have low symmetry of the crystal lattice (monoclinic or rhombic classes C_{2h}, D_{2h}; Refs. 11–13). Accordingly, the local symmetry of the rare-earth ions in them is rather low (C_1, C_2, D_2), and the static crystalline field splits the ground multiplet of the $4f$ shell into states which are nondegenerate with respect to the orbital moment. However, because the values of the splitting of the ground multiplet are small, this gives rise to a so-called pseudo-Jahn–Teller effect. Because of the weak coupling of the electrons of the $4f$ shell with the crystal lattice, low-energy electronic levels of the rare-earth ions that cross with acoustic or optical–acoustic vibrational branches are active in the pseudo-Jahn–Teller effect. In ARDMs the acoustic and optical–acoustic branches have low limiting frequencies at the Brillouin zone boundaries and zone center, and the low-energy electronic levels can cross the vibrational branches in the region where the density of states is maximal, leading to an unusual dynamics of these materials in the region of low-energy excitations.

This review is organized as follows. In Sec. 1 we discuss the research that has been done on the spectroscopy of ARDMs in the long-wavelength IR region and establish the

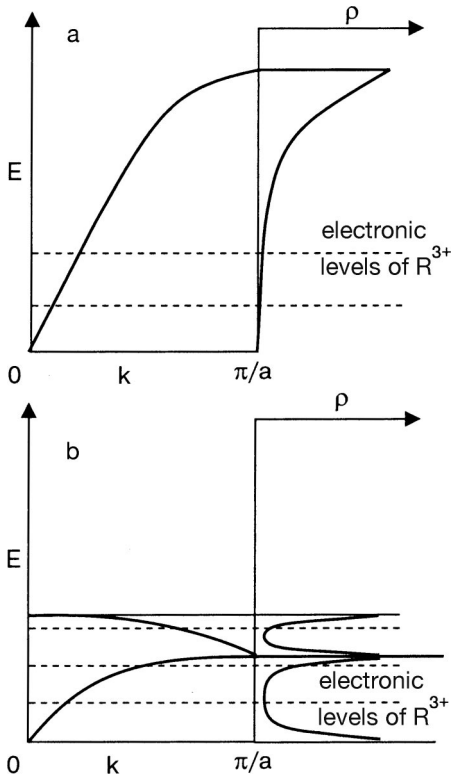

FIG. 1. The diagram of the structure of the low-energy spectrum of the weakly anisotropic (a) and highly anisotropic (b) Jahn–Teller crystals of the rare earth compounds. From the left the dispersion of the low energy vibrational branches in the Brillouin zone is shown; from the right the dependence of the density of vibrational states ρ on energy is shown. The horizontal dashed lines represent the electron levels of the rare earth ions.

mechanisms of formation of the low-energy excitation spectra. Taking cesium–dysprosium molybdate as an example, we show that the structure of the low-frequency vibrational spectrum of these materials is described to sufficient accuracy in the framework of a one-dimensional model. When the dynamic coupling of the electronic and ionic subsystems is taken into account, two qualitatively different scenarios emerge for the formation of the low-frequency electron–phonon spectra. On the basis of an analysis of the experimental data on the change of the electron spectra at structural phase transitions we determine a criterion of the active involvement of low-energy electronic levels in the CJTE.

In Sec. 2 we describe the equilibrium structure of diluted highly anisotropic Jahn–Teller systems. For the three model systems of solid solutions—$KY_{1-x}Dy_x(MoO_4)_2$, $KY_{1-x}Er_x(MoO_4)_2$, and $CsDy_{1-x}Bi_x(MoO_4)_2$—we demonstrate the role of the dynamic coupling of low-energy electronic excitations with crystal lattice vibrations in the formation of the low-frequency spectra and, accordingly, of the equilibrium structures.

In Sec. 3 we discuss research on the spectroscopy of ARDMs in an external magnetic field. It is learned that the dynamic coupling of low-frequency electronic excitations with crystal lattice vibrations in layered Jahn–Teller crystals exhibits significant sensitivity to an external magnetic field. The structure of the crystal lattice can change at relatively low values of the external magnetic field.

In Sec. 4 we analyze the experimental research on the formation of dissipative structures in layered Jahn–Teller crystals found in a highly nonequilibrium state. For the example of the Jahn–Teller crystal $KEr(MoO_4)_2$ it is found that the significant dynamic coupling between the low-energy excitations of the electronic and ionic subsystems makes it possible to create highly nonequilibrium states in the ionic subsystem by exciting the electron subsystem with a microwave field.

In the Conclusion we summarize the basic universal regularities displayed in the dynamics of highly anisotropic Jahn–Teller crystals of rare-earth compounds in respect to low-energy excitations.

1. FORMATION OF LOW-ENERGY EXCITATIONS IN LAYERED RARE-EARTH COMPOUNDS

Before turning to a discussion of the mechanisms of formation of low-energy electronic excitations of the rare-earth ions with allowance for their dynamic coupling with lattice modes, we should explain the features of the structure of the low-frequency phonon spectrum.

1.1. Structure of low-frequency vibrational spectrum of alkali–rare-earth double molybdates (ARDMs)

The vibrational spectra of ARDMs are rather complex. The large number of ions in the unit cell of these compounds makes for a large number of vibrational branches in the spectrum.[14] Because the valences of the constituent ions differ strongly—from 1 for the alkali ions to 6 for the molybdenum ions—the vibrational spectrum has a wide range of frequencies. The low-frequency part is of interest because these excitations determine the low-temperature thermodynamics of these materials. To elucidate the mechanisms of formation of the low-frequency vibrational spectrum, let us examine the features of the crystal structures.

On the whole, ARDM crystals consist of a set of layered packets $[R(Mo)_4)_2^-]_{\infty\infty}$ made up of polyhedra of rare-earth ions and $(MoO_4)^{2-}$ tetrahedra separated by monolayers of alkali ions. The fact that the $[R(MoO_4)_2^-]_{\infty\infty}$ layered packets, with the stronger bonding, are separated by layers of alkali ions $[A^+]_{\infty\infty}$, which are characterized by weak bonding, leads to a layered structure and strong anisotropy of the crystals. The layers have two types of packing: into structures in which neighboring layered packets are translationally equivalent (crystals with a structure of the $CsPr(MoO_4)_2$ type; see Fig. 2a), and into structures with translationally inequivalent layered packets (crystals with a structure of the $KY(MoO_4)_2$ type; see Fig. 2b).[15,16] As in molecular crystals, the low-frequency phonon spectrum in ARDMs is determined by interlayer vibrations (apparently this mechanism is characteristic for other layered compounds as well). Here the role of the molecules is played by the layered packet $[R(MoO_4)_2^-]_{\infty\infty}$. In Refs. 17 and 18 it was shown that the low-frequency vibrational spectra of ARDMs is described to sufficient accuracy by a one-dimensional model.

Let us consider the formation of the low-frequency vibrational spectrum for the example of the $CsDy(MoO_4)_2$ crystal. Figure 3 shows the transmission spectra of $CsDy(MoO_4)_2$ single crystals in the long-wavelength IR region ($13-100\ cm^{-1}$) in polarized light ($\mathbf{E}\|\mathbf{b}$, $\mathbf{E}\|\mathbf{c}$, where $\mathbf{b}$ and $\mathbf{c}$ are crystallographic axes) at a temperature $T=6$ K.[17] There are 5 absorption bands in the spectrum for the polar-

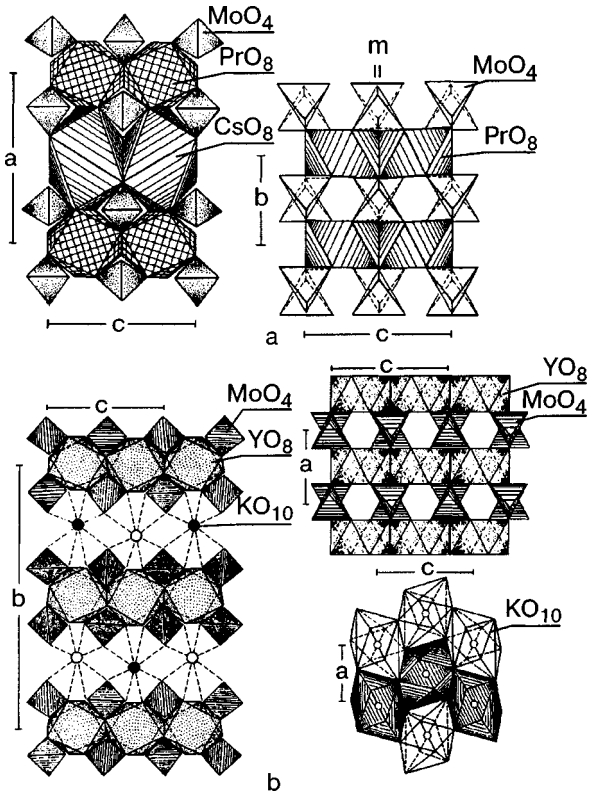

FIG. 2. a—Projection of the $CsPr(MoO_4)_2$ structure on the (010) plane; right—individual unit of the $CsPr(MoO_4)_2$ structure, parallel to (100). b—Projections of the $KY(MoO_4)_2$ structure on the *bc* plane (the K atoms located at heights $x=0$ and $x=1/2$ are represented by different circles) (left) and on the *ac* plane (upper right). Y is an octahedron (shaded by dots), K is a decahedron (unshaded). The wall consisting of ribbons of Y octahedra (shaded by dots) is connected by MoO_4 tetrahedra.[12] The wall consisting of the K decahedra (lower right).

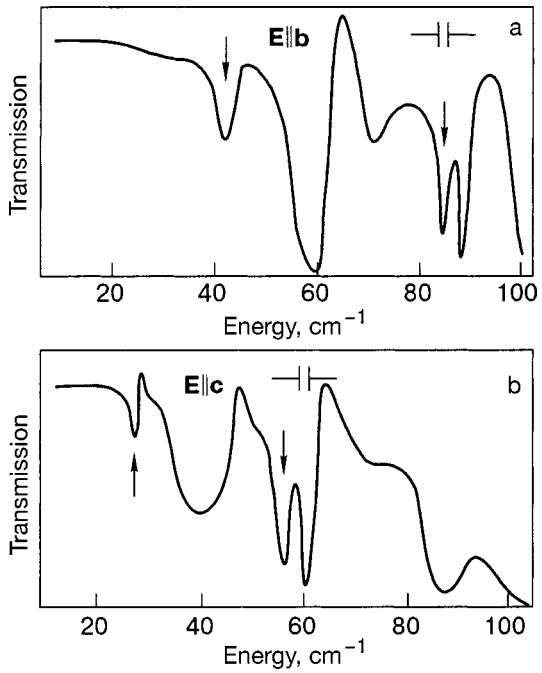

FIG. 3. Transmission spectrum of the $CsDy(MoO_4)_2$ crystal in the polarizations **E**‖**b** (a) and **E**‖**c** (b) at a temperature $T\sim 6$ K. The arrows indicate the absorption bands arising at a temperature below the phase transition ($T_{tr}\sim 40$ K).

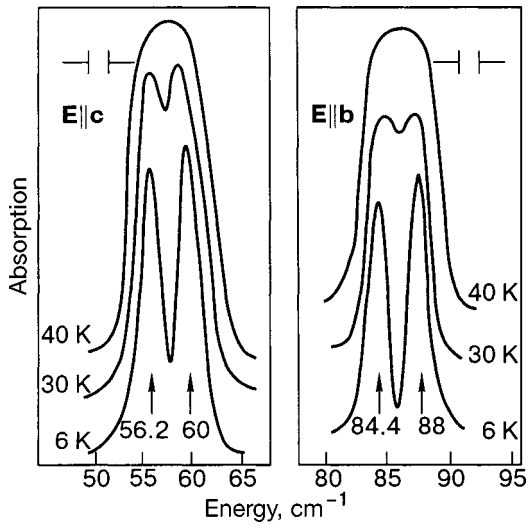

FIG. 4. The form of the absorption bands of the $CsDy(MoO_4)_2$ crystal, which has a doublet structure, for different temperatures.

ization **E**‖**b** and 6 absorption bands for the polarization **E**‖**c**. A characteristic feature is the presence of a doublet band in the 80 cm^{-1} energy region in the polarization **E**‖**b** and in the 60 cm^{-1} energy region in the polarization **E**‖**c**. It can be supposed that these bands are due to vibrations of the $[Cs^+]_{\infty\infty}$ layers relative to the layered packets $[Dy(MoO_4)_2^-]_{\infty\infty}$. At a temperature below the temperature of the structural phase transition ($T_{tr}=40$ K) there occurs a multiplication of the crystal lattice parameter in the direction perpendicular to the plane of the layered packets. This gives rise to Davydov splitting and to the formation of doublets of the absorption bands indicated above.

At a temperature above T_{tr} these bands do not exhibit the doublet structure; it is also absent in the spectrum of the isostructural crystal $CsTb(MoO_4)_2$, in which a phase transi-

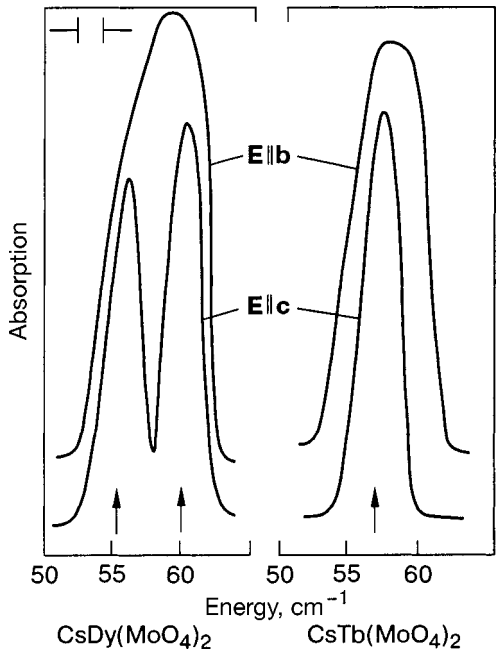

FIG. 5. Absorption bands of the crystals $CsDy(MoO_4)_2$ and $CsTb(MoO_4)_2$ at $T\sim 6$ K.

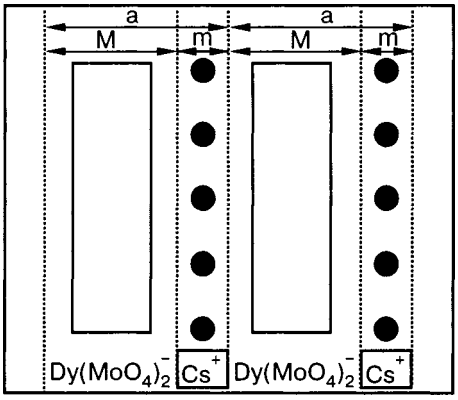

FIG. 6. Schematic illustration of the one-dimensional structure of $CsDy(MoO_4)_2$; the layers have different masses and are oppositely charged (the layers are bounded by the dotted lines).

tion does not occur (Figs. 4 and 5). These facts confirm that the doublet structure of the absorption bands in the $CsDy(MoO_4)_2$ crystal is due to a structural phase transition.[17]

For calculating the low-frequency vibrational spectrum of the $CsDy(MoO_4)_2$ crystal a model in the form of a one-dimensional chain consisting of $[Dy(MoO_4)_2^-]_{\infty\infty}$ layered packets and $[Cs^+]_{\infty\infty}$ layers has been proposed (see Fig. 6). The low-frequency spectrum was calculated according to the formula for the dispersion of the vibrational branches of a linear chain of atoms with masses m and M:

$$\omega^2=\alpha(1/m+1/M)\pm\alpha[(1/m+1/M)^2 - 4\sin^2 ka/mM]^{1/2}. \quad (1.1)$$

The plus sign corresponds to the upper, optical branch and the minus sign to the acoustic branch.

The values of the limiting frequencies of these branches are:

— optical branch

$$\omega_o=[2\alpha(1/m+1/M)]^{1/2} \text{ for } k=0, \quad (1.2)$$

$$\omega_o\mp[2\alpha/m]^{1/2} \text{ for } k=\pi/a; \quad (1.3)$$

— acoustic branch

$$\omega_a=[2\alpha k^2(a/2)^2/M+m]^{1/2} \text{ for } k\approx 0, \quad (1.4)$$

$$\omega_a=[2\alpha/M]^{1/2} \text{ for } k=\pi/a, \quad (1.5)$$

where a is the unit cell parameter, α is the shear force constant, $\omega=2\pi\nu$ is the angular frequency, and $\mathbf{k}$ is the quasi-wave vector.

Using the values of the frequencies at the Brillouin zone center at $k=0$, we calculated the values of the constants α and the dependence of the energies on the modulus of the wave vector $\mathbf{k}$ in the Brillouin zone for different directions of vibration of the layered packets (Fig. 7). The values of the calculated energies of the two transverse acoustic branches at the Brillouin zone boundary ($\nu_1=27\ \text{cm}^{-1}$ and $\nu_2=41\ \text{cm}^{-1}$) agree rather well with the values of the energies of the corresponding absorption bands below the phase transition (see Fig. 3), measured in the IR region of the spectrum. From these calculations the velocities of transverse sound were also obtained in the framework of a one-dimensional model; they agree rather well with the values measured by ultrasonic methods[19] (see Table I).

The one-dimensional model was used to calculate the dispersion of the low-frequency vibrational branches in the Brillouin zone of crystals with structure of the $KY(MoO_4)_2$ type, in which neighboring $[R(MoO_4)_2^-]_{\infty\infty}$ layered packets are translationally inequivalent. For these crystals the one-dimensional model was chosen in a somewhat different form (see Fig. 8).[18] The constants α were determined according to formula (1.2) using the values of the frequencies of optical–acoustic branches corresponding to the antiphase vibrations of neighboring $[R(MoO_4)_2^-]_{\infty\infty}$ layered packets (since these excitations are active in the IR spectrum at $k\approx 0$). The dispersion curves of the vibrational branches in the Brillouin zone of the isostructural crystals $KEr(MoO_4)_2$, $KY(MoO_4)_2$, and $KDy(MoO_4)_2$ are presented in Fig. 9. The longitudinal acoustic and optical–acoustic branches in these

TABLE I. Values of the shear force constants α, limiting energies of optical and acoustic branches ($\mathbf{k}\|[010]$ and $\mathbf{u}\|[001],[100]$), and the values $S\cdot 10^{-3}$ m/s of the transverse sound velocities ($\mathbf{k}\|\mathbf{a}$ and $\mathbf{k}\|\mathbf{b}$) calculated with the use of the optical spectra and measured experimentally by ultrasonic methods.

Substance	Polarization	α, N/m	Energy, cm^{-1} $k=0$	Energy, cm^{-1} $k=\pi/a$		Sound velocity $S\cdot 10^{-3}$ m/s	
				ω_o	ω_a	$\mathbf{k}\parallel\mathbf{a}$, $\mathbf{k}\parallel\mathbf{b}$ (calc.)	Experiment
$CsDy(MoO_4)_2$	E ∥ b	22.8	86.1	76.2	40	3.17	2.71 ± 0.2
	E ∥ c	10.4	58.1	51.5	27	2.15	1.74 ± 0.2
$KY(MoO_4)_2$	E ∥ a	2.21	18.7	13.8	12.6	1.57	1.75 ± 0.2
	E ∥ c	5.18	28	20.6	18.9	2.38	2.16 ± 0.2
$KEr(MoO_4)_2$	E ∥ a	2.42	18.5	13.6	12.6	1.51	1.55 ± 0.2
	E ∥ c	5.1	26	19.1	17.6	2.22	2.00 ± 0.2
$KDy(MoO_4)_2$	E ∥ a	2.41	17.7	13.0	12.0	1.51	1.5 ± 0.2
	E ∥ c	5.4	26.5	19.5	18.0	2.3	2.14 ± 0.2

Note: IR radiation with polarization $\mathbf{E}\|\mathbf{a}$, $\mathbf{E}\|\mathbf{b}$, and $\mathbf{E}\|\mathbf{c}$ excites displacements corresponding to sound waves propagating along **a** and **b**, with the polarization vector of the displacements $\mathbf{u}\|[100]$, $\mathbf{u}\|[010]$, and $\mathbf{u}\|[001]$, respectively.

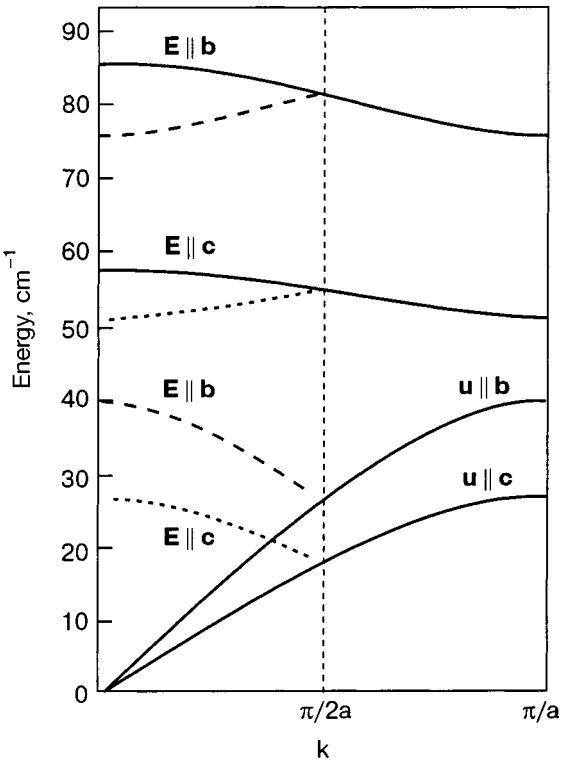

FIG. 7. Dispersion curves of the low-frequency vibrational spectrum of the $CsDy(MoO_4)_2$ crystal, calculated in the one-dimensional model[17] according to formula (1.1).

compounds were calculated using the values of the constants α obtained from the ratios of the sound velocities for the longitudinal and transverse polarizations, measured by ultrasonic methods.[19–21]

The good agreement between the velocities of transverse sound calculated from the optical spectra and the values measured experimentally by ultrasonic methods suggests that the one-dimensional model gives a rather good description of the low-frequency vibrational spectra of ARDMs.

The values of the sound velocities calculated from the optical spectra and measured experimentally by ultrasonic methods for several ARDMs are listed in Table I. Also given are the values of the shear force constants and the limiting energies of the optical–acoustic and acoustic branches at the boundary of the Brillouin zone calculated in the framework of one-dimensional models.

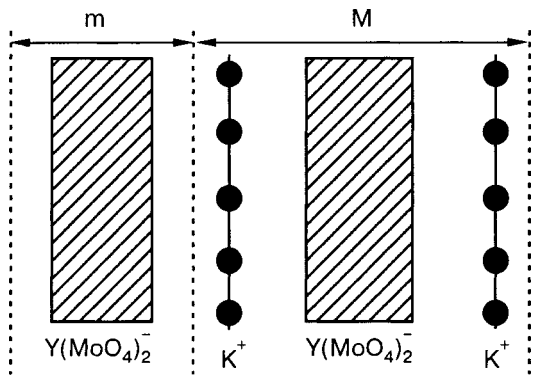

FIG. 8. Schematic illustration of the one-dimensional structure of $KY(MoO_4)_2$; the layers have different masses and are oppositely charged (the layers are bounded by the dotted lines).

1.2. Low-energy electronic spectrum of rare-earth ions in ARDMs

In addition to the bands due to excitation of lattice vibrations, the low-energy absorption spectrum of ARDMs in the long-wavelength IR region also contains absorption bands due the excitation of electrons of the $4f$ shell of the rare-earth ions. It is known that the static crystalline field in these compounds leads to lifting of the orbital degeneracy of the ground-state multiplets of the rare-earth ions. As a consequence of this, rather well developed structure of the electronic excitations appears in the low-energy spectrum. The main contribution to the formation of the electronic spectrum of the rare-earth ions comes from the static crystalline field of the ligands. Calculation of the electronic spectrum of ARDMs with the use of crystalline field theory is complicated by the fact that the local symmetry of the R^{3+} sites is quite low (C_1, C_2, D_2), and it would therefore seem necessary to take into account a rather large number of constants. This can lead to ambiguity in the determination of those constants. In calculating the constants of the crystalline field in these compounds (e.g., for the Dy^{3+} ions in $KDy(MoO_4)_2$) the problem can be simplified by choosing more highly symmetric sites, namely C_4 (Ref. 22). This can be explained by proceeding from the features of the crystalline structure of $KDy(MoO_4)_2$. The nearest-neighbor environment of the Dy^{3+} ions is a slightly distorted octahedron formed by oxygen ions, which makes for a local distortion close to tetragonal (see Fig. 2b); in this case the contribution of the rhombic component of the static crystalline field of the ligands is insignificant. Therefore for description of the electron spectrum of the $KDy(MoO_4)_2$ crystal one can use a Hamiltonian of tetragonal symmetry, which is given in operator form as

$$\mathcal{H}=\alpha B_2^0 O_2^0+\beta B_4^0 O_4^0+\gamma B_6^0 O_6^0+\beta B_4^4 O_4^4+\gamma B_6^4 O_6^4, \tag{1.6}$$

where B_n^m are the crystal-field parameters, O_n^m are equivalent operators, and α, β, and γ are the coefficients of conversion of the matrix elements from the coordinate notation to operator form.

The set of values of the parameters B_n^m (in cm^{-1}) giving the best agreement of the calculated and experimental data on the values of the position and splitting of the ${}^6H_{15/2}$, ${}^6F_{3/2}$, and ${}^6F_{5/2}$ terms of the Dy^{3+} ions and the g factors of the two lower levels of the ${}^6H_{15/2}$ term is presented in Table II.

The components of the g tensor of the ground and first excited states, determined by perturbation theory in weak magnetic fields, are

$$q_{\parallel}=2g_0\langle+\varphi_n|I_z|+\varphi_n\rangle,$$
$$q_{\perp}=2g_0\langle+\varphi_n|I_x|-\varphi_n\rangle, \tag{1.7}$$

where g_0 is the Lande factor of the free ion and the φ_n are the wave functions of the ground or first excited Kramers doublet.

The calculated components of the g tensor have the following values:

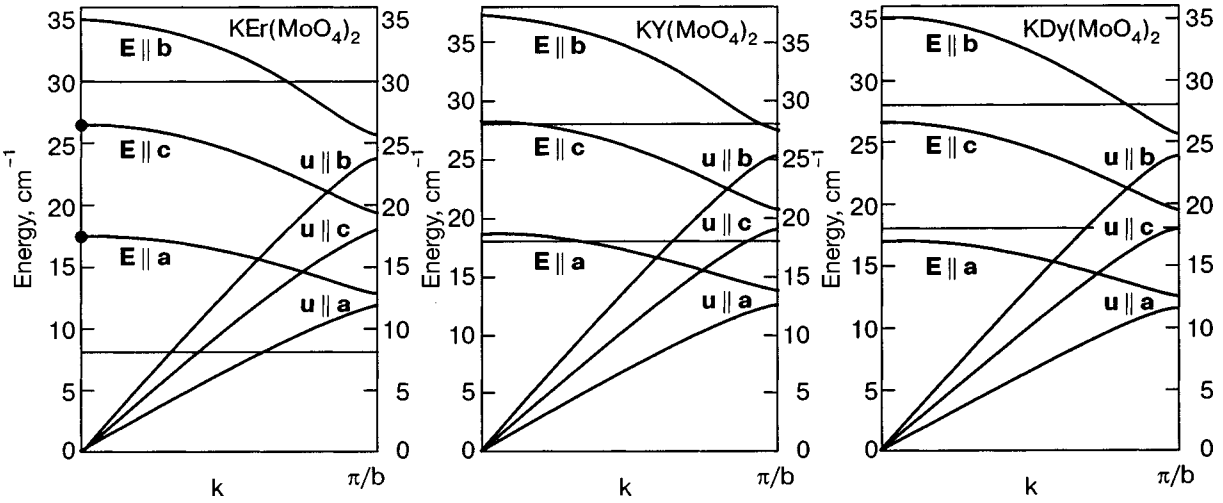

FIG. 9. Dispersion curves of the low-frequency vibrational spectrum of the crystals $KEr(MoO_4)_2$, $KY(MoO_4)_2$, and $KDy(MoO_4)_2$, calculated in the framework of a one-dimensional model. The horizontal lines show the positions of the electronic levels of the rare-earth ions in each compound. The horizontal lines on the dispersion curves of the $KY(MoO_4)_2$ crystal correspond to electronic excitations of Dy^{3+} ions introduced into the crystal.

$g_\parallel = 9.69$; $g_\perp = 0.67$ for the ground doublet;

$g_\parallel = 9.35$; $g_\perp = 0.34$ for the first excited doublet.

These are close to the values obtained experimentally for the g factors in the high-temperature phase of the $KDy(MoO_4)_2$ crystal,[22] which for the ground doublet are equal to $g_x = 9.23$, $g_y = 10.55$, and $g_z = 1.21$. Table III gives the energy spectrum of the ground term $^6H_{15/2}$, as calculated in the tetragonal approximation and determined experimentally in a study of the luminescence.[23] It is seen that the values are in good agreement.

However, along with the the static electric fields of the ligands, the coupling of the electronic and ionic excitations should also play a significant role in the low-energy electron spectrum of rare-earth ions in highly anisotropic compounds. For effective dynamic coupling, the following conditions must hold:

1. The symmetries of the electronic and phonon excitations should be the same.

2. The energies and the wave vectors of the interacting excitations should be equal.

Let us analyze how these conditions are satisfied in ARDMs. We shall consider the symmetry of the vibrational branches with which the low-energy electronic excitations of the rare-earth ions interact in each of these compounds.

Since the formation of the exciton spectrum is governed mainly by the local symmetry of the rare-earth ions while that of the high-frequency vibrational branches is governed mainly by the symmetry of the crystal, for the first condition to be fulfilled it is necessary to establish that the irreducible representations of the corresponding symmetry groups (the local symmetry group and the factor group of the crystal) be compatible. A group theoretical analysis shows that for ARDMs with a structure of the $KY(MoO_4)_2$ type (space group D_{2h}^{14}) the excitonic excitations can interact with two transverse acoustic and optical–acoustic branches or with one longitudinal acoustic and one optical–acoustic branch (see Table IV). In crystals with a structure of the $CsPr(MoO_4)_2$ type the excitonic excitations can interact only with one acoustic or optical–acoustic branch (see Table V).

In crystals with structure of the $CsPr(MoO_4)_2$ type the local symmetry of the rare-earth ions has group D_2, and it is therefore necessary to determine the compatibility of its irreducible representations and the irreducible representations of the factor group D_{2h} (see Table V).

It can be seen from the compatibility tables of the irreducible representations that symmetry allows dynamic coupling between the electronic excitations of the rare-earth ions and odd lattice vibrations. This is because of the rather low local symmetry of the rare-earth ion sites in these compounds. We note that if the dynamic coupling of low-energy excitonic excitations with the corresponding acoustic and optical–acoustic branches of the crystal lattice is allowed by symmetry at the Brillouin zone center, then coupling with these branches is also allowed at the zone boundary or inside the Brillouin zone, depending upon the particular region in

TABLE II. Parameters of the crystalline field B_n^m of the high-temperature phase of $KDy(MoO_4)_2$, calculated in the approximation of tetragonal symmetry.

Parameters, B_n^m	B_2^0	B_4^0	B_6^0	B_4^4	B_6^4
Values, cm^{-1}	−190	−140	4	−980	−220

TABLE III. Energy spectrum of the ground term $^6H_{15/2}$ of the Dy^{3+} ion in $KDy(MoO_4)_2$ in the high-temperature phase.

Level	E, cm^{-1} (calc.)	E, cm^{-1} (exper.[23])
E_0	0	0
E_1	18.2	15 ± 2
E_2	101.3	77 ± 2
E_3	118.3	125 ± 4
E_4	217.0	185 ± 7
E_5	313.6	246 ± 7
E_6	317.2	306 ± 7
E_7	459.3	555 ± 7

TABLE IV. Table of compatibility of the irreducible representations of the factor group D_{2h} and the local symmetry group of the rare-earth ions, C_2.

C_2	Γ_1	Γ_2
D_{2h}	$\Gamma_1^+\Gamma_1^-\Gamma_2^+\Gamma_2^-$	$\Gamma_3^+\Gamma_3^-\Gamma_4^+\Gamma_4^-$

which the crossing of the excitonic and vibrational branches of the spectrum occurs.

The energy position of the electronic levels relative to the vibrational branches determines the strength of their dynamic coupling with the vibrational spectrum. The experimental results show that there are several possible scenarios for the manifestation of this coupling in the low-frequency spectra.

When the electronic level crosses the vibrational branch between the Brillouin zone boundary and zone center, a restructuring of the low-frequency spectrum occurs, with the formation of hybrid electron–phonon branches and the formation of a ''quasigap'' in the spectrum.[18] In the $KEr(MoO_4)_2$ crystal, for example, the electronic level with energy $\nu=8\ \mathrm{cm}^{-1}$ crosses two transverse acoustic vibrational branches with which dynamic coupling is symmetry allowed, between the Brillouin zone center and boundary (see Fig. 9). The spectrum in the case of such a coupling of the electronic level with one vibrational branch is shown schematically in Fig. 10. It is seen that a ''quasigap'' is formed in the spectrum. This scenario is brought about by the relatively weak dynamic coupling, since in the region where the electronic level crosses the vibrational branches between the zone center and zone boundary, the density of vibrational states is insignificant.

A qualitatively different situation is realized in the crossing of acoustic or optical–acoustic vibrational branches by electronic levels near the Brillouin zone center or zone boundary. Since the structure of the vibrational spectrum is described by a one-dimensional model, the density of states of the vibrational branches in this case has its maximum value (see Fig. 1b). Therefore, when electronic levels cross vibrational branches near the Brillouin zone center or zone boundary, a strong dynamic coupling of the electron and ion subsystems arises, with the formation of vibronic states.[24]

Let us analyze how the strong coupling influences the low-frequency absorption spectrum. In the $KDy(MoO_4)_2$ crystal, for example, the electronic absorption band with maximum at $\nu\approx18\ \mathrm{cm}^{-1}$, corresponding to a transition to the first electronic level, which crosses an optical–acoustic vibrational branch near the Brillouin zone center and an acoustic branch near the zone boundary, has a half-width $\Delta\nu\approx14\ \mathrm{cm}^{-1}$ (see Figs. 9 and 11),[25,26] whereas in the $KEr(MoO_4)_2$ crystal at a weak dynamic coupling the half-width $\Delta\nu$ of the corresponding electronic absorption band is $\approx1.5\ \mathrm{cm}^{-1}$ (Ref. 18). In the $CsDy(MoO_4)_2$ crystal the electronic level with excitation energy $\nu\approx40\ \mathrm{cm}^{-1}$ crosses a transverse acoustic branch with which dynamic coupling is symmetry allowed, and therefore appreciable dynamic coupling between them occurs ($\Delta\nu\approx25\ \mathrm{cm}^{-1}$). The electronic level with energy $\nu\approx22\ \mathrm{cm}^{-1}$ in this last crystal crosses an acoustic vibrational branch with which dynamic coupling is symmetry allowed, between the Brillouin zone center and zone boundary, and their dynamic coupling is relatively weak ($\Delta\nu\approx2\ \mathrm{cm}^{-1}$) (see Fig. 12). Thus one can state that the half-widths of the low-energy electronic absorption bands are an indicator of dynamic coupling of low-energy electronic levels of the rare-earth ions with the vibrational branches.

TABLE V. Table of compatibility of the irreducible representations of the group D_{2h} and the group of local symmetry of the rare-earth ions, D_2.

D_2	Γ_1	Γ_2	Γ_3	Γ_4
D_{2h}	$\Gamma_1^+\Gamma_1^-$	$\Gamma_2^+\Gamma_2^-$	$\Gamma_3^+\Gamma_3^-$	$\Gamma_4^+\Gamma_4^-$

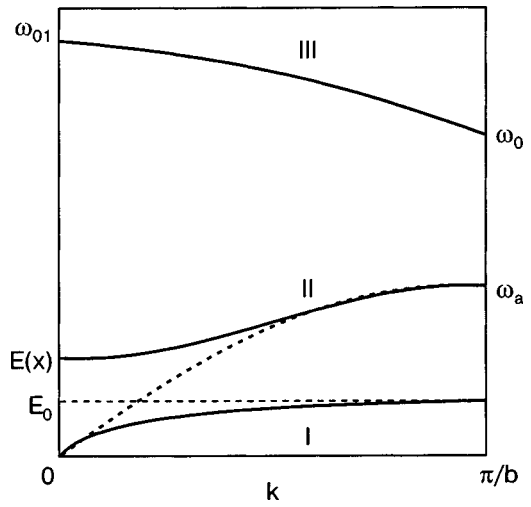

FIG. 10. Schematic illustration of the dispersion curves of the low-frequency spectrum of the $KEr(MoO_4)_2$ crystal in the case of weak dynamic coupling of the electronic excitation with the vibrational branches; I and II are electron–phonon branches, III is an optical–acoustic photon branch. The dashed line shows the position of the electronic level, and the dotted line the dispersion of the acoustic branch of the crystal in the absence of dynamic coupling (not drawn to scale).

1.3. Low-energy excitation spectrum of ARDMs and structural phase transitions of the cooperative Jahn–Teller effect (CJTE) type

The activity of low-energy electronic levels in ARDMs at structural phase transitions due to the CJTE is a topic of definite interest.

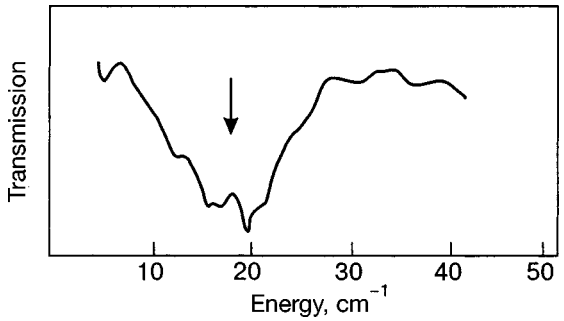

FIG. 11. Transmission spectrum of the $KDy(MoO_4)_2$ crystal in the long-wavelength IR range at $T>T_{tr}$.[25] The electronic absorption band is indicated by an arrow (its half-width is $\Delta\approx14\ \mathrm{cm}^{-1}$).

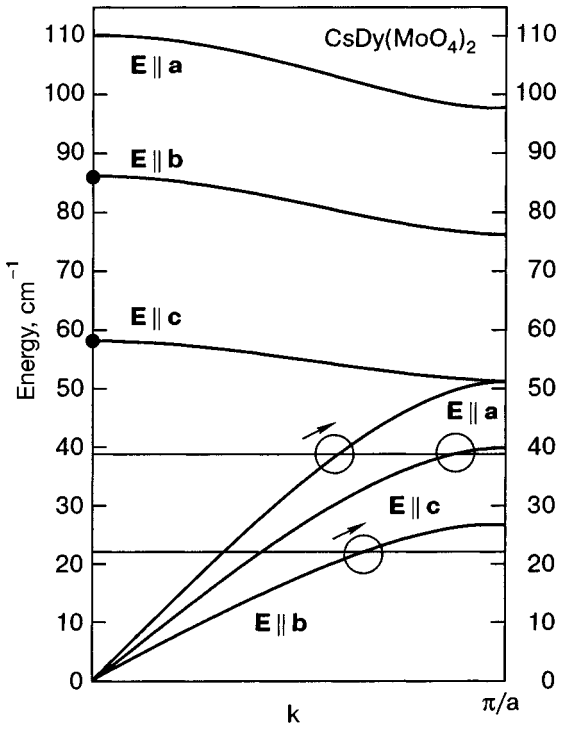

FIG. 12. Electronic and vibrational spectra of the $CsDy(MoO_4)_4$ crystal at a temperature $T>T_{tr}$. The horizontal lines are the electronic levels of the Dy^{3+} ions. The circles denote the crossing points of the electronic levels with the vibrational branches with which interaction is allowed by symmetry. The arrows indicate the direction of the shift of the crossing points upon the introduction of impurities that decrease the energy of the vibrational branches.

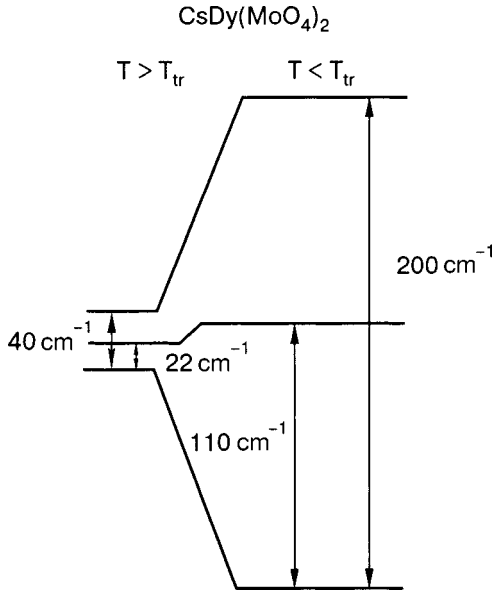

FIG. 13. Scheme of the splitting of the low-energy electronic levels of the Dy^{3+} ions in the $CsDy(MoO_4)_2$ crystal above and below the temperature of the structural phase transition ($T_{tr}=40$ K).

Since ARDMs have a layered crystal structure, low-temperature phase transitions due to anharmonicity of lattice vibrations involving the interlayer bonds can occur in them.[27] For example, the diamagnetic crystal $CsBi(MoO_4)_2$ has two phase transitions, at transition temperatures $T_{tr1}=135$ K and $T_{tr2}=290$ K.[28–30] Analogous phase transitions occur in crystals of rare-earth compounds,[31,32] but we shall mainly be concerned with the phase transitions due to the CJTE.

From what physical properties can we infer the presence of a CJTE mechanism? First, the temperatures at which these structural phase transitions occur are sensitive to external magnetic field. Second, it is sometimes possible to determine a CJTE origin from an estimate of the energy conversion at the structural phase transition. Here the relation $\Delta E \approx H + U$ must hold (ΔE is the lowering of the internal energy of the electron subsystem, H is the latent heat of the structural phase transition, and U is the elastic strain energy). For example, such estimates of the energy conversions at the structural phase transition ($T_{tr}=40$ K) have been made for the $CsDy(MoO_4)_2$ crystal: $\Delta E=1$ kJ,[29] $H=0.64$ kJ,[31] and the elastic strain energy determined from the values of the strains[33] at the phase transition and the values of the elastic constants[17] is $U=0.3$ kJ. Thus the relation given above is practically satisfied, and on that basis we can attribute this phase transition to the CJTE.

Let us consider the changes that occur in the electron spectrum at structural phase transitions due to the CJTE. Figure 13 shows a level scheme of the Dy^{3+} ions in the $CsDy(MoO_4)_2$ crystal at temperatures above and below the temperature T_{tr} of a structural phase transition of the CJTE type.[34–36] It is seen that the electronic level with energy $\nu_2 \approx 40$ cm^{-1} is active in the phase transition; it crosses an acoustic vibrational branch near the Brillouin zone boundary; the level with excitation energy $\nu_1 \approx 22$ cm^{-1} is not active; it crosses an acoustic branch with which dynamic coupling is symmetry allowed, between the Brillouin zone center and zone boundary, where the density of states is insignificant. An analogous situation is realized in the crystal $KDy(MoO_4)_2$: the first excited level ($\nu \approx 18$ cm^{-1}), which is active in the structural phase transition, crosses an optical–acoustic branch near the Brillouin zone center and an acoustic branch near the zone boundary, where the density of states is maximal (see Figs. 9 and 14). Thus one can say that in ARDMs the levels active in the structural phase transitions of the CJTE type are low-energy electronic levels that cross acoustic or optical–acoustic branches in the region of maximum density of states. This is confirmed by the absence of a

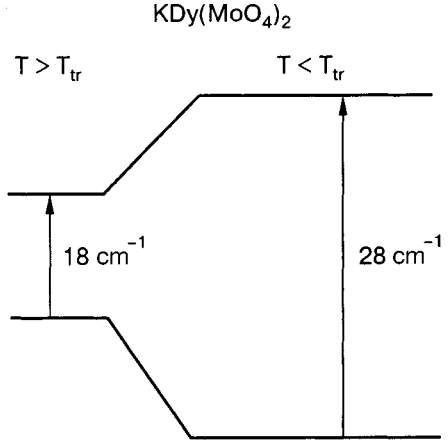

FIG. 14. Scheme of the splitting of the low-energy electronic level of the ions Dy^{3+} in the $KDy(MoO_4)_2$ crystal above and below the temperature of the structural phase transition ($T_{tr}=14$ K).

TABLE VI. Temperatures of the structural phase transitions of a number of ARDMs.

Substance	T_{tr}, K	Ref.
$KDy(MoO_4)_2$	14.3	[37,38]
$RbDy(MoO_4)_2$	19	[39,40]
$CsDy(MoO_4)_2$	59, 40	[41,42]
$CsHo(MoO_4)_2$	11	[36]

CJTE-induced phase transition in the $KEr(MoO_4)_2$ crystal. In this last compound the lowest energy level is only 8 cm^{-1} from the ground level but its crossing with the transverse acoustic branches with which its coupling is symmetry allowed occurs in the region between the Brillouin zone center and zone boundary, where the density of states is maximum.

Studies of the spectra and of the physical properties of a number of ARDMs have made it possible to establish the temperatures of the CJTE-induced structural phase transitions. The corresponding data are given in Table VI.

Thus the experiments have succeeded in establishing that different types of equilibrium structures exist in these compounds at low temperatures, depending on where in the Brillouin zone the crossing of the low-frequency vibrational branches with low-energy electronic levels of the rare-earth ion occurs. Consequently, one can say that by varying the strength of the dynamic coupling of the electron and ion subsystems one can influence the equilibrium structures of these materials. That is, by acting on the electron or ion subsystem to change the position of the electronic levels with respect to the vibrational spectrum, one can change the strength of the dynamic coupling and bring about a transformation of the ordering that arises in the CJTE.

In what follows it will be shown on the basis of experimental data that this can be brought about either by doping the crystals with isostructural impurities, thereby shifting the vibrational branches without materially altering the energy position of the electronic levels, or by changing the energy position of the electronic levels of the rare-earth ions with respect to the vibrational branches through the application of external influences, e.g., an external magnetic field.

2. FORMATION OF EQUILIBRIUM STRUCTURES OF DILUTED HIGHLY ANISOTROPIC JAHN–TELLER SYSTEMS

Diluted Jahn–Teller systems are of interest for several reasons. First, according to theoretical ideas, in solutions of substitution in which the Jahn–Teller ions are replaced by a diamagnetic analog, structural disorder of the Jahn–Teller glass type can arise.[43,44] Second, the substitution of the Jahn–Teller ion by a diamagnetic impurity alters the structure of the vibrational spectrum, and its relationship to the position of the electronic levels of the rare-earth ions changes. This can lead to a change in the strength of the coupling of the low-energy electronic excitations of the rare-earth ions with lattice vibrations. Increasing or decreasing the dynamic electron–phonon coupling can lead to stimulation or suppression of the Jahn–Teller effect.

Let us elucidate the features of the dynamics (in respect to low-energy excitations) of layered Jahn–Teller crystals diluted with a diamagnetic impurity. For this purpose we analyze the spectroscopic studies of several systems of isostructural solid solutions of the ARDM type: $KDy(MoO_4)_2-KY(MoO_4)_2$, $KEr(MoO_4)_2-KY(MoO_4)_2$, and $CsDy(MoO_4)_2-CsBi(MoO_4)_2$ and also of Jahn–Teller crystals diluted with trivalent non-Jahn–Teller impurities. Because in these compounds the paramagnetic Jahn–Teller ions were diluted with a diamagnetic analog, one can trace the evolution of the coupling of the low-energy electronic excitations of the rare-earth ions with crystal lattice vibrations as the concentration of the Jahn–Teller ions is increased or decreased.

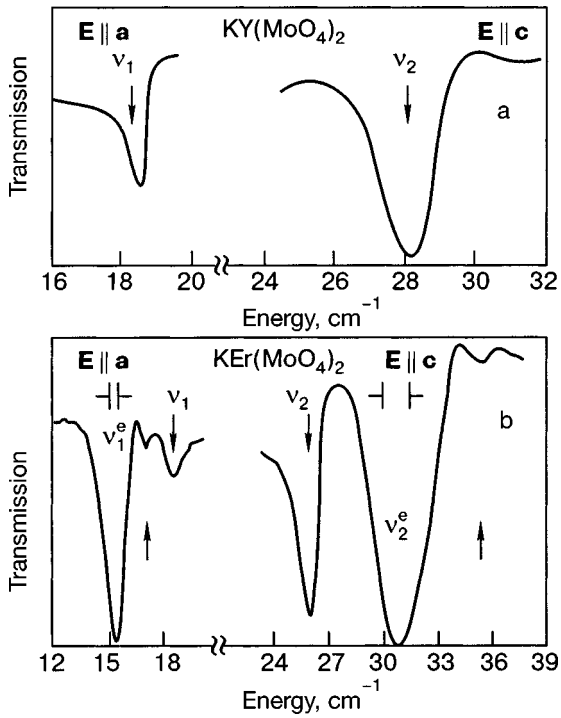

FIG. 15. Transmission spectra of the $KY(MoO_4)_2$ and $KEr(MoO_4)_2$ crystals in the frequency interval 12–40 cm^{-1} at a temperature of ~6 K in polarized light.

2.1. Low-energy spectrum of crystals of the solid solutions $KY(MoO_4)_2-KEr(MoO_4)_2$

Since the parameters of the crystal lattices of the pure end compounds $KY(MoO_4)_2$ and $KEr(MoO_4)_2$ are not much different,[11] it was assumed that the $KY_{1-x}Er_x(MoO_4)_2$ system under study forms a continuous series of solid solutions of isomorphic substitution in the entire composition interval $(0 \leqslant x \leqslant 1)$, in which case the Er^{3+} and Y^{3+} ions should be distributed randomly over the ion sites of the rare-earth lattice.

The long-wavelength IR transmission spectra of a series of $KY_{1-x}Er_x(MoO_4)_2$ single crystals of composition $x=0$, 0.05, 0.1, 0.2, 0.5, 0.7, and 1.0 were measured in polarized light ($\mathbf{E}\|\mathbf{a}$ and $\mathbf{E}\|\mathbf{c}$).[18] The main measurements of the transmission spectra were made at a temperature of ≈6 K. The transmission spectra of single crystals of the end compounds $KY(MoO_4)_2$ and $KEr(MoO_4)_2$ are shown in Fig. 15.

The transmission spectrum of $KY(MoO_4)_2$ exhibits two absorption bands with peak energies of $\nu_1^{ph}=18.7$ cm^{-1} (the polarization $\mathbf{E}\|\mathbf{a}$) and $\nu_2^{ph}=28.2$ cm^{-1} (in the polarization

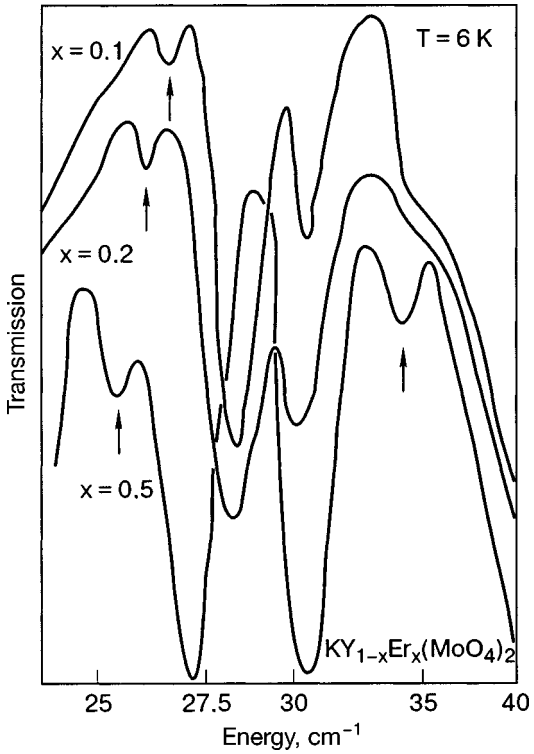

FIG. 16. Transmission spectra of the mixed crystals $KY_{1-x}Er_c(MoO_4)_2$ at a temperature of ~6 K. The spectra have not been normalized to the signal in the absence of a sample.

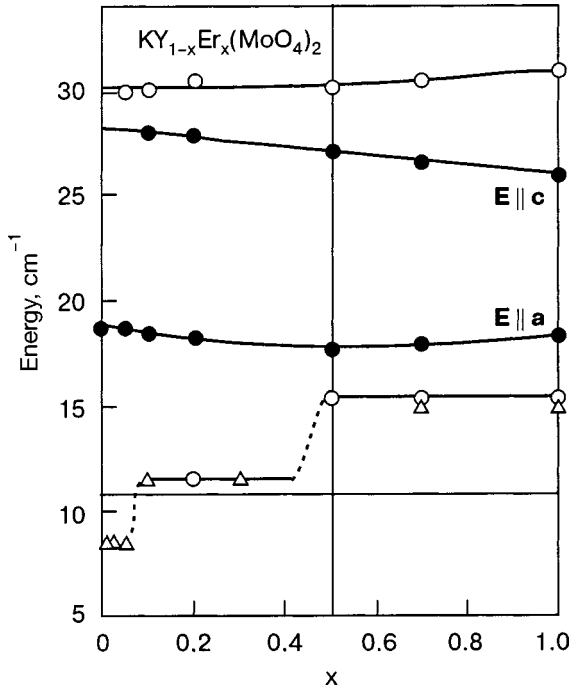

FIG. 17. Concentration dependence of the maxima of the absorption peaks in the spectra of the $KY_{1-x}Er_x(MoO_4)_2$ ($x=0$, 0.05, 0.1, 0.2, 0.5, 0.7, and 1.0) at a temperature $T\sim 6$ K. Data of Ref. 45 (△), vibrational bands (●); electronic bands (○).

E∥**c**). The transmission spectrum of the $KEr(MoO_4)_2$ crystal has a more complex form. In the polarizations **E**∥**a** and **E**∥**c** the $KEr(MoO_4)_2$ spectrum has absorption bands with peak energies $\nu_1^{ph}=18.5$ cm^{-1} and $\nu_2^{ph}=26$ cm^{-1}. In addition, there are intense bands whose maxima in unpolarized light are close to the energies $\nu_1^e=15.4$ cm^{-1} and $\nu_2^e=30.5$ cm^{-1} and which are due to excitation of the Er^{3+} ions. In the polarized spectra the maxima of these lines are possibly the same in the polarizations **E**∥**a** and **E**∥**c** ($\Delta\nu\sim 0.1$–0.2 cm^{-1}), indicating that these excitations are of a localized character. These bands are not observed in the spectrum of the $KY(MoO_4)_2$ crystal; dilution by even a small concentration of Er^{3+} impurity ions leads to the appearance of ν_1^e and ν_2^e bands (Fig. 16 shows the evolution of a part of the spectrum in mixed crystals upon a change in the Er^{3+} concentration from $x=0.1$ to $x=0.5$). The dependence of the energies of the absorption bands on the concentration of the components of the solution is shown in Fig. 17. It is seen that the position of the lowest-energy absorption band ($\nu_1^e=15.4$ cm^{-1}), which is due to excitation of the Er^{3+} ions, remains unchanged in the concentration interval $0.5\leqslant x\leqslant 1$. In the concentration interval $0.3<x<0.5$ its energy decreases to a value of 11.5 cm^{-1}, and for $x<0.07$ one has $\nu_1^e=8$ cm^{-1} (Ref. 45). All of these changes occur in a threshold manner in the impurity concentration. In contrast to ν_1^e, the position of the band with frequency ν_2^e changes little with the impurity concentration. The energy of this band increases from $\nu\sim 30$ cm^{-1} at a low Er^{3+} concentration to $\nu\sim 30.5$ cm^{-1} for the end compound $KEr(MoO_4)_2$. The transmission spectrum of $KEr(MoO_4)_2$ exhibits weak satellites, indicated by arrows in Fig. 16. Temperature measurements of the energy position of the lowest electronic excitation, with energy $\nu_1^e=15.4$ cm^{-1} in the IR region (see Fig. 18), showed that the intensity of this band decreases smoothly with increasing temperature. When the temperature was lowered from 35 to 2 K the ν_1^e band did not exhibit the change in position that is characteristic of the CJTE. This is

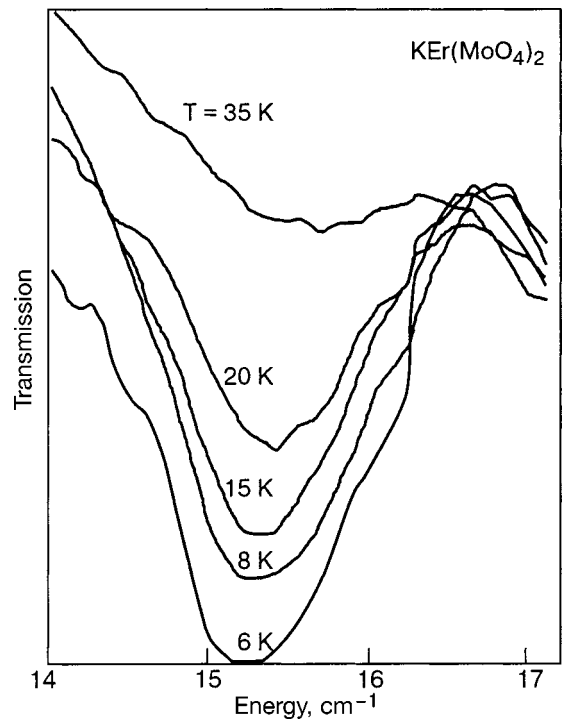

FIG. 18. Shape of the electronic absorption band formed by transition from the ground to the first excited state of the Er^{3+} ions in the crystal $KEr(MoO_4)_2$ at different temperatures.

evidence of the absence of a structural phase transition of the CJTE type in the temperature region 2–35 K.

Let us briefly discuss the evolution of the low-frequency spectrum in the system $KY_{1-x}Er_x(MoO_4)_2$ with changing composition. The compounds under study, both the pure end compounds and the mixed compounds, have a layered structure. The coupling forces within the layered packets $[Er_{1-x}Y_x(MoO_4)_2^-]_{\infty\infty}$ are much stronger than the interaction between these packets. The crystal structure of these compounds is such that the unit cell of the end compounds contains two translationally inequivalent layered packets. Therefore optical–acoustic branches (two transverse and one longitudinal) arise in the low-energy spectrum due to oscillations of the layered packets with respect to each other along different crystallographic directions. These are the lowest-energy optical vibrational branches in the crystals.[29]

The behavior of the vibrational spectra of the mixed crystals is explained with the use of a one-dimensional model. The concentration dependence of the frequencies of the vibrational modes (Fig. 17) can be explained qualitatively as follows. According to the experimental data, the isotope shift Δ—the change of the energy of phonon excitations on going from $KEr(MoO_4)_2$ to $KY(MoO_4)_2$—is not more than 2 cm^{-1}. According to general notions,[46] in the case $\Delta<\Gamma$, where Γ is a quantity characterizing the dispersion of the vibrational branches in the Brillouin zone, the behavior of the spectrum in mixed crystals should be single-mode, i.e., the vibrational energy should shift smoothly from one end value to the other. The difference in the vibrational energies for $k=0$ and $k=\pi/a$ has a value $\Gamma\sim 5-7$ cm^{-1} for each of the branches of the spectrum (see Table I), i.e., $\Delta<\Gamma$.

The single-mode behavior of the spectrum can also be explained on a qualitative level using the mechanism of formation of the low-frequency vibrational branches. The Y^{3+} and Er^{3+} impurity ions are distributed randomly over the layered packets $[Er_{1-x}Y_x(MoO_4)_2^-]_{\infty\infty}$, and therefore the masses of the layered packets will be equal, and their value is determined by the relative contribution from the impurities. Since the low-frequency vibrational branches are formed by vibrations of the layered packets as a whole, their energies will vary smoothly as the reduced mass of the layered packets varies from one end compound to the other. Experimentally one observes a linear dependence of the change in energy of the vibrational mode ν_2^{ph} on the impurity concentration, from one extreme value, 26 cm^{-1} for the $KEr(MoO_4)_2$ crystal, to the other, 28.2 cm^{-1} in $KY(MoO_4)_2$. The shift of the low-frequency vibrational mode ν_1^{ph} has a nonlinear character, which may be explained by the presence of a nearby electronic excitation.

Besides the bands of vibrational modes, the spectrum of the mixed crystals also exhibits two absorption bands due to transitions to the first two Stark levels of the ground multiplet $^4I_{15/2}$ of the Er^{3+} ions, which is split by the crystalline field. These bands behave differently with variation of the concentration of the components of the solid solution. The energy of the maximum of the absorption band $\nu_2^e \approx 30$ cm^{-1} changes insignificantly with variation of the concentration of the diamagnetic impurity, since the corresponding electronic level crosses only a longitudinal optical–acoustic branch with which dynamic coupling is forbidden by symmetry (see Fig. 9). On the other hand, the frequency of the lowest electronic excitation decreases significantly as the concentration of the diamagnetic impurity is increased (see Fig. 17), since the corresponding electronic level crosses two transverse acoustic branches with which dynamic coupling is symmetry allowed.

The concentration dependence of the position of the lowest electronic excitation and also the concentration threshold effect can be explained by invoking the concepts of cross splitting of the acoustic spectrum in crystals containing impurities, an effect predicted by Kosevich.[47] According to the model proposed in Ref. 47, the introduction of a heavy impurity into a crystal causes the frequency of its local vibrational modes to fall within the region of the continuous spectrum. When the heavy impurity concentration reaches a sufficient level ($x>x_{cr}$) a restructuring of the spectrum of long-wavelength oscillations of the crystal occurs, as a result of which the frequency of the quasilocal modes at the Brillouin zone center increases. This effect has a threshold character in the concentration of the rare-earth ions and is of a dynamic nature.

In the proposed system the static crystalline field splits the lowest multiplet $^4I_{15/2}$ of the Er^{3+} ions in such a way that the first excited levels $\nu_1^e=8$ cm^{-1} crosses two transverse and one longitudinal acoustic branches between the Brillouin zone center and zone boundary. The dynamic coupling of the excitation corresponding to the transition to this level with the two transverse acoustic branches also leads to the formation of a quasigap.

The existence of two concentration thresholds for mixed crystals with a highly anisotropic structure can be explained by the different strength of the interaction of the electronic excitation with two vibrational branches.[48] In Ref. 48 the idea of dynamic splitting of the vibrational spectrum was considered for low-dimensional systems, and it was shown that more than one concentration threshold can exist. This is explained by the anisotropy of the interaction of the impurity excitation with the continuous spectrum. In this case the cross interaction occurs with different acoustic branches and is characterized by a different value of the splitting, as is typical for the $KY_{1-x}Er_x(MoO_4)_2$ system.

We note that the energy of the excitonic branch at the Brillouin zone boundary remains unchanged over the whole interval of rare-earth ion concentrations. This is confirmed experimentally in measurements of the transmission spectra of $KY_{1-x}Er_x(MoO_4)_2$ crystals in the visible region of the spectrum. The value of the gap at the Brillouin zone boundary point was determined from the energy interval between the frequency of the 0–0 transition and the satellite corresponding to the transition to the first excited state of the crystal-field-split ground multiplet $^4I_{15/2}$, which appears in the spectrum as the temperature is raised. In the mixed crystals the gap remains practically unchanged over a wide range of Er^{3+} concentration and has the value 12–13 cm^{-1} characteristic for the $KEr(MoO_4)_2$ crystal.[18] This is consistent with the dynamic splitting scheme presented in Fig. 10.

Thus a comparison of the low-frequency spectra of the end compounds $KEr(MoO_4)_2$ and $KY(MoO_4)_2$ has enabled us to establish the main trend in their formation. We have

shown that the low-frequency vibrational spectrum can be formed by vibrations of the $[Y_{1-x}Er_x(MoO_4)_2]_{\infty\infty}$ layers. This makes for a single-mode character of the behavior of the low-frequency vibrational branches. The concentration dependences of the energies corresponding to the positions of the first and second excited levels of the Er^{3+} ions were explained by invoking the concepts of cross splitting of the acoustic and excitonic branches. The weak dynamic coupling of the low-energy electronic excitations with the vibrational branches in the $KEr(MoO_4)_2$ crystal is due to the absence of a structural phase transition of the CJTE type at zero magnetic field in that compound.

2.2. Features of the dynamics of crystals of $KY(MoO_4)_2$–$KDy(MoO_4)_2$ solid solutions

Unlike the $KY_{1-x}Er_x(MoO_4)_2$ crystals, the solid solutions $KY(MoO_4)_2$–$KDy(MoO_4)_2$ have rather complex dynamics in respect to low-frequency excitations. The end compound $KDy(MoO_4)_2$ has a phase transition at 14.3 K which is due to the CJTE and is accompanied by a change in structure of the low-energy electron spectrum. Dilution of the Jahn–Teller ions Dy^{3+} by the diamagnetic ions Y^{3+} causes a change in the phase transition temperature. Therefore, in experimental studies of this system, besides the mechanisms of formation of the low-frequency excitation spectra it was necessary to establish the (x,T) phase diagram of the equilibrium states of the system at different proportions of the solution components.

The parameters of the crystal lattice of the end compounds are not much different, and it was therefore assumed that isomorphic substitution of the Y^{3+} ions by Dy^{3+} occurs. The concentrations of the different ions were determined from their proportion in the initial growing stock. X-ray studies have shown that the lattice parameters of crystals of composition $KY_{1-x}Dy_x(MoO_4)_2$ varied smoothly as functions of the concentration x. The studies also showed the absence of superstructures in these solutions.[49]

The transmission spectra of $KY_{1-x}Dy_x(MoO_4)_2$ crystals were measured in the long-wavelength IR region ($\nu \sim 15$–$40\ cm^{-1}$).[49] Figure 19 shows the form of the transmission spectra at low temperature in the polarizations $\mathbf{E}\|\mathbf{a}$ and $\mathbf{E}\|\mathbf{c}$ at different concentrations of the solution components. It is seen that the spectrum of the compound $KY(MoO_4)_2$ has two absorption bands, with energies $\nu_1^{ph} = 18.5\ cm^{-1}$ in the polarization $\mathbf{E}\|\mathbf{a}$ and $\nu_2^{ph} = 28.2\ cm^{-1}$ in the polarization $\mathbf{E}\|\mathbf{c}$. These absorption bands must be due to vibrational modes, since $KY(MoO_4)_2$ does not have a low-energy electronic spectrum. As the concentration of Dy^{3+} ions increases, the intensity of the absorption in the region of the ν_1^{ph} band increases, and the band broadens significantly. The ν_2^{ph} band is shifted to lower energies, with slight changes in the width and intensity. At a concentration $x = 1.0$ a wide absorption band with energy $\nu_2^e \sim 28\ cm^{-1}$ is observed in the transmission spectrum in the polarizations $\mathbf{E}\|\mathbf{a}$ and $\mathbf{E}\|\mathbf{c}$. As x is decreased from 1.0 to 0.7 in the polarization $\mathbf{E}\|\mathbf{c}$, this band narrows, and a wide band appears on the low-frequency wing. In the polarization $\mathbf{E}\|\mathbf{c}$ the ν_2^e band broadens significantly and shifts to lower frequencies with decreasing Dy^{3+} concentration. This band must be due to an electronic transition, since studies show that its behavior is dependent on external magnetic field.[50] When the temperature is raised to ~ 20 K the ν_2^e band shifted to lower energy, down to $\nu_1^{ph} \sim 18$–$20\ cm^{-1}$ (Refs. 25, 49, and 50).

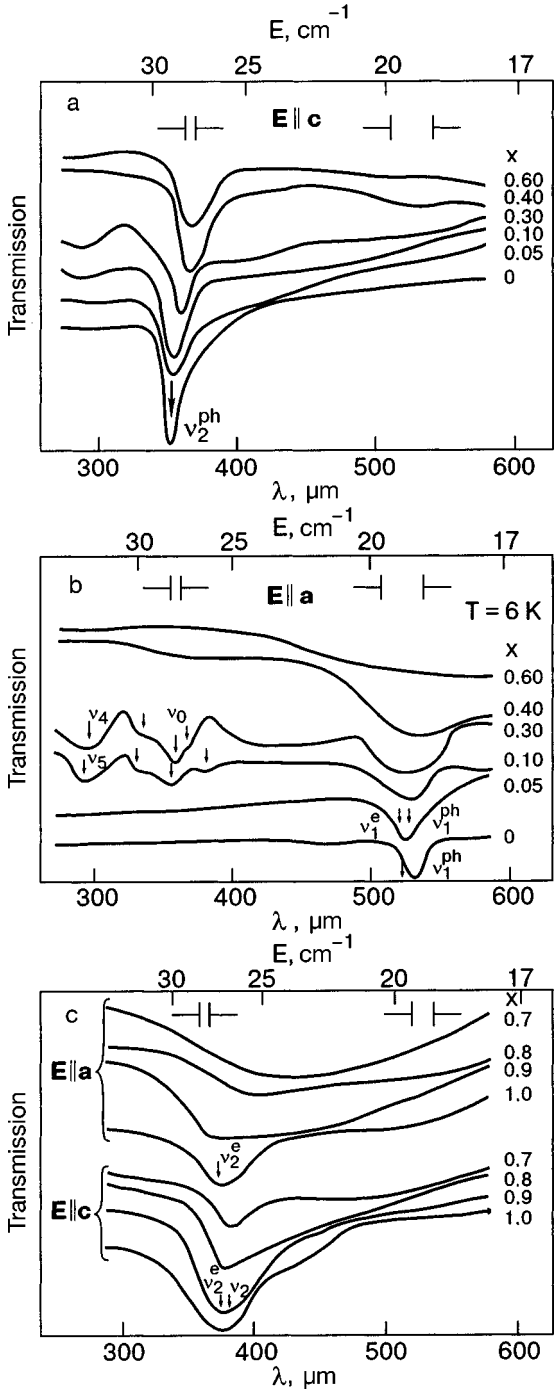

FIG. 19. Form of the transmission spectra of $KDy_xY_{1-x}(MoO_4)_2$ crystals in the region 15–$35\ cm^{-1}$ in the polarizations $\mathbf{E}\|\mathbf{a}$ and $\mathbf{E}\|\mathbf{c}$ at temperatures $T \sim 6$ K at different concentrations x.

It should be emphasized that the transmission spectra of these crystals with $x = 0.1$ and $x = 0.3$ has an absorption band in the polarization $\mathbf{E}\|\mathbf{a}$ with energy $\nu_0 \sim 28\ cm^{-1}$ (see Fig. 19b). It has structure in the form of side bands at intervals $\Delta\nu \approx \pm 2\ cm^{-1}$ from the center band in the case $x = 0.1$, and $\Delta\nu \approx \pm 1\ cm^{-1}$ for $x = 0.3$. At these same concentrations absorption bands arise in the spectrum at energies $\nu_4 \sim 32\ cm^{-1}$ ($x = 0.3$) and $\nu_5 \sim 34\ cm^{-1}$ ($x = 0.1$) with a predominant polarization $\mathbf{E}\|\mathbf{a}$. Figure 20 shows the frequency–

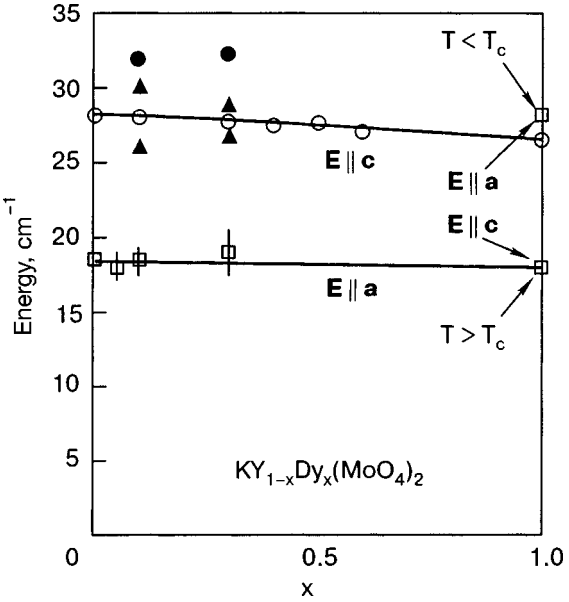

FIG. 20. Frequency–concentration curve of the absorption band of the low-frequency excitations of $KY_{1-x}Dy_x(MoO_4)_2$. The unfilled circles show the positions of the vibrational absorption bands, the filled circles and the squares show electronic absorption bands, the triangles show the side satellites of the $\nu_0 = 28\ cm^{-1}$ band. The vertical lines denote the half-widths of the corresponding absorption bands.

concentrationcurves constructed for this absorption band on the basis of the experimental data. In interpreting the corresponding absorption bands shown in this figure we have used the results obtained in measurements in the optical range[51,52] and also in the long-wavelength IR range in an external magnetic field.[53]

It is of interest to consider the increase in half-width of the 18–20 cm^{-1} absorption band with increasing Dy^{3+} concentration in this system of solid solutions, to a value $\Delta \sim 14\ cm^{-1}$ in the end compound $KDy(MoO_4)_2$ (Ref. 25). At Dy^{3+} concentrations $x=0.1$ and $x=0.3$ an absorption band appears in the spectrum at $\nu \sim 28\ cm^{-1}$, having structure in the form of side bands whose origin is also a topic of interest.

To explain the experimental results of long-wavelength IR spectroscopy let us analyze them qualitatively along with the results of experiments done in the optical, Raman scattering, and rf ranges.[51,54,55] We shall devote our attention mainly to elucidating the coupling of the low-frequency electronic excitations of the Dy^{3+} ions with the vibrational modes of the crystal lattice and the role of this coupling in the formation of the low-energy spectrum and the equilibrium structure in the given system of solid solutions at low temperatures.

Let us first discuss the low-frequency phonon spectrum. A model was proposed above which describes the formation of the low-frequency vibrational spectrum in the system of solid solutions of structurally analogous crystals $KY(MoO_4)_2$–$KEr(MoO_4)_2$. According to that model, the low-frequency vibrational branches (optical and acoustic) are formed as a result of shear vibrations of the layered packets $[Y_{1-x}Er_x(MoO_4)_2]_{\infty\infty}$ with respect to each other along the corresponding directions in the crystal. To calculate the dispersion of these vibrational branches in the Brillouin zone we have used a one-dimensional model.

In $KY_{1-x}Dy_x(MoO_4)_2$ crystals the vibrational spectrum is also formed by shear vibrations of layered packets $[Y_{1-x}Dy_x(MoO_4)_2^-]_{\infty\infty}$. Substitution of Y^{3+} by Dy^{3+} leads to a random dependence of ions over layered packets. Therefore, all of the layered packets have identical mass, corresponding to the relative contributions of the substituent ions. The low-frequency vibrational spectrum of the solution does not experience structural disorder of the alloy type and should have single-mode behavior, which is what is observed experimentally for ν_2^{ph}. The frequency position of the ν_1^{ph} band is very difficult to track because of the superposition of electronic absorption. According to estimates made from the change in reduced mass of the layered packets, the changes of the energies of the transverse vibrational modes in going from the compound $KY(MoO_4)_2$ to $KDy(MoO_4)_2$ are equal to $\Delta\nu_1 = 1.5\ cm^{-1}$ and $\Delta\nu_2 = 2.0\ cm^{-1}$, respectively, for the ν_1^{ph} and ν_2^{ph} modes. The fact that these values are close to those observed experimentally confirms the correctness of the model chosen for describing the formation of the low-frequency vibrational spectrum. The energy of the vibrational mode $\nu_2^{ph} = 26.5\ cm^{-1}$ of the end compound $KDy(MoO_4)_2$ is taken from the experimental data presented in Ref. 53. Analysis of the transmission spectra of the crystals at low temperatures shows that the energy ν_1^{ph} is approximately equal to $17.5\ cm^{-1}$ (Ref. 56). The solid curves in Fig. 20 give the concentration dependence of the energies of the vibrational modes of the system $KY_{1-x}Dy_x(MoO_4)_2$. It is seen that the observed shift of the vibrational modes corresponds to $\Delta\nu_1 \approx 1\ cm^{-1}$ and $\Delta\nu_2 \approx 1.7\ cm^{-1}$, values which are close to the estimates made.

Thus the behavior of the low-frequency vibrational spectra of the solid solution $KY_{1-x}Dy_x(MoO_4)_2$ has a single-mode character with an insignificant isotope shift on going from one pure end compound to the other; this is consistent with the mechanism of their formation.

Let us analyze the formation of the low-energy electron spectrum of excitations of the Dy^{3+} ions. A governing role in the formation of the structure of the electron spectrum is played by the static crystalline field of the nearest-neighbor environment (ligands) of the Dy^{3+} ions. The calculation of the electron spectrum of excitations of the Dy^{3+} ions in the end compound $KDy(MoO_4)_2$ with the use of crystalline-field theory was described above. In $KY_{1-x}Dy_x(MoO_4)_2$ the ground multiplet $^6H_{15/2}$ of the Dy^{3+} ions is split by the static crystalline field of the ligands so that the first excited level crosses optical–acoustic and acoustic vibrational branches (see Fig. 9). The second electronic level has an excitation energy of $\sim 54\ cm^{-1}$ and is observed much above the low-frequency vibrational branches; it does not play a role in the formation of spectral structure at low temperatures. Let us therefore discuss the formation of the low-energy electron–phonon spectrum taking into account only the first excited electronic state of the Dy^{3+} ions.

In the crystal of the end compound $KDy(MoO_4)_2$ of the system the unit cell contains four Dy^{3+} ions (pairwise related by inversion). One should observe Davydov splitting of the first electronic excitation in the spectrum because of the presence of two translationally inequivalent layered packets

in the unit cell. However, it is insignificant in value because of the weak coupling between the Dy^{3+} ions in neighboring $[Dy(MoO_4)_2]_{\infty\infty}$ layered packets and essentially is not observed experimentally. The largest value of the dynamic splitting of the electronic level of the Dy^{3+} ions is due to the interaction of excitations of the two inversion-related Dy^{3+} ions in the layered packet. In this case the electronic level is split into even and odd components, one of which is IR and Raman active while the second is only IR active. A comparison of the values of the energy of the first excited state of the Dy^{3+} ions obtained from the IR and Raman spectra gives a value of the splitting of $\sim 2-3\ \mathrm{cm}^{-1}$ (Ref. 25).

Besides the dynamic coupling of the electronic excitations of the Dy^{3+} ions among themselves, a significant role in the formation of the low-energy electron spectrum in the system under study is played by the interaction of electronic excitations with crystal lattice vibrations. As we have said above, for the efficient coupling of the electronic excitations with lattice vibrations it is necessary that the symmetries of the electronic and vibrational excitations coincide and that the wave vectors and energies of the excitations coincide.

In the crystals under study the local symmetry of the environment of the rare-earth ions Dy^{3+} is C_2 (Ref. 16). The symmetries of the wave functions of the corresponding energy levels transform according to twofold representations $(\Gamma_3+\Gamma_4)$ of the group C_2. The symmetries of the electronic excitations corresponding to transitions between levels can be xd represented by the irreducible representations Γ_1 and Γ_2. It follows from a comparison of the representations Γ_1 and Γ_2 of the local electronic transitions with the symmetries of the vibrational excitations of the crystal (see Table IV) that coupling of the electronic excitations with acoustic and optical–acoustic vibrational excitations is allowed in this system.

We note that the first electronic level falls within the region of the acoustic and optical–acoustic vibrational spectrum and crosses a transverse optical–acoustic branch with polarization $\mathbf{u}\|\mathbf{a}$ near the Brillouin zone center (see Fig. 9) and an acoustic branch with polarization $\mathbf{u}\|\mathbf{c}$ near the Brillouin zone boundary. This should lead to enhancement of the dynamic coupling of the electronic excitation with the vibrational branches, since the crossing occurs in a region where the density of vibrational states is maximal.

Let us consider the mechanism of formation of the $\nu \sim 28\ \mathrm{cm}^{-1}$ absorption band in the spectrum of the crystals $KY_{1-x}Dy_x(MoO_4)_2$, with fine structure in the form of side bands at intervals $\Delta\nu_1 \sim \pm 2\ \mathrm{cm}^{-1}$ and $\Delta\nu_2 \sim \pm 1\ \mathrm{cm}^{-1}$ from the center component at concentrations of the solid solution $x=0.1$ and $x=0.3$ (Fig. 19). It is seen from the frequency–concentration curves of the low-frequency spectrum (see Fig. 20) that the band arises in the region where the energy position of the electronic excitation $\nu_2^e \sim 28\ \mathrm{cm}^{-1}$, which is observed in the end compound $KDy(MoO_4)_2$ at $T<T_{\mathrm{tr}}$, crosses the optical–acoustic mode $\nu_2^{\mathrm{ph}}(x)$ near the Brillouin zone center. This leads to enhancement of the coupling of ν_2^e and ν_2^{ph} and to the formation of a local state of the Dy^{3+} ions with an excitation energy of $\nu_2^e \sim 28\ \mathrm{cm}^{-1}$. Apparently this band is an electronic excitation. This assumption is supported by the appearance of fine structure in the form of side bands with intervals of several inverse centimeters for the electronic excitations in the optical range.[49] If this assumption is correct, then two electronic excitations with frequencies ν_1^e and ν_2^e appear in the system at concentrations $x=0.1$ and $x=0.3$.

Let us discuss the proposed mechanism giving rise to the two bands. We can say that the appearance of two electronic bands in the spectrum is due to a dynamic coupling effect between the first electronic excitation with two vibrational branches. It is assumed that in the system consisting of a Dy^{3+} ion and its ligand environment, a double-minimum adiabatic potential is realized when the dynamic coupling of the low-energy electronic excitation with the transverse optical–acoustic branches is taken into account. The resonance coupling of the electronic excitation with the low-frequency vibrational modes causes the system to tunnel between the two minima.

If these ideas are correct, then in the concentration region $0.02<x<0.4$ a dynamic state with a double-minimum adiabatic potential is realized, with an energy difference $\Delta\nu \sim 5\ \mathrm{cm}^{-1}$.

In an analogous way one can analyze the dynamic state of the system at low temperature in the concentration region $0.6<x\leqslant 1.0$. According to the measured Raman scattering spectra, at a temperature $T=2$ K in the $KDy(MoO_4)_2$ crystal the excited electronic states $\nu_1^e \sim 20\ \mathrm{cm}^{-1}$ and $\nu_2^e \sim 30\ \mathrm{cm}^{-1}$ are observed.[25] At low temperature the absorption spectrum in the IR range has bands with energies $\nu_1^e \sim 18\ \mathrm{cm}^{-1}$ and $\nu_2^e \sim 28\ \mathrm{cm}^{-1}$ (Ref. 56). The appearance of two electronic bands in the IR and Raman spectra at low temperature cannot be explained by Davydov splitting in view of the large difference; we therefore assume that in this concentration region a double-minimum adiabatic potential is realized in the system in the electronic ground state of the Dy^{3+} ions.

Thus in the system $KY_{1-x}Dy_x(MoO_4)_2$ there exist four regions of concentrations of the components of the solution with different structure of the ground state of the Dy^{3+} ions. The concentration regions $0.02<x<0.4$ and $0.6<x<1.0$, where two-mode states $|\Psi\rangle=\alpha_1|\Psi_1\rangle+\alpha_2|\Psi_2\rangle$ are realized, and the regions $0<x<0.02$ and $0.4<x<0.6$, where the system is found in a single-mode state $|\Psi\rangle$. The concentrations $x_1 \approx 0.02$, $x_2 \approx 0.4$, and $x_3 \approx 0.6$ are bifurcation points of the ground state of the system with changing parameter x. From the intensity of the corresponding absorption or scattering bands one can assume that apparently $|\alpha_1| \geqslant |\alpha_2|$ in the concentration region $0.02<x<0.4$, while $|\alpha_1|<|\alpha_2|$ for $0.6<x\leqslant 1.0$.

The resonance interaction of the electronic state ν_2^e with the vibrational mode ν_2^{ph} in the concentration region $0.02<x<0.4$ can be described by a model of two coupled oscillators. In such a model we obtain two frequencies for the system under consideration:[57]

$$\nu_1=\nu_0 \quad \text{and} \quad \nu_2^2=\nu_0^2+2\alpha^2, \tag{2.1}$$

where ν_0 is the frequency of the oscillators in the absence of dynamic coupling, and α is the coupling energy of the oscillators. Under the condition $\alpha \ll \nu_0$ we obtain

$$\alpha=\pm(\Delta\nu\ \ \nu_0)^{1/2}. \tag{2.2}$$

The side bands observed in the spectrum at ν_2^e ($x=0.1$ and $x=0.3$) can be associated to the frequencies ν_1 and ν_2. Using the last relation, let us estimate the energy of dynamic coupling of the electronic excitation ν_0 with the vibrational branch for these concentrations. For $\nu_0 \sim 28\ \mathrm{cm}^{-1}$, $\Delta\nu_1 = 2\ \mathrm{cm}^{-1}$, and $\Delta\nu_2 = 1\ \mathrm{cm}^{-1}$ we obtain $\alpha_1 = 7.5\ \mathrm{cm}^{-1}$ for $x=0.1$ and $\alpha_2 = 5\ \mathrm{cm}^{-1}$ for $x=0.3$. Thus the coupling energies are comparable with the energies of lowering of the ground state in the splitting of the quasidoublet from 18 to $28\ \mathrm{cm}^{-1}$, which amounts to $\Delta = 5\ \mathrm{cm}^{-1}$. An analogous picture can be observed in the dynamic coupling of the electronic state ν_1^e with the vibrational mode ν_1^{ph} in this same concentration region, but here the side bands for ν_1^e are difficult to observe experimentally because of the poor signal-to-noise ratio in this frequency range. The concepts developed here permit interpretation of the fine structure that has been observed[49] in the electronic absorption bands in the optical region of the spectrum. This system in the form side bands of absorption lying several inverse centimeters from the center component cannot be explained by electron–phonon pair processes in view of the absence of peaks in the density of states in the vibrational spectrum at the corresponding energies and also the absence of a decrease in the energy of the high-frequency satellites of the bands as the temperature is lowered. It is therefore assumed that the appearance of the side bands in the exciton spectrum in the optical range is due to dynamic coupling of the first excited state of the Dy^{3+} ions with vibrational excitations and that the corresponding intervals are determined by the coupling energies of the low-frequency electronic states with phonon branches. The absorption band observed in the spectrum at $\nu_4 \sim 33\ \mathrm{cm}^{-1}$ (see Fig. 19a) lies a distance $\Delta\nu \sim 5\ \mathrm{cm}^{-1}$ ($x=0.3$) away from the electronic band ($\nu_2^e \sim 28\ \mathrm{cm}^{-1}$), in approximate agreement with the coupling energy of the electronic excitation with the vibrational mode for this concentration.

In the optical spectrum the exciton bands have a developed structure in the concentration intervals $0<x<0.4$ and $0.6<x<1.0$, where the dynamic coupling of the first excited state of the Dy^{3+} ions with vibrational excitations of the crystal lattice is the strongest; this confirms our ideas.

Valuable information about the dynamic coupling of low-frequency electronic excitations of the Dy^{3+} ion subsystem with lattice vibrations is given by ESR spectroscopy based on the Kramers doublet of the Dy^{3+} ions in the system under discussion. The ESR spectra at different concentrations of Dy^{3+} ions introduced into the $KY(MoO_4)_2$ crystal were measured in Ref. 55. According to these studies, the ESR spectrum at low concentrations of Dy^{3+} ions has two magnetically inequivalent centers that are rotated in the plane of the $[Y_{1-x}Dy_x(MoO_4)_2^{-1}]_{\infty\infty}$ layered packet by angles $\pm 14°$ with respect to the axes of the crystal. When an external magnetic field is oriented along one of the axes of the crystal, in which case there is no difference between these centers, a single absorption band with hyperfine structure and a spectroscopic splitting factor $g \sim 9$ is observed in the ESR spectrum for the Dy^{3+} concentration $x=0.005$ (see Fig. 21).[55] For $x=0.03$ an additional band appears in the ESR spectrum, with an intensity approximately equal to that of the main line but with a g factor corresponding to the maximum value of the g factor of the ground state of the Dy^{3+} ions of the low-temperature phase of $KDy(MoO_4)_2$ ($g \sim 18$).[51] The appearance of this additional band can be explained by the presence of a double-minimum adiabatic potential in the ground state of the Dy^{3+} ions in the system, which is manifested in the appearance of the corresponding electronic transitions ν_1^e and ν_2^e. Schematically this can be represented by the splitting of the ground state of the Dy^{3+} ions in an external magnetic field (see Fig. 22). It is seen that here four electronic levels are realized from the two Kramers doublets corresponding to two states of the electronic subsystem. Therefore at $x=0.03$ the ESR spectrum has two absorption bands.

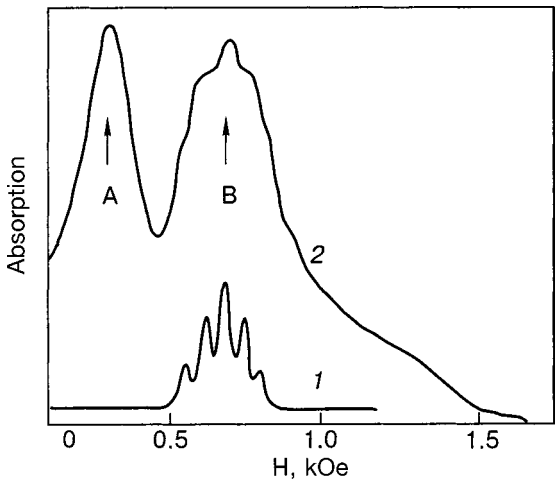

FIG. 21. Form of the microwave absorption spectrum of the $KY_{1-x}Dy_x(MoO_4)_2$ crystals in an external magnetic field.[55] Curve *1* is for $x=0.005$ (the comb structure of the band is due to the hyperfine structure of the ESR spectrum of the isolated Dy^{3+} ion); curve *2* is for $x=0.03$ (the arrows denote two absorption bands of the crystal). $\mathbf{H}\|\mathbf{c}$; the g factors of the two ESR centers are equivalent. $T=1.8$ K.

It is of interest to consider the phase diagram of the dynamical states of the system under study in the space of parameters (x,T). To elucidate its form we use the formalism developed in catastrophe theory, which is a branch of the theory of dynamical systems.

To determine the stationary solutions in a system with one variable and two parameters one can use the canonical form of a cubic equation of the general type[58]

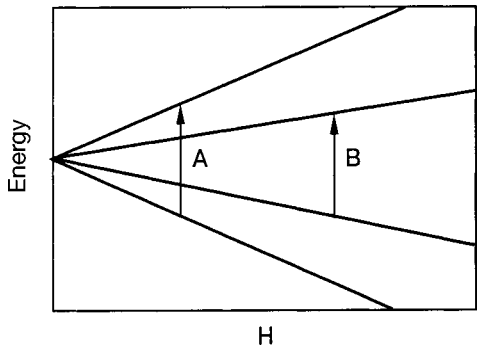

FIG. 22. Scheme of the splitting of the ground state of the Dy^{3+} ion in the $KY_{1-x}Dy_x(MoO_4)_2$ crystal at $0.02<x<0.4$ and $0.6<x<1$ in an external magnetic field. The vertical arrows denote electronic transitions upon microwave absorption (A is the transition corresponding to the state with excitation ν_2^e, and B is the transition corresponding to the state with excitation ν_1^e).

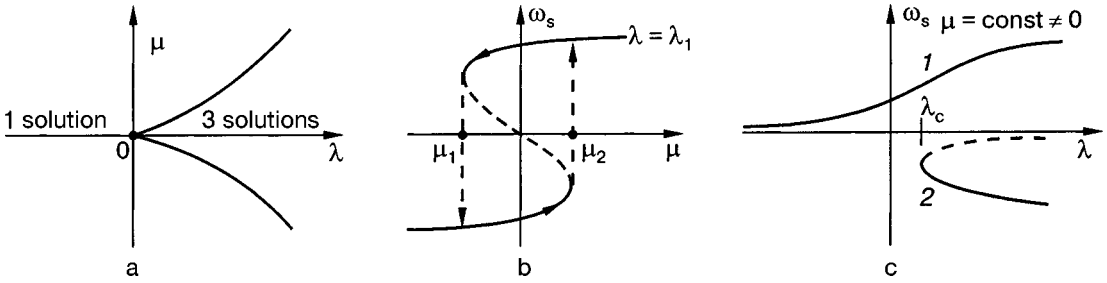

FIG. 23. Influence of the external parameters on the bifurcation of the stationary states of the system: the curve bounding the existence region of the three solutions in the space of parameters μ and λ (a); the hysteretic behavior of the system upon change in the parameter μ (with the parameter λ fixed) (b); the bifurcation of the stationary states with respect to the parameter λ when the parameter μ is fixed and nonzero (c).

$$-\omega_s^3+\lambda\omega_s+\mu=0, \tag{2.3}$$

where the parameters μ and λ are linearly related to the concentration x and the temperature, respectively, and ω_s is a quantity characterizing the dynamical stationary state of the system.

Why have we chosen this mathematical model? First, it has a universal character and describes the behavior of dynamical systems in the space of two parameters in the presence of a region of two stable equilibrium states. Second, it is simple, containing only one internal parameter characterizing the state of the dynamical system. In our case this parameter can be the frequency of the first electronic excitation of the system.

In the space of parameters (μ, λ) one can determine the curves separating the two regimes of dynamic coupling. These curves are shown in Fig. 23a. The existence region of three real solutions ends at a point having a singularity of the ''cusp'' type. Figures 23b,c show the dependence of the state of the dynamical system on the external parameters. The dependence of ω_s on the parameter μ at a fixed value of λ has an S-shaped form, due to the multiplicity of solutions in the interval $\mu_1<\mu<\mu_2$. Here two states in this region are stable simultaneously. The region of bistability ends at the points μ_1 and μ_2 (Fig. 23b). The dependence of ω_s on the parameter λ at a fixed value of μ consists of two individual curves (Fig. 23c). One of them is defined for all values of λ (curve *1*), while the second (curve *2*) is defined only for parameter values $\lambda\geqslant\lambda_c$, and there is a singularity of the limit-point type at λ_c. For parameter values $\lambda<\lambda_c$ there is one stable solution, and for $\lambda>\lambda_c$ there is bistability. The dependence $\omega_s(\lambda)$ qualitatively resembles of the temperature dependence of the frequency of an electronic transition in $KDy(MoO_4)_2$, as measured in the Raman scattering spectrum.[25] As can be seen in Fig. 24, a bifurcation of the ground state of the system occurs in the temperature interval $\sim$11–14 K. In the Raman spectrum this is manifested in splitting of the electronic band corresponding to a transition to the first excited state of the Dy^{3+} ions. The temperature curves of the magnetic susceptibility measured in Ref. 59 are consistent with our ideas. Those curves exhibit two singularities corresponding to the region of bifurcation of the ground state of the Dy^{3+} ions.

It is now important to find out how the universal phase diagram illustrated in Fig. 23a is realized in the system $KY_{1-x}Dy_x(MoO_4)_2$. It can be supposed that the singular point corresponding to $\mu=0$ falls within the concentration interval $0.02<x<0.4$ (μ is linearly related with the concentration x); this apparently corresponds to the crossing point of the vibrational mode ν_2^{ph} with the electronic mode ν_2^e. This should give rise to a feature in the phase diagram of the system in this concentration interval in the form a sharp

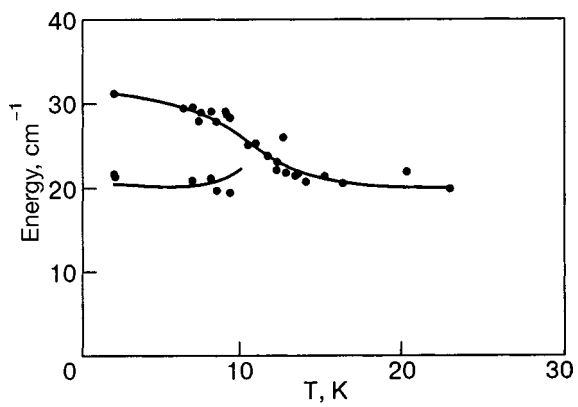

FIG. 24. Temperature dependence of the low-energy Raman-active mode of the $KDy(MoO_4)_2$ crystal. The experimental points are taken from Ref. 25, and the solid curves were drawn on the basis of ideas about the bifurcation of the ground state.

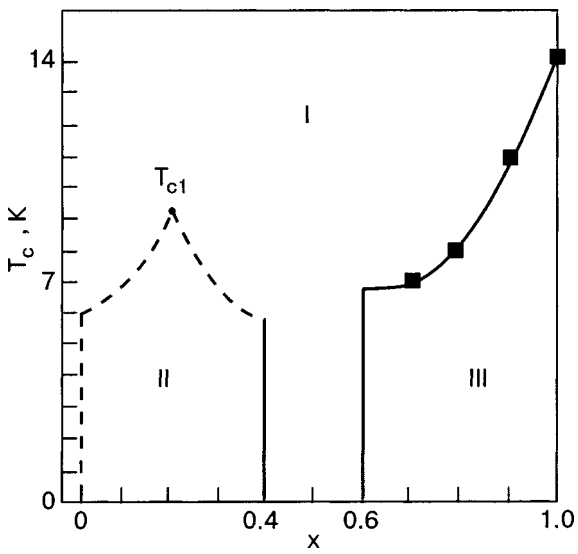

FIG. 25. The (x,T) phase diagram of the dynamical states of the electron subsystem of the Dy^{3+} ions in the system of solutions $KY_{1-x}Dy_x(MoO_4)_2$. I is a single-mode state; II and III are two-mode states. The solid lines denote first-order phase transitions. The dashed lines denote transitions that are in need of experimental verification.

spike (see Fig. 25). It should be emphasized, however, that this assumption must be checked experimentally.

The concentration interval $0.6<x<1.0$ lies above or below the cusp singular point shown on the universal phase diagram in Fig. 23a. This follows from the form of the phase diagram obtained in Ref. 49 and also from the temperature dependence of the frequencies of the lowest electronic excitations $\nu(T)$ in the compound $KDy(MoO_4)_2$ (Ref. 25). If the point $x=1.0$ corresponded to a singularity of the cusp type ($\mu=0$), then the $\nu(T)$ curve would have a bifurcation of the ''pitchfork'' type. Experimentally the observed concentration dependence of the transition temperature qualitatively resembles the dependence shown in Fig. 23c. Therefore the concentration interval $0.6<x<1.0$ does not include a point $\mu=0$ (see Fig. 23a), and the curve on the (x,T) phase diagram of the system at these concentrations should have a monotonic character. Based on these ideas, we have constructed an (x,T) diagram of the system (see Fig. 25). According to the material presented above, the temperatures of the phase transitions at the critical concentrations $x_c\sim0.6$ and $x_c\sim0.4$ should be finite, as is observed experimentally at $x\sim0.7$ ($T_c\sim7$ K). If we had the experimental possibility of varying the parameter x in a continuous manner, then at the values $x\sim0.4$ and $x\sim0.6$ we would apparently observe first-order phase transitions with hysteresis. We emphasize that the phase diagram shown in Fig. 25 must be checked experimentally in the concentration region $0.02<x<0.4$.

We note that the concentration region in which bistable states are realized are situated symmetrically about the concentration $x=0.5$. If this symmetry is not accidental, then it might be explained using results from percolation theory. Since we are investigating a system with a layered structure, we can take a two-dimensional square lattice as a model. In considering the site problem one obtains two critical concentrations, $x_{c1}\sim0.4$ and $x_{c2}\sim0.6$, which are symmetric about $x\sim0.5$.

Thus on the basis of the spectral data in the optical, IR, and Raman regions we have been able to establish that in the system of solid solutions $KY_{1-x}Dy_x(MoO_4)_2$ in the concentration region $0.02<x<0.4$ and $0.6<x<1.0$ the coupling of the low-energy electronic excitation of the Dy^{3+} ions with vibrational branches leads to the formation of an equilibrium structure with dynamic ordering of the orbital moments and the onset of bistability of the ground state of the Dy^{3+} ions.

This may be the reason that neutron scattering experiments have failed to find static Jahn–Teller distortions at $T<T_{tr}$ in the $KDy(MoO_4)_2$ crystal.[37] Confirmation for this idea is provided by measurements of the temperature dependence of the elastic constants by ultrasonic methods.[21] In the phase transition region ($T_{tr}\sim14.3$ K) the anomalies in the sound velocity are extremely slight ($\sim10^{-3}$), apparently because of the absence of spontaneous static deformations in the system in the phase transition region.[21] A criterion for manifestation of dynamic effects in systems with a degenerate orbital moment is known:[60] the energy of the Jahn–Teller stabilization must be comparable to the energy of zero-point vibrations of the nuclei.

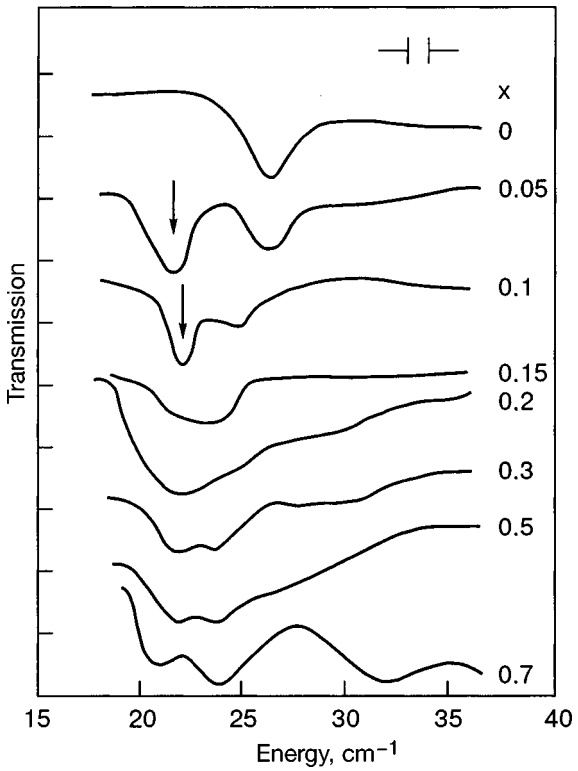

FIG. 26. Transmission spectra of $CsDy_{1-x}Bi_x(MoO_4)_2$ single crystals at a temperature $T\sim6$ K for different concentrations x. The arrows denote the absorption band due to electronic excitation of the Dy^{3+} ions.

2.3. Formation of low-frequency spectrum of the system of solid solutions $CsDy(MoO_4)_2$–$CsBi(MoO_4)_2$

Unlike the systems of isostructural solid solutions described above, where the rare-earth ions were replaced by the lighter diamagnetic ion Y^{3+}, in the series of solutions $CsDy(MoO_4)_2$–$CsBi(MoO_4)_2$ the Dy^{3+} ion is replaced by the heavier diamagnetic ion Bi^{3+}.

In studying this system, no doubt the first item of interest is the features of formation of the low-energy spectra with allowance for the dynamic couplings of the electronic and phonon excitations in these compounds when the Jahn–Teller ions Dy^{3+} are replaced by the heavier diamagnetic impurity Bi^{3+}.

In Ref. 61 the low-frequency absorption spectra were measured in $CsDy_{1-x}Bi_x(MoO_4)_2$ compounds with different concentrations of the solution components. The measurements were made in the spectral interval 15–40 cm^{-1} at a sample temperature of ~6 K. Since the parameters of the crystal lattices of $CsDy(MoO_4)_2$ and $CsBi(MoO_4)_2$ are close, it was assumed that isotopic substitution of the Dy^{3+} ions by Bi^{3+} ions occurs in the solution. The proportion of the components was determined from their concentration in the initial stock.

Figure 26 shows the transmission spectra of $CsDy_{1-x}Bi_x(MoO_4)_2$ single crystals with different concentrations of the solution components. It is seen that the absorption band at energy $\nu_1^{ph}\approx27$ cm^{-1} is shifted to lower energy with increasing Bi^{3+} concentration. Here an absorption band appears in the spectra with a peak energy of $\nu_1^e\approx22$ cm^{-1}, and its position remains practically unchanged as the bismuth concentration is increased. Upon the superpo-

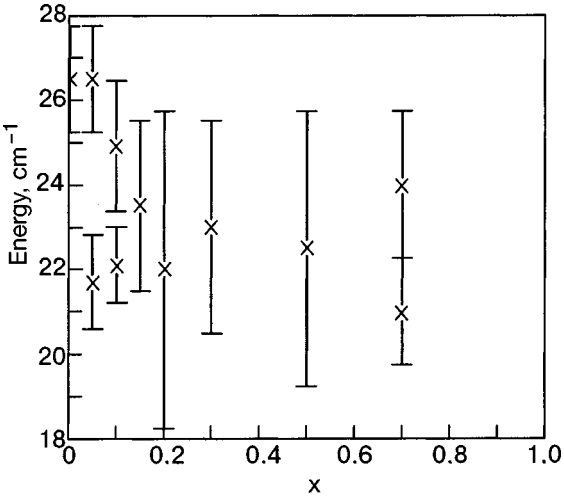

FIG. 27. Dependence of the half-width of the absorption bands on the concentration of the components of the solution $CsDy_{1-x}Bi_x(MoO_4)_2$.

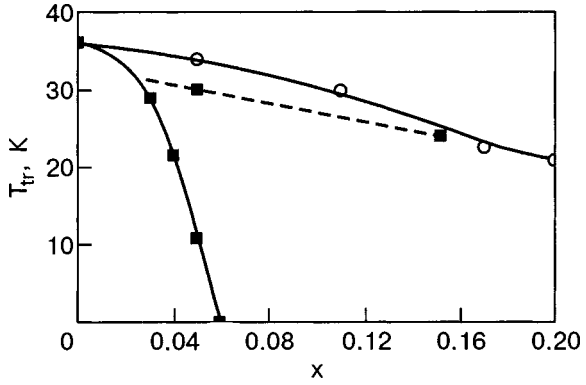

FIG. 28. Dependence on the dopant concentration of the temperature of the phase transition of the CJTE type in the crystal $CsDy(MoO_4)_2$ doped with trivalent impurities. The dashed line indicates a second-order phase transition. (■)—$CsDy_{1-x}Eu_x(MoO_4)_2$ (the introduction of the Eu^{3+} ions decreases the frequency of the acoustic vibrational branches); (○)—$CsDy_{1-x}Y_x(MoO_4)_2$ (the introduction of the Y^{3+} ions increases the frequency of the acoustic vibrational branches).[63,64]

sition of the absorption bands $\nu_1^{\rm ph}$ and ν_1^e, the absorption band is anomalously broadened (see Fig. 27). From the above analysis of the vibrational spectrum of $CsDy(MoO_4)_2$ it has been established that the band at energy 27 cm^{-1} is a low-energy vibrational mode, while the absorption band at 22 cm^{-1} is electronic.[62]

Let us briefly discuss the behavior of the spectrum of a $CsDy(MoO_4)_2$ crystal containing Bi^{3+} impurity ions and also other trivalent substitutional impurities. First, at a temperature below the phase transition the appearance of the 22 cm^{-1} electronic band upon the introduction of Bi^{3+} ions is due to an admixture of the high-temperature phase. Second, as can be seen in Fig. 13, the lowering of the frequencies of the vibrational branches upon the introduction of Bi^{3+} ions shifts the crossing point of the 22 cm^{-1} electronic level with the vibrational branch with which dynamic coupling is symmetry allowed to the Brillouin zone boundary. The zone boundary is a region of maximum density of vibrational states. This leads to enhancement of the coupling of the 22 cm^{-1} electronic excitation with the lattice vibration, i.e., it leads to broadening of the electronic absorption band. As a result, the 22 cm^{-1} electronic level becomes active in the CJTE.

Thus in the system $CsDy_{1-x}Bi_x(MoO_4)_2$ the slight shift of the frequencies of the acoustic vibrational branches upon the introduction of the diamagnetic impurity Bi^{3+} leads to a change in the dynamic coupling of the electronic and vibrational excitations and hence to a change in the equilibrium structure of the crystal.

Confirmation of what we have said comes from the (x,T) phase diagrams[63,64] of the equilibrium structures of $CsDy_xR_{1-x}(MoO_4)_2$ systems. The introduction of trivalent impurities that increase the frequencies of the acoustic and optical–acoustic vibrational branches leads to a smooth decrease of the CJTE phase transition temperature (see Fig. 28), whereas the introduction of trivalent impurity that lower the corresponding frequencies leads to a sharp decrease of the temperature of the first-order phase transition and to the appearance of a second-order phase transition.

These phase diagrams can be explained by starting from the real structure of the low-energy spectrum of the $CsDy(MoO_4)_2$ crystal, the spectrum of which in the Brillouin zone is presented in Fig. 12. When the energies of the vibrational branches decrease, the active electronic level with energy 40 cm^{-1} gets free of the vibrational branch near the Brillouin zone boundary and becomes inactive. The crossing point of the 22 cm^{-1} level with the acoustic branch is shifted toward the Brillouin zone boundary into the region of maximal density of states and it becomes active. Thus a changeover of the activity of the electronic levels of the Dy^{3+} ion occurs, and the phase transition due to the CJTE takes place on other degrees of freedom. The introduction of an impurity that increases the frequency of the vibrational branches shifts the crossing point of the 40 cm^{-1} level with the vibrational branch from the Brillouin zone boundary toward the zone center, into a region with a lower density of states. This leads to a decrease in the dynamic coupling of the electronic excitation with the vibrational branch and to a decrease in the phase transition temperature, but the crossing point of the 22 cm^{-1} electronic level with the vibrational branch with which dynamic coupling is symmetry allowed is also shifted toward the zone center, and it remains inactive in the CJTE.

A study of the phase diagram of the $CsDy(MoO_4)_2$ single crystal in the space of phase transition temperature versus external uniaxial pressure has revealed that when the external uniaxial pressure is applied perpendicular to the layered packets the phase transition temperature decreases with increasing pressure (see Fig. 29).[65] This is due to the increase of the elastic energy of the uniform strain arising in the system below the structural phase transition. An estimate of this relation based on general concepts and utilizing the Clausius–Clapeyron equation

$$PV/L = \Delta/T, \tag{2.4}$$

where P and V are the pressure and volume of the system, $\Delta T/T$ is the relative change of the temperature of the structural transition, and L is the latent heat of the phase transition. It is seen in Fig. 29 that the experimentally measured external dependence of the phase transition temperature on the external pressure is described well by relation (2.4).[66] However, the dependence of the structural phase transition in

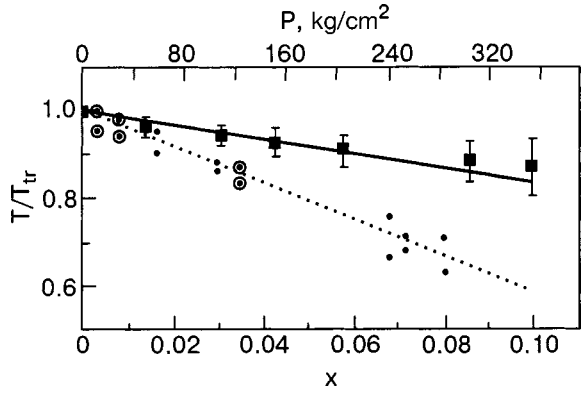

FIG. 29. Dependence of the temperature of the phase transition of the CJTE type in the crystal $CsDy(MoO_4)_2$ on the value of the external uniaxial pressure applied perpendicular to the plane of the layered packets (■). The solid line is the calculation with the use of the Clausius–Clapeyron equation. Also shown for comparison is the concentration dependence of the temperature of the phase transition of the CJTE type in the crystal $KDy_{1-x}Bi_x(MoO_4)_2$; the concentration of the Bi^{3+} impurity ions was scaled to a uniaxial pressure directed perpendicular to the plane of the layered packets (dotted line).[65,66]

the $CsDy_{1-x}Bi_x(MoO_4)_2$ crystal, when scaled to an external pressure, does not obey this phenomenological relation (the dependence is steeper). This is because at low temperatures the dynamic coupling of the low-energy electronic levels with acoustic vibrational branches plays a substantial role in the formation of the structure of these compounds at low temperatures.

With increasing concentration of Bi^{3+} ions the frequencies of the acoustic vibrational branches decrease slightly, but this does not materially diminish the dynamic coupling of the electronic level of the Dy^+ ions at energy $\nu = 40\ cm^{-1}$ with the vibrational branch near the Brillouin zone boundary (see Fig. 12).

Thus on the basis of an analysis of the electronic results, we have established for three model systems that when the Jahn–Teller ions are diluted by diamagnetic impurities, a substantial role in the formation of the equilibrium structures at low temperatures is played by the dynamic coupling of the low-energy electronic excitations of the rare-earth ions with vibrational excitations.

3. INFLUENCE OF EXTERNAL MAGNETIC FIELD ON THE EQUILIBRIUM STRUCTURES IN ARDMs

We have discussed the features of the dynamics of highly anisotropic Jahn–Teller crystals diluted with diamagnetic impurities and have established that impurities of substitution for the Jahn–Teller ions have an influence on the dynamic coupling of the low-energy excitations of the rare-earth ions with lattice vibrations and, accordingly, on the equilibrium structures. The non-Jahn–Teller ions can not only destroy but can also stimulate the CJTE. This allows one to influence the structure of the low-energy spectrum by introducing isostructural impurities that alter the frequencies of the vibrational branches and their position with respect to the electronic excitations. However, the structure of the spectrum can also be changed by acting on the electron subsystem with an external electric or magnetic field. An external magnetic field can affect the position of the low-frequency electronic levels with respect to the vibrational spectrum and can influence the electron–phonon coupling.

In ARDMs the low symmetry of the static crystalline field of the ligands of the rare-earth ions can lead to rotation of the principal axes of the g tensor of the spectroscopic splitting of the excited levels with respect to the principal axes of the g tensor of the ground state. The rather strong local anisotropy and the significant spin–orbit coupling make for a large anisotropy of the g factor of the spectroscopic splitting of the ground and excited Kramers doublets. Therefore, in these compounds a large difference of the values of the g factors of the spectroscopic splitting of the ground and excited Kramers doublets can arise for a certain direction of the external magnetic field. Thus a relatively low external magnetic field can cause a substantial change in the frequencies of the electronic transitions. On the other hand, the structure of the low-frequency vibrational spectrum of these compounds makes it possible to alter the value of the dynamic coupling of the electronic and phonon excitations significantly by applying an external magnetic field. This can be done by shifting the position of the electronic levels with respect to the peaks of the density of states of the vibrational spectrum. The above facts are good prerequisites for inducing changes in the structure of the crystal lattice of ARDMs by means of experimentally achievable external magnetic fields.

The experimental studies described below were undertaken with the goal of ascertaining the influence of external magnetic field on the dynamic coupling of low-energy electronic excitations with lattice vibrations and, hence, on the formation of equilibrium structures at low temperatures in ARDMs.

3.1. Manifestation of the dynamic coupling of excitations of the rare-earth ions with lattice vibrations in an external magnetic field

The $KEr(MoO_4)_2$ and $KDy(MoO_4)_2$ crystals belong to an isostructural series of ARDMs having the $KY(MoO_4)_2$ structure with symmetry space group D_{2h}^{14}, which contains four formula units of the substance in the unit cell.[15,16] It has been established from the ESR spectra that the ground state of the rare-earth ions is a Kramers doublet with a highly anisotropic value of the g factor of the spectroscopic splitting factor of the ground Kramers doublet. The relative centers are characterized by large values of the g factor of the spectroscopic splitting of the ground state ($g \sim 20$).

Let us consider the features of the absorption spectra of the compounds $KEr(MoO_4)_2$ and $KDy(MoO_4)_2$ in external magnetic fields. The low-frequency absorption spectrum of the $KEr(MoO_4)_2$ crystal is formed by both transitions within the ground term of the Er^{3+} ions (transitions between Kramers doublets formed when the sixteenfold degenerate term $^4I_{15/2}$ is split into eight Kramers doublets in a field of local symmetry C_2) and also by low-frequency vibrational modes. The absorption spectrum of the $KEr(MoO_4)_2$ crystal exhibits vibrational modes with energies $\nu_1 = 18.5\ cm^{-1}$ and $\nu_2 = 26\ cm^{-1}$ and two electronic transitions with energies $\nu_1 = 15.4\ cm^{-1}$ and $\nu_2 = 30.5\ cm^{-1}$. The bands with energies $18.5\ cm^{-1}$ and $26\ cm^{-1}$ are strictly polarized.

Figures 30, 31, and 32 show the frequency–field curves

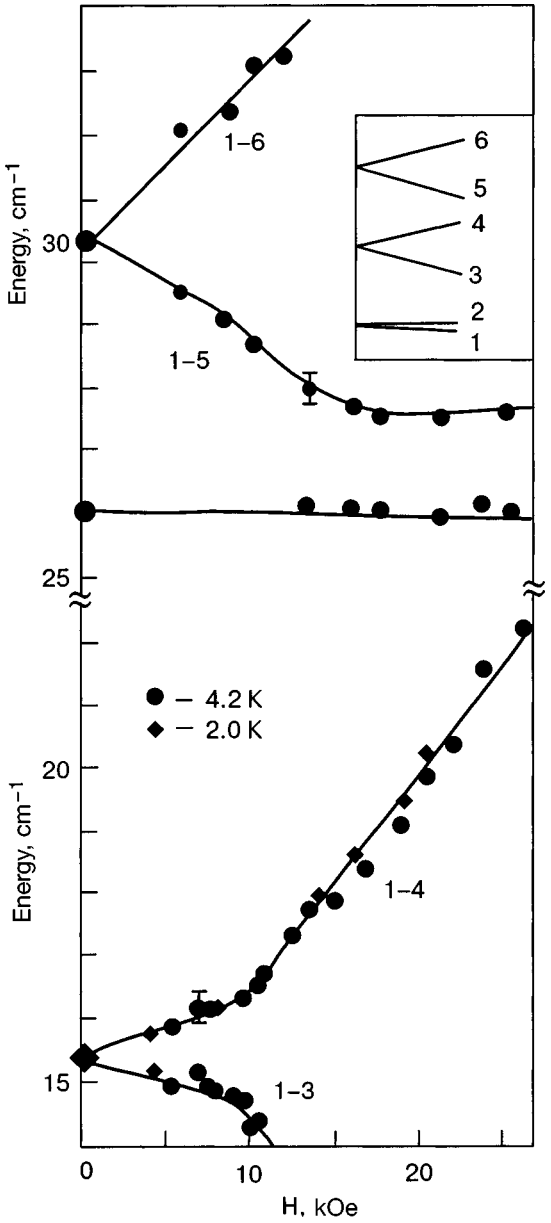

FIG. 30. Frequency–field curves of the splitting of the electronic levels of the $KEr(MoO_4)_2$ crystal for **H**‖**a**. The inset shows the scheme of the splitting of the ground and first two excited electronic levels and their numbering. The numbers on the curves indicate transitions between the corresponding sublevels.

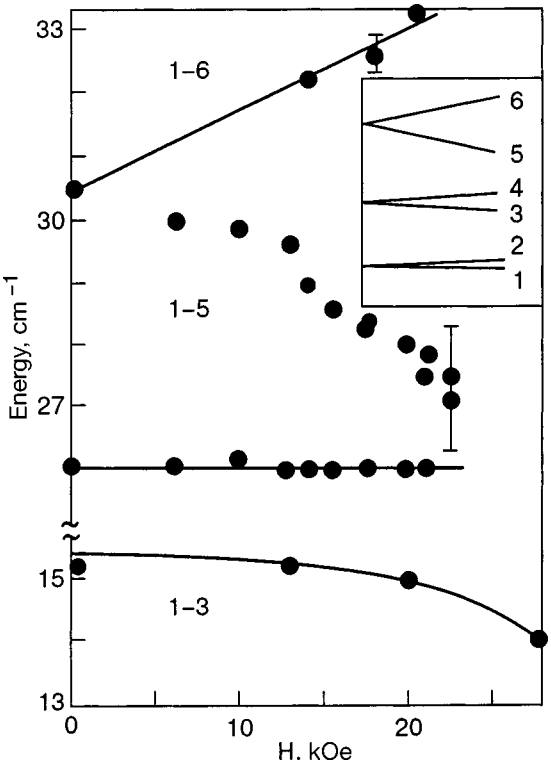

FIG. 31. Frequency–field curves of the splitting of the electronic levels of the $KEr(MoO_4)_2$ crystal for **H**‖**b**. The inset shows the scheme of the splitting of the ground and first two excited electronic levels and their numbering. The numbers on the curves indicate transitions between the corresponding sublevels.

of the absorption spectra for external fields **H** parallel to the **a**, **b**, and **c** axes of the crystal.[67] For the field orientation **H**‖**a** the frequency–field curve of one of the components of the 15.4 cm^{-1} band has a kink at a field of 9 kOe. Note the unusual behavior of components *1–5* (see Fig. 30) of the split 30.5 cm^{-1} band near the crossover with a phonon excitation whose energy position (26 cm^{-1}) remains unchanged in magnetic field: for $H>15$ kOe the electronic band is not shifted in energy. This is due to the interaction of the split components of the 30.5 cm^{-1} electronic level with the 26 cm^{-1} vibrational mode.

For the external field direction **H**‖**b** (see Fig. 31) near the crossover of the low-frequency component *1–5* of the split 30.5 cm^{-1} band with the vibrational mode 26 cm^{-1} a strong broadening occurs. Splitting of the 15.4 cm^{-1} band is not observed, only a slight shift to lower energies.

We note that for **H**‖**c** (see Fig. 32) the band corresponding to the transition to the second electronic level is split into three components, while the band corresponding to transition to the third electronic level (the 30.5 cm^{-1} band) is split into two. At a field larger than 20 kOe one observes a band whose origin we ascribe to a transition between components of the ground term *1–2*. In this geometry the g factor of the ground state is maximal. From the frequency–field curves obtained for band *1–2* it follows that at fields $H>20$ kOe the g factor of the ground levels reaches a value $g_c=19\pm1$.

Thus in an external magnetic field the electronic spectrum of the $KEr(MoO_4)_2$ crystal displays complex behavior. The anisotropy of the splitting of the electronic levels is a consequence of the rather low local symmetry and appreciable local anisotropy of the paramagnetic ions Er^{3+}. One also observes dependence of the value of the g factors of the spectroscopic splitting of the low-frequency excitations on the value of the external magnetic field. Table VII gives the values of the g factors of the spectroscopic splitting of the three lowest electronic levels of the Er^{3+} ions in the $KEr(MoO_4)_2$ crystal.

Let us briefly discuss these experimental results. It follows from studies of the absorption spectra of diluted Jahn–Teller crystals that the dynamic interaction of the electronic levels with vibrational branches leads to a change in the frequency position of the electronic levels or in their substantial broadening as the concentration of the Jahn–Teller ions increases. These differences in zero magnetic field are determined by the energy position of the electronic level engendered by the splitting of the ground multiplet by the static

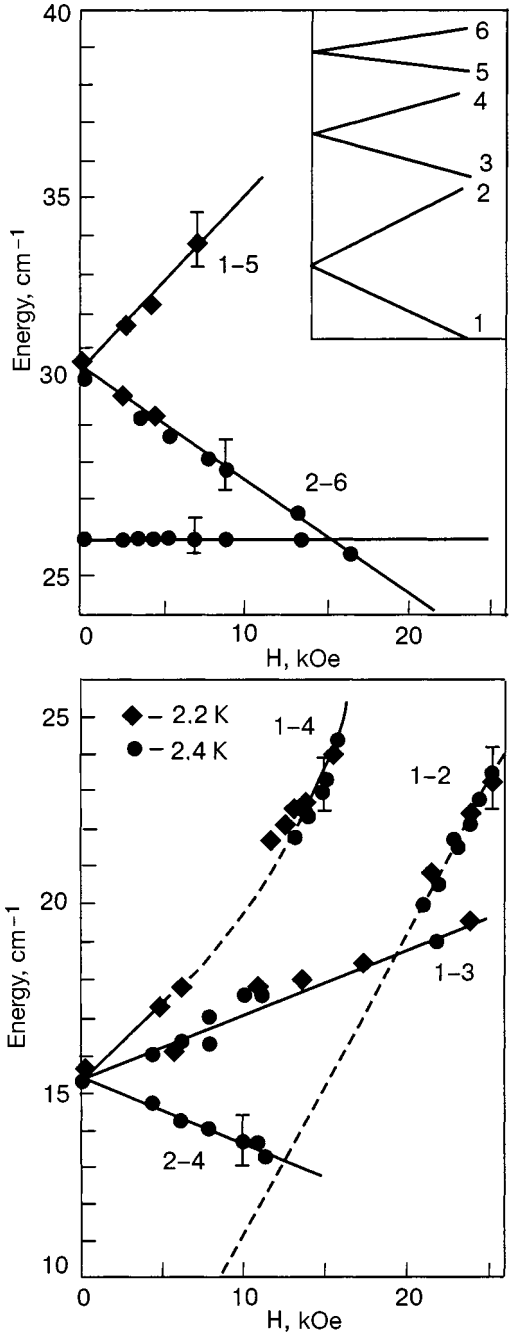

FIG. 32. Frequency–field curves of the splitting of the electronic levels of the $KEr(MoO_4)_2$ crystal for **H**‖**c**. The inset shows the scheme of the splitting of the ground and first two excited electronic levels and their numbering. The numbers on the curve indicate transitions between the corresponding sublevels.

crystalline field, with respect to the vibrational spectrum of the crystal.

By varying the strength of the external magnetic field one can vary the energy position of the electronic levels with respect to the vibrational spectrum. There are several possibilities for the manifestation of the dynamic coupling of the low-frequency excitations:

—the electronic level approaches an optical–acoustic branch from the high-energy side;

—the electronic level crosses an acoustic branch, and the external magnetic field shifts the crossing point into the region of the vibrational state with the larger density of states (e.g., toward the Brillouin zone boundary) from the low-energy side;

—the electronic level is found in a region of high density of vibrational states, and the magnetic field shifts it to a region with a low density of vibrational states.

TABLE VII. Values of the g factors of the spectroscopic splitting of the three lowest electronic states of the Er^{3+} ions in the crystal $KEr(MoO_4)_2$.

E	ν, cm^{-1}	g_a	g_b	g_c
E_1	0	~ 0.7	2 ± 1	14 (H < 10 kOe) 19 (H > 10 kOe)
E_2	15.4	3.3 ± 1 (H < 9 kOe) 12 ± 1 (H > 9 kOe)	~ 0	6 ± 1 (H < 20 kOe)
E_3	30.5	8 ± 1 (H > 15 kOe)	5 ± 1	3 ± 1 (H < 20 kOe)

Thus the experimental frequency–field curves are observed to repel the corresponding absorption bands when an electronic level crosses an optical–acoustic mode from the high-energy side (see Fig. 30). One can estimate the coupling energy of the electronic level ν_2^e with the optical–acoustic mode ν_2^{ph} using the formula for two interacting oscillators (2.2). In our case $\nu_0 = 26\ cm^{-1}$ and $\Delta\nu = 1.5\ cm^{-1}$, from which we get $\alpha = 6.3\ cm^{-1}$.

From an analysis of the behavior of the electron spectrum of the $KEr(MoO_4)_2$ crystal we can establish the following rule. If an electronic level approaches a region of maximal density of vibrational states from the low-energy side, then a broadening of the corresponding electronic absorption band occurs. This broadening is so large that the absorption band is hardly observed in the spectrum. The dynamic coupling of the electronic and vibrational excitations is quite significant, and a vibronic state arises. The repulsion of the electronic mode, as a rule, occurs when the electronic levels approaches the region of maximal density of vibrational states from the high-frequency side. Formally this difference in behavior is apparently due to the fact that the density of phonon states changes in a jump from the high-energy side, whereas it increases smoothly on the low-energy side.

These experimental results suggest the following. The electronic mode ($\nu_2^e = 30.5\ cm^{-1}$) lies higher in energy than the optical–acoustic vibrational branch ($\nu_2^{ph} = 26\ cm^{-1}$) and is a rather localized electronic excitation. In an external magnetic field **H**‖**a** or **H**‖**b** in the region of the where a split component of this mode crosses the vibrational mode ν_2^{ph} the two modes interact. For **H**‖**c** the split component is not coupled to the vibrational mode because of the different symmetry of the electronic and vibrational excitations (see Fig. 32).

In zero magnetic field the low-energy electronic level ν_1^e falls within the region of the transverse acoustic modes and undergoes a dynamic interaction with the low-frequency transverse acoustic modes in the form of cross splitting of the spectrum in the Brillouin zone. In an external magnetic field this electronic level also manifests coupling with the low-frequency optical–acoustic branches ν_1^{ph} and ν_2^{ph}. The dynamic coupling leads to broadening of the high-frequency component of the ν_1^e band, split in a field **H**‖**c**, as that com-

ponent approaches the region of maximum density of states from the low-energy side (see Fig. 32).

The most interesting feature is a kink on the frequency–field curve of the $\nu_1^e = 15.4$ cm^{-1} absorption band in a field $\mathbf{H}\|\mathbf{a}$ (see Fig. 30). It was assumed that the kink on the frequency–field curves of the splitting of this band at a field $H = 9$ kOe is due to a change in the coupling between the electronic and vibrational excitations. If this effect were accompanied by static distortions of the crystal lattice, then this would be reflected in the frequency–field curve of the high-frequency electronic mode. However, this is not observed experimentally. Apparently the kink arises as a result of a change in the dynamic coupling of the electronic excitation ν_1^e with an acoustic phonon branch.

In conclusion it should be noted that the observed features on the frequency–field curves of the spectrum of $KEr(MoO_4)_2$ are evidence of different scenarios for the manifestation of the dynamic coupling of the vibrational and electronic branches formed by the first and second excited states of the Er^{3+} ions.

Studies of the absorption spectra of $KDy(MoO_4)_2$ crystals in the millimeter and submillimeter wavelength ranges in an external magnetic field[22,50] have made it possible to determine the positions of the electronic levels of the Dy^{3+} ions at low temperatures ($T < T_{tr}, T_{tr} = 14.3$ K). Measurements were made in weak ($H < 30$ kOe) and strong ($H > 30$ kOe) magnetic fields.

The absorption spectra in the high-temperature phase ($T \sim 20$ K) were measured on a millimeter spectrometer of the cavity type at a frequency of 102 GHz.[22] For an orientation of the external magnetic field along the **a**, **b**, and **c** axis of the $KDy(MoO_4)_2$ crystal a single resonance line was observed in the spectrum, at a position determined by the effective g factors of the ground state: $g_a \approx g_b \approx 10$, $g_c \sim 2$. In a study of the angular dependence of the ESR spectra in the ac crystallographic plane a splitting of the resonance lines was observed which was due to rotation of the local axes of the paramagnetic centers. Thus in the high-temperature phase of the $KDy(MoO_4)_2$ crystal there exist two magnetically equivalent Dy^{3+} centers. The principal axis of the g tensors of the ground states of these centers are rotated in the ac plane by angles of $\pm 14°$ from the crystal axes. This position agrees with the results of the measurements of the ESR spectra in the isostructural crystal $KY(MoO_4)_2$ doped with a low concentration of Dy^{3+} ions,[55] and it is consistent with the crystal structure describing the $KDy(MoO_4)_2$ crystal. According to crystallography, two of the four Dy^{3+} ions belonging to the unit cell of the crystal are pairwise magnetically equivalent, since they are related by a center of symmetry. It should also be emphasized that the Dy^{3+} ions found in the layered packet $\{Dy(MoO_4)_2\}_{\infty\infty}$ are related by translational symmetry or a center of symmetry, and therefore each layered packet gives one paramagnetic magnetically equivalent center.

The low-frequency electronic spectra of the $KDy(MoO_4)_2$ crystal in the low-temperature phase ($T < T_{tr}$) were measured at low magnetic fields ($H < 30$ kOe) at $T = 4.2$ in the millimeter and submillimeter IR ranges (wavelengths $0.3 < \lambda < 1.25$ mm). It was found that for the orientation with the magnetic field **H** along the crystallographic axes **a** and **b** the absorption spectrum consists of one intense electronic band. The value of the g factor at these magnetic field strengths is not much different from the values of the g factor in the high-temperature phase. A substantial difference of the g factor in the low- and high-temperature phases arises when the magnetic field **H** deviates from the **b** axis in the crystallographic planes ab and bc. In those field directions one does observe splitting of the ESR lines, which is absent in the spectra in the high-temperature phase. The data suggest that in the low-temperature phase the ESR spectrum of the $KDy(MoO_4)_2$ crystal is formed by four magnetically inequivalent paramagnetic centers. The components of the g tensor of the ground state of each of the Dy^{3+} ion centers for $H < 30$ kOe have the following values: $g_z \sim g_y \sim 2$, $g_x \sim 17$.

Besides the absorption bands due to transitions between components of the lowest Kramers doublet, the spectrum exhibits absorption bands corresponding to transitions between the ground level and the first excited Stark levels of the ground multiplet $^6H_{15/2}$ of the Dy^{3+} ions, which is split by the static crystalline field. The measurements yielded an energy splitting at zero external magnetic field of $\Delta \approx 28$ cm^{-1} at 4.2 K and a value for the anisotropy of the g factor of the spectroscopic splitting of the first excited state: for $H < 30$ kOe the components of the g tensor of the first excited level had the values $g'_z \approx g'_x < 2$, $g_y = 16$. Thus it was learned that the direction of maximum values of the g factors of the ground and first excited Kramers doublets are rotated with respect to each other by an angle of $\pi/2$ in the ab plane of the crystal.

The absorption spectra of $KDy(MoO_4)_2$ crystals were also measured in the submillimeter wavelength range at high magnetic fields ($H > 30$ kOe). At such fields one observes a change in the values of the g factors of the ground and first excited Kramers doublets due to the interaction between the electronic excitations and vibrational branches and also between the electronic modes.[50] Measurements of the angular dependence of the spectra made it possible to determine the frequencies of the transitions from the components of the ground doublet to the components of the first excited doublet of the Dy^{3+} ion and the changes in the values of the effective g factors.

In the direction $\mathbf{H}\|\mathbf{b}$ all four centers of the Dy^{3+} ions are magnetically equivalent, leading to coincidence of their transition frequencies. The frequency–field curves of the transitions between components of the ground doublet and transitions from the components of the ground doublet to components of the first excited doublet in this field direction are shown in Fig. 33. Bands *1–2* correspond to transitions between components of the ground doublet, bands *1–3* and *1–4* to transitions to the excited doublet, and *2–3* and *2–4* to transitions from the upper components of the ground doublet to the excited doublet.

For the orientation of the field **H** in the crystallographic plane ab at a 45° angle to the **b** axis the four paramagnetic Dy^{3+} centers are pairwise equivalent, i.e., the observed frequencies of two pairs of paramagnetic centers do not coincide. The frequency–field curves of transitions between components of the two lowest doublets for such a direction of the external magnetic field are shown in Fig. 34. Bands *1–2* and *1′–2′* are due to transitions between the split com-

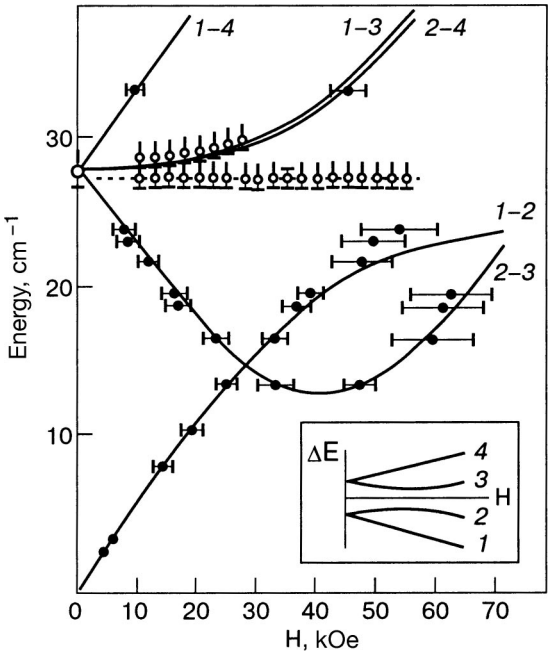

FIG. 33. Frequency–field curves of the electronic excitations of the $KDy(MoO_4)_2$ crystal for **H**‖**b**; the chalcogenides are experimental, the solid curves are calculated. The inset shows the scheme of splitting of the electronic levels and their numbering. The numbers on the curves indicate transitions between the corresponding sublevels.

ponents of the ground Kramers doublets, bands *1–3*, *1–4*, $1'-3'$, and $1'-4'$ to transitions from the lower components of the ground doublets, and *2–3*, *2–4*, $2'-3'$, and $2'-4'$ to transitions from the upper components of the ground doublets to components of the excited doublets for each pair of Dy^{3+} centers, respectively.

It can be seen in Figs. 33 and 34 that at magnetic fields $H>30$ kOe for **H**‖**b** the frequency–field curves display a ''repulsion'' of the electronic absorption bands. At fields $H<30$ kOe an interaction of the electronic excitation $\nu_2^e=28\ \mathrm{cm}^{-1}$ with the optical phonon branch ν_2^{ph} in view of the nonlinear frequency–field curve of the position of the electronic mode. One also observes a broadening of the electronic absorption band *1–2* as the region of maximum density of vibrational states of the optical–acoustic branch ν_2^{ph} is approached from the low-energy side.

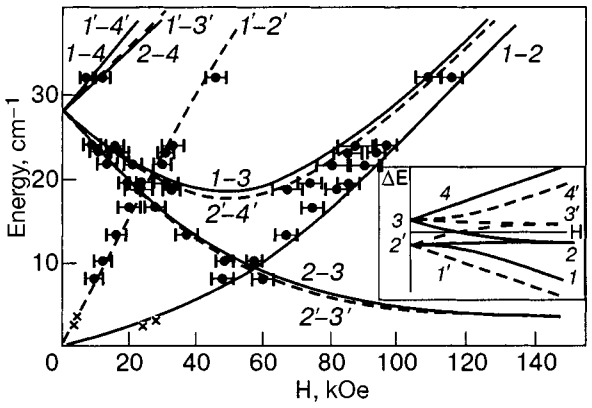

FIG. 34. Frequency–field curves of the electronic excitations of the $KDy(MoO_4)_2$ crystal in an external magnetic field oriented at a 45° angle to the **b** axis in the *ab* plane; the points are experimental, the solid curves are calculated. The inset shows the scheme of the splitting of the ground and first excited electronic levels and their numbering. The numbers on the curves indicate transitions between the corresponding sublevels.

Thus the measurements of the frequency–field curves of the microwave absorption spectra of $KDy(MoO_4)_2$ crystals in the low-temperature phase have established experimentally the presence of a dynamic interaction between the electronic and vibrational excitations and also between electronic modes.

The effect of magnetic field on the system was treated in the framework of crystalline field theory. The Zeeman energy operator $\mathcal{H}$ can be written in the following form for arbitrary orientation of the external magnetic field **H**:

$$\mathcal{H}=g_0\mu_B(H_xI_x+H_yI_y+H_zI_z), \tag{3.1}$$

where μ_B is the Bohr magneton, g_0 is the Lande factor, I_x, I_y, and I_z are the projections of the total moment, and H is the strength of the external magnetic field.

The splitting of the two lowest Kramers doublets was calculated at temperatures of 20 and 4.2 K, corresponding to the high-temperature and low-temperature phases of the crystal. These splittings are reflected on the frequency–field curves obtained by the method of long-wavelength IR laser spectroscopy, by the ESR method, and by far- and near-IR spectroscopy (see Figs. 33 and 34).

3.2. Magnetic-field-induced structural phase transitions of the CJTE type in ARDMs

It was shown above that the governing role in the activity of low-energy electronic excitations of rare-earth ions in the CJTE is played by their coupling with acoustic or optical–acoustic vibrational branches (see Sec. 1). By applying an external magnetic field one can change the position of the electronic excitations with respect to the vibrational spectrum and thereby alter the dynamic coupling of the low-energy electronic excitations with the vibrational branches.

All of this is a good prerequisite for stimulation or suppression of the CJTE by an external magnetic field in ARDMs.

The magnetic-field-induced structural phase transition was first observed by Leask *et al.*[38] in a member of the series of ARDMs—the compound $KDy(MoO_4)_2$. At zero magnetic field this compound undergoes a structural phase transition of the CJTE type ($T_{\mathrm{tr}}=14.3$ K) with the formation of an ordered structure in the low-temperature phase. Here the lowest electronic ''quasidoublet'' $\nu_1^e\sim 18\ \mathrm{cm}^{-1}$, which is active in the phase transition, is split to a value $\nu_2^e\approx 28\ \mathrm{cm}^{-1}$. In Ref. 38 the frequency–field curves of the absorption spectra were measured in the optical range in an external magnetic field. Figure 35 shows the magnetic-field dependence of the frequencies of the optical transitions measured in Ref. 38. It is seen from the figure that these curves have a kink at a field of ~ 4 T which was attributed by the authors to a phase transition induced by the external magnetic field.

We note that, according to Ref. 38, below the structural phase transition the $KDy(MoO_4)_2$ crystal takes on an antiferrodistortive Jahn–Teller ordering, unlike the thoroughly studied substance $DyVO_4$, where the ordering is of a ferrodistortive character. The presence of two sublattices permit-

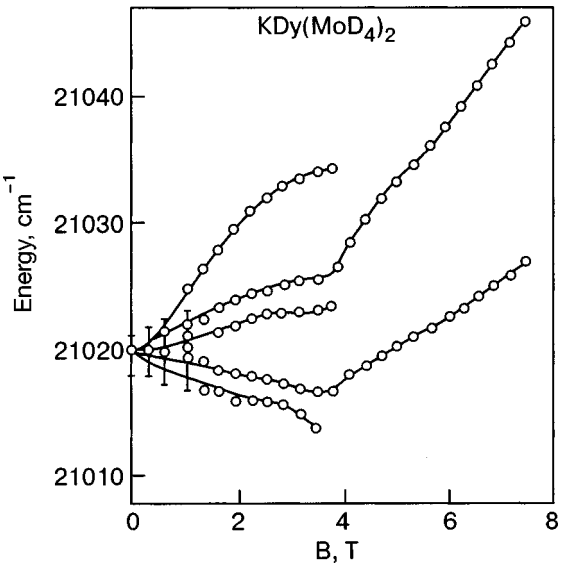

FIG. 35. Zeeman splitting of the 21019.7 cm^{-1} absorption band of the Dy^{3+} ions in the $KDy(MoO_4)_2$ crystal at $T=4.2$ K as a function of the magnitude of an external magnetic field oriented in the ab plane at a 45° angle to the axes.[38]

ted the authors of Ref. 38 to formally associate the structural phase transition in $KDy(MoO_4)_2$ to a "spin-flip" transition in antiferromagnets. The two-sublattice model used there[38] in the molecular field approximation gives a satisfactory qualitative description of the experimental results.

However, starting from the real structure of the low-energy spectrum of the $KDy(MoO_4)_2$ crystal, one can say that the transition from the ordered phase to the paraphase in an external magnetic field is due to a significant decrease in the dynamic coupling of the electronic excitations $\nu_1^e \sim 18\ cm^{-1}$ with the low-frequency vibrational branches.

For destroying the Jahn–Teller ordering the direction of the external magnetic field was chosen so as to maximize the difference of the g factors of the spectroscopic splitting of the ground and first excited electronic levels of the rare-earth ions (see Fig. 36). This field direction is at an angle of ~45° to the axes of the crystal in the ab plane. Here, if in one

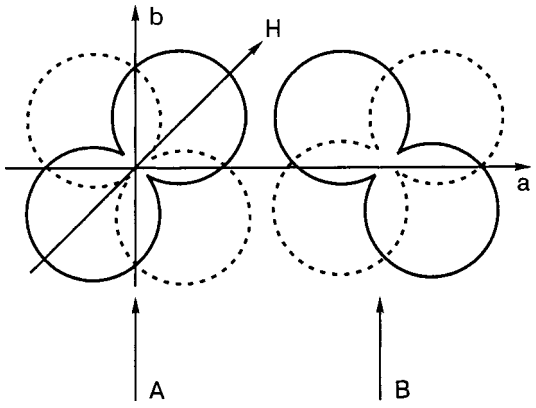

FIG. 36. Shape of the g tensor of the spectroscopic splitting of the ground and first excited states of the Dy^{3+} ions in the $KDy(MoO_4)_2$ crystal in the ab plane. The dotted line shows the shape of the g tensor of the excited state. A and B are the sublattices of the Dy^{3+} ions. The arrows denote the field direction corresponding to the maximum difference of the g factors of the spectroscopic splitting of the ground and first excited states.

sublattice the g factor of the spectroscopic splitting for the ground Kramers doublet is maximal, then it is minimal for the excited state, and just the opposite is true for the other sublattice (it was shown in Ref. 53 that the maximum values of the g factors of the ground and first excited doublets are rotated by an angle of $\pi/2$; see Fig. 34). This gives the maximum shift of the electronic excitations of the Dy^{3+} ions with respect to the vibrational spectrum at relatively low magnetic fields and thus decreases their dynamic coupling considerably. Ultimately this should lead to destruction of the Jahn–Teller ordering. The destruction of the Jahn–Teller ordering in a magnetic field in the $KDy(MoO_4)_2$ crystal was observed by an optical method. It was found that the transition occurs through an intermediate phase.

Thus we have investigated the influence of external magnetic field on the ordered structure in the ARDM $KDy(MoO_4)_2$. We have learned that an external magnetic field of a certain orientation can bring the crystal to a disordered phase (paraphase).

An external magnetic field can also have a stimulating influence on the cooperative Jahn–Teller effect. This is confirmed by studies of the low-energy spectrum of the crystal $KEr(MoO_4)_2$ in an external magnetic field.[67]

The $KEr(MoO_4)_2$ crystal does not undergo a structural phase transition of the CJTE type at temperatures down to 2 K.[18] This is indicated by the temperature dependence of the position of the first excited level of the Er^{3+} ions (see Fig. 18), although a spectroscopic study reveals the presence of dynamic coupling of the first excited state of the Er^{3+} ions ($\nu=8\ cm^{-1}$) with the acoustic vibrational spectrum of the crystal. The absence of a structural phase transition at zero magnetic field is due to the fact that the value of the correlation of the Jahn–Teller centers is insufficient for realization of the CJTE. However, the distortions of the Jahn–Teller centers are manifested in a dynamic manner: a softening of the elastic constants obtained from the temperature dependence of the ultrasound velocity occurs in an interval of temperatures comparable to the energy of the lowest electronic excitation.[20]

Considering this phenomenon in the framework of the molecular field approximation, we can state that the value of the molecular field $A<\Delta$, where $\Delta=8\ cm^{-1}$ and $A \sim 4\ cm^{-1}$ (Ref. 69; Δ is the energy interval to the first end level of the Er^{3+} ion). This relation can be violated if an external magnetic field is applied. In a study of the low-density spectrum of the $KEr(MoO_4)_2$ crystal it was found that for $\mathbf{H}\|\mathbf{c}$ the g factor of the spectroscopic splitting of the first excited electronic level of the Er^{3+} ions is larger than the g factor of the ground state.[67] At a certain value of the external magnetic field the first excited level can approach the ground level, i.e., there is "quasidegeneracy" with respect to the orbital moment. On the other hand, as the energy of the first excited electronic level decreases, the point of its crossing with the acoustic vibrational branch shifts toward the Brillouin zone center, into the region of maximal density of states. This leads to an increase in their dynamic coupling.

With the goal of obtaining a magnetic-field-induced structural phase transition of the CJTE type, the microwave absorption spectrum in $KEr(MoO_4)_2$ was studied in Ref. 70. The angular dependence of the ESR spectra of the Er^{3+} ions

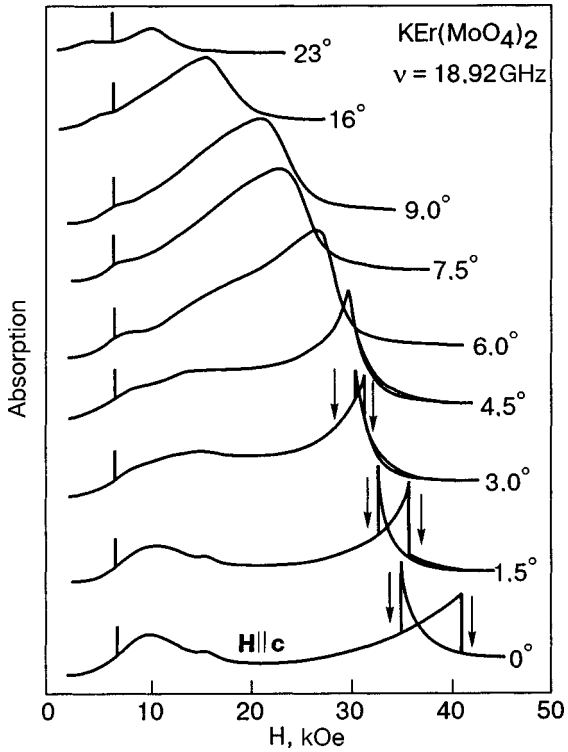

FIG. 37. Magnetic-field dependence of the microwave absorption spectra of the $KEr(MoO_4)_2$ crystal for different directions of **H** in the ac plane at a temperature of 1.8 K. The arrows indicate the anomalous changes in the absorption with increasing or decreasing magnetic field.

was measured in all crystallographic planes of this compound, and the frequency–field curves were measured for **H**‖**c**. Figure 37 shows the value of the microwave absorption of the Er^{3+} ions in $KEr(MoO_4)_2$ as a function of external magnetic field at different values of the angle of the field **H** with respect to the **c** axis of the crystal. It is seen that for **H**‖**c** the microwave absorption spectrum shows an abrupt decrease (jump) of the absorption intensity when the magnetic field is increased to 41 kOe. As the external magnetic field is decreased there is also an abrupt decrease in absorption but at a lower field. In other words, a hysteresis with respect to magnetic field is observed which amounts to $\Delta H \sim 5.6$ kOe. Measurements were made at a temperature of 1.8 K. At that temperature the $KEr(MoO_4)_2$ crystal is found in a paramagnetic state ($T_N = 0.9$ K). When the magnetic field direction deviates from the **c** axis one observes a decrease in the hysteresis, which vanishes completely at a critical angle $\varphi_c = \pm 4.5°$. Then a peak of nonresonance form is observed in the spectrum. As the angle φ is increased further, the shape of the peak is initially modified to an asymmetric form and then to the usual ESR absorption line. From the experimental data obtained, the (H,φ) phase diagram of the equilibrium states of the $KEr(MoO_4)_2$ crystal was constructed. It has a critical point at which the first-order phase transition ends (see Fig. 38). The (H,T) phase diagram was measured experimentally, and the critical temperature ($T_c \approx 5$ K) and critical field ($H_c \approx 41.5$ kOe) were measured (see Fig. 39).

A theoretical model of the structural phase transition in the $KEr(MoO_4)_2$ crystal was proposed in Refs. 71 and 72. Without going into the details of these approaches, we only note that the papers cited were able to give only a qualitative

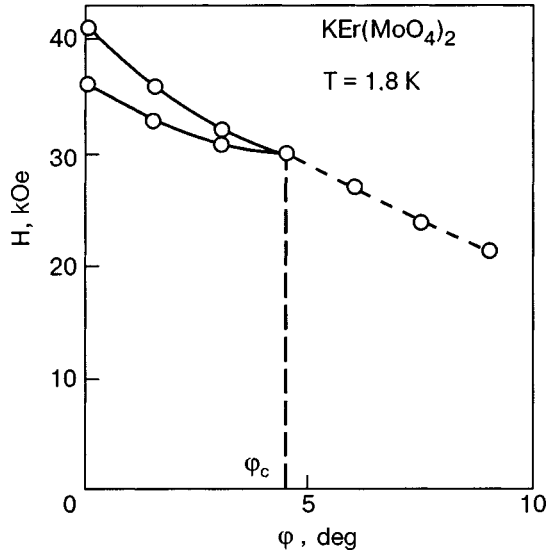

FIG. 38. Angular dependence of the values of the magnetic field at which the structural phase transition occurs in the $KEr(MoO_4)_2$ crystal at $T = 1.8$ K.

explanation of the (H,T) and (H,φ) phase diagrams. Apparently the discrepancy between the calculated and measured phase diagrams is due to the fact that the real structure of the low-energy exciton and phonon spectra was not taken into account.

It should be noted that analogous phase transitions with stimulation of the CJTE by an external magnetic field have also been observed[73,74] in the compounds $CsEr(MoO_4)_2$ and $KTm(MoO_4)_2$.

4. HIGHLY NONEQUILIBRIUM STATES IN LAYERED JAHN–TELLER CRYSTALS

In the previous Sections we have been considering the equilibrium structures of layered Jahn–Teller crystals of rare-earth compounds at low temperatures and have estab-

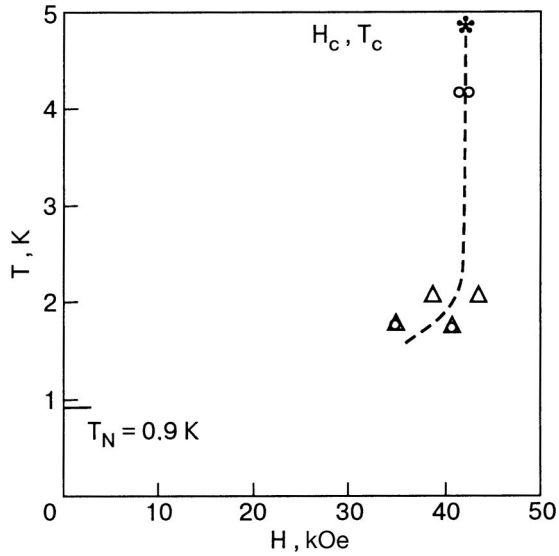

FIG. 39. Dependence of the phase transition temperature of the $KEr(MoO_4)_2$ crystal on the value of the external magnetic field. Δ—microwave absorption data; ○—data of magnetic susceptibility measurements.

lished the role of the dynamic coupling of low-energy excitations of the rare-earth ions with crystal lattice vibrations in the formation of those structures. We have investigated the spectra of elementary excitations of Jahn–Teller crystals near thermodynamic equilibrium. The external alternating fields applied in the study of these spectra were relatively low, so the response of the system was treated in the linear approximation.

However, when the external rf electric or magnetic field is increased, a transition to a nonlinear regime of vibrations can occur, and that makes the mode interaction processes substantially more complicated. Here the dynamics of the system is governed by nonlinearities that exist in it. Coherent behavior of a large ensemble of atoms or molecules can arise, and under favorable conditions nonequilibrium (dissipative) structures form.

In an irreversible process structure formation occurs under certain conditions. Here, as in the the equilibrium phase transitions, one observes a jump (phase transition) at threshold values of certain parameters. However, a significant deviation from equilibrium is insufficient for the formation of dissipative structures. It is necessary to have coherent behavior of the system, which can occur under certain conditions in the presence of certain interactions.

The following conditions are necessary for the formation of dissipative structures:

—the system must be open, i.e., it must exchange energy or matter with a medium;

—the dynamical equations describing the system must be nonlinear;

—the deviation from equilibrium must exceed a critical value;

—the microscopic motions in the system must occur coherently, i.e., in a matched manner.

We emphasize that coherent behavior of a system is due to causes engendered at the microscopic level. We note that nonlinearity is the first cause of high sensitivity of dynamical systems to the initial conditions, which leads to chaotic behavior and is a typical property of many dynamical systems. In the solution of nonlinear differential equations it has been established that chaos can be observed in all dynamical systems with a number of degrees of freedom $r>2$, and consequently at sufficiently long times their behavior becomes unpredictable.

So-called deterministic chaos in dynamical systems is actively studied today. Methods of diagnostics of chaotic behavior have been developed, and quite a few general rules have been found. The scenario of the transition from regular to chaotic motion in many dynamical systems has a universal character and is reminiscent of ordinary second-order phase transitions. The introduction of renormalization-group methods opens up new prospects for the study of deterministic chaos.

Jahn–Teller crystals are convenient model objects for studying phenomena in a highly nonequilibrium state. They can not only be nonlinear but can also serve as an active medium capable of generating or enhancing vibrations of a certain type. The nonlinear interaction of waves in this medium leads to a redistribution of energy between the different degrees of freedom and makes it possible to use these crystals for studying problems of the nucleation of turbulence (dynamical chaos). The main effect that can arise in these materials in a highly nonequilibrium state is the generation of coherent elastic vibrations under excitation of a sufficiently large number of Jahn–Teller centers by a microwave pump. The initial set of excitations of Jahn–Teller centers in this case is incoherent. Let us consider the nonequilibrium phase transitions for the $KEr(MoO_4)_2$ crystal as an example.

4.1. Nonequilibrium phase transitions induced by an external high-frequency magnetic field in the Jahn–Teller crystal $KEr(MoO_4)_2$

In the $KEr(MoO_4)_2$ crystal in an external magnetic field with the orientation $\mathbf{H}\|\mathbf{a}$ the g factor of the spectroscopic splitting of the first excited electronic level of the Er^{3+} ion is larger than the g factor of the ground level.[67] Therefore, in an external magnetic field the ground and first excited levels draw closer together, and at a certain value, when the condition $A>\Delta$ is satisfied, a magnetic-field-induced structural phase transition of the CJTE type occurs. The (H,T) and (H,φ) phase diagrams of the dynamical states of the $KEr(MoO_4)_2$ crystal were used to determine the critical temperature ($T_c\sim 5$ K), critical magnetic field ($H_c \approx 41.5$ kOe), and critical angles ($\varphi_c=\pm 4.5°$) at which the first-order phase transitions go over to second-order.

At these critical points and also on lines of second-order phase transitions the microwave absorption spectrum has a sharp spike due to absorption of the radiation in the critical region of the structural transition. With changing frequency of the high-frequency magnetic field the position of this peak in respect to the external magnetic field remains unchanged. It is therefore assumed that this absorption is nonresonance and that the observed peak is of a relaxational nature. In Ref. 75 the behavior of the $KEr(MoO_4)_2$ crystal in a highly nonequilibrium state was investigated in the critical region of the structural phase transition under conditions of microwave pumping. In view of the fact that the system possesses substantial nonlinearity in the region where the relaxation absorption is observed and in view of the long relaxation times, there are grounds for assuming that the threshold power of the microwave field for the creation of a nonlinear regime of motion under these conditions will be significantly lower than for systems found under conditions far from the critical region.

Measurements were made at a bath temperature of 1.9 K and a frequency of 18.7 GHz in the following sequence. First the sample was rotated in the (010) plane so that the magnetic field vector was oriented along the **a** axis. Then the power of the microwave pump was increased. Figure 40 shows the dependence of the absorption spectra of the $KEr(MoO_4)_2$ crystal on the value of the external magnetic field at different levels of microwave pump power. It is seen in the figure that at low microwave power the absorption spectrum has a relaxation peak, the maximum of which corresponds to a field of 38.5 kOe. When the microwave power reaches a certain level a narrow dip appears in the region of the maximum of the relaxation peak and increases in depth with increasing microwave pump power. As the microwave power increases further, the dip broadens and a new absorption peak appears at the center of the dip. The position of the maximum of this absorption peak in respect to magnetic field

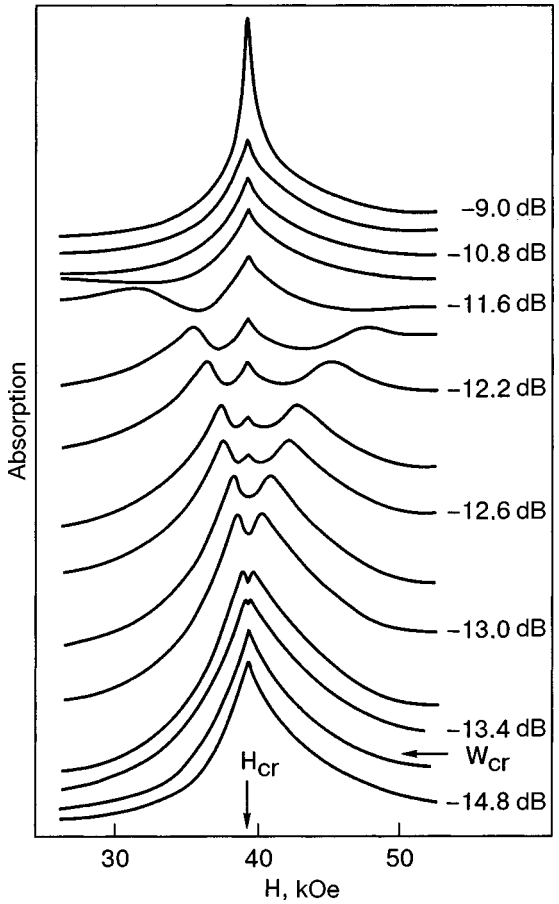

FIG. 40. Absorption spectra of the $KEr(MoO_4)_2$ crystal in an external magnetic field for different values of the microwave absorption in the region of the first bifurcation.

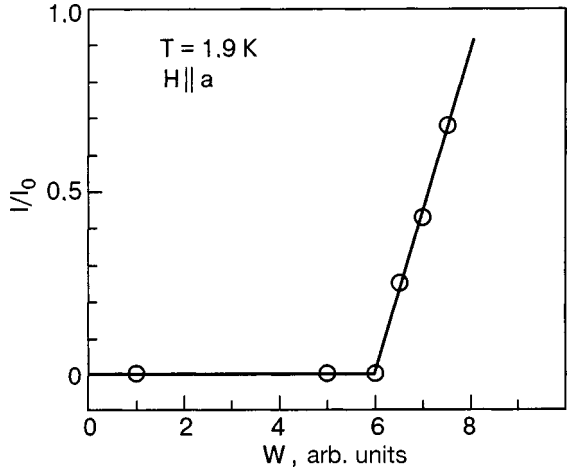

FIG. 41. Relative intensity of the the dip at the maximum of the relaxation absorption versus the power of the microwave field (I_0 is the intensity of the relaxation absorption at the maximum).

coincides with the position of the maximum of the peak that is observed at low power of the microwave pump. With the appearance of the new peak the microwave absorption band has three maxima. As the microwave power increases, the two side maxima are shifted to the low-field and high-field sides from the center peak and then vanish. As the microwave power is increased further, the new absorption peak grows in intensity and becomes narrower.

The evolution of the absorption spectrum described above cannot be caused by overheating of the sample or by the influence of saturation of the absorption bands, effects usually observed in the ESR spectrum. The concept of nonequilibrium temperature was invoked to explain it. The justification for this was that the change in the spectrum has a threshold character in respect to the power of the microwave pump.

Furthermore, as is seen in Fig. 41, the value of the dip on the relaxation peak depends linearly on the value of the microwave power W. Usually in spectroscopy the intensity of the absorption bands that rise at second-order structural phase transitions varies in proportion to the square of the order parameter. Therefore, in the case illustrated one has a dependence of the type

$$\eta \sim \alpha (W - W_{\rm cr})^{1/2} \tag{4.1}$$

(η characterizes the concentration of the ordered phase). Such a dependence is also characteristic for nonequilibrium second-order phase transitions.[76]

A third important factor is that the system is found in the critical region of a structural phase transition induced by external magnetic field. That is, it can easily be brought to a nonlinear regime of motion, which is a necessary condition for a nonequilibrium phase transition with the formation of a dynamic nonequilibrium structure.

Let us briefly discuss the experimental results presented in Fig. 40. In the critical region of the structural phase transition in the $KEr(MoO_4)_2$ crystal an electronic relaxation mode is excited by the rf field. Here a pumping of the electron subsystem occurs, and its excitation is transferred to the phonon subsystem. As a consequence of the strong dynamic coupling, this excitation is transferred to the phonon subsystem in a very short time. The phonon subsystem transfers energy to the bath much more slowly, since the crystal is found in the critical region of the structural phase transition, where, because of the strong anharmonicity, phonon–phonon interaction processes are efficient. On the other hand, the low-energy vibrational spectrum of the $KEr(MoO_4)_2$ crystal is nondecaying, and the thermalization time of the phonon excitations is large, i.e., a so-called ''phonon bottleneck'' is realized. The significant difference of the relaxation time of the electron subsystem from the time from the time required to establish thermodynamic equilibrium in the phonon subsystem ($\tau_{e\rm ph} \ll \tau_{\rm ph}$) causes a highly nonequilibrium state to arise in the phonon subsystem: ''overheated'' phonons are formed.[75]

The decay of the relaxation excitation to phonons must obey the energy and momentum conservation laws:

$$\mathbf{k} + \sum_n k_n = 0, \quad \omega + \sum_n \omega_n = 0, \tag{4.2}$$

where $\omega_n = \omega_n(\mathbf{k})$ is the dispersion relation for the nth branch of the phonon spectrum ($\mathbf{k}$ is the wave vector).

In the case when the main role is played by three-particle processes, the conservation laws take the form

$$\omega(\mathbf{k}) = \omega(\mathbf{k}_1) + \omega(\mathbf{k}_2), \quad \mathbf{k} = \mathbf{k}_1 + \mathbf{k}_2, \tag{4.3}$$

i.e., a decay of the electronic branch into two phonon branches occurs. For this process to be efficient, it is necessary that the condition $\omega(\mathbf{k})_{k=0} \neq 0$ hold, and it does in fact hold in the case under consideration.

Let us consider what branches of the vibrational spectrum interact with the relaxation mode. The $KEr(MoO_4)_2$ crystal has symmetry point group D_{2h}. Since the relaxation mode is excited by an electromagnetic wave with wave vector $k \sim 0$, it can be associated with combinations of phonons of the form

$$(q_x,0,0)+(-q_x,0,0);\quad (0,q_y,0)+(0,-q_y,0);$$

$$(0,0,q_z)+(0,0,-q_z), \tag{4.4}$$

The representations of the space group for these combinations of vectors contain irreducible representations of the point group D_{2h}. The symmetry of the relaxation mode is B_{1g}. A group theoretical treatment shows that the relaxation excitation can interact with pairs of low-frequency oscillations of the following symmetry types:

$$B_{2u}(0,0,q_z)+B_{3u}(0,0,-q_z);$$

$$B_{2u}(q_x,0,0)+B_{3u}(-q_x,0,0);$$

$$B_{2u}(0,q_y,0)+B_{3u}(0,-q_y,0). \tag{4.5}$$

We note that in the first variant, transverse acoustic modes are excited, and in the second and third, a transverse and a longitudinal mode. It is usually assumed that the decay of an electronic excitation into two transverse modes is more probable, since they are lower-energy.[60] Concrete calculations of the relaxation of an electronic excitation into lattice vibrations are complicated.

In view of the Jahn–Teller nature of the magnetic-field-induced structural phase transition, it is natural to assume that at least one phonon mode is linearly coupled to the relaxation (pseudospin) mode that is the order parameter of the structural phase transition.

It should be noted that the unusual dependence of the relaxation absorption on the power of the microwave field and also the narrowing of the relaxation peak at microwave powers above the threshold value suggest that at a certain microwave pumping level a coherent structure arises for a coupled electron–phonon excitation in the $KEr(MoO_4)_2$ crystal.

The low threshold of formation of this structure in respect to the microwave power (according to estimates, several W/cm^3 of the substance) is apparently due to the fact that the $KEr(MoO_4)_2$ crystal is found in the critical region of a structural phase transition.

This raises the question of the possible scenario for the transition of the system from regular motion to dynamical chaos. We stress that there is no single mechanism of transition to chaotic motion in highly nonequilibrium systems. Since a highly nonequilibrium state is described by nonlinear equations, in the space of their parameters a whole hierarchy of instabilities accompanying the transition from regular motion to deterministic chaos is observed. In other words, in a macroscopic system the regions far from thermodynamic equilibrium are characterized by a great diversity of dynamical regimes.

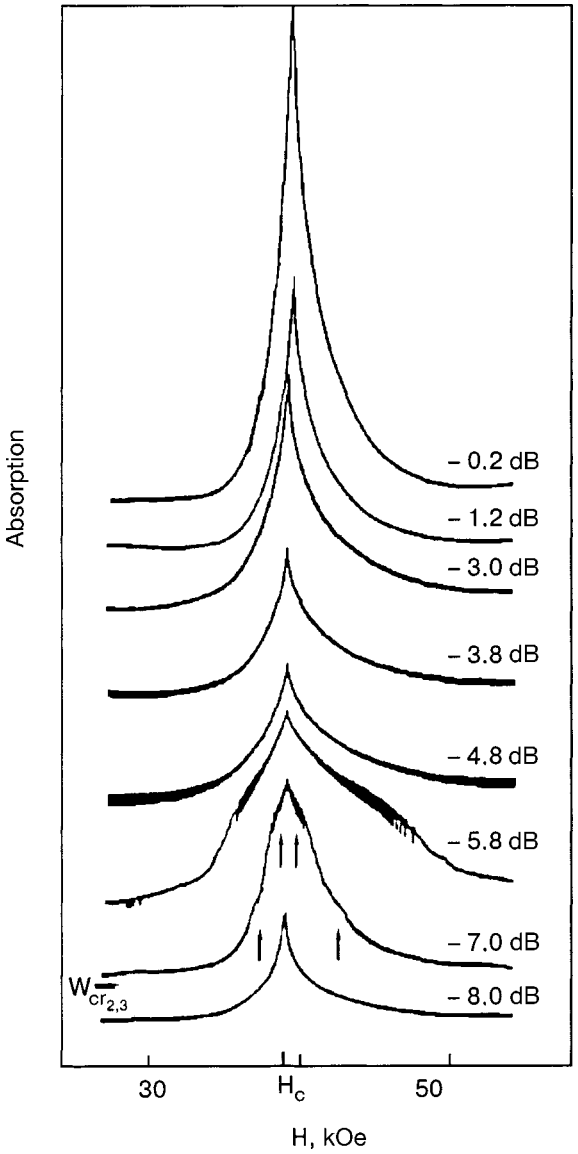

FIG. 42. Microwave absorption spectra of the $KEr(MoO_4)_2$ crystal in an external magnetic field for different values of the microwave power in the region of the second and third bifurcations.

For studying the scenario of the transition of the system to dynamical chaos, measurements of the microwave absorption in the region of the structural phase transition induced by an external magnetic field in $KEr(MoO_4)_2$ were carried out at high power levels of the microwave pump.[77,78]

Figure 42 shows the dependence of the microwave absorption of the $KEr(MoO_4)_2$ crystal on the value of the external magnetic field H at higher microwave power levels than in Fig. 40. After the first bifurcation in the absorption spectrum there are a second and third. The behavior of the spectrum in the region of the second and third bifurcations differs in the fact that while the relaxation peak practically vanishes upon the first bifurcation, upon the second and third it is only broadened, and structure appears on it. As a result of the first bifurcation the width of the relaxation peak narrows noticeably, while after the second and third bifurcations such narrowing does not occur. In the spectral region adjacent to the third bifurcation, low-frequency noise appears on the wings of the relaxation peak.

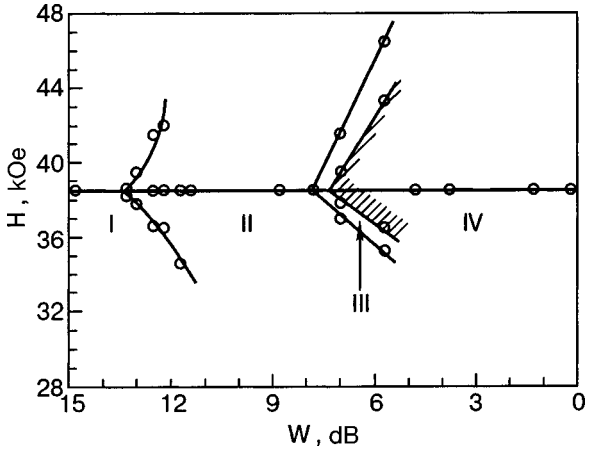

FIG. 43. Phase diagram of the dynamic states of $KEr(MoO_4)_2$ in the plane of the parameters H,W: I region of the stationary state; II, III, and IV—regions of regular motion; the region of the low-frequency noise is shaded.

As the power of the microwave radiation is increased further, the region of low-frequency noise divides into two parts, which are shifted to higher and lower fields with respect to the relaxation peak. Then the low-frequency noise vanishes. After that a relaxation peak similar to the peak prior to the second and third bifurcations is restored.

According to the experimental data presented in Figs. 40 and 42 a diagram was constructed displaying the values of the magnetic field at which the absorption maxima are observed on the relaxation peak as functions of the microwave power W of the microwave field (see Fig. 43).

In discussing the evolution of the microwave absorption spectrum the concept of a sequence of nonequilibrium phase transitions in a dissipative system was invoked, since the phenomena described have a threshold character in relation to the power of the microwave pump[75] and the system is found in the region of a structural phase transition, where high lability is typical. We stress that the microwave power is at once pumped into three degrees of freedom of the system which are active in the structural phase transition, since in the critical region the frequencies of these degrees of freedom soften and fall within the microwave absorption region. Ours is also an open system with significant absorption of microwave radiation and energy transfer to the surrounding medium.

Let us briefly discuss the possible mechanisms of the transition to deterministic chaos in the system. The first scenario of the transition to turbulence in a hydrodynamic system was proposed by Landau.[79] According to that scenario in a dynamical system with increasing departure from equilibrium, new frequencies of motion appear as a result of a sequence of Hopf bifurcations, until the whole low-frequency spectrum is filled. This is the criterion of the transition to turbulence. Later the theoretical concepts of the evolution of physical systems to deterministic chaos would undergo intensive development.[80,81] According to the modern ideas, the transition of a system to chaotic motion occurs according to one of three scenarios which are characteristic for a wide class of physical dissipative systems.

The best-studied of them is the Feigenbaum scenario,[82] according to which the evolution of a system starts from a Hopf bifurcation, which is a transition with a change in the character of the motion of the system from a stable focus to a stable limit cycle with frequency f. Upon further change of the control parameter a sequence of period-doubling bifurcations occurs, leading to periodic motion with the frequencies $f/2, f/4, f/8, f/16\ldots$. The dependence of the bifurcations on the parameter and shape of the spectrum in this case is of a universal character. The scaling law can be written in the form

$$(W_{k+1}-W_k)/(W_k-W_{k-1})=1/\delta, \tag{4.6}$$

where $\delta=4.6692$ is a universal constant, and W_k is the power of the microwave field of the pump at which the kth bifurcation occurs. The rate of convergence of W to W_∞ can be represented approximately by the asymptotic formula

$$W_k=W_\infty+A\delta^{1-k}, \tag{4.7}$$

where W_∞ is the power of the microwave field at which the transition of the system to chaotic motion occurs. One can estimate W_∞ in terms of W_1 and W_2:

$$W_\infty\approx W_1+1.3(W_2-W_1). \tag{4.8}$$

Analysis of the experimental results obtained in Ref. 78 shows that the first three bifurcations observed do not fit into a series of period-doubling bifurcations.

The transition to deterministic chaos by the Pomeau–Manneville scenario can be viewed as a transition to chaotic motion via intermittency of chaotic and regular motions.[83] Ruelle and Takens proposed a mechanism for the onset of turbulence[84] wherein two sequential Hopf bifurcations occur in the system and then after the third bifurcation the transition of the system to chaotic motion occurs. The behavior of our system resembles the Ruelle–Takens scenario, since the manifestation of low-frequency noise in it appears in the region adjacent to the third bifurcation. The low-frequency noise is apparently indicative of the onset of chaotic motion in this region (see Fig. 42).

In summary, we can say that for the system under study at the given value of the pump power the Ruelle–Takens scenario is qualitatively the closest of the three paths to dynamical chaos usually observed.

The question of the evolution of a system and the mechanism of the transition from regular motion to dynamical chaos in the Jahn–Teller elastic $KEr(MoO_4)_2$ upon further increase in pump power remains incompletely answered. To state unambiguously that in this region the system exhibits its motion of the strange attractor type will require careful mathematical analysis of the low-frequency noise. It should also be emphasized that of the three bifurcations observed in the absorption spectrum, the first is the strongest. This indicates that the first bifurcation entails the strongest channels of coupling of the electron and phonon subsystems. It is therefore assumed that the subsequent evolution of the system will take place via the path of increasing departure from equilibrium on these degrees of freedom, and that should ultimately lead to a sequence of period-doubling bifurcations, and so the system should follow the Feigenbaum scenario. To answer this question it will be necessary to study further the microwave absorption spectra of $KEr(MoO_4)_2$ using more powerful radiation sources.

CONCLUSION

As a result of the foregoing analysis of the experimental results from the spectroscopy of layered Jahn–Teller crystals—in particular, ARDMs, which are model objects of highly anisotropic Jahn–Teller crystals of rare-earth compounds—some rules have been established for the formation of the low-energy states in these compounds.

1. It has been shown that a substantial role in the formation of the low-energy spectrum in anisotropic Jahn–Teller crystals is played by the dynamic coupling of the electronic excitations of the Jahn–Teller centers with crystal lattice vibrations.

2. It has been established that the two forms of dynamic coupling of electronic excitations with lattice vibrations are observed. A weak coupling forms when the electronic levels of the rare-earth ions cross vibrational branches in a region of low density of states; in this case a splitting of the acoustic vibrational branches occurs, with the formation of a ''quasi-gap'' in the spectrum. When the electronic levels cross vibrational branches in the region of maximal density of states, strong dynamic coupling is formed. In the latter case the formation of vibronic states occurs in the crystal.

3. It has been shown that the electronic levels active in the pseudo-Jahn–Teller effect are those characterized by strong dynamic coupling with the vibrational branches of the crystal lattice (vibronic).

4. It has been established experimentally that the equilibrium structures of highly anisotropic Jahn–Teller crystals manifest a high sensitivity to substitutional impurities and also to external magnetic field.

5. The strong dynamic coupling of the electron and ion subsystems promotes the formation of dissipative structures in anisotropic Jahn–Teller elastics. Upon the creation of a highly nonequilibrium state in the electron subsystem in the critical region of a structural phase transition of the CJTE type one should observe self-organization of the Jahn–Teller systems, with the formation of dissipative structures.

The author thanks M. M. Bogdan, E. S. Syrkin, and N. F. Kharchenko for perusing the manuscript and offering critical comments.

*E-mail: kutko@ilt.kharkov.ua

[1] G. A. Gehring and K. A. Gehring, Rep. Prog. Phys. **38**, 1 (1975).
[2] R. J. Elliott, R. T. Harley, W. Hayes, and S. R. P. Smith, Proc. R. Soc. London, Ser. A **328**, 217 (1972).
[3] K. I. Kugel' and D. I. Khomskiĭ, Usp. Fiz. Nauk **136**, 621 (1982) [Sov. Phys. Usp. **25**, 231 (1982)].
[4] D. M. Kaplan and B. G. Vekhter, *Cooperative Phenomena in Jahn-Teller Crystals*, Plenum Press, New York–London (1995).
[5] E. S. Syrkin and S. B. Feodos'ev, Fiz. Nizk. Temp. **5**, 1069 (1979) [Sov. J. Low Temp. Phys. **5**, 506 (1979)].
[6] E. S. Syrkin and S. B. Feodos'ev, Fiz. Nizk. Temp. **8**, 760 (1982) [Sov. J. Low Temp. Phys. **8**, 381 (1982)].
[7] M. A. Mamalui, E. S. Syrkin, and S. B. Feodosyev, Fiz. Nizk. Temp. **24**, 779 (1998) [Low Temp. Phys. **24**, 583 (1998)].
[8] M. A. Mamalui, E. S. Syrkin, and S. B. Feodosev, Fiz. Nizk. Temp. **25**, 976 (1999) [Low Temp. Phys. **25**, 732 (1999)].
[9] A. M. Kosevich, E. S. Syrkin, and S. B. Feodosyev, Phys. Low-Dimens. Semicond. Struct. **3**, 47 (1994).
[10] A. M. Kosevich, *Theory of the Crystal Lattice* [in Russian], Vishcha Shkola, Kharkov (1988).
[11] M. V. Mokhosoev, F. P. Alekseev, and V. L. Butukhanov, *Double Molybdates and Tungstenates* [in Russian], Izd-vo Nauka SO, Novosibirsk (1981).
[12] P. V. Klevtsov and R. F. Klevtsova, Zh. Strukt. Khim. **18**, 419 (1977).
[13] V. A. Vinokurov and P. V. Klevtsov, Kristallografiya **17**, 127 (1972) [Sov. Phys. Crystallogr. **17**, 102 (1972)].
[14] J. Hanuza and V. V. Fomitsev, J. Mol. Struct. **66**, 1 (1980).
[15] P. V. Klevtsov, V. A. Vinokurov, and R. F. Klevtsova, Kristallografiya **17**, 284 (1972) [Sov. Phys. Crystallogr. **17**, 240 (1972)].
[16] R. F. Klevtsova and S. V. Borisov, Dokl. Akad Nauk SSSR **177**, 1333 (1967) [Sov. Phys. Dokl. **12**, 1095 (1968)].
[17] V. I. Kut'ko, Fiz. Nizk. Temp. **24**, 383 (1998) [Low Temp. Phys. **24**, 291 (1998)].
[18] V. I. Kut'ko, Yu. N. Kharchenko, N. M. Nesterenko, and A. A. Gurskas, Fiz. Nizk. Temp. **22**, 785 (1996) [Low Temp. Phys. **22**, 603 (1996)].
[19] G. A. Zvyagina, S. V. Zherlitsyn, V. D. Fil', and A. A. Gurskas, Ferroelectrics **110**, 35 (1990).
[20] G. A. Zvyagina and A. A. Zvyagin, Fiz. Nizk. Temp. **26**, 482 (2000) [Low Temp. Phys. **26**, 354 (2000)].
[21] I. M. Vitebskiĭ, S. V. Zherlitsyn, A. I. Zvyagin, A. A. Stepanov, and V. D. Fil', Fiz. Nizk. Temp. **12**, 1108 (1986) [Sov. J. Low Temp. Phys. **12**, 626 (1986)].
[22] V. A. Bagulya, A. I. Zvyagin, M. I. Kobets, A. A. Stepanov, and A. S. Zaika, Fiz. Nizk. Temp. **14**, 493 (1988) [Sov. J. Low Temp. Phys. **14**, 270 (1988)].
[23] I. E. Paukov, L. E. Reznik, and G. I. Frolova, Fiz. Tverd. Tela (Leningrad) **24**, 3473 (1982) [Sov. Phys. Solid State **24**, 1976 (1982)].
[24] I. B. Bersuker, B. G. Vekhter, and I. Ya. Ogurtsov, Usp. Fiz. Nauk **116**, 605 (1975) [Sov. Phys. Usp. **18**, 569 (1975)].
[25] D. Mihailovic, J. F. Ryan, and M. C. K. Wiltshire, J. Phys. C **20**, 3047 (1987).
[26] V. A. Bagulya, A. I. Zvyagin, V. I. Kut'ko, A. A. Mil'ner, and I. V. Skorobogatova, Fiz. Nizk. Temp. **14**, 1215 (1988) [Sov. J. Low Temp. Phys. **14**, 673 (1988)].
[27] E. S. Syrkin, S. B. Feodos'ev, L. N. Pelikh, and A. A. Gurskas, Fiz. Tverd. Tela (Leningrad) **24**, 2076 (1982) [Sov. Phys. Solid State **24**, 1184 (1982)].
[28] L. N. Pelikh and A. I. Zvyagin, Fiz. Tverd. Tela (Leningrad) **20**, 1912 (1978) [Sov. Phys. Solid State **20**, 1106 (1978)].
[29] M. Maczka, S. Kojima, and J. Hanuza, J. Phys.: Condens. Matter **10**, 8093 (1998).
[30] A. I. Zvyagin and V. I. Kut'ko, Fiz. Nizk. Temp. **13**, 537 (1987) [Sov. J. Low Temp. Phys. **13**, 303 (1987)].
[31] V. I. Fomin, V. P. Gnezdilov, V. V. Eremenko, and N. M. Nesterenko, Fiz. Tverd. Tela (Leningrad) **31**(5), 266 (1989) [Sov. Phys. Solid State **31**, 871 (1989)].
[32] E. E. Anders, A. I. Zvyagin, and L. S. Shestachenko, Fiz. Nizk. Temp. **6**, 1980 (1980) [Sov. J. Low Temp. Phys. **6**, 661 (1980)].
[33] S. D. El'chaninova, A. I. Zvyagin, and Z. A. Kazeĭ, Fiz. Nizk. Temp. **8**, 303 (1982) [Sov. J. Low Temp. Phys. **8**, 152 (1982)].
[34] S. D. El'chaninova and A. I. Zvyagin, Fiz. Nizk. Temp. **9**, 1200 (1983) [Sov. J. Low Temp. Phys. **9**, 619 (1983)].
[35] N. M. Nesterenko, V. I. Fomin, V. I. Kut'ko, and A. I. Zvyagin, Preprint 26-82 [in Russian], B. Verkin Institute for Low Temperature Physics and Engineering, National Academy of Sciences of Ukraine, Kharkov (1982).
[36] L. N. Pelikh, A. A. Gurskas, and A. I. Zvyagin, Fiz. Tverd. Tela (Leningrad) **22**, 262 (1980) [Sov. Phys. Solid State **22**, 155 (1980)].
[37] A. I. Zvyagin, T. S. Stetsenko, V. G. Yurko, and R. A. Vaĭshnoras, JETP Lett. **17**, 135 (1973).
[38] M. J. M. Leask, O. C. Tropper, and M. L. Wells, J. Phys. C **14**, 3481 (1981).
[39] I. V. Skorobogatova and A. I. Zvyagin, Fiz. Nizk. Temp. **4**, 800 (1978) [Sov. J. Low Temp. Phys. **4**, 381 (1978)].
[40] I. V. Skorobogatova and E. M. Savchenko, Fiz. Nizk. Temp. **6**, 112 (1980) [Sov. J. Low Temp. Phys. **6**, 55 (1980)].
[41] A. I. Zvyagin, S. D. El'chaninova, T. S. Stetsenko, L. N. Pelikh, and E. N. Khats'ko, Fiz. Nizk. Temp. **1**, 79 (1975) [Sov. J. Low Temp. Phys. **1**, 39 (1975)].
[42] A. A. Gurskas, A. I. Zvyagin, and L. N. Pelich, Ferroelectrics **48**, 81 (1983).
[43] M. A. Ivanov, V. Ya. Mitrofanov, and A. Ya. Fishman, Fiz. Tverd. Tela (Leningrad) **20**, 3023 (1978) [Sov. Phys. Solid State **20**, 1744 (1978)].
[44] F. Mehran and K. W. H. Stevens, Phys. Rev. B **22**, 2899 (1983).
[45] A. M. Pshisukha, A. I. Zvyagin, and A. S. Chernyi, Fiz. Nizk. Temp. **2**, 339 (1976) [Sov. J. Low Temp. Phys. **2**, 170 (1976)].
[46] Kh. Betger, *Principles of Dynamic Lattice Theory* [Russian translation], Mir, Moscow (1986).

[47] A. M. Kosevich, JETP Lett. **1**, 25 (1965).
[48] D. M. Bercha, M. N. Botvinko, L. Yu. Germanskaya, and M. A. Ivanov, Fiz. Nizk. Temp. **12**, 287 (1986) [Sov. J. Low Temp. Phys. **12**, 162 (1986)].
[49] V. I. Kut'ko, I. V. Skorobogatova, V. A. Bagulya, Yu. N. Kharchenko, and A. I. Zvyagin, Fiz. Nizk. Temp. **17**, 1023 (1991) [Sov. J. Low Temp. Phys. **17**, 533 (1991)].
[50] V. A. Bagulya, A. I. Zvyagin, V. I. Kut'ko, and I. V. Skorobogatova, Fiz. Nizk. Temp. **14**, 1218 (1988) [Sov. J. Low Temp. Phys. **14**, 673 (1988)].
[51] Ya. I. Zagvozdina, N. M. Nesterenko, and Yu. N. Kharchenko, Ferroelectrics **239**, 197 (2000).
[52] T. S. Stetsenko, A. M. Pshisukha, S. D. El'chaninova, and A. I. Zvyagin, Opt. Spectrosc. **34**, 405 (1973).
[53] V. A. Bagulya, A. I. Zvyagin, V. I. Kut'ko, A. A. Milner, and I. V. Skorobogatova, Ferroelectrics **110**, 21 (1990).
[54] D. Mihailovic, J. F. Ryan, and M. C. K. Wiltshire, J. Phys. C **20**, 3063 (1987).
[55] A. I. Zvyagin, T. S. Stetsenko, S. D. El'chaninova, A. M. Pshisukha, V. G. Yurko, R. A. Vaĭshnoras, L. N. Pelikh, and M. I. Kobets, Trudy FTINT, Fiz. Kond. Sost. Vol. XXVI, Kharkov (1973).
[56] A. I. Zvyagin, V. I. Kut'ko, I. V. Skorobogatova, V. A. Bagula, and Yu. N. Kharchenko, *Xth Intern. Symp. Jahn-Teller Effect*, Kishinev (1989).
[57] G. Peĭn, *Physics of Oscillations and Waves* [Russian translation], Mir, Moscow (1979).
[58] G. Nicolis and I. Prigogine, *Exploring Complexity*, Freeman, New York (1987), Mir, Moscow (1990).
[59] N. F. Kharchenko, Yu. N. Kharchenko, R. Szymczak, and M. Baran, Fiz. Nizk. Temp. **24**, 915 (1998) [Low Temp. Phys. **24**, 689 (1998)].
[60] A. Abragam and B. Bleaney, *Electron Paramagnetic Resonance of Transition Ions*, Clarendon Press, Oxford (1970), Mir, Moscow (1973).
[61] V. I. Kut'ko, S. S. Gerashchenko, and N. Yu. Nedbailo, Fiz. Nizk. Temp. **25**, 1320 (1999) [Low Temp. Phys. **25**, 992 (1999)].
[62] E. N. Khats'ko and A. S. Chernyĭ, Fiz. Nizk. Temp. **7**, 1048 (1981) [Sov. J. Low Temp. Phys. **7**, 509 (1981)].
[63] S. D. El'chaninova and A. I. Zvyagin, Fiz. Nizk. Temp. **4**, 1465 (1978) [Sov. J. Low Temp. Phys. **4**, 690 (1978)].
[64] S. D. El'chaninova, A. F. Ilyushin, and Yu. G. Litvinenko, Fiz. Nizk. Temp. **12**, 616 (1986) [Sov. J. Low Temp. Phys. **12**, 349 (1986)].
[65] I. V. Skorobogatova, E. M. Savchenko, and A. I. Zvyagin, Izv. Akad. Nauk SSSR, Ser. Fiz. **47**, 491 (1983).
[66] S. S. Gerashcenko, O. V. Miloslavskaya, Yu. N. Kharchenko, V. I. Kut'ko, N. M. Nesterenko, L. Masalik, K. Hermanowicz, and M. Maczka, J. Hanuza, Material Science **20**, 81 (2002).
[67] V. I. Kut'ko, Yu. N. Kharchenko, N. M. Nesterenko, and A. A. Stepanov, Fiz. Nizk. Temp. **20**, 361 (1994) [Low Temp. Phys. **20**, 288, Erratum 671 (1994)].
[68] Yu. N. Kharchenko, Fiz. Nizk. Temp. **22**, 394 (1996) [Low Temp. Phys. **22**, 306 (1996)].
[69] V. I. Kut'ko, V. A. Pashchenko, and M. I. Kobets, Fiz. Nizk. Temp. **19**, 1354 (1993) [Low Temp. Phys. **19**, 962 (1993)].
[70] V. I. Kut'ko, M. I. Kobets, V. A. Pashchenko, and E. N. Khats'ko, Fiz. Nizk. Temp. **21**, 441 (1995) [Low Temp. Phys. **21**, 345 (1995)].
[71] Yu. V. Pereverzev, Fiz. Nizk. Temp. **22**, 289 (1996) [Low Temp. Phys. **22**, 226 (1996)].
[72] A. S. Loginov, Fiz. Nizk. Temp. **28**, 1056 (2002) [Low Temp. Phys. **28**, 755 (2002)].
[73] E. N. Khats'ko, Yu. V. Pereverzev, M. I. Kobets, V. A. Pashchenko, and V. I. Kut'ko, Fiz. Nizk. Temp. **21**, 1061 (1995) [Low Temp. Phys. **21**, 816 (1995)].
[74] M. I. Kobets, Fiz. Nizk. Temp. **26**, 96 (2000) [Low Temp. Phys. **26**, 72 (2000)].
[75] V. I. Kut'ko and M. I. Kobets, Fiz. Nizk. Temp. **21**, 1169 (1995) [Low Temp. Phys. **21**, 898 (1995)].
[76] W. Horsthemke and R. Lefever, *Noise-Induced Transitions: Theory and Applications in Physics, Chemistry and Biology*, Springer-Verlag, Berlin/New York (1984), Mir, Moscow (1987).
[77] V. I. Kut'ko and M. I. Kobets, Fiz. Nizk. Temp. **22**, 1477 (1996) [Low Temp. Phys. **22**, 1099 (1996)].
[78] V. I. Kut'ko and M. I. Kobets, Ferroelectrics **204**, 299 (1997).
[79] L. D. Landau, Dokl. Akad. Nauk **44**, 339 (1944).
[80] J. P. Eckman, Rev. Mod. Phys. **53**, 643 (1981).
[81] Ott Edward, Rev. Mod. Phys. **53**, 655 (1981).
[82] M. Feigenbaum, *Universal Behavior in Nonlinear Systems*, Los Alamos Science (1980).
[83] P. Manneville and Y. Pomeau, Physica **10**, 219 (1980).
[84] D. Ruelle and F. Takens, Commun. Math. Phys. **20**, 167 (1971).

Translated by Steve Torstveit

QUANTUM LIQUIDS AND QUANTUM CRYSTALS

Giant asymmetry of the processes of separation and homogenization of ^{3}He–^{4}He solid mixtures

V. N. Grigor'ev, V. A. Maidanov, A. A. Penzev, A. V. Polev, S. P. Rubets, E. Ya. Rudavskii, A. S. Rybalko,* and Ye. V. Syrnikov

B. Verkin Institute for Low Temperature Physics and Engineering, National Academy of Sciences of Ukraine, pr. Lenina 47, Kharkov 61103, Ukraine

(Submitted May 28, 2004; revised June 22, 2004)
Fiz. Nizk. Temp. **31**, 43–49 (January 2005)

A comparison of the kinetics of the separation processes and homogenization of ^{3}He–^{4}He solid mixtures is made with the use of precision barometry for samples of three types—dilute mixtures of ^{3}He in ^{4}He and of ^{4}He in ^{3}He and concentrated ^{3}He–^{4}He mixtures. It is found that in all types of mixtures studied the rate of the initial stage of homogenization can exceed the rate of separation by more than 500 times. An appreciable rate of phase separation in the concentrated mixtures, where, according to existing ideas, the impurity atoms in quantum crystals should be localized, attests to a new, unknown mechanism of mass transfer under those conditions, while the fast homogenization indicates that this process is nondiffusional in nature. © *2005 American Institute of Physics.* [DOI: 10.1063/1.1820353]

1. INTRODUCTION

In recent years considerable progress has been made in the study of the kinetics of nucleation and separation of ^{3}He–^{4}He solid mixtures. The development of a technique for growing high-quality crystalline samples and the use of precision low-temperature methods have permitted us to obtain reliable, well-reproducible experimental data. As a result, we have registered unusual features in the mass transfer at the phase transition and have determined the effective cofficient of the mass diffusion[1–3] and have shown experimentally that phase separation can be realized in ^{3}He–^{4}He solid mixtures via the mechanism of homogeneous nucleation.[4–6]

However, the majority of experiments on the kinetics of ^{3}He–^{4}He solid mixtures undergoing phase separation have been devoted to the study of the phase transition from the homogeneous to the separated state, when second-phase inclusions are randomly distributed in the crystalline matrix. The reverse transition from the two-phase to the homogeneous state has been investigated only in Refs. 1 and 2 for dilute mixtures of ^{3}He in ^{4}He. The experiment was done using rapid heating of the separated mixture from the same initial temperature T_i to different final temperatures T_f; this made it possible to obtain the first information about the kinetics of the dissolution of bcc solid inclusions of ^{3}He in the hcp matrix of the mixture (almost pure ^{4}He). One of the most interesting results was the observation of anomalously rapid mass transfer during the dissolution of the inclusions, this process having a threshold character with respect to the the difference between the final and initial temperatures, $\Delta T = T_f - T_i$ (Ref. 7). These effects have been explained qualitatively in the framework of the proposed model of a multistep process of dissolution of ^{3}He inclusions,[2] a key aspect of which is the presence of nondiffusive ballistic transport of impurity atoms.

In this connection it was of interest to study the kinetics of homogenization of separated ^{3}He–^{4}He solid mixtures at high impurity concentrations in the matrix, in which case the ballistic regime cannot be realized. Under these conditions the mass transfer occurs at very large concentration gradients. In this paper the results obtained previously for dilute mixtures of ^{3}He in ^{4}He (with concentrations of $\sim 2\%$ ^{3}He) are supplemented by new experiments with concentrated mixtures (30–35% ^{3}He) and dilute mixtures of ^{4}He in ^{3}He ($\sim 2\%$ ^{4}He). The goal was to compare and contrast the results obtained for mixtures of different concentration, to compare the kinetics of separation and homogenization, and to study the possible influence of the supersaturation, the bcc–hcp structural phase transition, the concentration of new-phase nuclei, and other factors.

2. FEATURES OF THE EXPERIMENTAL TECHNIQUE

Experiments were done in the same measurement cell described in Refs. 1 and 2. The crystal under investigation had the shape of a cylinder 9 mm in diameter and 1.5 mm in height, the pressure in the sample was measured *in situ* with the aid of a capacitive pressure gauge. The cell was in constant thermal contact with the plate of the mixing chamber, the temperature of which was registered by a ^{3}He melting curve thermometer.

Three types of samples were studied: A—dilute mixtures of ^{3}He in ^{4}He; B—dilute mixtures of ^{4}He in ^{3}He; C—concentrated mixtures of ^{3}He in ^{4}He (Table I). We note that besides the initial concentration x_0 the samples differed in their crystallographic structure. The dilute mixtures of ^{3}He in ^{4}He had an hcp structure in the homogeneous state, while the new phase was bcc; for the dilute mixtures of ^{4}He in ^{3}He the situation was just the opposite. As to the concentrated mixtures, under the conditions of the experiment both the

TABLE I. Characteristics of the investigated samples of ^{3}He–^{4}He solid mixtures.

Type of sample	Initial Concentration, x_0	P_0, bar	Crystal structure			T_s, mK	τ_{f1}, 10^3 s	τ_{eff}, s
			In the uniform state	After separation				
				Matrix	Inclusions			
A	2.6% ^{3}He	34.7	hcp	hcp	bcc	231	1.80–4.68	25–280
B	2.3% ^{4}He	38.6	bcc	bcc	hcp	202	0.36–39.60	102–1900*
	2.65% ^{4}He	34.8	bcc	bcc	hcp	202	0.36–36.00*	214–320*
	1.9% ^{4}He	31.6	bcc	bcc	hcp	194	0.54–54.00*	40–380
	2.9% ^{4}He	35.5	bcc	bcc	hcp	211	0.72–25.20	66**
	3.3% ^{4}He	33.0	bcc	bcc	hcp	221	0.72–7.56	630*–860*
C	30.5% ^{3}He	36.4	bcc	bcc	bcc	360	1.8–63.00	79–170
	34.2% ^{3}He	30.3	bcc	bcc	bcc	380	2.16–17.28	63–176

Note: An asterisk * denotes data for samples that apparently had the nonequilibrium structure; ** indicates that only one sample was studied.

initial homogeneous mixture and the two separated phases had the bcc structure. X-ray studies[8,9] have established that the initial bcc structure of the mixtures is readily supercooled, and, as a rule, the transition to the equilibrium hcp structure begins only upon heating. This last circumstance was confirmed in our experiments with concentrated mixtures.

The samples were subjected to heat treatment by multiple cycling of the temperature from 100 mK to the homogeneous region; as was shown previously[2] this improves the quality of the crystals and makes for reproducible results. In particular, the values found experimentally for the phase separation temperature T_s (Table I) agree within the error limits with the equilibrium phase diagram calculated in Ref. 10. It is well known that the isotope concentrations in a solid can differ noticeably from those in the initial gaseous mixture. The concentration x_0 of a uniform mixture *in situ* was refined with the Mullin formula,[11] which, in the case of cooling from a uniform state to a temperature T_i, can be written in the form

$$x_0(1-x_0)-x_i(1-x_i)=2.5\beta V_\mu(P_i-P_0), \qquad (1)$$

where P_0 is the equilibrium pressure of the mixture in the uniform state, x_i and P_i are the equilibrium values of the concentration and pressure in the separated mixture at temperature T_i, and β and V_μ are the compressibility and molar volume of the sample. For dilute mixtures x_0 was calculated directly from the measured difference $\Delta P_i=P_i-P_0$ and the values of x_i were calculated from the state diagram. For β we used the known values of the compressibility of pure ^{4}He or ^{3}He. In the case of concentrated mixtures, for which the values of β are unknown, curves of $x_i(1-x_i)$ versus ΔP_i were plotted, and the value of $x_0(1-x_0)$ was found by extrapolation to $\Delta P_i=0$. An example of such a plot for a 30.5% ^{3}He mixture is shown in Fig. 1. The value of β can be found from the slope of the straight line. For the given mixture $\beta=2.8\times10^{-3}$ bar^{-1}, which is approximately 40% lower than the additive value for the initial mixture.

The experiment was done as follows. The sample was cooled from a uniform state to a temperature T_i in the two-phase region and then heated to a temperature T_0 in the uniform region (the experimental scheme is illustrated on the phase diagram in Fig. 2). For each of the three types of samples the value of T_i was varied over an appreciable range so as to vary the supersaturation of the matrix, $\Delta x=x_0-x(T_i)$. In the majority of experiments the values of T_i were reached by a stepwise cooling of the sample. In that case, under conditions when $\Delta T_1 \geqslant T_{1+i}$ a special role was played by the value of the first cooling step, $\Delta T_1=T_{s0}-T_{f1}$. It is then that a certain density of new-phase nuclei is created in the sample, and, according to customary assumptions, further cooling causes only the diffusional growth of those nuclei.

3. RESULTS AND DISCUSSION

Typical curves of the time dependence of the pressure, $P(t)$, reflecting the kinetics of phase separation and subsequent homogenization of samples of types A, B, and C are

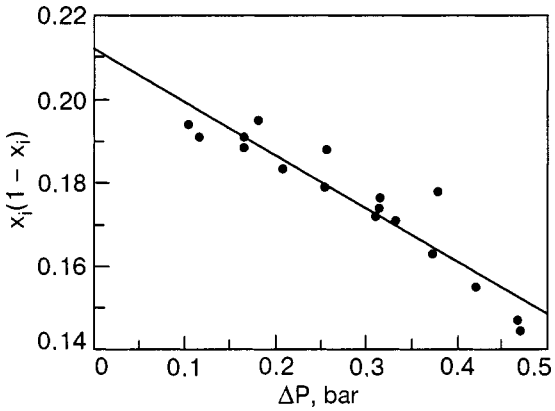

FIG. 1. Plot of $x_i(1-x_i)$ versus ΔP_i for a 30.5% ^{3}He mixture.

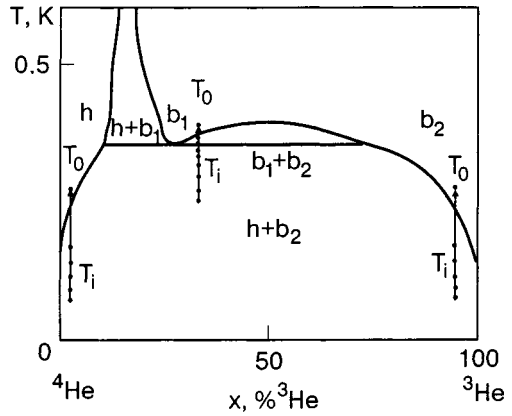

FIG. 2. Illustration of the equilibrium phase diagram of ^{3}He–^{4}He solid mixtures at a pressure of 35.1 bar and the lines of heating for samples of types A, B, and C from different initial temperatures T_i to a final temperature $T_{f;}$: h is the hcp phase, b_1 and b_2 are bcc phases.

presented in Fig. 3. It is seen that the character of these curves is the same in all cases, the differences being only of a quantitative character.

As we have stated previously more than once, the time dependence of the pressure change $\Delta P(t)$, which reflects the variation of the average concentration of the matrix during the separation process, is described well at sufficiently long times by an exponential dependence of the form

$$\Delta P(t)=P_f-P(t)(P_f-P_i)\exp(-t/\tau), \tag{2}$$

where P_i and P_f are the initial and final equilibrium pressures in the sample, and τ is the characteristic time constant governing the kinetics of the process. In the given experiments, too, the separation kinetics for all three types of samples was also described well by relation (2).

The process of homogenization of the mixture in a number of cases could be described to within the experimental scatter using two characteristic times, corresponding to two stages of the process—a fast time τ_1 and a slow time τ_2, with a weighting factor h:

$$\Delta P=[h\exp(-t/\tau_1)+(1-h)\exp(-t/\tau_2)](P_f-P_i), \tag{3}$$

as is shown in the inset in Fig. 3c, which also shows the time dependence of the temperature and its approximation by an exponential function. In this case the time constant for the change in temperature, τ_T, has a value of $\sim$50 s, which is close to the value of the characteristic time τ_1 of the fast stage of the dissolution. This means that the rate of homogenization under these conditions is determined by the rate of change of the temperature. If the time for the temperature variation is much less than 50 s (the lower limit τ_T is set by the Kapitza thermal boundary resistance at the interface between the solid helium and the wall of the cell), then relation (3) cannot be used to describe the pressure variation upon homogenization: the weighting factor h comes out greater than 1, apparently as a consequence of the very rapid change ΔP. As to the second homogenization step, governed by the time τ_2, a processing shows that τ_2 is at least an order of magnitude larger than τ_1.

It turned out that it was only for samples with very small supersaturations that it was possible to describe the change in

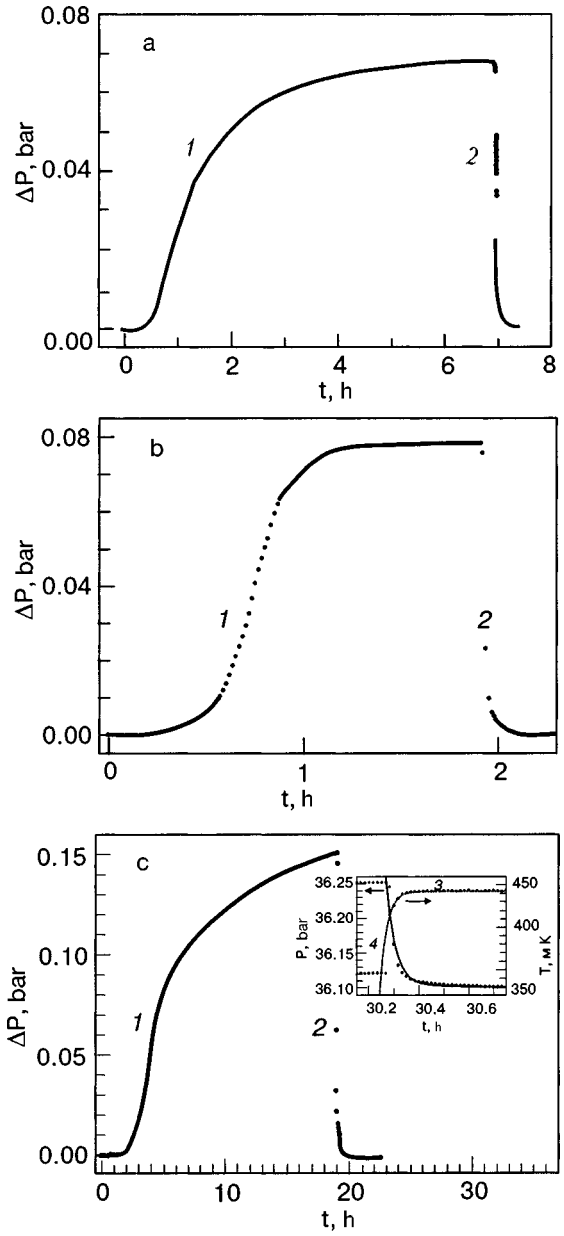

FIG. 3. Typical kinetics of the change in pressure of a sample during phase separation (*1*) and subsequent homogenization (*2*). Sample A, $P_0=35.9867$ bar (a); sample B, $P_0=31.4368$ bar (b); sample C, $P_0=31.4368$ bar (c). The inset shows the temperature variation (*3*) and the corresponding pressure variations (*4*) for the initial stage of heating of the sample. The solid curve *4* was calculated according to formula (3) for $h=0.96$, $\tau_1=135$ s, and $\tau_2=2217$ s; the dashed line *3* corresponds to the approximation of the temperature variation by a function with a single exponential.

pressure upon homogenization using relation (3) and thereby to obtain a value of τ_1 much greater than the time constant τ_T for the temperature relaxation. For uniform dilute mixtures of ^{3}He in ^{4}He and of ^{4}He in ^{3}He this could not be done, apparently because of the influence of the bcc–hcp transition. Figure 4 shows the dependence of the values of τ_1 found in this case as a function of the time constant τ_{f1} for the decomposition of the uniform mixture, which is a measure of the concentration of new-phase nuclei obtained upon supercooling to the "preparation temperature" T_{f1} of a given sample.

It can be seen from Fig. 4 that τ_1 grows significantly

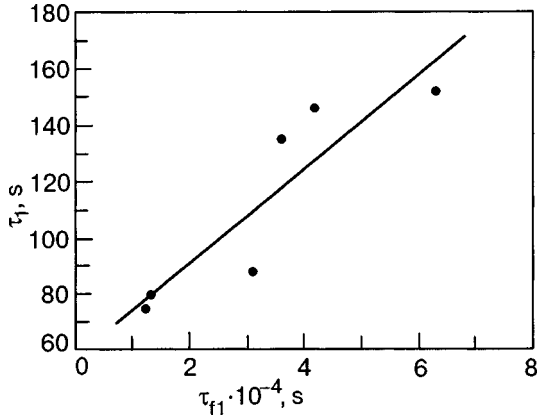

FIG. 4. Dependence of the characteristic time of the fast stage of the homogenization on the value of τ_{f1} in a mixture with an initial concentration of 30.5% ^{3}He.

with increasing τ_{f1}. We note that Fig. 4 gives only a very qualitative reflection of the processes that are occurring. The real $\tau_1(\tau_{f1})$ dependence is apparently stronger, since the minimum values of τ_1 observed at larger supersaturations are clearly overstated because of the proximity to the characteristic temperature relaxation time (at large supersaturations the value of τ_1 is only 20–30% larger than τ_T, while at the lowest supersaturations it is 2–3 times larger). The range of τ_{f1} values found for samples of a given concentration is indicated in Table I. At small supersaturations the values of τ_{f1} for all the samples decreased rapidly with increasing ΔT_1, and at larger supersaturations they approached a constant value, as had been observed in previous experiments.[3,6] Also given for comparison are the values of τ_{eff} obtained by processing the time dependence with a single exponential; these values characterize the rate of homogenization in order of magnitude.

Our previous studies (see Refs. 1–5) have reliably established that the kinetics of decomposition of solid solutions is governed by diffusion processes, for which the decomposition time is inversely proportional to the square of the distance l between new-phase inclusions. Therefore the noticeable growth of τ_1 can be linked to an increase in l, which is attested to by the growth of τ_{f1}. The presence of two exponentials in this case is quite natural, if only because of the simultaneous occurrence of the processes of ^{4}He penetration into a nucleus and ^{3}He transfer out of it. It is possible that these processes are of a diffusional character. There are several obstacles that keep us from reaching a more definite conclusion.

1. The lack of data on the sizes of the nuclei for samples of type C.

2. The fact that the solution to the corresponding diffusion equation is unknown.

3. The complete lack of information about the diffusion processes in concentrated ^{3}He–^{4}He mixtures: not only are the values of the diffusion constants unknown, but there is no understanding of a mechanism that could bring about the transport of atoms.

According to the existing ideas, the mass transfer at such low temperatures can take place only through tunneling processes. In dilute mixtures of ^{3}He in ^{4}He the tunneling of impurities leads to a quantum diffusion effect, which (in uniform mixtures) is well studied both theoretically and experimentally (see, e.g., Refs. 12 and 13). In dilute solutions of ^{4}He in ^{3}He the coherent motion of the impurities that is characteristic for quantum diffusion is impossible because of the absence of ideal periodicity owing to the random orientation of the nuclear spins of the ^{3}He, and mass transfer takes place through random tunneling. In both cases, increasing the impurity concentration tends to weaken the diffusive motion because of the distortion of the energy levels of the impurities in different lattice sites due to the interaction between impurities. When this distortion of the levels in neighboring lattice sites exceeds the width of the energy band of the impurity quasiparticles, tunneling is impossible, and this should lead to localization of the impurities. The localization effect has been observed in NMR experiments[14] on mixtures of ^{3}He in ^{4}He. Both experiment and theoretical estimates show that the critical concentration at which localization should set in in ^{3}He–^{4}He is less than 10%, and it might have been expected that no mass transfer should occur at all in more-concentrated mixtures.

However, experiments on the decomposition of ^{3}He–^{4}He mixtures, including those reported in the present paper, refute that point of view and attest to the observation of rather intense mass transfer in concentrated mixtures, at least under conditions of phase separation. Moreover, when samples obtained at large supersaturations were homogenized under conditions of maximum heating rates the time of the first stage of dissolution of inclusions decreased to values unmeasurable in the given experiments, as is indicated by the impossibility of processing the primary time dependences even with the use of two exponentials. Apparently this fact can be regarded as evidence of the existence of a very fast and most likely nondiffusional mechanism of mass transfer. It should be stressed that such a situation arises in all the mixtures studied, including nonconcentrated ones. It can be assumed that in all such cases the characteristic time of the first stage of homogenization of molten mixtures is not more than 20–30 s, while the decomposition time can reach 2–3 hours, i.e., the characteristic time for homogenization can be at least a factor of 300–400 smaller than the corresponding decomposition time. An even larger difference was observed for the concentrated mixtures.

Formally the processes of growth and dissolution differ in respect to the direction of the concentration gradient ∇x. It is known that the solution of the diffusion problem in a spherical geometry at constant inner and outer radii is symmetric with respect to ∇x. Taking the variation of the radius of the inclusion into account introduces a certain asymmetry. However, the resulting difference in the characteristic times does not exceed an order of magnitude (see, e.g., Ref. 15) and cannot account for the stronger asymmetry, which undoubtedly has an underlying physical cause, i.e., a difference in the mechanisms of mass transfer during the growth of the inclusions and during their dissolution.

We note that in five experiments (out of more than 50) with dilute mixtures of ^{4}He in ^{3}He we found values of τ_1 exceeding 200 s. The samples in those experiments were obtained at the lowest supersaturations, and we assume that nuclei with the nonequilibrium structure (bcc instead of hcp)

appeared in them. The subsequent heating of such samples during the homogenization, as we have said, stimulated a bcc–hcp transition, and that process was superimposed on the process of dissolution of the inclusions.

4. CONCLUSION

Thus the results of our study have shown that in the processes of separation and homogenization the helium atoms in the crystal maintain a rather high mobility, which ensures the establishment of an equilibrium state even at impurity concentrations much greater than the critical value that leads to self-localization in uniform mixtures. Here the growth of the new-phase nuclei apparently takes place by a diffusion mechanism, while the dissolution occurs much faster than is implied by theoretical estimates for purely diffusion processes. A characteristic feature of the dissolution process is the presence of large concentration gradients at the initial time. In nonideal mixtures such as ^{3}He–^{4}He this gives rise to a significant motive force that causes the impurity atoms to undergo jumps in the direction of the gradient (see, e.g., Ref. 16). It is possible that such an effect can ''unblock'' the self-localization of impurities. It might also be that the diffusion equations themselves must be altered at high concentration gradients. Clarification of these questions and the search for other, more unconventional explanations, e.g., the possible role of nonequilibrium vacancies in the mass transfer (it has been proposed[17,18] that such vacancies arise as the temperature of a separated mixture is raised) require further experimental and theoretical studies.

The authors thank M. A. Strzhemechny for helpful discussions.

This study was supported in part by the Ukrainian Government Foundation for Basic Research (Project 02.07.00391, agreement F7.286-2001).

*E-mail: rybalko@ilt.kharkov.ua

[1] A. N. Gan'shin, V. A. Maidanov, N. F. Omelaenko, A. A. Penzev, E. Ya. Rudavskii, and A. S. Rybalko, Fiz. Nizk. Temp. **24**, 1117 (1998) [Low Temp. Phys. **24**, 840 (1998)].
[2] A. N. Gan'shin, V. N. Grigor'ev, V. A. Maĭdanov, N. F. Omelaenko, A. A. Penzev, É. Ya. Rudavskiĭ, A. S. Rybalko, and Yu. A. Tokar', Fiz. Nizk. Temp. **25**, 796 (1999) [Low Temp. Phys. **25**, 592, Erratum 928 (1999)].
[3] V. N. Grigor'ev, V. A. Maĭdanov, A. A. Penzev, É. Ya. Rudavskiĭ, A. S. Rybalko, and E. V. Syrnikov, Fiz. Nizk. Temp. **29**, 1165 (2003) [Low Temp. Phys. **29**, 883 (2003)].
[4] A. Penzev, A. Ganshin, V. Grigor'ev, V. Maidanov, E. Rudavskii, A. Rybalko, V. Slezov, and Ye. Syrnikov, J. Low Temp. Phys. **126**, 151 (2002).
[5] A. Smith, V. Maidanov, E. Rudavskii, V. Grigor'ev, V. Slezov, M. Poole, J. Saunders, and B. Cowan, Phys. Rev. B **67**, 245314 (2003).
[6] V. N. Grigor'ev, V. A. Maidanov, A. A. Penzev, É. Ya. Rudavskii, A. S. Rybalko, V. V. Slezov, and E. V. Syrnikov, Fiz. Nizk. Temp. **30**, 177 (2004) [Low Temp. Phys. **30**, 128 (2004)].
[7] A. Ganshin, V. Grigor'ev, V. Maidanov, N. Omelaenko, A. Penzev, E. Rudavskii, and A. Rybalko, J. Low Temp. Phys. **116**, 349 (1999).
[8] S. N. Ehrlich and R. O. Simmons, J. Low Temp. Phys. **68**, 125 (1987).
[9] B. A. Fraas and R. O. Simmons, Phys. Rev. B **36**, 97 (1987).
[10] D. O. Edwards and S. Balibar, Phys. Rev. B **39**, 4083 (1989).
[11] W. J. Mullin, Phys. Rev. Lett. **20**, 254 (1968).
[12] A. Andreev, Prog. Low Temp. Phys. **8**, 67 (1982).
[13] V. N. Grigor'ev, Fiz. Nizk. Temp. **23**, 5 (1997) [Low Temp. Phys. **23**, 3 (1997)].
[14] V. A. Mikheev, V. A. Maidanov, and N. P. Mikhin, Fiz. Nizk. Temp. **8**, 1000 (1982) [Sov. J. Low Temp. Phys. **8**, 505 (1982)].
[15] B. Ya. Lyubov, *Diffusion Processes in Inhomogeneous Solid Media* [in Russian], Nauka, Moscow (1981).
[16] J. R. Manning, *Diffusion Kinetics for Atoms in Crystals*, Van Nostrand, New York (1968), Mir, Moscow (1971).
[17] A. N. Gan'shin, V. N. Grigor'ev, V. A. Maĭdanov, A. A. Penzev, É. Ya. Rudavskiĭ, A. S. Rybalko, and E. V. Syrnikov, Zh. Éksp. Teor. Fiz. **73**, 329 (2001) [JETP **46**, 289 (2001)].
[18] A. N. Gan'shin, V. N. Grigor'ev, V. A. Maĭdanov, A. A. Penzev, É. Ya. Rudavskiĭ, A. S. Rybalko, and E. V. Syrnikov, Fiz. Nizk. Temp. **29**, 487 (2003) [Low Temp. Phys. **29**, 362 (2003)].

Translated by Steve Torstveit

On the description of electrical effects in the two-fluid model of superfluidity

A. M. Kosevich*

B. Verkin Institute for Low Temperature Physics and Engineering, National Academy of Sciences of Ukraine, pr. Lenina 47, Kharkov 61103, Ukraine
(Submitted July 29, 2004; revised October 6, 2004)
Fiz. Nizk. Temp. **31**, 50–54 (January 2005)

A model description of the electrothermal effect in a superfluid liquid is proposed. It is hypothesized that the superfluid state is an ordered state with an isotropic quadrupole moment which does not manifest electrical properties in an equilibrium liquid. The polarization properties of the liquid are excited by an inhomogeneous distribution of the superfluid flow. The Landau equations of superfluid hydrodynamics are supplemented by an equation relating the electrical polarization of the medium with the density of the superfluid component and the inhomogeneity of the superfluid flow. The value of the expected oscillations of the electrical potential in a second-sound wave agrees with the measurements of A. S. Rybalko, Fiz. Nizk. Temp. **30**, 1321 (2004) [Low Temp. Phys. **30**, 994 (2004)]. [DOI: 10.1063/1.1820356]

Some members of the Editorial Board do not share the ideas set forth in this paper about the electrical activity of superfluid helium. However, in view of the topical nature of the problem addressed in it in connection with the experimental results of A. S. Rybalko, Fiz. Nizk. Temp. **30**, *1321 (2004) [Low Temp. Phys.* **30**, *994 (2004)], the Editorial Board has advised publication.*

The two-fluid model of the superfluidity of He II and Landau's superfluid hydrodynamics based on it[1] are directly confirmed by the experimental observation of second sound. In recent experiments Rybalko[2] has shown that second sound in He II is accompanied by oscillations of the electrical potential. A phenomenological model of two-fluid hydrodynamics has been proposed which permits description of the electrical effects related to the superfluidity. The superfluid state has a noteworthy feature that is manifested in a redistribution of the atomic electric charges in this macroscopic quantum system.

The neutral He atom in the $1S_0$ ground state does not have an intrinsic (in the absence of electric field) dipole moment but it does have an important microscopic electrical characteristic—an isotropic quadrupole moment (IQM)[1] $q_{ik}^{at} = \delta_{ik} q_0$, which has a value per unit mass of the order of $q_0 = (e/m)a^2$ (e is the charge of the electron, a is the atomic radius, and m is the mass of an He^4 atom). From the standpoint of macroscopic physics this is a ''latent'' atomic characteristic, since in macroscopic interactions of electrical systems in vacuum the quantity $q_{ik}^{at} - (1/3) q_{ll}^{at} \delta_{ik}$ goes to zero in the given case.

However, we conjecture that an ordered coherent superfluid state characterized by a continuous distribution in the space of all its physical characteristics has a mean IQM. In the Landau theory it is assumed[1)] that the density ρ_s of the superfluid component is determined by the square modulus of the condensate wave function, while the density of the normal component is related to the density of elementary excitations in the superfluid (phonons in the case of low temperatures). The phonons are unrelated to the transport of electric charge, and the dynamics of the isotropic quadrupole moment under discussion can be determined only by the dynamics of the superfluid state.

We denote by Q the density (value per unit volume) of the mean IQM, assuming that it is a continuous function of the coordinates. In the equilibrium state the liquid is electrically neutral and $Q = \text{const}$, but in a spatially inhomogeneous state the IQM acquires an inhomogeneous admixture. Therefore a bound electric charge appears in the system, with a density

$$en = \frac{1}{2} \Delta Q. \tag{1}$$

The presence of the charge density (1) leads to a Poisson equation for the electrostatic potential:

$$\varepsilon \Delta \varphi = -2\pi \Delta Q, \tag{2}$$

where ε is the dielectric constant of He^4, which in the base approximation can be assumed equal to unity ($\varepsilon = 1$). Since the electrical potential of the walls of the vessel containing the helium can be assumed equal to zero (or a constant) and Q does not have meaning outside the liquid, it follows from this last equation that

$$\varphi = -2\pi Q. \tag{3}$$

Consequently, the electric field in the superfluid liquid depends completely on the evolution of the isotropic quadrupole moment density Q. In particular, the electric field $\mathbf{E}$ is determined by the gradient of Q:

$$\mathbf{E} = 2\pi \operatorname{grad} Q, \tag{4}$$

where $Q=q\rho$, with q being the isotropic quadrupole moment of a unit mass of the liquid. The value of q is the main electrical characteristic of the superfluid state and can be written in the form

$$q=\left(\frac{e}{m}\right)l_0^2.$$

where l_0 is a parameter with units of length which is a fundamental phenomenological characteristic of the model; in the general case l_0 is a function of p and T.

Based on Rybalko's results,[2] we shall assume that the electrical ''activity'' of the IQM arises only in a nonuniform state in the presence of relative motion of the normal and superfluid components of He II. If Q is some characteristic of the superfluid state specifically, then it is natural to assume that its transport occurs via superfluid flow. Starting from the general scheme of two-fluid hydrodynamics,[1] we write the momentum flux density in the form (using the notation adopted in Ref. 1):

$$j=j_n+j_s, \tag{5a}$$

$$j_n=\rho\mathbf{v}_n,\quad j_s=\rho_s(\mathbf{v}_s-\mathbf{v}_n), \tag{5b}$$

where ρ is the mass density of He II. The first term (j_n) in Eq. (5a) gives a contribution to the normal transport (which, when multiplied by the entropy per unit mass, s, gives the entropy flux density),[1] while the second term j_s, proportional to the velocity difference $\mathbf{v}_s-\mathbf{v}_n$, is naturally assumed to be responsible for the transport of the superfluid characteristics. We therefore find that the flux density $\mathbf{J}$ of the isotropic quadrupole moment is given by

$$\mathbf{J}=q\rho_s(\mathbf{v}_s-\mathbf{v}_n)=q\mathbf{j}_3, \tag{6}$$

and the balance equation for the IQM has the form (we write it in the linear approximation in small deviations from the equilibrium state)

$$\frac{\partial Q}{\partial t}=-q\rho_s\,\mathrm{div}\,\mathbf{w},\quad \mathbf{w}=\mathbf{v}_s-\mathbf{v}_n. \tag{7}$$

The balance equation (7) is the main model assumption of the proposed phenomenological theory. At present it has not been confirmed by a rigorous microscopic calculation (an analogous relation for a slightly nonideal Bose gas at $T=0$ is derived in the Appendix). Let us use the following analogy. As we have said above, the entropy flux energy $\mathbf{J}_{\mathrm{ent}}$ in two-fluid hydrodynamics has the form

$$\mathbf{J}_{\mathrm{ent}}=S\mathbf{v}_n=s\mathbf{j}_n,\quad S=\rho s, \tag{8}$$

where S is the entropy density (the entropy of a unit volume of liquid), and the evolution of the entropy of a unit mass of liquid is described by the equation[1]

$$\rho\frac{\partial s}{\partial t}=s\,\mathrm{div}\,\mathbf{j}_s. \tag{9}$$

But the entropy is transported by the normal fluid flow, while, by assumption, the IQM is transported only by the superfluid flow. Comparing (7) and (8) with (6), we note the following relation between the entropy flux density (8), transported by the normal flow, and the continuity equation for the entropy, (9), with vectors $\mathbf{j}_n$ and $\mathbf{j}_s$. Because the normal and superfluid components appear in a somewhat symmetric manner, it can be assumed that the following formula for the IQM transported by the superfluid flow will differ from (8) and (9) by the switching of the flux densities $\mathbf{j}_n$ and $\mathbf{j}_s$: the analog of Eq. (8) is Eq. (6), and the relation describing the evolution of the IQM of a unit mass, q, is

$$\rho\frac{\partial q}{\partial t}=q\,\mathrm{div}\,\mathbf{j}_n, \tag{10}$$

which implies that

$$\frac{\partial q}{\partial t}=q\,\mathrm{div}\,\mathbf{v}_n. \tag{11}$$

Finally, taking into account the independence of the normal and superfluid flows, we shall assume that the continuity equations for the two components are autonomous:

$$\frac{\partial\rho_n}{\partial t}+\rho_n\,\mathrm{div}\,\mathbf{v}_n=0,\ \frac{\partial\rho_s}{\partial t}+\rho_s\,\mathrm{div}\,\mathbf{v}_s=0. \tag{12}$$

By definition the IQM density $Q=q\rho$. We calculate the derivative of Q with respect to time. A calculation with the use of (11) and the second equation in (12) leads us to relation (7).

We differentiate (4) twice with respect to time and use Eq. (7):

$$\frac{\partial^2\mathbf{E}}{\partial t^2}=-2\pi q\rho_s\frac{\partial}{\partial t}\mathrm{div}\,\mathbf{w}. \tag{13}$$

Since the electrical effect is expected to be weak, the superfluid flux density can be found using the equations of standard superfluid hydrodynamics:[1]

$$\frac{\partial}{\partial t}(\mathbf{v}_s-\mathbf{v}_n)=\left(\frac{\rho}{\rho_n}\right)s\nabla T. \tag{14}$$

Substituting (14) into (13), we obtain an expression relating the second derivative of the electric field with respect to time and the nonuniformity of the temperature:

$$\frac{\partial^2\mathbf{E}}{\partial t^2}=-2\pi q\frac{\rho_s}{\rho_n}\rho s\,\mathrm{grad}\,T. \tag{15}$$

We apply Eq. (15) to the description of the electrothermal effect in a wave:

$$\varphi',T'\propto e^{i(kx-\omega t)}. \tag{16}$$

It follows from (16) with $\mathbf{E}=-\mathrm{grad}\,\varphi$ that

$$u^2\varphi'=2\pi q\rho\frac{\rho_s}{\rho_n}sT',\ u=\frac{\omega}{k}. \tag{17}$$

Relation (17) can be used in a discussion of Rybalko's results,[2] which pertain to a second-sound wave, $u=u_2$, where u_2 is the velocity of second sound in the superfluid.

At temperatures not too close to T_λ one has $\rho_n u_2^2=T(s^2/c)\rho_s$, where c is the heat capacity per unit mass, and therefore

$$\delta\varphi=2\pi\frac{e}{m}l_0^2\frac{c}{s}\rho\frac{\delta T}{T}. \tag{18}$$

For $T\to0$ we have $\rho_n u_2^2=(1/3)sT\rho$, $\rho_s\approx\rho$, and therefore

$$\delta\varphi = 6\pi \frac{e}{m} l_0^2 \rho \frac{\delta T}{T}. \tag{19}$$

In both cases

$$\delta\varphi = (0{,}1-1)\frac{e l_0^2}{a^3}\frac{\delta T}{T}. \tag{20}$$

What values can be expected for the parameter $(e/m)l_0^2$? The appearance of the superfluid state involves an energy of the order of $T_\lambda \approx 1$ K. The energy that stabilizes the charge distribution in the atom and the the quantity q_0 are of the order of magnitude 10 eV$\approx 10^5$ K. Consequently, the relative contribution to the atomic energy from the energy that brings about the superfluid state is of the order of 10^{-5}. Thus it can be expected that the value of the isotropic quadrupole moment Q, which is related to the superfluid component, can comprise a 10^{-5} part of $(1/m)q_0$:

$$\frac{e}{m} l_0^2 \approx \frac{e}{m} a^2 10^{-5} \approx 10^{-7} \text{ cgs esu.}$$

The experimental results of Rybalko[2] at a temperature of 1 K give the following value in accordance with formula (17):

$$\frac{e l_0^2}{a^3} \sim 0.1 \times 10^{-6} = 10^{-7}.$$

It follows from the above estimate that in He II the the value of the parameter l_0^2 is equal in order of magnitude to $l_0^2 \sim (10^{-5}-10^{-4})a^2$. Analysis of the experiments shows[2] that l_0^2 is proportional to the square of the temperature. Therefore for complete agreement of the proposed model with the results of Ref. 2 one should assume a quadratic dependence of this parameter on temperature: $l_0^2 \propto (T/T_\lambda)^2$. This temperature dependence of l_0^2 eliminates the quandary that would otherwise arise in the analysis of (19) in the limit $T \to 0$.

Interestingly, in a wave of fourth sound[1] its velocity at $T \to 0$ tends toward the velocity of first sound, and therefore the limiting form of relation (17) for $T \to 0$ is

$$\delta\varphi = 2\pi \frac{e l_0^2}{m} \rho \frac{\delta T}{T}. \tag{21}$$

Consequently, the ratio $\delta\varphi/\delta T$ in a possible experiment with fourth sound will differ by a factor of three from that observed in Rybalko's experiments.[2]

We note that the main results of the present article are unambiguously attributed to higher dispersion, i.e., terms of order $(l_0 k)^4$, which are usually neglected in stating the equations of hydrodynamics. The problem of taking them into account in a consistent way is the subject of a separate paper.

Finally, in accordance with Ref. 2, we point out the possibility that the properties of the superfluid state can be linked to features of the electric charge distribution in the superfluid due not to the external electric field but to the quantum characteristic of the motion. Helium II is a quantum fluid in which the collective electron subsystem is a constituent. The electrothermal effect under discussion is undoubtedly due to the dynamics of the electrons. The interaction between moving neutral atoms is always due to their electron shells. One can therefore think that the specific ''superfluid'' properties of the two-fluid hydrodynamics are due to the electron subsystem. However this phenomenological sort of concept requires theoretical confirmation at the microscopic level.

We shall confine ourselves to the semi-microscopic level. Since the superfluid state is akin to the Bose condensate, we use the concept of Bose condensation of an ideal gas of atoms to explain the possible participation of the electronic system in macroscopic processes in He II. In the process of Bose condensation a finite fraction of the atoms of an ideal gas go into a state with momentum $\mathbf{p}=0$, forming a coherent collective state in which all of the Bose atoms are found in the same single-particle quantum state. We recall that the helium atom contains Fermi electrons. In order to understand the state in which they can be found we use the standard sorts of arguments for explaining the formation of electron energy bands in a crystal. Let E_0 be the ground level of one electron in a helium atom. Since all the atoms of the condensate are found in the same quantum state, the electronic level E_0 should be the same in all the atoms. By virtue of the uniform continuous distribution of atoms this level should be N_0-fold degenerate, where N_0 is the number of atoms in the condensate. In a nonideal gas this degeneracy is lifted. Taking that circumstance into account, e.g., leads to the conclusion that the well-known conclusion that the excitations of the condensate have a Bogolyubov spectrum is in need of refinement. But whatever the concrete results of the analysis of this problem, the electronic degrees of freedom manifest themselves in the electrical properties of the condensate.

APPENDIX. EVOLUTION OF THE IQM DENSITY IN AN ALMOST IDEAL BOSE GAS

In a slightly nonideal Bose gas at $T=0$ the preponderance of the atoms, N_0 in number $(N-N_0 \ll N)$, is found in the state with $\mathbf{p}=0$, forming a condensate. Let $\Psi(\mathbf{X},\xi)$ be the the wave function of an atom in the condensate, where $\mathbf{X}$ is the coordinate of the center of mass of the atom (nucleus) and ξ is a generalized coordinate of the electrons in the atom (reckoned from the nucleus). In the usual adiabatic approximation one can write

$$\Psi(\mathbf{X},\xi) = \Phi(\mathbf{X})\psi(\xi), \tag{A1}$$

where the wave function $\psi(\xi)$ is normalized to unity, while the wave function $\Phi(\mathbf{X})$ is conveniently normalized to the atomic mass m. The charge density in the atom is

$$en(\xi) = e_0(\delta(\xi) - |\psi(\xi)|^2), \tag{A2}$$

where e_0 is the charge of the nucleus. We suppose that the atom is found in an S state; then

$$\int \xi |\psi(\xi)|^2 d\Gamma_\xi = 0, \tag{A3}$$

where $d\Gamma_\xi$ is the differential of the electron coordinates.

We calculate the distribution of the mean IQM of an atom:

$$Q_{ik}^{at}(\mathbf{X}) = \frac{e}{m}|\Phi(X)|^2 \int (X_i+\xi_i)(X_k+\xi_k)|n(\xi)d\Gamma_\xi. \tag{A4}$$

Using (A2) and (A3), one may be convinced that (A4) reduces to the IQM:

$$Q_{ik}^{at}=-\frac{e_0}{m}|\Phi(\mathbf{X})|^2\int \xi_i\xi_k|\psi(\xi)|^2d\Gamma_\xi$$

$$=-\frac{e_0}{3m}|\Phi(\mathbf{X})|^2\int \xi^2|\psi(\xi)|^2d\Gamma_\xi\delta_{ik}=Q^{at}\delta_{ik}. \quad \text{(A5)}$$

Let us determine the IQM density in the condensate, taking into account that all the atoms of the condensate are found in the same quantum state:

$$Q=N_0Q^{at}. \quad \text{(A6)}$$

We denote the density of atoms in the condensate as $\rho_c=N_0|\Phi(\mathbf{X})|^2$; then

$$Q=-\frac{e_0}{m}\rho_c l_0^2,\ \ l_0^2=\frac{1}{3}\int \xi^2|\psi(\xi)|^2d\Gamma_\xi. \quad \text{(A7)}$$

Since the superfluid component of a quantum Bose liquid is defined as the square modulus of the condensate wave function, its analog in a slightly nonideal gas is the quantity ρ_c introduced above.

Since Bogolyubov phonons do not affect the state of the condensate (it is ''split off'' and is treated as a fixed ground state), at $T=0$ the dynamics in the leading approximation is autonomous:

$$\frac{\partial\rho_c}{\partial t}+\operatorname{div}\rho_c\mathbf{v}_c=0, \quad \text{(A8)}$$

where $\mathbf{v}_c$ is the macroscopic velocity of the condensate as a function of the coordinates and time.

We calculate the time derivative of (A7) with (A8) taken into account:

$$\frac{\partial Q}{\partial t}=-\frac{e_0l_0^2}{m}\frac{\partial\rho_c}{\partial t}=\frac{e_0l_0^2}{m}\operatorname{div}\rho_c\mathbf{v}_c=\frac{e_0l_0^2}{m}\rho_c\operatorname{div}\mathbf{v}_c \quad \text{(A9)}$$

Relation (A9) links the evolution of the IQM with the velocity $\mathbf{v}_c$. Let us proceed from the fact that the superfluid state of a quantum liquid is akin to the Bose condensate in a slightly nonideal Bose gas. In such a case ρ_c and $\mathbf{v}_c$ play the role of the density and velocity of the superfluid component in a quantum liquid. Since phonons are absent at $T=0$, in the two-fluid hydrodynamics picture there is no normal component of the motion and, hence, $\mathbf{v}_n=0$. Therefore, formula (A9) with the sign of the charge and the definition of l_0^2 taken into account is the analog of the main statement of this article in the form of relation (9), which pertains to the superfluid liquid.

The author thanks A. S. Rybalko for fruitful discussions and for providing the manuscript of Ref. 2 prior to its publication, to the participants at the seminar of the Verkin Institute of Low Temperature Physics for a discussion, to V. A. Mikheev and V. D. Natsik for advice, to V. M. Loktev and V. G. Manzhelii for support, and to the referees for useful criticism.

*E-mail: kosevich@ilk.kharkov.ua

[1)] The value q of the IQM is given by the formula $q_{ik}=\Sigma ex_ix_k$, where the summation is over all electric charges in the system.

[1] L. D. Landau and E. M. Lifshitz, *Fluid Mechanics*, 2nd ed., Pergamon Press, Oxford (1987), translation of 3rd Russ. ed., Nauka, Moscow (1986).
[2] A. S. Rybalko, Fiz. Nizk. Temp. **30**, 1321 (2004) [Low Temp. Phys. **30**, 994 (2004)].

Translated by Steve Torstviet

SUPERCONDUCTIVITY, INCLUDING HIGH-TEMPERATURE SUPERCONDUCTIVITY

Paramagnetic effect of magnetic field on superconductors with charge-density waves

T. Ekino

Hiroshima University, Faculty of Integrated Arts and Sciences, 1-7-1 Kagamiyama Higashi-Hiroshima 739-8521, Japan

A. M. Gabovich* and A. I. Voitenko

Crystal Physics Department, Institute of Physics of the National Academy of Sciences, 46 Nauki Ave., Kiev 03028, Ukraine

(Submitted May 17, 2004)
Fiz. Nizk. Temp. **31**, 55–62 (January 2005)

The limiting external magnetic field H_p that destroys paramagnetically the ordered state of spin-singlet superconductors with charge density waves (CDWs) with coexisting superconducting and dielectric order parameters is calculated self-consistently. It is shown that H_p always exceeds the Pauli limits for both pure superconducting and pure CDW phases. Relevant experimental data for inorganic and organic superconductors with high upper critical magnetic fields are analyzed and are shown to be in qualitative agreement with the proposed theory. © *2005 American Institute of Physics.* [DOI: 10.1063/1.1820359]

1. INTRODUCTION

Clogston[1] and Chandrasekhar[2] discovered theoretically the Pauli paramagnetic suppression of the spin-singlet Cooper pairing. In the framework of the original Bardeen-Cooper-Schrieffer (BCS) theory of superconductivity[3] they obtained a limit

$$H_p^{BCS}=\frac{\Delta_{BCS}(T=0)}{\mu_B^*\sqrt{2}} \tag{1}$$

from above on the upper critical magnetic field H_{c2} at zero temperature T. Here $\Delta_{BCS}(T)$ is the superconducting energy gap, $\mu_B^*=e\hbar/2m^*c$ is the effective Bohr magneton, e is the elementary charge, $\hbar$ is Planck's constant, m^* is the effective electron mass, and c is the velocity of light.

This conclusion may be violated in the dirty case, when a large concentration of strong spin–orbit scattering sites exist and the spins of the electrons constituting the Cooper pairs are flipped.[4] A corresponding enhancement of H_{c2} has been indeed observed in Al films coated by monolayers of Pt.[5] The Pt atoms served there as strong spin–orbit scatterers due to their large nuclear charge Z. On the other hand, a similar contamination of another superconductor, the A15 compound V_3Ga, exhibiting a Pauli paramagnetic effect in the absence of impurities, altered neither H_{c2} nor the Zeeman splitting of the tunnel conductance.[6] Therefore, the spin–orbit mechanism of overcoming the Clogston–Chandrasekhar limit remains open to investigation.

There exists another collective state revealing a paramagnetic effect similar to the Clogston–Chandrasekhar one[1,2] inherent to the BCS s-wave superconductivity. It is a charge-density wave (CDW) low-T insulator or a CDW metal (CDWM), where only certain sections of the Fermi surface (FS) are gapped below the critical structural transition temperature T_d.[7,8] The same description is applicable on a phenomenological level to both a Peierls insulator emerging due to the electron–phonon interaction[9] and an excitonic insulator caused by the Colulomb electron–hole attraction.[10,11] The dielectric CDW instability is a consequence of the nesting condition

$$\xi_1(\mathbf{p})=-\xi_2(\mathbf{p}+\mathbf{Q}), \tag{2}$$

characterizing the electron spectrum at the FS sections labeled by $i=1,2$, where $\mathbf{Q}$ is the CDW vector. So, here, the electron spectra are degenerate (d) and a CDW-related order parameter $\widetilde{\Sigma}$ appears on those nested sections. The rest of the FS $(i=3)$ remains undistorted, and its spectrum branch $\xi_3(\mathbf{p})$ is nondegenerate (n).

In the weak-coupling approximation, the superconducting Δ and dielectric $\widetilde{\Sigma}=\Sigma e^{i\varphi}$ order parameters obey self-consistency equations of the same form.[3,11] Here φ is the phase of the CDW, usually pinned by defects or the background crystal lattice in subthreshold electrostatic fields.[9,12] Those properties of the low-T phases, which are not dependent on the peculiar differences between the so-called diagonal and off-diagonal long-range orders,[10,11,13,14] should be quite close to one another. That was indeed proved true for the Peierls insulator[15] (see also Refs. 16–18). A physical reason for the similarity consists in the fact that the electron–hole pairing couples the bands (in the excitonic insulator) or the different parts of the one-dimensional self-congruent band (in the Peierls insulator) with the same spin direction, contrary to the SDW case, where current carriers with the opposite spin directions are paired. When H is switched on, both congruent FS sections having the chosen spin projection $(\pm)$ shift either up or down in energy. Therefore, the corresponding nesting CDW vectors $\mathbf{Q}_+$ and $\mathbf{Q}_-$ no longer coincide, and the initial CDW state is gradually destroyed.[19]

In normal CDWMs, the highest possible magnetic field H_p^{CDWM} (when only the paramagnetic effect is taken into account!) can be easily found from the same simple considerations as in the superconducting case,[3] so that

$$H_p^{CDWM}=\frac{\Sigma_*}{\mu_B^*}\sqrt{\frac{\mu}{2}}. \tag{3}$$

Here, $0\leqslant\mu\leqslant 1$ is the relative portion of the FS sections gapped by CDWs, $\Sigma_*=\pi T_d/\gamma$ is the bare CDW gap at $T=0$ in the absence of superconductivity, and $\gamma=1.7810\ldots$ is the Euler constant. The parameter μ is defined by the relation

$$\mu=N_d(0)/N(0), \tag{4}$$

where $N(0)=N_n(0)+N_d(0)$ is the total initial (above T_d) electronic DOS on the FS, and $N_d(0)$ and $N_n(0)$ are the relevant DOSs on the *d* and *n* FS sections, respectively.

At the same time, the diamagnetic reaction of substances gapped by CDWs is much weaker[20] than that in superconductors, with their complete Meissner diamagnetism below the first critical magnetic field.[3] Nevertheless, it always manifests itself in CDW metals or insulators and can even modify the CDW wave vector itself.[21–25] Therefore, in calculating the total response both the paramagnetic (spin) and diamagnetic contributions should be taken into account.[18,26–33]

In this connection, Eq. (3), similar to the case of BCS superconductors, gives a limiting upper value for H that does not destroy the CDW state. One should note, however, that CDW-triggered persistent currents were claimed to be observed far above the Pauli limit (3) in ac susceptibility measurements for the compound α-$(BEDT\text{-}TTF)_2KHg(SCN)_4$ (Ref. 22). The authors of Refs. 22 and 34 suggested the existence of the Fröhlich ideal conductivity[35] in this substance. These intriguing conclusions have not yet been confirmed by other groups.

It is well known[7,8] that there are plenty of materials in which CDWs and superconductivity coexist at $T<T_c<T_d$. Here T_c is the critical temperature of the superconducting state. It is important to stress that the assumed superconductivity is possible only if the CDW gapping of the electron spectrum is partial,[7,8,36] i.e., the distorted phase remains metallic. From the aforesaid, it is natural to expect that in the mixed phase, possessing two spin-singlet order parameters Δ and $\tilde{\Sigma}$, the paramagnetic limit H_p exceeds both expressions (1) and (3) inherent to the states with either of two orderings.

Indeed, some time ago[37] the inequality $H_p>H_p^{BCS}$ was demonstrated to be valid for all possible values of the parameters inherent to the Bilbro–McMillan model.[36] That result, as is shown below, remains correct in a more accurate approach. Nevertheless, our previous considerations[37–39] had a significant limitation. Specifically, the treatment of the superconducting phase with CDWs was not self-consistent, which quite unexpectedly made the whole problem more rather than less involved. In our current calculations we use the results of the self-consistent calculations of the thermodynamic properties[40] applied to a metal with two order parameters: a dielectric one $\tilde{\Sigma}(T)$, existing on the nested FS sections, and a superconducting one $\Delta(T)$, unique for both the *d* and *n* sections.[36] The ratio H_p/H_p^{BCS}, contrary to its counterpart in the non-self-consistent approach,[37] turns out to be described by a simple analytical formula.

On the other hand, the relationship between H_p and H_p^{CDWM} is examined for the first time, and an additional inequality $H_p>H_p^{CDWM}$ is proved below to be valid for any set of the input parameters. We obtain several phase diagrams in the parameter space for $T=0$ and carry out their analysis in terms of the observed variables. Relevant experimental data are discussed.

2. CALCULATION OF PHASE DIAGRAMS

To calculate the paramagnetic limit, one must consider the free energies F per unit volume for all possible ground-state phases in an external magnetic field H. The parent nonreconstructed phase (actually existing only above T_d!), with both superconducting and electron–hole pairings switched off and in the absence of H, serves as a reference point. At $T<T_d$, we deal with relatively small differences δF reckoned from this hypothetical ''doubly-normal'' state.[3]

Since we assume the Meissner diamagnetic response to be negligibly small, the external magnetic field H should coincide with that inside the specimen and be almost uniform. Therefore, the additional energy of the paramagnetic phase in the magnetic field, when both Δ and $\tilde{\Sigma}$ are equal to zero, takes the form[41]

$$\delta F_p=-N(0)(\mu_B^*H)^2. \tag{5}$$

The reconstructed superconducting state with the FS gapped both by superconductivity and CDWs constitutes another thermodynamic phase at $T<T_c$. Its free energy can be obtained from the following simple arguments. In the adopted Bilbro–McMillan model,[36] the order parameters $\Delta(T)$ and $\tilde{\Sigma}(T)$ satisfy a self-consistent system of equations.[40] This system has a solution, which determines two different T-dependent energy gaps on the *n* and *d* sections of the FS. Specifically, there is the superconducting energy gap $\Delta(T)=\Delta_{BCS}(\Delta_0,T)$ below T_c on the *n* sections, whereas the *d* sections are influenced by the effective gap $D(T)=\Delta_{BCS}(D_0,T)$. Here $\Delta_{BCS}(G,T)$ is the Mühlschlegel gap function of the BCS theory with $G=\Delta_{BCS}(T=0)$, so Δ_0 and D_0 are the values of the relevant gaps at $T=0$. The effective quantity $D(T)$ is a combination of both constituent gaps:

$$D(T)=\sqrt{\Delta^2(T)+\Sigma^2(T)}. \tag{6}$$

The value D_0 is equal to the parameter Σ_* defined in the Introduction. The assumed equality of the superconducting gaps Δ_n and Δ_d on the *n* and *d* FS sections, respectively, is a consequence of the strong mixing of the electron spectrum branches by the matrix elements of the effective four-fermion interaction Hamiltonian.

Thus on both parts of the FS, BCS-like (but different!) gap functions are developed. The change of the free energy δF_s at $T=0$ is determined by their zero-T values in the conventional manner:[3]

$$\delta F_s=-N_n(0)\frac{\Delta_0^2}{2}-N_d(0)\frac{\Sigma_*^2}{2}. \tag{7}$$

Finally, a paramagnetic superconducting CDW phase should be considered. The free energy of this phase, characterized by two order parameters $\Delta(T)$ and $\tilde{\Sigma}(T)$, depends on H explicitly. Moreover, both gaps depend on H in a strange way, increasing with H. Such a phase is a generalization of the metastable phase found theoretically by Sarma for BCS superconductors (see, e.g., Refs. 3 and 42). The free energy of the paramagnetic superconducting CDW phase is higher than that given by Eq. (7) for all values of H up to the limiting value H_p at which superconductivity ceases to exist,[37] so that it cannot be realized in the system. Of course, the same is true for the Sarma phase in BCS superconductors.

It is worth noting that any orbital magnetic field effects favorable for the CDW state are not taken into account, because the values of H relevant to the problem concerned are considerably smaller than those which reduce the dimensionality of the electron spectrum.[21,27,33] We also do not take into account the possibility of the Larkin–Ovchinnikov–Fulde–Ferrel (LOFF) inhomogeneous superconducting state,[3] although there are some hints that it might have been observed in low-dimensional organic compounds.[43]

Thus, with the assumption of the order parameter homogeneity, the procedure of the paramagnetic limit determination is formally the same as that used by Clogston[1] and Chandrasekhar.[2] Namely, one should equate δF_p and δF_s. This leads to a basic relationship for the actual paramagnetic limit H_p of the mixed phase with two superconducting gaps Δ and $\tilde{\Sigma}$:

$$(\mu_B^* H_p)^2 = \frac{1}{2}[(1-\mu)\Delta_0^2 + \mu\Sigma_*^2]$$

$$= \frac{1}{2}[\Delta_0^2 + \mu(\Sigma_*^2 - \Delta_0^2)]. \tag{8}$$

Since $\Sigma_* = D_0 > \Delta_0$, which is a consequence of equation (6), the limiting magnetic field H_p in a CDW superconductor *always exceeds* the Clogston–Chandrasekhar value H_p^{BCS} (1). At the same time, H_p is *always larger* than the paramagnetic upper limit H_p^{CDWM} (3) in the normal CDWMs.

The quantity $D_0 = \Sigma_*$, as has been indicated in the Introduction, is linked to the structural (excitonic) transition temperature T_d by the BCS relationship. The same is true for the pair Δ_0 and T_c (Ref. 40). Hence, it comes about that

$$\left(\frac{H_p}{H_p^{BCS}}\right)^2 = 1 + \mu\left[\left(\frac{D_0}{\Delta_0}\right)^2 - 1\right] = (1-\mu) + \mu\left(\frac{T_d}{T_c}\right)^2 \tag{9}$$

and

$$\left(\frac{H_p}{H_p^{CDW}}\right)^2 = 1 + \frac{(1-\mu)}{\mu}\frac{\Delta_0^2}{D_0^2} = 1 + \frac{(1-\mu)}{\mu}\left(\frac{T_c}{T_d}\right)^2. \tag{10}$$

All quantities in Eqs. (9) and (10) can be easily measured or inferred from the experimental data. The corresponding contour curves are displayed in Fig. 1. One can readily see that for typical $T_c/T_d \approx 0.05-0.2$ (some A15 compounds are rare exceptions[7,8]) and moderate values of $\mu \approx 0.3-0.5$, the augmentation of the paramagnetic limit (9) becomes very large. Of course, this outcome may be essentially reduced by the spin–orbit scattering.[5] At the same time, the Pauli limitation on H_p^{CDWM} is not so conspicuous, because the role of superconductivity itself in the Δ-$\tilde{\Sigma}$ symbiosis is subdominant.

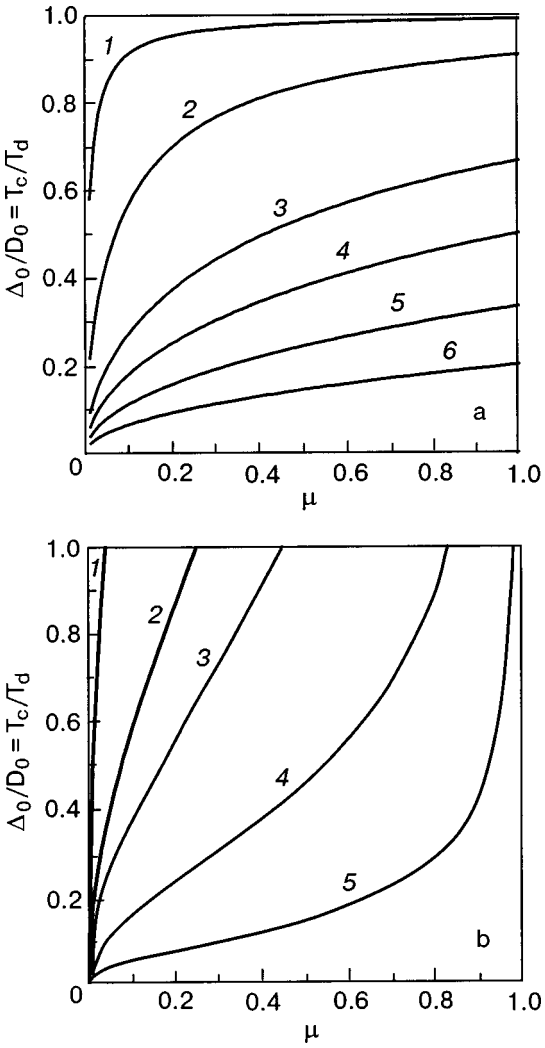

FIG. 1. Contour plot of the ratios H_p/H_p^{BCS}: 1.01 (*1*); 1.1 (*2*); 1.5 (*3*); 2 (*4*); 3 (*5*); 5 (*6*) (panel a) and H_p/H_p^{CDWM}: 5 (*1*); 2 (*2*); 1.5 (*3*); 1.1 (*4*); 1.01 (*5*) (panel b) on the plane $(T_c/T_d, \mu)$. Here H_p, H_p^{BCS}, and H_p^{CDWM} are the paramagnetic limits for superconductors with charge-density-waves (CDWs), BCS spin-singlet superconductors, and CDW metals, respectively, T_c and T_d are the observed critical temperatures of the superconducting and CDW transitions, respectively, and μ is the portion of the nested Fermi surface sections where the CDW gap develops.

There is another way of representing the results. To this end a primordial superconducting gap Δ_* at $T=0$ in the absence of CDWs is introduced. The observable superconducting order parameter Δ_0 can be expressed in terms of the bare input parameters in the following way:[40]

$$\Delta_0 = \Sigma_*\left(\frac{\Delta_*}{\Sigma_*}\right)^{1/1-\mu}. \tag{11}$$

Then the increase of the relevant paramagnetic limit over their primordial values is given by the formulas

$$\left(\frac{H_p}{H_p^{BCS}}\right)^2 = (1-\mu) + \mu\left(\frac{\Sigma_*}{\Delta_*}\right)^{2/1-\mu} \tag{12}$$

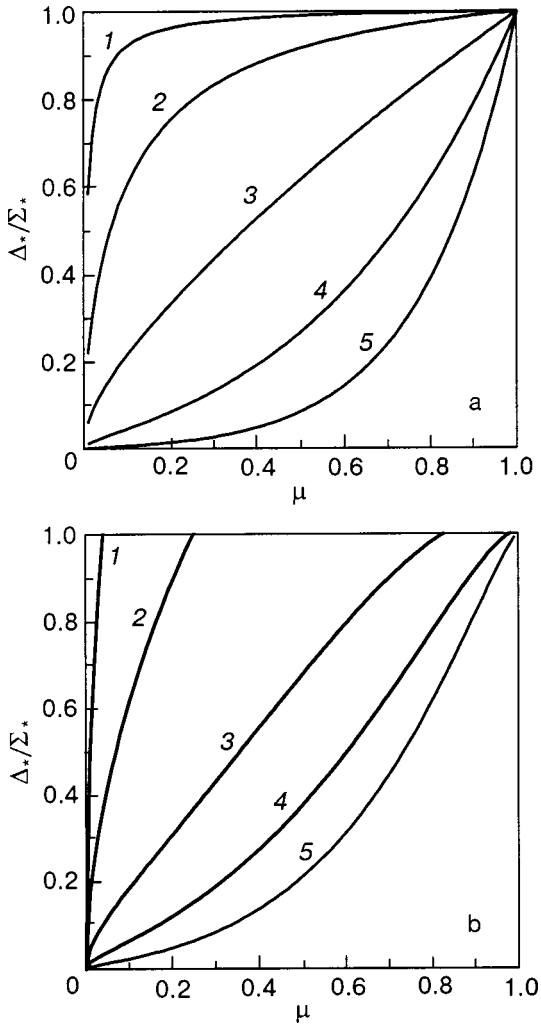

FIG. 2. Contour plot of the ratios H_p/H_p^{BCS}: 1.01 (*1*); 1.1 (*2*); 2 (*3*); 10 (*4*); 100 (*5*) (panel a) and H_p/H_p^{CDWM}: 5 (*1*); 2 (*2*); 1.1 (*3*); 1.01 (*4*); 1.001 (*5*) (panel b) on the plane $(\Delta_*/\Sigma_*, \mu)$. Here Δ_* and Σ_* are bare values of the order parameters in parent phases with only Cooper or CDW pairing, respectively.

and

$$\left(\frac{H_p}{H_p^{CDW}}\right)^2 = 1 + \frac{(1-\mu)}{\mu}\left(\frac{\Delta_*}{\Sigma_*}\right)^{2/1-\mu}. \qquad (13)$$

The level lines of H_p/H_p^{BCS} and H_p/H_p^{CDW} on the phase planes $(\Delta_*/\Sigma_*, \mu)$ are shown in Fig. 2. It is clear from the plots that the smaller the ratio between the superconducting and CDW coupling constants, the larger the excess of the paramagentic limit.

The dimensionless parameters Δ_*/Σ_* and μ are independent of each other. As has been mentioned above, the latter can be determined experimentally, in particular, by resistive, specific heat, or optical measurements.[7,8] On the other hand, the bare gaps Δ_* and Σ_* are difficult to measure, because to get rid of either superconductivity or CDWs it is necessary to apply pressure, external magnetic field, or alloying. Therefore, various background electronic and crystal lattice properties would be inevitably altered, including gaps (some insight can be obtained from Refs. 11, 44, 45).

Physically, the rise of H_p over H_p^{BCS} and H_p^{CDW} in CDW superconductors is quite natural. Both Cooper and electron–hole pairings are simultaneously depressed by the paramagnetic effect, whereas, in the calculation of H_p^{BCS} and H_p^{CDW}, the detrimental influence of the external field H on either of the order parameters (energy gaps) is taken into account. Therefore, larger fields H are required to produce the same effect as in the absence of a partner gap.

It is of interest that recently the enhancement of the paramagnetic limit for superconductors has been also found theoretically for a model related to the CDW model and taking into account the Van Hove singularity of the two-dimensional electron density of states.[46]

3. DISCUSSION

From the aforesaid it becomes clear that there is a unique Pauli limit in the mixed phase, which, in principle, can be attributed either to the superconducting or dielectric order parameters. Since in the case of the coexistence between Δ and $\tilde{\Sigma}$ experimentalists are most often interested in superconducting properties, the apparent exceeding of the Clogston–Chandrasekhar paramagnetic limit is interpreted without any reference to CDWs. Therefore, to verify our theory it would be desirable to prove the coexistence between CDWs and superconductivity in the same samples where $H_p > H_p^{BCS}$. Unfortunately, such a direct verification is still lacking.

In principle, photoemission experiments might confirm simultaneous superconducting and CDW gapping of FSs and give FS momentum-space maps in the high-T (ungapped) and low-T (gapped) states.[47] In particular, such measurements might verify or disprove the strong-mixing concept discussed in the previous Section. There are, however, methodological difficulties which can hamper the unambiguous identification of the magnitudes as well as the directional and temperature dependences of Δ and Σ (see, e.g., the analysis in Ref. 48 as applied to $Bi_2Sr_2CaCu_2O_{8+y}$). Another important point is a three-dimensionality of the FS in cuprates.[49] If such warnings are ignored, the situation with gapping in the photoemission spectra for $Bi_2Sr_2CaCu_2O_{8+y}$ (a high-T_c oxide, the most suspicious from the CDW point of view) looks as follows.[47] The superconducting gap Δ has a d-wave momentum dependence in the $k_x - k_y$ plane, with definite nodes. The same features are appropriate to pseudogaps, earlier identified by us as CDW ones.[7,8] Therefore, a clear-cut division of the cuprates' FS into two parts, one non-nested and gapped by Δ and the other nested and gapped by both Σ and Δ [see Eq. (6)] is so far unconfirmed.

The FSs and their gapping in layered dichalcogenides have been studied extensively by the photoemission method as well as by tunneling. In particular, the tunnel measurements[50] for $2H$-polytype compounds showed a conspicuous anticorrelation between Σ (or T_d) and T_c. For $2H$-$NbSe_2$ the CDW gap $\Sigma \approx 34$ MeV is the smallest nonzero one, whereas T_c is 7.2 K. Nevertheless, Σ has escaped detection by photoemission, although a much smaller superconducting gap was disclosed![51,52] The authors of Ref. 52 believe that this result is due to the fact that the nested FS portion (μ in our terms) is tiny. This explanation does not seem satisfactory, since all FS sheets and all directions in **k** space were investigated. At the same time, a superconducting gapping was found for the Γ-centered[51] and K-centered[52] FS cylinders. Notwithstanding substantially different electron–

phonon coupling strengths at various points of FS cylinders surrounding the K point, the gap $\Delta \approx 1$ MeV is uniform there. This behavior counts in favor of the strong-mixing paradigm adopted here. All the preceding means that the microscopic relationships between two types of gapping in layered dichalcogenides are far from being resolved.

Let us turn back to the paramagnetic properties of CDW superconductors. It seems quite plausible that the phenomenon predicted in this article has already been observed in the C15 compound $Hf_{1-x}Zr_xV_2$, where $H_{c2}(T) = 230$ or 208 kG for $x = 0.5$ and 0.6, respectively, and $H_p^{BCS} \leqslant 190$ kG if the simplest possible estimate is made. On the other hand, in these solid solutions the CDW gapping was found directly by resistive measurements.[53]

More recently the necessary correlations between the increase of the paramagnetic limit and the appearance of a CDW have been revealed for organic superconductors. For example, $H_{c2}(0)$ in the layered κ-(BEDT-TTF)$_2$Cu(NCS)$_2$ with $T_c \approx 10.4$ K and the FS prone to nesting,[54] overtakes the corresponding H_p^{BCS} (Ref. 55). At the same time, the T dependence of the resistance for this compound demonstrates a high and wide peak in the range 85–100 K, interrupting the metallic trend appropriate both to low and room temperatures.

Most probably, this behavior reflects the partial CDW-gapping.[56] The competition between CDW insulating state and superconductivity, triggered by an external pressure P in the related compound (BEDT-TTF)$_3$Cl$_2\cdot$2H$_2$O, can be considered as additional indirect evidence for the possible presence of a CDW in the superconducting state of κ-(BEDT-TTF)$_2$Cu(NCS)$_2$ (Ref. 54). κ-(BEDT-TTF)$_2$Cu[N(CN)$_2$]Cl is another charge-transfer salt with the κ-packing arrangement in which $H_{c2}(0)$ conspicuously exceeds H_p^{BCS} (Ref. 57). It is remarkable that this substance is an insulator at ambient pressure but becomes metallic and superconducting for $P > 0.3$ kbar. In view of such a proximity between dielectric and superconducting phases, it seems quite possible that κ-(BEDT-TTF)$_2$Cu[N(CN)$_2$]Cl retains nesting properties of its FS for higher P. The observed[57] positive curvature of $H_{c2}(T)$ in the neighborhood of T_c, a feature appropriate to superconductors with density waves,[58] agrees with the assumption made. At the same time, at larger $P = 6$ kbar the critical temperature T_c reaches a rather high value of 12.8 K.[54] In the framework of our model[7,8,36] it corresponds to the FS distortion with $\mu \to 0$. The authors of Ref. 57 point out that spin–orbit scattering cannot lead to $H_{c2}(0)$ exceeding H_p^{BCS} in the case discussed, since the Shubnikov–de Haas quantum oscillations in this compound are distinctly seen under pressure.[54]

In the layered superconductor α-(BEDT-TTF)$_2$NH$_4$Hg(SCN)$_4$ the value of $H_{c2}(0)$ is comparable to H_p^{BCS} (Ref. 59). This salt, with $T_c \approx 1$ K, is the only superconductor of the α-(BEDT-TTF)$_2$MHg(SCN)$_4$ family, while other sister compounds demonstrate a ground state of the density-wave type, and $T_d \approx 8$ K for M = K or Tl and 10 K for M = Rb.[54] A comparison of critical temperatures shows that density-wave correlations are stronger than superconducting ones, which imply large Σ_*/Δ_* and hence favor the increase of the ratio H_p/H_p^{BCS}. It should be noted that the CDW nature of the low-T insulating state in nonsuperconducting salts stems from observed paramagnetic effects[21,24,30,32,33,60] not appropriate to the SDW phase.[19]

Application of external pressure P to the initially insulating compound α-(BEDT-TTF)$_2$KHg(SCN)$_4$ leads to complete suppression of CDWs for $P > P_0 \approx 2.5$ kbar and to the appearance of superconductivity with $T_c \approx 0.1$ K.[61] This agrees well with our concept, and one should expect that $H_{c2}(0)$ will exceed H_p^{BCS} under pressure $P < P_0$, when the CDW is not completely destroyed. Such behavior is similar to what has been revealed[57] in κ-(BEDT-TTF)$_2$Cu[N(CN)$_2$]Cl. On the other hand, the superconducting transitions become extremely broad at pressures below P_0, demonstrating something like incomplete superconductivity,[61] which is not covered by our theory.[7,8] However, this behavior may also stem from experimental artifacts, such as unattained thermal equilibrium or internal strains. In any case, magnetic studies of α-(BEDT-TTF)$_2$KHg(SCN)$_4$ would be very important for elucidating the nature of the CDW, superconducting, and superconducting + CDW phases.

A new oxide KOs_2O_6 with a defect pyrochlore structure and $T_c = 9.6$ K is the most recently synthesized superconductor with $H_{c2} > H_p^{BCS}$ (Ref. 62). Since many oxides exhibit structural metal–insulator transitions with low-T phases of a CDW nature,[7,8,63–65] it would be of interest to check whether CDWs actually coexist with superconductivity in this compound.

To summarize, we have obtained simple formulas describing the increase of the Pauli paramagnetic limit for $H_{c2}(0)$ in CDW superconductors over the Clogston–Chandrasekhar value of the BCS theory as well as over the paramagnetic limit in the partially gapped normal CDWM phase. The similarity of the paramagnetic properties for s-wave superconductors and CDW partially gapped metals and the interplay of the two coexisting order parameters are responsible for the effect. There are strong experimental grounds to link the observed experimental data with the proposed concept.

A. M. Gabovich is grateful to the Japan Society for the Promotion of Science for support of his visit to the Hiroshima University (Grant ID No. S-03204) and to the Mianowski Foundation for support of his visit to Warsaw University. The research has been partly supported by the NATO grant PST.CLG.979446 and the grants COE (No. 13CE2002) and Scientific Research (No. 15540346) of the Ministry of Education, Culture, Sports, Science and Technology of Japan. The authors are also grateful to Jun Akimitsu (Tokyo), Serguei Brazovskii (Kyoto), Kenji Ishida (Kyoto), Yoshiteru Maeno (Kyoto), and Mai Suan Li (Warsaw) for fruitful discussions of the paramagnetic properties of the charge-density-wave state.

*E-mail: gabovich@iop.kiev.ua

[1] A. M. Clogston, Phys. Rev. Lett. **9**, 266 (1962).
[2] B. S. Chandrasekhar, Appl. Phys. Lett. **1**, 7 (1962).
[3] A. A. Abrikosov, *Fundamentals of the Theory of Metals*, North-Holland, Amsterdam (1987).
[4] P. Fulde, Adv. Phys. **22**, 667 (1973).

[5] P. M. Tedrow and R. Meservey, Phys. Rev. Lett. **43**, 384 (1979).
[6] R. Meservey and P. M. Tedrow, Phys. Rep. **238**, 173 (1994).
[7] A. M. Gabovich and A. I. Voitenko, Fiz. Nizk. Temp. **26**, 419 (2000) [Low Temp. Phys. **26**, 305 (2000)].
[8] A. M. Gabovich, A. I. Voitenko, and M. Ausloos, Phys. Rep. **367**, 583 (2002).
[9] G. Grüner, *Density Waves in Solids*, Addison-Wesley, Reading, Massachusetts (1994), p. 259.
[10] B. I. Halperin and T. M. Rice, Solid State Phys. **21**, 115 (1968).
[11] Yu. V. Kopaev, Trudy Fiz. Inst. Akad. Nauk SSSR **86**, 3 (1975).
[12] I. V. Krive, A. S. Rozhavskii, and I. O. Kulik, Fiz. Nizk. Temp. **12**, 1123 (1986) [Sov. J. Low Temp. Phys. **12**, 635 (1986)].
[13] W. Kohn and D. Sherrington, Rev. Mod. Phys. **42**, 1 (1970).
[14] M. A. Eggington and A. J. Leggett, Collect. Phenom. **2**, 81 (1975).
[15] W. Dieterich and P. Fulde, Z. Phys. **265**, 239 (1973).
[16] T. Tiedje, J. F. Carolan, A. J. Berlinsky, and L. Weiler, Can. J. Phys. **53**, 1593 (1975).
[17] M. Matos, G. Bonfait, R. T. Henriques, and M. Almeida, Phys. Rev. B **54**, 15307 (1996).
[18] D. Graf, J. S. Brooks, E. S. Choi, S. Uji, J. C. Dias, M. Almeida, and M. Matos, Phys. Rev. B **69**, 125113 (2004).
[19] R. H. McKenzie, cond-mat/9706235.
[20] D. Jérome, T. M. Rice, and W. Kohn, Phys. Rev. **158**, 462 (1967).
[21] D. Andres, M. V. Kartsovnik, W. Biberacher, H. Weiss, E. Balthes, H. Müller, and N. Kushch, Phys. Rev. B **64**, 161104 (2001).
[22] N. Harrison, C. H. Mielke, A. D. Christianson, J. S. Brooks, and M. Tokumoto, Phys. Rev. Lett. **86**, 1586 (2001).
[23] N. Harrison, Phys. Rev. B **66**, 121101 (2002).
[24] D. Andres, M. V. Kartsovnik, P. D. Grigoriev, W. Biberacher, and H. Müller, Phys. Rev. B **68**, 201101 (2003).
[25] N. Harrison, J. Singleton, A. Bangura, A. Ardavan, P. A. Goddard, R. D. McDonald, and L. K. Montgomery, Phys. Rev. B **69**, 165103 (2004).
[26] A. Bjeliš and K. Maki, Phys. Rev. B **42**, 10275 (1990).
[27] D. Zanchi, A. Bjeliš, and G. Montambaux, Phys. Rev. B **53**, 1240 (1996).
[28] N. Biskup, J. A. A. J. Perenboom, J. S. Brooks, and J. S. Qualls, Solid State Commun. **107**, 503 (1998).
[29] A. Bjeliš, D. Zanchi, and G. Montambaux, cond-mat/9909303.
[30] J. S. Qualls, L. Balicas, J. S. Brooks, N. Harrison, L. K. Montgomery, and M. Tokumoto, Phys. Rev. B **62**, 10008 (2000).
[31] P. Christ, W. Biberacher, M. V. Kartsovnik, E. Steep, E. Balthes, H. Weiss, and H. Müller, JETP Lett. **71**, 300 (2000).
[32] M. V. Kartsovnik, D. Andres, W. Biberacher, C. Christ, E. Steep, E. Balthes, H. Weiss, H. Müller, and N. D. Kushch, Synth. Met. **120**, 687 (2001).
[33] A. G. Lebed, JETP Lett. **78**, 138 (2003).
[34] N. Harrison, L. Balicas, J. S. Brooks, and M. Tokumoto, Phys. Rev. B **62**, 14212 (2000).
[35] H. Fröhlich, Proc. R. Soc. London, Ser. A **223**, 296 (1954).
[36] G. Bilbro and W. L. McMillan, Phys. Rev. B **14**, 1887 (1976).
[37] A. M. Gabovich, A. S. Gerber, and A. S. Shpigel, Phys. Status Solidi B **141**, 575 (1987).
[38] A. M. Gabovich, E. A. Pashitskii, and A. S. Shpigel, JETP Lett. **28**, 277 (1978).
[39] A. M. Gabovich, E. A. Pashitskii, and A. S. Shpigel, Sov. Phys. JETP **50**, 583 (1979).
[40] A. M. Gabovich, M. S. Li, H. Szymczak, and A. I. Voitenko, J. Phys.: Condens. Matter **15**, 2745 (2003).
[41] L. D. Landau and E. M. Lifshitz, *Electrodynamics of Continuous Media*, 2nd ed., rev. and enl., by E. M. Lifshitz and L. P. Pitaevskii, Pergamon Press, Oxford (1984), Nauka, Moscow (1982).
[42] Yu. A. Izyumov and Yu. N. Skryabin, Phys. Status Solidi B **61**, 9 (1974).
[43] M. A. Tanatar, M. Suzuki, T. Ishiguro, H. Tanaka, H. Fujiwara, H. Kobayashi, T. Toito, and J. Yamada, Synth. Met. **137**, 1291 (2003).
[44] V. L. Ginzburg and D. A. Kirzhnitz (eds.), *The Problem of High-Temperature Superconductivity* [in Russian], Nauka, Moscow (1977).
[45] E. G. Maksimov, Usp. Fiz. Nauk **170**, 1033 (2000).
[46] R. G. Dias and J. A. Silva, Phys. Rev. B **67**, 092511 (2003).
[47] A. Damascelli, Z. Hussain, and Z.-X. Shen, Rev. Mod. Phys. **75**, 473 (2003).
[48] A. A. Kordyuk, S. V. Borisenko, M. Knupfer, and J. Fink, Phys. Rev. B **67**, 064504 (2003).
[49] N. E. Hussey, M. Abdel-Jawad, A. Carrington, A. P. Mackenzie, and L. Balicas, Nature (London) **426**, 814 (2003).
[50] C. Wang, B. Giambattista, C. G. Slough, R. V. Coleman, and M. Subramanian, Phys. Rev. B **42**, 8890 (1990).
[51] T. Kiss, T. Yokoya, A. Chainani, S. S. Nohara, and H. Takagi, Physica B **312–313**, 666 (2002).
[52] T. Valla, A. V. Fedorov, P. D. Johnson, P-A. Glans, C. McGuinness, K. E. Smith, E. Y. Andrei, and H. Berger, Phys. Rev. Lett. **92**, 086401 (2004).
[53] V. M. Pan, V. G. Prokhorov, and A. S. Shpigel, *Metal Physics of Superconductors* [in Russian], Naukova Dumka, Kiev (1984).
[54] J. Singleton, Rep. Prog. Phys. **63**, 1111 (2000).
[55] F. Zuo, J. S. Brooks, R. H. McKenzie, J. A. Schlueter, and J. M. Williams, Phys. Rev. B **61**, 750 (2000).
[56] H. Mori, Int. J. Mod. Phys. B **8**, 1 (1994).
[57] Y. Shimojo, T. Ishiguro, H. Yamochi, and G. Saito, J. Phys. Soc. Jpn. **71**, 1716 (2002).
[58] A. M. Gabovich and A. S. Shpigel, Phys. Rev. B **38**, 297 (1988).
[59] Y. Shimojo, T. Ishiguro, M. A. Tanatar, A. E. Kovalev, H. Yamochi, and G. Saito, J. Phys. Soc. Jpn. **71**, 2240 (2002).
[60] D. Andres, M. V. Kartsovnik, W. Biberacher, T. Togonidze, H. Weiss, E. Balthes, and N. Kushch, Synth. Met. **120**, 841 (2001).
[61] D. Andres, M. V. Kartsovnik, W. Biberacher, K. Neumaier, and H. Müller, J. Phys. IV **12**, Pr9-87 (2002).
[62] S. Yonezawa, Y. Muraoka, Y. Matsushita, and Z. Hiroi, J. Phys.: Condens. Matter **16**, L9 (2004).
[63] J. M. Honig and L. L. Van Zandt, Annu. Rev. Mater. Sci. **5**, 225 (1975).
[64] A. M. Gabovich and D. P. Moiseev, Usp. Fiz. Nauk **150**, 599 (1986) [Sov. Phys. JETP **29**, 1135 (1986)].
[65] A. K. Raychaudhuri, Adv. Phys. **44**, 21 (1995).

This article was published in English in the original Russian journal. Reproduced here with stylistic changes by AIP.

Evidence for superconductivity and a pseudogap in the new magnetic compound $PrAg_6In_6$

V. M. Dmitriev*

Grenoble High Magnetic Field Laboratory, Max-Planck-Institut für Festkörperforschung and Centre National de la Recherche Scientifique, B.P. 166, F-38042 Grenoble Cedex 9, France; B. Verkin Institute for Low Temperature Physics and Engineering of the National Akademy of Sciences of Ukraine, 47 Lenin Ave., Kharkov 61103, Ukraine; International Laboratory of High Magnetic Fields and Low Temperatures, 53-421 Wroclaw, Poland

L. F. Rybaltchenko

Grenoble High Magnetic Field Laboratory, Max-Planck-Institut für Festkörperforschung and Centre National de la Recherche Scientifique, B.P. 166, F-38042 Grenoble Cedex 9, France; B. Verkin Institute for Low Temperature Physics and Engineering of the National Akademy of Sciences of Ukraine, 47 Lenin Ave., Kharkov 61103, Ukraine

P. Wyder and A. G. M. Jansen

Grenoble High Magnetic Field Laboratory, Max-Planck-Institut für Festkörperforschung and Centre National de la Recherche Scientifique, B.P. 166, F-38042 Grenoble Cedex 9, France

N. N. Prentslau

B. Verkin Institute for Low Temperature Physics and Engineering of the National Akademy of Sciences of Ukraine, 47 Lenin Ave., Kharkov 61103, Ukraine

W. Suski

International Laboratory of High Magnetic Fields and Low Temperatures, 53-421 Wroclaw, Poland; W. Trzebiatowski Institute of Low Temperatures and Structure Research, Polish Academy of Sciences, 50-950 Wroclaw, Poland

(Submitted June 4, 2004)
Fiz. Nizk. Temp. **31**, 63–67 (January 2005)

Direct evidence for superconductivity in the new magnetic compound $PrAg_6In_6$ is revealed for the first time. The distinct Andreev-reflection current is observed in metallic point contacts (PC) based on this compound. The data obtained provide reason enough to suggest that the rise of superconductivity depends strongly on the local magnetic order varying over the sample volume. The triangular-shaped PC spectra ($dV/dI(V)$) in the vicinity of the zero-bias voltage suggest an unconventional type of superconducting pairing. As follows from the temperature and magnetic field dependences of the PC spectra, the superconducting energy gap structure transforms into the pseudogap one as the temperature or the magnetic field increases. [DOI: 10.1063/1.1820362]

According to the conventional views, only a perfect antiferromagnetic (AFM) order is well compatible with superconductivity in a quite broad temperature range. New magnetic superconductors whose magnetic structures are far from having perfect AFM order provide a new insight into the problem of interplay between magnetism and superconductivity. A few years ago, a new class of magnetic superconductors with the $ThMn_{12}$-type crystal structure was perceived to exist. Radio-frequency impedance and heat capacity measurements carried out on several compounds of this family have revealed distinct features in the corresponding characteristics which might be associated with superconductivity in some regions of the samples. Such indications of superconductivity have been found in $LuFe_4Al_8$, $ScFe_4Al_8$, YCr_4Al_8, YFe_4Al_8, and $PrAg_6In_6$.[1,2] These compounds crystalize with the comparatively simple tetragonal body-centered structure of space group $I4/mmm$ (D_{4h}^{17}, nr. 139). In spite of the AFM transition well above 100 K, the magnetic structure remains very complicated.[3,4] So far, only very restricted information about the electronic structure is available.[5] Recently,[6] we have proved the existence of a superconducting phase in YFe_4Al_8 by the point-contact (PC) Andreev-reflecton technique. The character of the measured PC spectra (differential resistance versus voltage, $dV/dI(V)$) implied an unconventional type of superconductivity in this compound.

Here we present for the first time the direct evidence for superconductivity found in Andreev-reflection experiments on another recently synthesized compound, $PrAg_6In_6$.[7] This fact appears to be very impressive, because the Pr component is very antagonistic to superconductivity and can destroy it entirely. That is what occurs in $PrBa_2Cu_3O_x$ unless special preparation techniques are used. We studied point contacts with the metallic conductivity of the needle-anvil geometry between Ag and freshly fractured surfaces of a $PrAg_6In_6$ polycrystal prepared by arc melting. According to the stan-

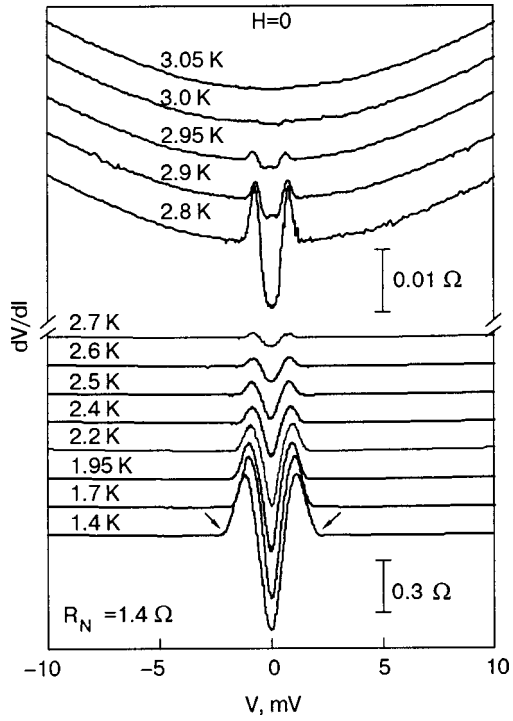

FIG. 1. $dV/dI(V)$ characteristics of the point contact Ag–$PrAg_6In_6$ measured at different temperatures indicated at each curve. For clarity, the curves are shifted vertically and the upper part of the spectra is shown on an enlarged scale.

dard x-ray examination, the sample had the proper $ThMn_{12}$-type lattice without noticeable traces of additional phases. The PC method employed enables one to measure on N–S contacts the Andreev-reflection current, whose energy and temperature dependences allow to infer the basic superconducting characteristics. The high reliability of PC Andreev-reflection method can be seen by comparing the gap values of high-T_c superconductors measured by this method and by tunneling spectroscopy[8] as well as by the photoemission technique.[9] The contact sizes varied within 5–70 nm. The standard modulation technique was used to register the $dV/dI(V)$ characteristics.

Figure 1 shows the typical PC spectra of the $PrAg_6In_6$ compound measured at different temperatures, which furnish direct evidence for superconductivity in this material. Indeed, as is well known, the resistance decrease of metallic contacts near zero bias voltage is due to the Andreev reflection of quasiparticles, which is always occurring at an N–S interface. Thus, the zero-bias resistance minimum which first arises on the 3 K curve and whose amplitude then increases with decreasing temperature (Fig. 1) is a distinct indication of probing the superconducting region. Such indications of superconductivity with a critical temperature T_c varying within 1.7–3.3 K were found in many parts of the fractured sample surface (sometimes, up to 10% of the total surface). Noticeably, the radio-frequency experiments carried out on the same sample resulted in $T_c \sim 8$ K in the first measurements and in an irregular lowering of T_c in subsequent tests. Perhaps the reason is connected with some variations of magnetic structure when the AFM transitions happen. The critical magnetic field could reach about 0.5 T in some cases, which essentially excluded the possibility of superconductivity arising in In clusters, which could appear, for instance, due to composition variations. Then, if the superconducting features in our spectra were caused by Andreev reflection from In clusters, the shape of spectra would agree with that typical for N–S contacts based on conventional superconductors.[10] Because such spectra were never observed, this is reliable proof that superconductivity in $PrAg_6In_6$ is not due to a free In component. Moreover, the In clusters should result in wide variations of gap-feature voltages in different contacts,[11] and that was not observed either.

The PC spectra have a very unusual shape as compared to those of conventional BCS superconductors and show a number of striking features. When the temperature goes down, the $dV/dI(V)$ characteristic develops into a triangular-shaped structure at low voltages. This behavior is not consistent with the fully gapped Fermi surface expected for conventional BCS superconductors and may be taken as an indication of the presence of nodes or lines of nodes in the gap function. Indeed, according to the Blonder-Tinkham-Klapwijk (BTK) theory[10] of N–S contacts based on conventional superconductors, near $V=0$ the PC spectra should display either a double minimum structure if a potential barrier occurs at the N–S boundary or a flat bottom if this barrier is absent. The measured spectra are characterized by the horn structure that is often observed in low-ohmic contacts, although its origin is not understood fully even for conventional superconductors. Besides, it is seen that the width of the superconducting structure does not change strongly with temperature and remains nonzero up to $T=3.05$ K, where no structure can be seen at all. Because of the extremely unusual type of PC spectra measured, the standard BTK model cannot be used for finding the gap parameter. Hence, the spectra may be characterized only phenomenologically. Each curve is described by the depth of the resistance minimum $R_0 = R_N - R_S$, where R_N and R_S are the contact resistances at $V=0$ in the normal and superconducting states, respectively, and by the width of the zero-bias minimum at its half depth, 2δ.

As is seen in Figs. 1 and 2, with rising temperature the resistance parameter R_0 decreases and slowly approaches zero at 3.05 K. Correspondingly, the relative parameter R_S increases and goes to R_N. Such behavior does not agree with the BTK theory (see inset in Fig. 2). Both of these dependences change their slopes near 2.8 K, showing that the amplitude variations are about 98% below this temperature and only about 2% above it. Near $T=2.8$ K, the $R_S(T)$ curve looks very much like the smeared resistive N–S transition. Therefore, we may quite reasonably take this temperature as the critical temperature T_c. In the vicinity of and above 2.8 K, the behavior of the $R_0(T)$ and $R_S(T)$ dependences is probably determined by superconducting fluctuations, i.e., Cooper pairs arising above T_c. It is worth noting that the width of the whole superconducting $dV/dI(V)$ structure (see the arrows on the 1.4 K curve in Fig. 1) and the distance between horns decrease slowly (by $\sim 40\%$) as the temperature increases up to 2.8 K and then remain practically unchanged in the temperature range from 2.8 to 3.05 K.

The width 2δ of the resistance minimum has another remarkable temperature dependence. When the temperature increases, 2δ first decreases (by $\sim 25\%$) but then, near T_c,

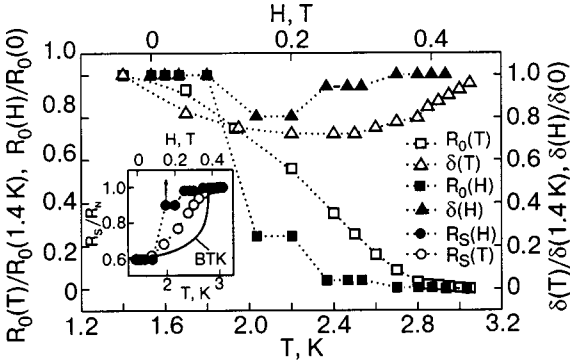

FIG. 2. Temperature and magnetic field dependences of the main parameters for the $dV/dI(V)$ structure: the depth $R_0=R_N-R_S$ and the width δ of the zero-bias resistance minimum (squares and triangles, respectively) for the contact presented in Figs. 1 and 3. Inset: the analogous dependences of the zero-bias contact resistance R_S (circles) together with the dependence expected from BTK theory, $R_S(T)$ (solid line).

comes back practically to its initial value, thus passing through a minimum near 2.2 K. The δ parameter of the $dV/dI(V)$ structure is usually associated with the energy gap or order parameter in superconductors. On the other hand, the resistance parameters R_0 and R_S are associated with the number of superconducting quasiparticles involved in the Andreev-reflection processes. So, it is reasonable to suppose that near 2.8 K we see the smooth transformation of the superconducting gap (or order parameter) into a pseudogap with the same energy scale at this temperature, and that only a small number of fluctuating paired quasiparticles persist in the pseudogap regime.

Our scenario is in qualitative accordance with the results of tunneling spectroscopy of $Bi_2Sr_2CaCu_2O_{8+\delta}$ single crystals,[12] and with the measurements of a coherent boson current in the normal state of the high-T_c superconductor

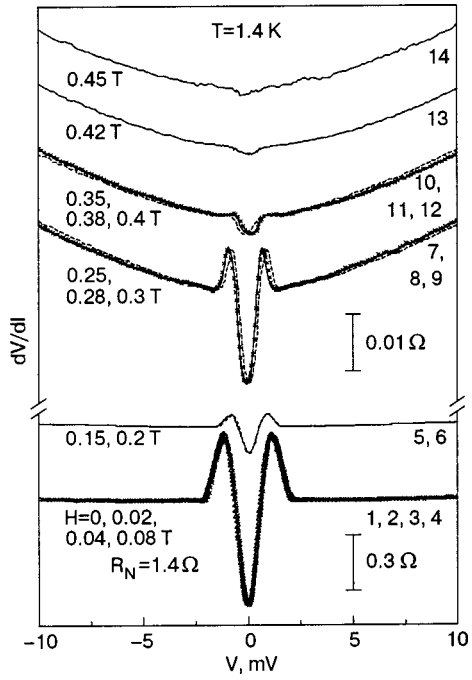

FIG. 3. $dV/dI(V)$ characteristics of the point contact Ag–$PrAg_6In_6$ measured at different magnetic fields, indicated at each curve. For clarity, the curves are shifted vertically and the upper parts of the spectra are shown on an enlarged scale.

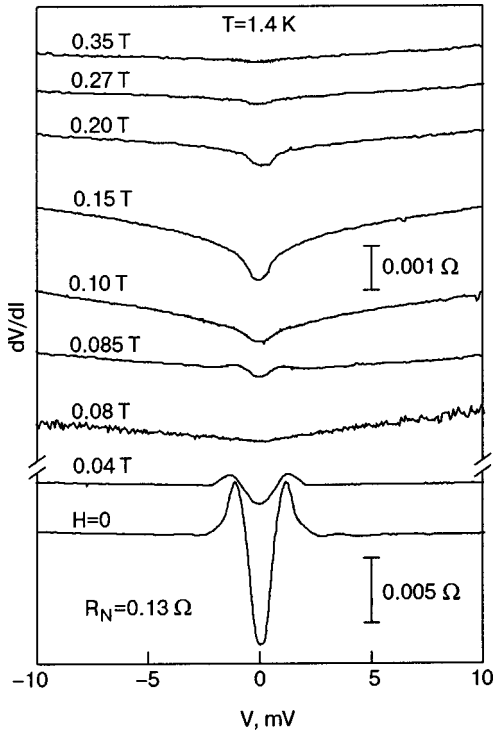

FIG. 4. Another type of $dV/dI(V)$ characteristics for the point contact Ag–$PrAg_6In_6$ measured at different magnetic fields indicated at each curve. For clarity, the curves are shifted vertically and the upper parts of the spectra are shown on an enlarged scale. As is seen, the new pseudogap-like structure arises after practically full disappearance of the superconducting Andreev-reflection structure near $H=0.08$ T.

$YBa_2Cu_3O_y$ (Ref. 13). If the pseudogap model is valid, this may imply that we are dealing with the *d*-wave type of superconductivity proved for high-T_c superconductors, for which the pseudogap is known to be typical. In this case the Fermi surface is not gapped entirely, and this explains the unusual shape of our $dV/dI(V)$ characteristics.

The triangular-shaped PC Andreev-reflection spectra were recently observed by us[6] in YFe_4Al_8. Earlier, similar behavior of the PC spectra was reported in Ref. 14 for the heavy-fermion UPt_3. This behavior was attributed to the *d*-wave symmetry of the order parameter in that superconductor. The BTK theory extended for N–S contacts based on the $d_{x^2-y^2}$ superconductors also predicts a triangular shape of the PC spectra for most crystallographic directions if the contact barrier transparency is enough high, i.e., the dimensionless barrier strength factor $Z<1$.[15]

The effect of magnetic field on the PC spectra of $PrAg_6In_6$ is very surprising, resulting in steplike behavior of the spectra in varying field (see Fig. 3 for the same contact as in Fig. 1). Without additional experiments it is difficult to explain this phenomenon clearly. The nonuniform distribution of the superconducting parameters over the sample volume (cf. Figs. 3 and 4) gives evidence for intrinsic structural or/and magnetic inhomogeneities in the given materials, as was earlier seen in contacts with YFe_4Al_8 single crystals.[6] In this case, a lot of uncompensated magnetic moments of irregular ordering should appear, which may result in an exotic symmetry of the Cooper pairing and the unconventional behavior of PC spectra in the field.

Remarkably, the main tendencies in the magnetic field

dependences of the resistance parameters characterizing the Andreev-reflection structure remain practically the same as in the case of temperature variations. As is seen in Figs. 2 and 3, the resistance minimum (parameters R_0 and R_S) vanishes at $H=0.45$ T. However, the main changes of the parameters (about 98%) take place below 0.25 T (we may take this value as a critical field), showing that only a very small number of paired quasiparticles persist in the field range 0.25–0.45 T. In this field range, zero-bias minima may be considered as an exhibition of the pseudogap state.

The magnetic field dependence of the energy parameter δ, mirroring the gap or the order parameter, is presented in Fig. 2. Neglecting the steps, one can see that the $\delta(H)$ dependence resembles that of $\delta(T)$, passing through a minimum within the 0.15–0.20 T range. Note that the magnetic field dependences of the width of the whole superconducting structure in $dV/dI(V)$ and the distance between the horns, which also correlate with the superconducting gap (order parameter), resemble very much the temperature dependences discussed above.

On some of the point contacts we observed quite interesting behavior of the PC spectra in an applied magnetic field (Fig. 4). In these spectra, after practically full suppression of the low-magnetic-field Andreev-reflection structure typical for $PrAg_6In_6$ (at 0.08 T for the contact in Fig. 4), there arises another pseudogap-like structure. The latter first increases with field but then disappears at a higher field, slightly above 0.35 T for the given contact. In some cases this high-field structure could persist up to $H=2.5$ T.

The data presented above strongly imply that the arising of the pseudogap state is attributable to superconductivity. Indeed, nothing other than the Andreev reflection associated with fluctuating Cooper pairs can result in the zero-bias resistance minimum on the PC spectra above T_c or H_{c2}. If the pseudogap were not caused by superconductivity, its sign would be opposite to that observed in our experiments, as was observed earlier in the electron-doped cuprate superconductor $Pr_{2-x}Ce_xCuO_4$, where the pseudogap was shown to be governed by nonsuperconducting factors.[16] As was shown in Ref. 17, the Andreev reflection in the pseudogap state can occur from the phase-incoherent preformed Cooper pairs whose possible existence above T_c was suggested by Emery and Kivelson.[18]

The effect of magnetic field on the pseudogap structure (see Figs. 3 and 4) indicates that the interior magnetic structure of $PrAg_6In_6$ interacts with preformed pairs above H_{c2} in some unusual way and that interaction is specified strongly by the variations of magnetic ordering over the sample volume. A closely similar situation was discussed for Bi-2201 crystals of different doping levels,[19] which could be compared with the spin variations in our sample. However, at the moment the machanism of this interaction cannot be explained properly.

In conclusion, direct evidence for superconductivity in the new ternary magnetic compound $PrAg_6In_6$ has been obtained for the first time in point-contact Andreev-reflection experiments. Observation of the pseudogap and steplike structures in the Pr compound is further (besides the triangular-shaped Andreev features of the same width in different contacts and the high critical magnetic field indicated above) strong proof that the superconductivity cannot be connected with hypothetical chemically free In atoms, but rather originates from the primary crystal structure. The small amount of superconducting phase ($<10\%$ of total sample volume) may result from some distortions of the crystal structure, e.g., when slight displacements of the magnetic Pr atoms may provide significant changes of the local magnetic structure, and so the superconducting phase can appear only in separate sample regions with certain magnetic order. The unconventional shape of the point-contact characteristics $dV/dI(V)$ strongly implies non-s-wave symmetry of the Cooper pairing. The basic parameters of the $dV/dI(V)$ structure which undoubtedly are associated with the energy gap or the order parameter in superconductors do not become zero when the temperature or magnetic field increases up to the critical value. Here the superconducting spectra are transformed smoothly into another gaplike structure, demonstrating gradual conversion of the superconducting gap (order parameter) into a pseudogap. This means that between the superconducting and normal states there exists an unusual intermediate (pseudogap) state which possesses properties of both the normal and superconducting phases.[20] According to our knowledge, this is the first observation of the pseudogap regime in a non-high-T_c superconductor. Finally, exciting steplike transitions of the $dV/dI(V)$ Andreev-reflection spectra caused by the magnetic field have been discovered in $PrAg_6In_6$.

We would like to thank G. A. Gogadze for very helpful discussions and V. Zaremba for preparing the $PrAg_6In_6$ samples.

*E-mail: dmitriev@ilt.kharkov.ua

[1] A. M. Gurevich, V. M. Dmitriev, V. N. Eropkin, L. A. Ishchenko, N. N. Prentslau, and L. V. Shlyk, Fiz. Nizk. Temp. **25**, 15 (1999) [Low Temp. Phys. **25**, 10 (1999)].
[2] A. M. Gurevich, V. M. Dmitriev, V. N. Eropkin, B. Yu. Kotur, N. N. Prentslau, V. Suski, A. T. Terekhov, and L. V. Shlyk, Fiz. Nizk. Temp. **27**, 1308 (2001) [Low Temp. Phys. **27**, 967 (2001)].
[3] P. Schobinger-Papamantellos, K. H. J. Buschow, and C. Ritter, J. Magn. Magn. Mater. **186**, 21 (1998).
[4] J. A. Paixão, M. R. Silva, J. C. Waerenborgh, A. P. Gonçalves, G. H. Lander, P. J. Brown, M. Godinho, and P. Burlet, Phys. Rev. B **63**, 054410 (2001).
[5] E. Talik, M.-E. Lucas, W. Suski, and R. Troć, J. Alloys Compd. **350**, 72 (2003).
[6] V. M. Dmitriev, L. F. Rybaltchenko, P. Wyder, A. G. M. Jansen, N. N. Prentslau, and W. Suski, Fiz. Nizk. Temp. **28**, 374 (2002) [Low Temp. Phys. **28**, 260 (2002)].
[7] V. I. Zaremba, Ya. M. Kalychak, Ya. V. Galadzhun *et al.*, J. Solid State Chem. **145**, 216 (1999).
[8] J. R. Kirtley, Inter. J. Mod. Phys. **4**, 181 (1990).
[9] T. Timusk and B. Statt, Rep. Prog. Phys. **62**, 61 (1999).
[10] G. E. Blonder, M. Tinkham, and T. M. Klapwijk, Phys. Rev. B **25**, 4515 (1982).
[11] O. I. Shklyarevskii, A. M. Duif, A. G. M. Jansen, and P. Wyder, Phys. Rev. B **34**, 1956 (1986).
[12] Ch. Renner, B. Revaz, J.-Y. Genoud, K. Kadowaki, and Ø. Fischer, Phys. Rev. Lett. **80**, 149 (1998).
[13] K. Kawabata, S. Tsukui, Y. Shono, O. Michikami, H. Saakura, K. Yoshiara, Y. Kakehi, and T. Yotsuya, Phys. Rev. B **58**, 2458 (1998).
[14] Y. De Wilde, J. Heil, A. G. M. Jansen, P. Wyder, R. Deltour, W. Assmus, A. Menovsky, W. Sun, and L. Taillefer, Phys. Rev. Lett. **72**, 2278 (1994).
[15] Y. Tanuma, Y. Tanaka, and S. Kashiwaya, Phys. Rev. B **64**, 214519 (2001).

[16] A. Biswas, P. Fournier, V. N. Smolyaninova, R. C. Budhani, J. S. Higgins, and R. L. Greene, Phys. Rev. B **64**, 104519 (2001).
[17] H.-Y. Choi, Y. Bang, and D. K. Campbell, cond-mat/9902125 (unpublished).
[18] V. J. Emery and S. A. Kivelson, Nature (London) **374**, 434 (1995).
[19] A. N. Lavrov, Y. Ando, and S. Ono, Europhys. Lett. **57**, 267 (2002).
[20] A. A. Abrikosov, Phys. Rev. B **64**, 104521 (2001).

This article was published in English in the original Russian journal. Reproduced here with stylistic changes by AIP.

LOW-TEMPERATURE MAGNETISM

Kinetic properties and magnetic susceptibility of $Pr_{0.67}Ca_{0.33}MnO_3$ under hydrostatic pressure

E. S. Itskevich,* V. F. Kraidenov, and E. A. Petrova

Institute of High Pressure Physics of the Russian Academy of Sciences, Troitsk, Moscow Region, 142190, Russia

(Submitted April 29, 2004)
Fiz. Nizk. Temp. **31**, 68–76 (January 2005)

Measurements of the magnetic susceptibility χ, thermopower α, and resistivity ρ of the manganate $Pr_{1-x}Ca_xMnO_3$ with $x=0.33$ are made on single-crystal samples in the temperature range 77–300 K and at pressures up to $P=13$ kbar. At $P\geqslant 8.8$ kbar a metal-insulator transition is observed. The phase transition temperatures and their pressure dependence are obtained: the temperature of a possible structural transition $T_n\approx 250$ K ($\partial T_n/\partial P=-1.7$ K/kbar); the charge-ordering temperature $T_{co}\approx 230$ K ($\partial T_{co}/\partial P=-0.8$ K/kbar); the Néel temperature $T_N\approx 140$ K ($\partial T_N/\partial P=-1.1$ K/kbar); the temperature of the appearance of a spontaneous ferromagnetic moment $T_C\approx 100$ K ($\partial T_C/\partial P=-1.2$ K/kbar), and the temperature of the metal-insulator transition T_{MI} ($\partial T_{MI}/\partial P=2.8$ K/kbar). The $\alpha(T)$ curve is dome-shaped and is shifted into the negative region with increasing pressure, twice changing sign with the variation of the temperature. As T_C is approached the thermopower $\alpha<0$, with $|\alpha|>500$ μV/K. © *2005 American Institute of Physics.* [DOI: 10.1063/1.1820364]

Among the many manganites possessing colossal magnetoresistance (CMR), the compounds $Pr_{1-x}Ca_xMnO_3$ are distinguished by a number of outstanding properties.

1. Because of the close values of the radii of the ions Pr^{3+} and Ca^{2+} (1.18 Å),[1] the mean radius $\langle r_A\rangle$ and, hence, the angle θ formed by the Mn–O–Mn line and the value of the exchange interaction between Mn ions, which depends on that angle, change weakly as the Ca concentration x in the compounds is varied. Therefore, in a study of the dependence of the various physical parameters on x in the compounds $Pr_{1-x}Ca_xMnO_3$ (Pr–Ca) this factor can in many cases be neglected.

2. For all values of x, at temperatures $T<300$ K and at atmospheric pressure these compounds lack the ferromagnetic metallic (FMM) phase present in the Pr–Sr, Sm–Sr,[2] La–Sr,[3] and La–Ca[4] compounds.

3. In the Pr-Ca compounds in the temperature region 100–250 K a transition to a charge-ordered (CO) state of the Mn^{3+} and Mn^{4+} ions is observed. And, while in the La–Ca compounds the CO state is realized in the narrow region $x=0.48-0.52$, i.e., near $x=0.5$, in Pr–Ca it is observed from $x=0.3$ with the CO temperature $T_{co}\approx 200$ K to $x=0.85$ with $T_{co}\approx 100$ K, with the maximum value of $T_{co}\approx 250$ K at $x=0.5$.[2] The fact that the CO state is preserved over such a wide range of x may be due to additional ordering of the excess Mn^{3+} and Mn^{4+} ions.[5]

4. The Pr–Ca compounds with $x=0.3-0.5$ at low T can be brought from the CO antiferromagnetic insulator (AFI) state to a ferromagnetic metallic state by an external influence: the application of magnetic field,[6–13] pressure,[13–15] or electric field,[16] or irradiation by a laser pulse,[17] visible light,[18] x rays,[19] or an electron beam.[20] At $T<60$ K the FMM phase thus obtained persists in a metastable state for quite some time after the external influence is removed.

The Pr–Ca compounds with $x=0.3-0.33$ are of particular interest, since they lie near a boundary. On one side of this boundary (for $x<0.3$) the CO state is not realized, and the sample goes into a ferromagnetic insulator (FMI) state at $T<T_C$. On the other side, they are quite far from the compound with $x=0.5$, in which the CO state is most stable and can be destroyed only by a high magnetic field ~ 24 T.[11] These compounds have been investigated in many studies by the methods of x-ray,[21–24] neutron,[7,22,23,25–27] and electron[20,28] diffraction, magnetic methods,[6,9,12,14,26,29] and by measurement of the resistivity,[6,13,14] heat capacity,[9,11,12,26] thermopower,[5,22,30] thermal expansion,[31] and spin-muon relaxation.[26] It has been found that the compound $Pr_{0.67}Ca_{0.33}MnO_3$ exhibits a number of magnetic, charge, and structural phase transformations as the temperature is lowered. At room temperature the sample is found in a paramagnetic (PM) state and has a quasi-tetragonal lattice of the class *Pbnm* with parameters $b>a\approx c/\sqrt{2}$ with weak Jahn-Teller (JT) distortions. As the temperature is lowered in the region $T_n=250-260$ K there is a structural transition from one quasi-tetragonal phase to another: $(b>a\approx c/\sqrt{2})\rightarrow(b\approx a>c/\sqrt{2})$.[21] At a temperature $T_{co}=180-230$ K a charge and orbital ordering arises. As the temperature is decreased further, at $T_N=130-150$ K the CO phase undergoes a transition from the PM state to an antiferromagnetic (AFM) state with a known pseudo-charge-exchange (pseudo-CE) ordering.[23,25] In this ordering the magnetic moments of the Mn ions are coupled antiferromagnetically in a zig-zag chain in the *ab* plane, and the chains themselves are coupled ferromagnetically. In the direction of the *c* axis the coupling of the planes

is also ferromagnetic. At a temperature $T_C = 100-120$ K a spontaneous magnetic moment appears in the sample. The number of FM clusters in the AFM matrix increases with decreasing T, but the number necessary for percolation to occur ($\approx 17\%$ by volume)[9] is not attained on cooling down to helium temperatures. The phase-separation picture, as against the canted antiferromagnet hypothesis,[25] has recently found experimental and theoretical support.[7–9,22,23,26,32]

In $Pr_{67}Ca_{0.33}MnO_3$ the change of T_C under pressure to the temperature T_{MI} of the insulator-metal transition has not been studied. It follows from the magnetic measurements[29] that T_C decreases with increasing field H. It was shown in Refs. 13 and 15 that at a pressure $P > 5$ kbar $Pr_{0.7}Ca_{0.3}MnO_3$ undergoes a transition to a metallic state at T_{MI}, and that T_{MI} also increases with increasing pressure. This relation between these temperatures and the reason why they behave differently with pressure (and magnetic field) are questions of no small interest.

In the present study we measure the magnetic susceptibility χ, resistivity ρ, and thermopower α in the temperature range 80–300 K and at hydrostatic pressures up to 13 kbar.

SAMPLES

A $Pr_{0.67}Ca_{0.33}MnO_3$ single crystal was grown by the floating zone method with radiant heating in A. M. Balbashov's laboratory at the Moscow Power Institute.[33] The samples for study were cut from the cylindrical boule, the axis of which lay along the [100] direction of the crystal.

MAGNETIC SUSCEPTIBILITY

The magnetic susceptibility χ was measured by a modulation method at an ac frequency of 19 Hz with a magnetic field amplitude of ≈ 10 Oe. The method is explained in detail in Ref. 34.

Figure 1 shows the temperature dependence of the magnetic susceptibility χ of a $Pr_{0.67}Ca_{0.33}MnO_3$ sample at different pressures. The maxima in the $T \sim 100$ K region are identified with the temperature T_C at which ferromagnetic ordering (a spontaneous magnetic moment) arises in the sample. Here the bulk of the sample remains in the AFM state. Up to a pressure $P = 6$ kbar the maxima of χ are shifted to lower temperatures at a rate of $\partial T_C/\partial P = -1.2$ K/kbar ($\partial \ln T_C/\partial P = -1.1 \times 10^{-2}$ kbar^{-1}). At a pressure of 12 kbar the maximum of χ is shifted in the opposite direction.

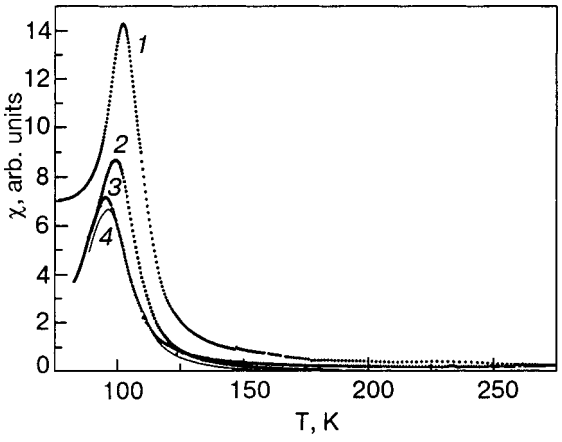

FIG. 1. Temperature dependence of the magnetic susceptibility of $Pr_{0.67}Ca_{0.33}MnO_3$ at different pressures P [kbar]: 0 (*1*), 2.0 (*2*), 6.0 (*3*), 12 (*4*). The pressure values given are the averages for the temperature intervals corresponding to the phase transitions.

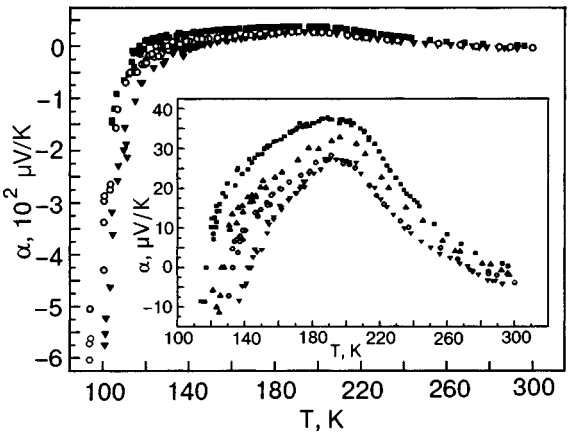

FIG. 2. Temperature dependence of the thermopower of $Pr_{0.67}Ca_{0.33}MnO_3$ at pressures P [kbar]: 0 (■), 5.0 (△); 8.0 (○); 12.7 (▼). The pressure corresponds to room temperature.

THERMOPOWER

Measurements of the thermopower were made in the dynamic regime on cooling and heating of the high-pressure chamber by the method set forth in Ref. 34. Figure 2 shows the temperature dependence of the thermopower α at different pressures. One can notice some common traits of all the curves.

1. All of the $\alpha(T)$ curves are dome-shaped with a positive maximum at $T_{max} \approx 190$ K, which with increasing pressure decreases in height and shifts to higher temperatures.

2. With increasing pressure all of the $\alpha(T)$ curves are similarly shifted toward negative values of α.

3. In the temperature region $T < T_{01} = 115-145$ K the sign of α changes from positive to negative ($\alpha < 0$). With increasing pressure the temperature T_{01} increases at a rate of $\partial T_{01}/\partial P - 2.3$ K/kbar ($\partial \ln T_{01}/\partial P = 2 \times 10^{-2}$ kbar^{-1}).

4. For $T \geqslant 270$ K at the point T_{02} the sign of α also changes from positive to negative. With increasing pressure the temperature T_{02} decreases at a rate of $\partial T_{02}/\partial P = -2.8$ K/kbar ($\partial \ln T_{02}/\partial P = -10^{-2}$ kbar^{-1}).

5. In the temperature region $T \approx 250$ K the $\alpha(T)$ curves have a kink, which is especially noticeable at atmospheric pressure. It is seen most clearly on a plot of $\alpha = f(1/T)$ (see Fig. 4b).

6. At $T > T_{02}$ the thermopower tends toward a constant negative value α_∞, which increases in absolute value with increasing pressure.

7. As the temperature approaches T_C (Fig. 2) the thermopower tends toward large negative values ($|\alpha| > 500$ μV/K).

RESISTIVITY

For the resistivity measurements we used two samples 5.5 mm in height. The resistivity at room temperature and

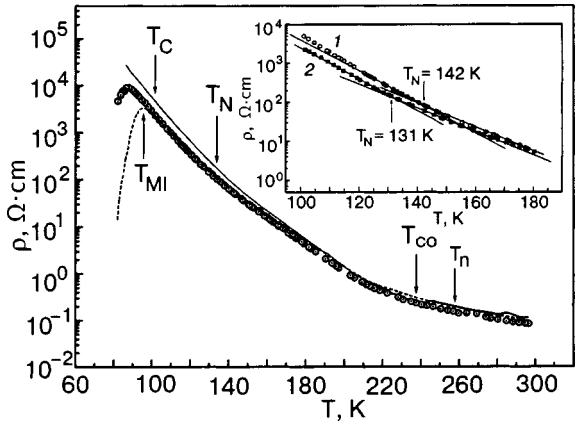

FIG. 3. Temperature dependence of the resistivity of $Pr_{0.67}Ca_{0.33}MnO_3$ at pressures P [kbar]: 0 (—); 11.0 (○); 12.7 (— — —). The pressure corresponds to room temperature. The inset shows the temperature dependence of the resistivity in the region of the Néel temperature T_N at P [kbar]: 0 (*1*), 12.7 (*2*).

atmospheric pressure was $\rho_{300\,K}=0.1\ \Omega\cdot$cm. The measurements of ρ were made by the 4-contact method. The technique is explained in detail in Ref. 34.

Figure 3 shows $\rho=f(T)$ on a semilogarithmic scale for different pressures. It can be seen that the resistivity of the samples decreases slightly with increasing pressure. The curves can be approximated over appreciable temperature intervals by straight lines, and the points at which slope changes occur are identified as phase transition points. The inset in Fig. 3 illustrates the determination of the antiferromagnetic transition temperature $T_N\approx 140$ K, at which a transition from the PM phase to an AFM phase of the pseudo-CE type occurs. The characteristic temperatures T_n, T_{co}, and T_C indicated on the plot were determined as follows. The temperature $T_n\approx 250$ K is the kink point between two straight lines on the plot of $\alpha=f(1/T)$ (Fig. 4b). The charge- and orbital-ordering temperature $T_{co}\approx 225$ K was determined by an analogous method but from a plot of $\ln\rho=f(1/T)$ (Fig. 4a), and the Curie point $T_C\approx 100$ K from a plot of $\chi(T)$ (Fig. 1). Finally, the temperature T_{MI} of the transition from the insulator to the ferromagnetic metal state was observed on the same $\chi(T)$ and $\ln\rho=f(T)$ curves at a pressure $P\geqslant 8.8$ kbar ($P_{300\,K}=11$ kbar) (Fig. 3). The pressure dependence of these characteristic temperatures is shown in Fig. 5. The temperatures T_n, T_{co}, T_N, and T_C decrease with increasing pressure: $\partial T_n/\partial P=-1.7$ K/kbar ($\partial\ln T_n/\partial P=-6.5\times10^{-3}$ kbar^{-1}), $\partial T_{co}/\partial P=-0.8$ K/kbar ($\partial\ln T_{co}/\partial P=-3.3\times10^{-3}$ kbar^{-1}), $\partial T_N/\partial P=-1.1$ K/kbar ($\partial\ln T_N/\partial P=-7.6\times10^{-3}$ kbar^{-1}), $\partial T_C/\partial P=-1.2$ K/kbar ($\partial\ln T_C/\partial P=-1.1\times10^{-2}$ kbar^{-1}). The temperature T_{MI}, on the contrary, increases with pressure, as is typical for manganates: $\partial T_{MI}/\partial P=2.8$ K/kbar ($\partial\ln T_{MI}/\partial P=4.3\times10^{-2}$ kbar^{-1}).

The curves of $\ln\rho=f(1/T)$ (Fig. 4a) and $\ln\rho=f(1/T^{1/4})$ (Fig. 6) have a characteristic bend at $T\approx 190$ K. It can be assumed that a transition from an activational type of conductivity to variable-length hopping occurs in this temperature region.

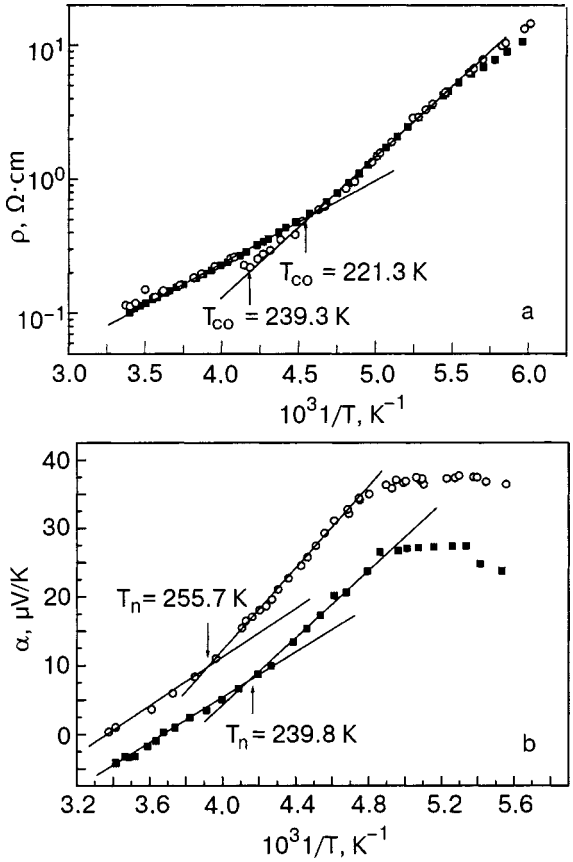

FIG. 4. Plots of the resistivity $\rho=f(T^{-1})$ (a) and thermopower $\alpha=f(T^{-1})$ (b) for $Pr_{0.67}Ca_{0.33}MnO_3$ at pressures P [kbar]: 0 (○); 12.7 (■). The pressure corresponds to room temperature.

DISCUSSION OF THE RESULTS

As is seen in Fig. 2, the maximum of the thermopower α occurs at $T\approx 190$ K, when a charge-ordered state is already established in the sample in the PM phase. However, a broad maximum (hump) of α in this temperature region has also been observed previously in perovskite structures, where neither charge ordering nor orbital ordering is present. Among those compounds are the manganate $La_{0.9}Sr_{0.1}MnO_3$ (Ref. 34), and yttrium and mercury HTSC cuprates.[35] A theoretical

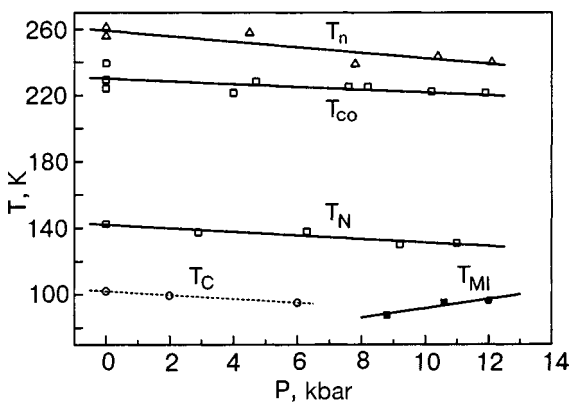

FIG. 5. Pressure dependence of the phase transition points T_n, T_{co}, T_N, T_C, and T_{MI}, obtained from measurements of the thermopower (△), resistivity ρ (□,■), and magnetic susceptibility χ (○,●). The pressure values are given with allowance for the pressure relief with decreasing temperature.

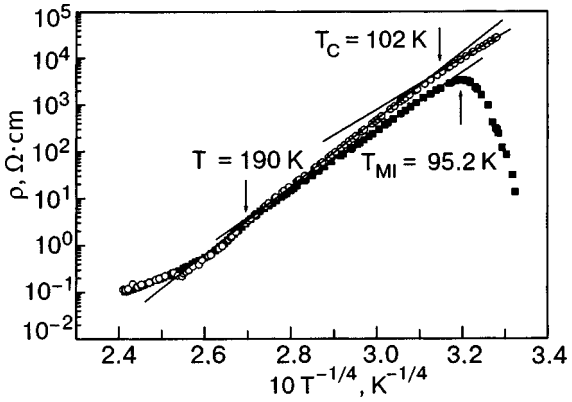

FIG. 6. Temperature dependence of the resistivity $\rho = f(T^{-1/4})$ for $Pr_{0.67}Ca_{0.33}MnO_3$ at pressures P [kbar]: 0 (○), 12.7 (■).

attempt to explain this maximum on the basis of strong electron–lattice coupling was made in Ref. 36 (correlated polaron theory).

According to Refs. 5 and 37, at high temperatures the sign of the derivative $\partial\alpha/\partial T$ determines the sign of the charge carriers. If $\partial\alpha/\partial T > 0$, then the carriers are electrons, while if $\partial\alpha/\partial T < 0$, they are holes. As the number of carriers decreases, the value of $|\partial\alpha/\partial T|$ increases, and vice versa.

On the basis of these considerations it can be stated that for $T > T_{\alpha_{\max}} \approx 190$ K the thermopower is due to holes, while for $T < T_{\alpha_{\max}}$ it is due to electrons.

As is seen in Fig. 4, the temperature dependences of $\rho(1/T)$ and $\alpha(1/T)$ have an activational character from room temperature down to $T \approx 190$ K at least. Then, according to Ref. 37,

$$\rho = \text{const} \cdot \exp(\Delta E_p / kT), \tag{1}$$

where ΔE_p is the activation energy of the conductivity.

The thermopower can be described using the expression characteristic for semiconductors:[37]

$$\alpha = \frac{k}{e}\left(\frac{\Delta E_s}{kT} + A_p\right), \tag{2}$$

where ΔE_s is the activation energy of the thermopower, and A_p is a coefficient characterizing the charge carrier scattering process.

It is seen in Fig. 4 that in the temperature region $T \approx 220-260$ K the $\ln\rho(1/T)$ and $\alpha(1/T)$ curves each have a kink, but at temperatures ~20 K apart. We identify the temperature ≈230 K of the kink on the $\ln\rho(1/T)$ curve as the ordering temperature T_{co}, and the temperature ≈250 K of the kink on the $\alpha(1/T)$ curve as the point T_n of a structural phase transition. In the majority of neutron studies known to us the structural transition either is not mentioned at all or else it coincides with the charge-ordering temperature.

At the kink points T_{co} and T_n the activation energy undergoes a jump; at atmospheric pressure ΔE_p increases from $\Delta E_{p1} = 112$ MeV to $\Delta E_{p1} = 212.5$ MeV, while ΔE_s increases from $\Delta E_{s1} = 16$ MeV to $\Delta E_{s2} = 25$ MeV.

The different activation energies for the conductivity (ΔE_p) and thermopower (ΔE_s) indicate that in this region of temperatures hopping conductivity via localized states is realized, with the activation energy of a hop $w = \Delta E_p - \Delta E_s$. In the region $T > T_n$ it has the value $w_1 \approx 100$ MeV, while in the region $T < T_{co}$ its value is $w_2 \approx 190$ MeV.

It is interesting to note the coincidence of the value of these gap $\Delta E_{p1} \approx 112$ MeV (=1300 K) obtained by the authors from measurements of ρ in the temperature range 225–300 K and the value of the energy gap $\Delta E = 1380$ K obtained from measurements of the recovery time of the resistivity of a sample brought from the insulator to the metallic state by a magnetic field, after the field is switched off.[8] It is possible that relaxation of the metastable metallic state occurs via the same local centers.

At a temperature $T < 190$ K, which corresponds to the maximum of the thermopower α, the temperature dependence of the resistivity obeys the Mott law (Fig. 6):

$$\rho \sim \exp(B/T^{1/4}), \tag{3}$$

where $B = \text{const}$.

This dependence is indicative of hopping conductivity via localized states, with a variable hopping length.

On the basis of the general argument that the value of the exchange coupling increases with increasing pressure,[34] one expects that the activation energy should decrease with increasing pressure. However, the large scatter of the values of ΔE_p and ΔE_s obtained under pressure do not permit us to determine their pressure dependence. It is possible that the scatter is due to an incomplete structural transition in the sample in the heating–cooling cycle that unavoidably accompanies changes in the chamber pressure.

The sharp increase of $|\alpha|$ and ρ in $Pr_{0.67}Ca_{0.33}MnO_3$ with decreasing temperature below ~120 K correlates with the results of experiments on the irradiation of $Pr_{0.67}Ca_{0.33}MnO_3$ by muons, when the rate of relaxation increases sharply as the Curie point T_C is approached.[26] The general cause of these effects is probably scattering of carriers on ferromagnetic fluctuations, which grow as T_C is approached; such fluctuations arises both from FM clusters and from the FM interactions between layers of an antiferromagnet with a structure of the pseudo-CE type.

The CO state is characteristic for those manganates in which the average ion radius $\langle r_A \rangle$ is small (Pr–Ca, La–Ca), so that because of the large canting of the MnO_6 octahedra and the decrease of the exchange coupling between Mn^{3+} ions the width W of the one-electron band is rather small, which stabilizes the CO and AFM structure of the manganate.

The effect of pressure and magnetic field on the temperature T_{co} can be understood qualitatively on the basis of the double-exchange theory:

$$b = b_0 \cos(\Delta\Theta/2), \tag{4}$$

where b is the effective integral of the transition of an e_g electron to a neighboring ion, b_0 is the transition integral without spin scattering, and $\Delta\Theta$ is the relative angle between the t_{2g} spins of neighboring ions.

Pressure increases the width W of the band of carriers, their mobility, and thereby the value of b_0 (Ref. 34). A magnetic field H decreases $\Delta\Theta$, aligning all the spins along the field. Both factors increase the integral of the transition between b ions and makes it harder to establish charge ordering. Our value $\partial \ln T_{co}/\partial P = -3.3\times10^{-3}$ kbar^{-1} is some-

what greater than the value for Pr–Ca samples with $x=0.35$ ($\approx 2\times 10^{-3}$ kbar^{-1} from Ref. 14). With increasing x the derivative $\partial \ln T_{co}/\partial P$ and $\partial \ln T_{co}/\partial H$ increase, but their ratio remains constant, in the range 6–9 kG/kbar.[14] The relation between the pressure and magnetic field is also maintained on passage through the other characteristic temperatures. For example, from the P and H dependence of the metal-insulator transition temperature T_{MI} in $Pr_{0.7}Ca_{0.3}MnO_3$ the following relationship has been established: a pressure of 1 kbar is equivalent to a field of ~ 6 kG.[14] Interestingly, in Ref. 38 a similar relationship was found in a study of the effect of pressure and magnetic field on the transition temperature T_{co} to the charge-ordered state of a ferromagnetic insulator in the manganate $La_{0.9}Sr_{0.1}MnO_3$: a pressure of 1 kbar was equivalent to 6.2 kG. In both cases the temperatures T_{MI} and T_{co} increased with increasing P and H, indicating that both of these factors tend to increase the delocalization of the carriers.

The decrease of T_C with increasing pressure in our experiments is confirmed by measurements of the magnetic susceptibility χ of the manganate $Pr_{0.7}Ca_{2.3}MnO_3$ as a function of T and H in Ref. 29. The appearance of the second maximum on the $\chi'(H)$ curve at $T=T_C\approx 120$ K and $H>0.2$ T and its shift to higher temperatures with increasing H complicate the picture of the transition of the sample to the FM state. Ferromagnetic clusters appear when the sample is still in the paramagnetic phase[27,29] and are probably due to local dynamic JT distortions of the lattice. The establishment of the CO state through growth of the local stresses[23,29] should facilitate cluster formation. However, because of the disorientation of the spins, they do not contribute to the magnetic moment of the sample. A spontaneous magnetic moment appears only at $T=T_C$,[27,29] due to correlation of the spins of individual clusters.[23] Pressure will prevent the interaction of clusters, causing a lowering of the temperature T_C. At a temperature T_C' (the second maximum on the $\chi'(H)$ curve)[29] the creation of FM clusters in the magnetic field occurs. With increasing field the temperature T_C' increases at a rate of 0.6 K/kG, which corresponds to ~ 3.6 K/kbar if one uses the coefficient found above for the equivalence between pressure and magnetic field. The value obtained for the pressure-induced shift of the metal-insulator transition temperature in $Pr_{0.67}Ca_{0.33}MnO_3$, $\partial T_{MI}/\partial P=2.8$ K/kbar, is close to this value. We assume that at the temperature T_{MI} a long-range spin order is established between the FM clusters, the number of which satisfies the percolation condition, and an insulator-metal transition occurs on account of the double exchange.

According to our estimates, the shift of the temperature T_{MI} under hydrostatic pressure in Ref. 13 had a value close to 4.6 K/kbar. However, as was mentioned in Ref. 13, an analogous shift of T_{MI} can occur not only under external pressure but also under internal (chemical) pressure. The underlying basis for the correspondence between the two factors is the increase in the hopping integral b_0 in Eq. (4) as a result of a decrease in the angle of deviation of the Mn–O–Mn line from 180°. External pressure does this by decreasing the disparity between the ionic radii of the elements and causing a closer packing of the oxygen ions around the ion at site A, while internal pressure works by increasing the tolerance factor. Based on a study[13] of manganates of the composition $A_{0.7}A'_{0.3}MnO_3$, the coefficient of equivalence between the two pressures was calculated (3×10^{-4} Å/kbar), and it was found that T_{MI} has a strongly nonlinear dependence on $\langle r_A\rangle$. With increasing $\langle r_A\rangle$ the temperature T_{MI} increases, going to saturation (Fig. 4 in Ref. 13), and the derivative $\partial T_{MI}/\partial\langle r_A\rangle$ decreases. This also presupposes a decrease of $\partial T_{MI}/\partial P$ with increasing $\langle r_A\rangle$ and/or pressure. For example, for $La_{0.7}Ca_{0.3}MnO_3$ ($T_{MI}=255$ K; $\langle r_A\rangle=1.205$ Å) the value $\partial T_{MI}/\partial P=1.5$ K/kbar is obtained,[13] and for $La_{0.7}Sr_{0.3}MnO_3$ ($T_{MI}=364.4$ K, $\langle r_A\rangle=1.244$ Å) the value $\partial T_{MI}/\partial P=0.5$ K/kbar.[14] The mean radius $\langle r_A\rangle=1.18$ Å of $Pr_{0.7}Ca_{0.3}MnO_3$ is too small for the metal-insulator transition to occur without external assistance. The transition begins at a pressure of 5 kbar ($T_{MI}\approx 50$ K). The $T_{MI}(P)$ curve is clearly nonlinear and $\partial T_{MI}/\partial P$ actually decreases with increasing pressure.[14]

The interrelation between the external pressure and $\langle r_A\rangle$ in $Pr_{0.7}Ca_{0.3}MnO_3$ can also be traced in the thermopower data. In Ref. 30 the change in $\langle r_A\rangle$ was achieved by a partial substitution of the Ca^{2+} ions in the compound $Pr_{0.7}Ca_{0.3}MnO_3$ by Sr^{2+} ions. Despite a certain fundamental difference from our data under pressure at low temperatures (α changes sign for us and $\alpha\approx 0$ in Ref. 30), there are also some common traits: 1) $|\alpha|$ decreases with increasing pressure and increasing $\langle r_A\rangle$; 2) the temperature of the maximum of α increases; 3) features which are probably due to a structural transition are observed at $T\approx 250$ K; 4) α decreases and changes sign at $T=290$ K with increasing P and $\langle r_A\rangle$.

The behavior of the thermopower α with pressure at $T=290$ K is interesting. At atmospheric pressure the thermopower is positive and equal to 1.6 μV/K. With increasing pressure, however, α_{290} changes sign to negative at $P\approx 3.7$ kbar and increases almost linearly at a rate of $\partial\alpha_{290}/\partial P=-0.46$ μV/(K·kbar). Such behavior of α_{290}, but as a function of the hole concentration x, has been observed for a large class of manganates: Pr–Ca, La–Ca, and La-Sr,[30] in autodoped $LaMnO_3$ (Ref. 39), and in HTSC cuprates, in which the sign change of α_{290} occurs at $x\approx 0.16$.[40] In Ref. 30 the dependence of α_{290} on the mean radius $\langle r_A\rangle$ was traced; the sign of α_{290} changes at $\langle r_A\rangle\approx 1.02$ Å. The underlying cause of this dependence of α_{290} on P, x, and $\langle r_A\rangle$ is probably the overlap of the Mn–O orbitals in the manganates and of the Cu–O orbitals in HTSC cuprates. The same effect is achieved by different influences.

The magnetic and transport characteristics of the manganates and, in particular, $Pr_{0.67}Ca_{0.33}MnO_3$ can to a large degree be due to the presence of spin and charge disorder in them. These factors have been used[11] to explain the large value of the linear term γT ($\gamma\approx 30$ mJ/mole·K) in the expression for the heat capacity of $Pr_{0.7}Ca_{0.3}MnO_3$. The formation of a state resembling a spin glass has been used[23,25] to explain the small value of the total magnetic moment per Mn ion ($\mu_{\text{tot}}\approx 2.36\mu_B$ instead of the expected $3.7\mu_B$). It was assumed in Ref. 29 that this same cause is responsible for the dependence of the maximum of the magnetic susceptibility χ' and temperature T_C on the modulation frequency.

When the temperature is decreased below T_N in $Pr_{0.67}Ca_{0.3}MnO_3$, in addition to the spin and charge disorder there is phase separation into a charge-ordered CE-type an-

tiferromagnetic insulator phase CO and a weak-ferromagnetic ''spin-glass-like'' phase ROO.[27] When the temperature is further lowered below T_C the degree of localization of the carriers and the orbital ordering in the CO and ROO phases behave in opposite ways; this, in the opinion of the authors, gives rise to significant stress at the boundary of the two phases. This stress is the source of the existence and stability of two phases of mesoscopic dimensions (500–2000 Å). At the microscopic level the formation of FM clusters ~ 5 Å in size occurs already at temperatures $T > T_{co}$. For $T < T_N$, with the formation of the AF order in the CO phase, the formation of FM clusters occurs exclusively in the ROO phase. Here with decreasing temperature the cluster size increases to 15 Å, and the neutron scattering becomes more and more elastic; this is strongly reminiscent of the spin dynamics in a spin glass.

In Ref. 26 it was concluded on the basis of calorimetric and neutron measurements that the degree of magnetic order in $Pr_{0.67}Ca_{0.33}MnO_3$ in the low-temperature region is low. There are regions where neither FM nor AFM order are present, i.e., regions close to a spin glass. The FM and AFM regions do not have clear boundaries and are interpenetrating. Their energies are quasi-degenerate and local transitions between them can occur.

A large role in $Pr_{0.67}Ca_{0.33}MnO_3$ is probably played by the interaction of the magnetic moments of the Mn^{3+} and Pr^{3+} ions. On the basis of measurements of the heat capacity and magnetothermal effects at high magnetic fields it was concluded in Ref. 12 that the magnetism of the Pr^{3+} ions with $T_C = 60$ K makes the canted AF state, which resembles a spin glass, unstable with respect to the FM phase at $T < 60$ K and stabilizes the metastable FMM phase at $T < 60$ K.

CONCLUSIONS

1. We have studied the behavior of the resistivity ρ, thermopower α, and magnetic susceptibility χ of the manganate $Pr_{0.67}Ca_{0.33}MnO_3$ in the temperature range 80–300 K under hydrostatic pressure up to 13 kbar. At pressures $P \geqslant 8.8$ kbar a metal–insulator transition is observed.

2. On the basis of these measurements we have determined the pressure coefficients of the phase transition temperatures:

—the temperature of a possible structural transition $T_n \approx 250$ K ($\partial T_n/\partial P = -1.7$ K/kbar);

—the charge-ordering temperature $T_{co} \approx 230$ K ($\partial T_{co}/\partial P = -0.8$ K/kbar);

—The Néel temperature $T_N \approx 140$ K ($\partial T_N/\partial P = -1.1$ K/kbar);

—The temperature at which a spontaneous FM moment appears, $T_C \approx 100$ K ($\partial T_C/\partial P = -1.2$ K/kbar);

—The temperature of the metal-insulator transition T_{MI} ($\partial T_{MI}/\partial P = 2.8$ K/kbar);

2. A change of sign of the thermopower α is observed at $T_{01} \approx 110$ K and $T_{02} \approx 290$ K. These temperatures are affected differently by pressure: $\partial T_{01}/\partial P = 2.3$ K/kbar, while $\partial T_{02}/\partial P = -2.8$ K/kbar.

3. As the temperature approaches T_C the thermopower α reaches large negative values; this correlates with a sharp increase in the resistivity in this temperature region.

4. At temperatures $T > 180$ K the resistivity ρ and thermopower α have an activational character. For $T < 180$ K the resistivity is due to variable-length hopping.

The authors thank V. A. Ventsel' and A. V. Rudnev for help in this study.

This study was was supported by Grant No. 03-02-16237 from the Russian Foundation for Basic Research and by a grant from INTAS (Project No. 99-1136).

*E-mail: itskev@ns.hppi.troitsk.ru

[1] R. D. Shannon, Acta Crystallogr., Sect. A: Cryst. Phys., Diffr., Theor. Gen. Crystallogr. **32**, 751 (1976).
[2] C. Martin, A. Maignan, M. Hervieu, and B. Raveau, Phys. Rev. B **60**, 12191 (1999).
[3] A. Urushibara, Y. Moritomo, T. Arima, A. Asamitsu, G. Kido, and Y. Tokura, Phys. Rev. B **51**, 14103 (1995).
[4] A. P. Ramirez, S.-W. Cheong, and P. Schiffer, J. Appl. Phys. **81**, 5337 (1997).
[5] S. Yamada, T.-H. Arima, H. Ikeda, and K. Takita, J. Phys. Soc. Jpn. **69**, 1278 (2000).
[6] Y. Tomioka, A. Asamitsu, H. Kuwahara, Y. Moritomo, and Y. Tokura, Phys. Rev. B **53**, R1689 (1996).
[7] S. Katano, J. A. Fernandez-Baca, and Y. Yamada, Physica B **276–278**, 786 (2000).
[8] A. Anane, J.-P. Renard, L. Reversat, C. Dupas, P. Veillet, M. Viret, L. Pinsard, and A. Revcolevschi, Phys. Rev. B **59**, 77 (1999).
[9] V. Hardy, A. Wahl, C. Martin, and Ch. Simon, Phys. Rev. B **63**, 224403 (2001); V. Hardy, A. Wahl, and C. Martin, *ibid.* **64**, 064402 (2001).
[10] M. R. Lees, J. Barratt, G. Balakrishnan, D. McK. Paul, and M. Yethiraj, Phys. Rev. B **52**, R14303 (1995).
[11] V. N. Smolyaninova, A. Bismas, X. Zhang, K. H. Kim, B.-G. Kim, S.-W. Cheong, and R. L. Greene, Phys. Rev. B **62**, R6093 (2000).
[12] M. Roy, J. F. Mitchell, A. P. Ramirez, and P. Schiffer, Phys. Rev. B **62**, 13876 (2000).
[13] H. Y. Hwang, T. T. M. Palstra, S.-W. Cheong, and B. Batlogg, Phys. Rev. B **52**, 15046 (1995).
[14] Y. Moritomo, A. Asamitsu, and Y. Tokura, Phys. Rev. B **51**, 16491 (1995); Y. Moritomo, H. Kuwahara, Y. Tomioka, and Y. Tokura, *ibid.* **55**, 7549 (1997).
[15] H. Yoshizawa, R. Kajmoto, H. Kawano, Y. Tomioka, and Y. Tokura, Phys. Rev. B **55**, 2729 (1997).
[16] A. Asamitsu, Y. Tomioka, H. Kuwahara, and Y. Tokura, Nature (London) **388**, 50 (1997).
[17] M. Fiebig, K. Miyano, Y. Tomioka, and Y. Tokura, Science **280**, 1925 (1998).
[18] K. Miyano, T. Tanaka, Y. Tomioka, and Y. Tokura, Phys. Rev. Lett. **78**, 14257 (1997).
[19] V. Kiryukhin, D. Casa, J. P. Hill, B. Keimer, A. Vigliante, Y. Tomioka, and Y. Tokura, Nature **386**, 813 (1997).
[20] M. Hervieu, A. Barnabe, C. Martin, A. Maignan, and B. Raveau, Phys. Rev. B **60**, R726 (1999).
[21] E. Pollert, S. Krupicka, and E. Kuzmicova, J. Phys. Chem. Solids **43**, 1137 (1982).
[22] Z. Jirak, S. Krupicka, Z. Simsa, M. Dlouha, and S. Vratislav, J. Magn. Magn. Mater. **53**, 153 (1985).
[23] D. E. Cox, P. G. Radaelli, M. Marezio, and S.-W. Cheong, Phys. Rev. B **57**, 3305 (1998).
[24] C. S. Nelson, M. V. Zimmerman, Y. J. Kim, J. P. Hill, D. Gibbs, V. Kiryukhin, T. Y. Koo, S.-W. Cheong, D. Casa, B. Keimer, Y. Tomioka, Y. Tokura, T. Gog, and C. T. Venkataraman, Phys. Rev. B **64**, 174405 (2001).
[25] H. Yoshizawa, H. Kawano, Y. Tomioka, and Y. Tokura, Phys. Rev. B **52**, R13145 (1995).
[26] C. Frontera, J. L. Garcia-Munoz, A. Llobet, M. Respaud, J. M. Broto, J. S. Lord, and A. Planes, Phys. Rev. B **62**, 3381 (2000).
[27] P. G. Radaelli, G. Iannone, D. E. Cox, M. Marezio, H. Y. Hwang, and S.-W. Cheong, Physica B **241–243**, 295 (1998); P. G. Radaelli, R. M. Ibberson, D. N. Argyriou, H. Casalta, K. H. Andersen, and J. F. Mitchell, Phys. Rev. B **63**, 172419 (2001).
[28] T. Asaka, S. Yamada, S. Tsutsumi, C. Tsuruta, K. Kimoto, T. Arima, and Y. Matsui, Phys. Rev. Lett. **88**, 097201 (2002).
[29] I. G. Deac, J. F. Mitchell, and P. Schiffer, Phys. Rev. B **63**, 172408 (2001).

[30] J. Hejtmanek, Z. Jirak, D. Sedmidubsky, A. Maignan, Ch. Simon, V. Caignaert, C. Martin, and B. Raveau, Phys. Rev. B **54**, 11947 (1996).
[31] J. M. De Teresa, M. R. Ibarra, C. Marquina, P. A. Algarabel, and S. Oserroff, Phys. Rev. B **54**, R12689 (1996); J. M. De Teresa, M. R. Ibarra, P. A. Algarabel, C. Ritter, C. Marquina, J. Blasko, J. Garcia, A. del Moral, and Z. Arnold, Nature **386**, 256 (1997).
[32] M. Yu. Kagan and K. I. Kugel', Usp. Fiz. Nauk **171**, 577 (2001).
[33] A. M. Balbashov, S. G. Karabashev, Ya. M. Mukovskii, and S. A. Zverkov, J. Cryst. Growth **167**, 365 (1996).
[34] E. S. Itskevich, V. F. Kraidenov, A. E. Petrova, V. A. Ventcel', and A. V. Rudnev, Fiz. Nizk. Temp. **29**, 39 (2003) [Low Temp. Phys. **29**, 30 (2003)].
[35] V. F. Kraĭdenov, and E. S. Itskevich, Fiz. Nizk. Temp. **22**, 1028 (1996) [Low Temp. Phys. **22**, 784 (1996)]; E. S. Itskevich, V. F. Kraĭdenov, and I. G. Kuzemskaya, Zh. Éksp. Teor. Fiz. **118**, 647 (2000) [JETP **91**, 562 (2000)].
[36] J. B. Goodenough and J. S. Zhou, Phys. Rev. B **49**, 4251 (1994); J. S. Zhou and J. B. Goodenough, *ibid.* **51**, 3104 (1995).
[37] N. F. Mott and E. A. Davis, *Electronic Processes in Non-Crystalline Materials*, Clarendon Press, Oxford (1971), Mir, Moscow (1982).
[38] R. Senis, V. Laykhin, B. Martinez, J. Fontcuberta, X. Obradors, A. A. Arsenov, and Y. M. Mukovskii, Phys. Rev. B **57**, 14680 (1998).
[39] R. Mahendiran, S. K. Tiwary, A. K. Raychaudhuri, R. Mahesh, and C. N. R. Rao, Phys. Rev. B **54**, R9604 (1996).
[40] S. D. Obertelli, J. R. Cooper, and J. L. Tallon, Phys. Rev. B **46**, 14928 (1992).

Translated by Steve Torstveit

ELECTRONIC PROPERTIES OF METALS AND ALLOYS

Spin-polarized electron tunneling between charge-density-wave metals

T. Ekino

Hiroshima University, Faculty of Integrated Arts and Sciences, 1-7-1 Kagamiyama, Higashi-Hiroshima, 739-8521, Japan

A. M. Gabovich and A. I. Voitenko

*Crystal Physics Department, Institute of Physics, National Academy of Sciences, 46 Prospekt Nauki, Kiev, 03028 Ukraine**

(Submitted April 16, 2004)
Fiz. Nizk. Temp. **31**, 77–93 (January 2005)

For junctions between metals partially gapped by charge density waves (CDWs), the quasiparticle tunnel currents $J(V)$ and conductances $G(V)$ in external magnetic fields H are calculated as functions of H, the bias voltage V, temperature T, the dielectric gaps Σ, and the gapped portions μ of the Fermi surface (FS). The paramagnetic effect of H is taken into account, whereas orbital effects are neglected. General expressions are obtained for different CDW metal electrodes. Analytical formulas are obtained for $T=0$. Explicit numerical calculations are carried out for symmetrical junctions. The results are substantially unlike those for junctions between superconductors. It is shown that due to the interplay between quasiparticles from nested and non-nested FS sections the junction properties involve features appropriate to both symmetrical and asymmetrical setups. In particular, for $H=0$ discontinuities at $eV=\pm 2\Sigma$ and square-root singularities at $eV=\pm\Sigma$ should coexist. Here e is the elementary charge. For $H\neq 0$ the former remain intact, while the latter split. It is suggested to use the splitting as a verification of the CDW nature of the pseudogap in high-T_c superconducting oxides. © *2005 American Institute of Physics.* [DOI: 10.1063/1.1820368]

1. INTRODUCTION

Instabilities of the parent metallic electron spectrum leading to the formation of charge density waves (CDWs)[1–3] are in some sense similar to the superconducting Cooper pairing phenomenon.[4] Namely, although the *coherent* properties of the reconstructed low-temperature (low-T) phases are quite different, the resulting gapping of the Fermi surface (FS) due to many-body correlations is described by the same equations, at least in the weak-coupling limit. Therefore, the so-called semiconducting aspects of both superconductors and excitonic[1,2] or Peierls[3] insulators are analogous. Nevertheless, as has been demonstrated previously,[5] they are by no means identical. It is worth noting that the quasiparticle electron density of states (DOS) of conventional nondegenerate semiconductors, adequately described by the one-body band theory, is nonsingular,[6] contrary to what happens in the models both for superconductors[4] and many-body insulators.[1–3]

In this publication we want to call attention once more to the quasiparticle tunneling between metals partially gapped by CDWs (CDWMs). The expressions for the tunnel current-voltage (I-V) characteristics $J(V)$ in the general case of different CDWM electrodes are obtained, and a number of practically important particular cases are considered in more detail. Their analysis shows that due to the coexistence of gapped and nongapped FS sections, the I-V characteristics of tunnel junctions with CDWMs on both sides of the potential barrier possess some unconventional features. They are analogous to those observed in the setup where one of the electrodes is a normal metal without any electron spectrum distortion and the other one is a partially gapped CDW conductor.[5,7]

If an external magnetic field H is applied, the dual nature of the partially gapped CDWM should result in the Zeeman (spin) splitting of the peaks in the conductance-voltage (G–V) characteristics $G(V)$, which, e.g., in the case of superconductivity are appropriate to S–I–N junctions rather than to the S–I–S ones (compare with Refs. 4, 8–10). In this article we obtain the corresponding expressions for G(V) in a *symmetrical* CDWM-I-CDWM structure and demonstrate the existence of the peak splitting. On this basis, relevant inferences are drawn for recognized CDW materials and high-T_c cuprates, strongly suspected of belonging to this class.[11,12]

2. THEORY

As has long been understood (see review[13]), the I–V characteristics for tunneling between two superconductors in an external magnetic field H, which induces Zeeman splitting of the electronic DOS due to the Pauli paramagnetism of electrons, nevertheless, does not exhibit splitting of the gap-related peaks. The nonexistance of the splitting in S′–I–S junctions is explained by equal shifts in energy of electron subbands possessing the same spin projection value on both sides of the barrier and the conservation of spin direction

while tunneling in the absence of the spin-orbital effect.[14] On the other hand, tunneling across S–I–N junctions reveals such a splitting, because in this situation $G(V)$ is proportional to the superconducting and normal electron DOSs shifted with respect to each other in the magnetic field.[4,8–10]

As concerns the paramagnetic properties, a CDWM described either by the excitonic[1,2] or Peierls[3] models is quite similar[15-18] to an *s*-wave Bardeen-Cooper-Schrieffer (BCS) superconductor.[13,14] This means that for H not exceeding a certain value, mathematically analogous to the Clogston-Chandrasekhar paramagnetic limit,[4] the CDW gap $\Sigma(T)$ may be considered as a BCS-like one, not dependent on H. Such an expectation is supported by experiment. For example, the destructive influence of H on the critical temperature T_d of the structural phase transition was observed to be extremely small at low fields for such different substances with CDWs as the A15 compound V_3Si (Ref. 19; $T_d = 20.15$ K at $H=0$ and is reduced by -0.6 K at $H=156$ kOe) and the quasi-one-dimensional organic metal $Per_2[Au(mnt)_2]$ (Ref. 20) and could not be detected for any other CDW compounds.

On the other hand, in the following analysis we are going to completely ignore the diamagnetic response of the CDWM. The experimental reason for this neglect was cited above. From the theoretical point of view, it may be justified as follows. Due to the different type of long-range order in comparison to that for superconductors, the Meissner effect is absent in excitonic or Peierls insulators,[1,2,11,12] although other interesting coherent phenomena may occur.[21–24] The more conventional orbital effects of the magnetic field should exist, but their influence on the CDW phase is not destructive. On the contrary, according to Refs. 25 and 26, the inevitable paramagnetic effects are augmented by diamagnetic ones, favorable to CDWs due to the reduction of the electron spectrum dimensionality for large H.[4] These considerations are supported by recent experiments[27] for the organic metal α-$(BEDT\text{-}TTF)_2KHg(SCN)_4$, where a series of phase transitions between subphases with different values of the nesting vector $\mathbf{Q}$ was observed. A stabilization of CDWs by the restricted orbital motion in the magnetic field is analogous to the emergence of field-induced spin-density waves (SDWs) in $(TMTSF)_2X$ organic salts.[28] Therefore, this phenomenon, which preserves CDWs, would be helpful for the spin splitting of CDW-driven peaks in $G(V)$, although it might make the interpretation of the spectra more ambiguous.

2.1. CDW metal

2.1.1. Zero magnetic field

The starting point of our approach is the mean-field Hamiltonian of the partially gapped superconducting CDW metal proposed by Bilbro and McMillan.[29] For our current purposes we need a simpler case of a normal CDW metal, which can be obtained from the original model when the superconducting gap is identically zero.[5] According to this model, the FS of the CDWM is split into degenerate (nested, $i=1,2$) and nondegenerate (non-nested, $i=3$) sections. For the former, the bare quasiparticle spectrum branches reckoned from a common Fermi level are linked by the relation

$$\xi_1(\mathbf{p}) = -\xi_2(\mathbf{p}+\mathbf{Q}), \tag{1}$$

where $\mathbf{Q}$ is the CDW vector. Due to the interaction of quasiparticles from different ($i=1,2$) nested FS sections, a many-body correlation (leading to a pairing, which is a close analog of Cooper pairing) appears between them. The CDW pairing can be described by a dielectric order parameter $\tilde{\Sigma}$, and a relevant dielectric gap Σ emerges at both nested sections. If this interaction is mainly of a Coulomb origin[1,2] and the branches $\xi_{1,2}(\mathbf{p})$ represent the electron and hole bands, respectively, the CDW gapping corresponds to the excitonic insulator. Another possibility appears if the degenerate spectrum $\xi_{1,2}(\mathbf{p})$ is quasi-one-dimensional and the quasiparticle interaction is mediated by phonons. Then CDW gapping results in the emergence of a Peierls insulator state.[3] In both CDW cases, the coupling occurs between quasiparticles with oppositely directed spins (singlet pairing). Those alternatives can be considered in the framework of the same approach. The rest of the FS remains undistorted by CDWs and is described by the nondegenerate electron spectrum branch $\xi_3(\mathbf{p})$. The portion of the FS gapped by the CDW instability (partial gapping) is determined by the dielectric-gapping (dielectrization) parameter

$$\mu = N_{d0}(0)/N_0(0), \tag{2}$$

where $N_0(0) = N_{n0}(0) + N_{d0}(0)$ is the total initial (above T_d) electronic DOS on the FS, and $N_{d0}(0)$ and $N_{n0}(0)$ are the relevant DOSs on the degenerate (d) and nondegenerate (n) FS sections, respectively.

In principle, CDWs may be commensurate or incommensurate with the background crystal lattice. In the excitonic insulator model, the Coulomb-induced distortion below the transition temperature T_d is commensurate. Moreover, the phase of the order parameter in excitonic insulators is always pinned,[30,31] and $\tilde{\Sigma}$ is an either positive or negative quantity.[2,11,12,32,33] On the other hand, in Peierls insulators, incommensurate CDWs with the order parameters $\tilde{\Sigma} = \Sigma e^{i\varphi}$ may exhibit a rich dynamics, although in the direct current measurements they are usually pinned with arbitrarily frozen phases φ.[3,23]

In the framework of the approach adopted, the partially gapped nonsuperconducting CDW metal (CDWM) in the absence of an external magnetic field H is described by the following temporal Green's functions $G_{ij}(\omega)$, where $i,j = 1,2,3$ are the subscripts labeling the FS sections (see above):

$$G_{11} = G_{22} \equiv G_d, \tag{3}$$

$$G_{12} = G_{21} \equiv G_c, \tag{4}$$

$$G_{33} \equiv G_n. \tag{5}$$

For all the other ij combinations, $G_{ij}=0$. The function G_c describes the electron-hole pairing. It is "normal" in a conventional sense,[10] since it is not a product of either creation or annihilation operators only, but is, nevertheless, "anomalous" in analogy with the Gor'kov Green's function, because it is proportional to the CDW order parameter $\tilde{\Sigma}$. All technical details of the calculations and explicit expressions for the functions G_d, G_c, and G_n can be found in our previous publications.[5,11,12]

Thus, one sees that in the Bilbro-McMillan model[29] adopted by us here and in accord with the division of the FS into d and n sections, the electron states are of two different kinds, dubbed from here on as n and d states. Nevertheless, it is important to comprehend that whatever the distinctions of the electron spectrum between quasiparticle branches, the whole system has a common chemical potential pinned to that of the metallic n component and disposed inside the dielectric gap Σ inherent to d states. On the other hand, in the model of the doped excitonic insulator, the Fermi level is supposed to be located above or below the gap edge in its nearest neighborhood. Decades ago, a significant enhancement of the superconducting T_c due to the DOS increase in the indicated energy range was expected to happen if such a situation were to be realized.[2,34] Unfortunately, these hopes turned out to be vain, and in all compounds in which superconductivity and CDW gapping have been proved to coexist, the latter is detrimental to the former.[11,12]

Thus in the reconstructed CDW phase below T_d the density of the n states, $N_n(\omega)$, may be considered as that in the absence of CDW gapping. Hereafter, the energy distance from the Fermi level will be denoted as ω. Since the phenomena investigated in this publication are determined only by the states in a narrow shell near the FS, the energy dependence of $N_n(\omega)$ can be neglected, i.e., $N_n(\omega)=N_{n0}(0)$. At the same time, the energy spectrum of the d states involves a dielectric gap below T_d, so that its DOS takes on a superconducting-like appearance[2]

$$N_d(\omega)=N_{d0}(0)\frac{|\omega|\,\theta(|\omega|-\Sigma)}{\sqrt{\omega^2-\Sigma^2}}. \tag{6}$$

As was shown by Frenkel[35,36] (see also extensive accounts in Refs. 9 and 37), the tunnel current J across the biased barrier between metal electrodes is given by the algebraic sum of the forward and backward components. The voltage dependence of J is exponential for large and Ohmic for small V.[37] We shall not extend the subsequent analysis beyond the Ohmic regime, since experimentally relevant dielectric gap energies fall within the range $0.5\ \text{meV}<\Sigma<30$ MeV, whereas the deviations from Ohm's law, indicating a changeover to the Fowler-Nordheim tunneling, emerge when the electron energy gain eV becomes comparable to the conduction band width W for either of electrodes. (Hereafter, $e>0$ is the elementary charge). Actually, in the majority of metals the energy W exceeds 1 eV, so that the existing power-law corrections to conductances $G(V)\equiv dJ/dV$ of the tunnel junctions involving such metals[9] are not important for our purposes. One can imagine, however, a hypothetical situation when more than one conduction band for each metal take part in tunneling, which is plausible for narrow-band metals. In that case additional features in $G(V)$ may appear.[38]

In studying tunnel currents between CDW metals, we shall use a fruitful analogy between the latter and BCS superconductors. The standard way of handling tunneling between superconductors is the tunnel Hamiltonian method.[4,39,40] Then $J(V)$ constitutes an integral of electronic DOSs and the difference between the Fermi distribution functions of the two electrodes.[4,9,41] Insofar as the conductivity in the superconducting state is Ohmic, one can introduce a unique parameter R representing the junction resistance in the normal state. The quantity R is inversely proportional to the averaged square of the tunnel matrix elements.[4,42] The same theoretical approach has been demonstrated to be applicable for tunneling between normal CDW metals and superconductors.[5,11,12]

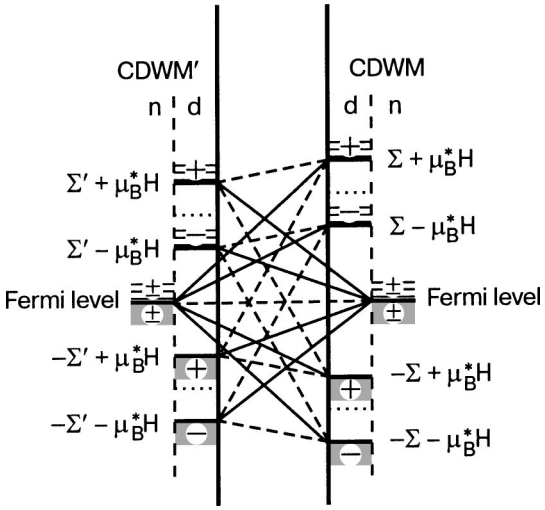

FIG. 1. The energy level scheme in a tunnel junction between partially gapped metals with charge-density waves (CDWs) affected by an external magnetic field H at zero bias voltage. Quasiparticle energies for non-nested (n) and nested (d) Fermi surface (FS) sections are depicted separately on both sides of the insulating barrier. Σ' and Σ are the CDW gaps on the left and on the right, respectively. μ_B^* is the Bohr magneton. "+" and "−" denote spin subbands with projections along H and in the opposite direction. The dashed and solid lines correspond to the possible tunnel transitions without spin flipping, which contribute to the current components that do not depend or do depend on H, respectively.

2.1.2. Nonzero magnetic field

If an external magnetic field H (the spatial z axis is chosen to be aligned with H) is switched on, the d and n states exhibit quite different paramagnetic properties. To describe them properly, it is convenient at first to restrict the respective reasoning to the limiting situation $T=0$. For nonzero H (hereafter we consider values of H less than the paramagnetic limit H_p for CDWM, see below), electrons with the spin projection $s_z=+1/2$ onto H increase their energies by μ_B^*H, while the electrons with the opposite spin direction, $s_z=-1/2$, reduce their energies by the same amount.[43] Here $\mu_B^*=e\hbar/2m^*c$ is the effective Bohr magneton, $\hbar$ is Planck's constant, c is the velocity of light, and m^* is the effective mass of the current carriers. Henceforth, quasiparticles with either spin direction will be labeled by "+" or "−." The quasiparticle level scheme is shown in Fig. 1.

Quasiparticles belonging to the n section, for which the Fermi level segregates occupied and empty states, behave in a conventional manner inherent to normal metals.[43,44] Namely, the states from the "+" spin subband, for $H=0$ coinciding in energy with its "−" counterpart and, therefore, equally populated, shift upwards in energy. As a consequence of the quasiparticle transfer from the "+" to the "−" subband, the former becomes more and more depleted as H increases, whereas the number of occupied states in the "−" subband rises simultaneously by the same amount. This field-induced spin-polarization results in a change of the

chemical potential $\tilde{\mu}$, the latter coinciding with the Fermi energy E_F of the n electrons at $T=0$. For small H the relative corrections to $\tilde{\mu}$ are of the order of $(\mu_B^* H/E_F)^2$. Since we are interested in the effects when $\mu_B^* H$ is, at least, smaller than Σ, the inequality $(\mu_B^* H/E_F)^2 \ll 1$ is valid, and we may neglect the changes to $\tilde{\mu}$ altogether. It should be kept in mind that in itinerant Stoner ferromagnets this is not the case, and $\tilde{\mu}$ is altered conspicuously by the respective spin polarizations[44] (see also an account of concomitant phenomena in Refs. 45 and 46).

Thus the electronic DOS and the Fermi distribution function in the phenomenological expressions for the tunnel current are not affected, in a first approximation, by magnetic fields which are of the order of the energy parameters reflecting many-body gapping of the parent electron spectrum.[4]

The paramagnetic splitting of quasiparticle states from the gapped FS sections can be examined analogously to that for superconductors.[13,14] The reason for the similarity is due to the fact that both CDW (electron-hole) and Cooper pairs are spin-singlet and therefore are prone to the destructive action of the Zeeman splitting.[15–18,47,48] As a result, the quasiparticles of the gapped "+" and "−" subbands shift in opposite directions in energy for $H \neq 0$. All spin-flip processes leading to the smearing of the ideal splitting are ignored hereafter, because we are interested in a qualitative picture only.

Once formed from the praphase, the electron system of the partially gapped CDWM is stable against the influence of magnetic fields in the range defined below, the chemical potential $\tilde{\mu}$ being pinned at the original Fermi level.

When T is finite, the Fermi distribution factors are no longer steplike functions and the thermally excited electronlike and holelike quasiparticles appear above and below the gap Σ, respectively. At the same time, the chemical potential $\tilde{\mu}$ decreases with T, the relative correction being of the order $(k_B T/E_F)^2$ (Ref. 4). Here k_B is Boltzmann's constant.

In what follows, we shall describe tunneling in a magnetic field $H \neq 0$ with the help of the Green's functions G_d, G_c, and G_n mentioned above. The only modification, in comparison to the expressions of Refs. 5, 11, and 12, is that now the number of Green's functions is doubled: six relevant H-dependent functions G_{ds}, G_{cs}, and G_{ns} are denoted by an extra subscript $s=\pm$. They are functions of the relevant variables $\omega \mp \mu_B^* H$, the signs being inverse to those of s.

2.1.3. Paramagnetic limit for CDWMs

As has been indicated above, there exists Pauli limitation to CDW pairing similar to the Clogston–Chandrasekhar limit[47,48] for superconductors. Since the Meissner orbital effect is absent in excitonic or Peierls insulators,[1,2,12] the paramagnetic effect manifests itself here just as it is. The evaluation of the paramagnetic limit H_p for CDWMs is methodologically the same as in the case of BCS superconductors.[4] Specifically, one should compare the free energy of the partially gapped phase δF_{CDWM} with that of the paramagnetic state in the presence of the magnetic field δF_p. Moreover, we should take into account that the paramagnetic CDWM phase (the analog of the Sarma state in superconductors) is energetically unfavorable.[49]

Since the gap $\Sigma(T)$ appears only on the d (nested) FS sections, we obtain

$$(\mu_B^* H_p)^2 = \frac{\mu}{2}\Sigma_0^2, \tag{7}$$

where $\Sigma_0 = \Sigma(T=0)$, so that

$$H_p = \frac{\Sigma_0}{\mu_B^*}\sqrt{\frac{\mu}{2}}. \tag{8}$$

The reduction of the actual H_p in comparison to the limiting value of the complete gapping ($\mu=1$) should be allowed for when comparatively analyzing orbital and spin effects in CDW substances. In particular, one should mention the organic substances α-$(ET)_2MHg(SCN)_4$ (M=K, Tl, Rb, etc.).[18,50–52]

2.2. Current–voltage characterictics

General expressions for quasiparticle currents across tunnel junctions between dissimilar CDWMs (a CDWM′–I–CDWM junction) are given in Appendix A. But the main features of the investigated phenomena are appropriate also to a simpler case of symmetrical junctions with identical CDWM electrodes. In the Bilbro-McMillan model[29] this means equality of the parameters $\tilde{\Sigma}$ and μ. At the same time, the I–V and G–V characteristics become much less cumbersome. Indeed, the singularity positions, depending on the CDWM′ and CDWM gap magnitudes, merge in the symmetrical case, and certain pre-integral factors become equal.

But in making use of the emerging simplifying symmetry one should be very careful. For example, consider the pair J_{cn+} and J_{nc-}. It is easy to ascertain from generic equations (A3) or by analyzing the translation-containing symmetry properties (A17) and (A18) of the current components, that $J_{cn+}(eV)+J_{nc-}(eV)=0$. If we calculate the overall charge transfer regardless of the spin projection, the pairs of components like J_{cn+} and J_{nc-} may be neglected from the outset. However, it is a spin-splitting analysis. A premature mutual cancellation of the terms J_{cn+} and J_{nc-} would result in misleading results for each of the "+" and "−" components. Therefore, the best way to automatically avoid such traps is to add up the components with a certain s separately before making the final comparison between $J_+(V)$ and $J_-(V)$.

Nevertheless, for symmetrical CDWM–I–CDWM junctions, we can exclude the $cd\pm$ and $dc\pm$ components from consideration, since $J_{cds}(eV) = -J_{dcs}(eV)$ for each s.

Thus a complete set of components of the quasiparticle tunnel current through a symmetrical CDWM–I–CDWM junction is as follows:

$$J_{dd\pm} = \frac{\mu^2}{4eR}\int_{-\infty}^{\infty} d\omega K|\omega_\mp|f(\omega_\mp,\Sigma)|\omega_\mp - eV| \times f(\omega_\mp - eV,\Sigma) \tag{9}$$

$$J_{cc\pm} = \frac{(\mu\Sigma)^2}{4eR}\int_{-\infty}^{\infty} d\omega K \,\mathrm{sgn}(\omega_\mp) f(\omega_\mp,\Sigma) \times \mathrm{sgn}(\omega_\mp - eV) f(\omega_\mp - eV,\Sigma), \tag{10}$$

$$J_{nn\pm}=\frac{(1-\mu)^2V}{2R}, \tag{11}$$

$$J_{dn\pm}=\frac{\mu(1-\mu)}{4eR}\int_{-\infty}^{\infty}d\omega K|\omega_{\pm}|f(\omega_{\mp},\Sigma), \tag{12}$$

$$J_{nd\pm}=\frac{\mu(1-\mu)}{4eR}\int_{-\infty}^{\infty}d\omega K|\omega_{\mp}-eV|f(\omega_{\mp}-eV,\Sigma), \tag{13}$$

$$J_{cn\pm}=\frac{\mu(1-\mu)\Sigma}{4eR}\int_{-\infty}^{\infty}d\omega K\,\mathrm{sgn}(\omega_{\mp})f(\omega_{\mp},\Sigma), \tag{14}$$

$$J_{nc\pm}=\frac{\mu(1-\mu)\Sigma}{4eR}\int_{-\infty}^{\infty}d\omega K\,\mathrm{sgn}(\omega_{\mp}-eV)\times f(\omega_{\mp}-eV,\Sigma), \tag{15}$$

where the factor $K=K(\omega,eV)$, generated by the Fermi distributions of current carriers in the two electrodes, and the tunnel resistance R are determined by Eqs. (A5) and (A4), respectively.

For $T=0$, all the current components except the trivial Ohmic term $J_{nn\pm}$ can be expressed in terms of elliptic integrals. The relevant expressions are given in Appendix B. For $T\neq 0$, numerical calculations were made (see the next Section).

3. CALCULATIONS

The representative quantities of the setup under investigation (a symmetrical CDWM–I–CDWM junction in a magnetic field) are as follows: the critical temperature of the CDW phase transition T_d or, equivalently, the zero-temperature dielectric gap $\Sigma_0=(\pi/\gamma)T_d$, and the gapping parameter μ [Eq. (2)] in either electrode, the junction resistance R [Eq. (A4)], the temperature T, and the external magnetic field H. Here $\gamma=1.78\ldots$ is the Euler constant. Hereafter, we use the dimensionless parameters $t=k_BT/\Sigma_0$ and $h=\mu_B^*H/\Sigma_0$.

3.1. Conductance–voltage characteristics

It is well known that the differential tunnel G–V characteristics $dJ(V)/dV$ are much more informative than the original I–V characteristics $J(V)$, with the former acting as an amplifier of the gap-driven peculiarities.[9] In particular, the G–V characteristics give direct information about the energy dependence of the electronic DOS, renormalized due to Cooper[4,8,9,53] or CDW[5,54] pairings for junctions between ''normal'' electrodes and those having a ''gapped'' electron spectrum. Thus, for brevity, we shall confine ourselves below to the analysis of tunnel G-V characteristics and introduce dimensionless spin-dependent conductance components

$$g_{ijs}=RdJ_{ijs}/dV. \tag{16}$$

The G–V characteristics for a symmetrical CDWM–I–CDWM tunnel junction are shown in Fig. 2a for the cases where the external magnetic field H is absent or present. For the sake of definiteness, we shall restrict the numerical calculations in this Section to the case $\varphi=0$. The main properties of the overall conductance versus voltage dependence and its splitting in the magnetic field survive for arbitrary

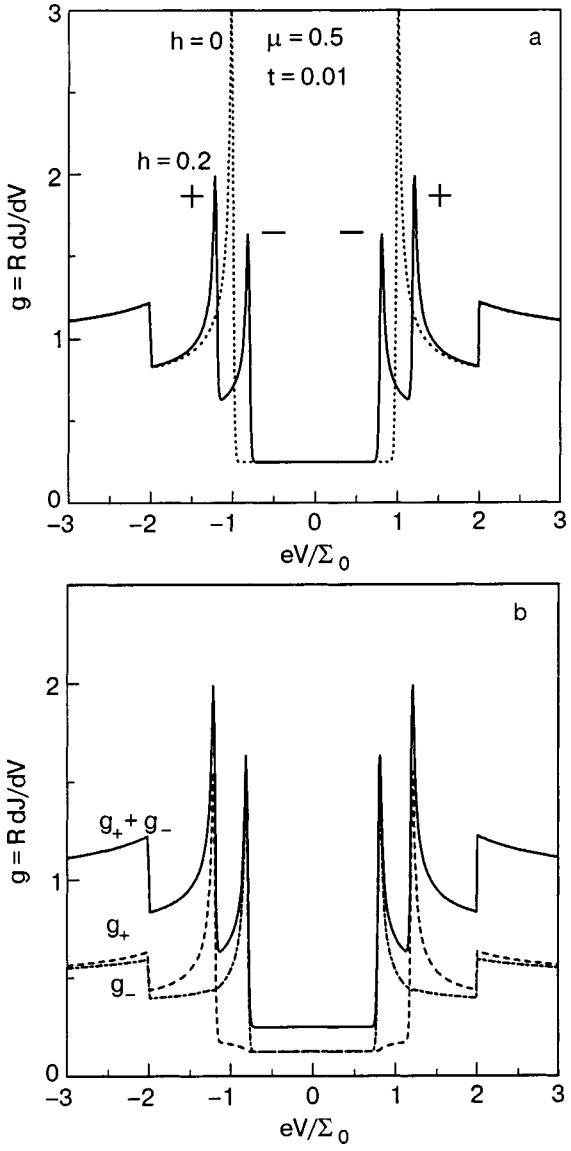

FIG. 2. The dimensionless conductance $g=RdJ/dV$ of the symmetrical tunnel junction between similar CDW metals is shown as a function of the dimensionless bias voltage eV/Σ_0. Here R is a tunnel junction resistance in the undistorted state above the critical temperature T_d of the CDW transition, $\Sigma_0=\pi T_d/\gamma$ is the CDW gap at $T=0$, J is the quasiparticle current, e is the elementary charge, $\gamma=1.78\ldots$ is the Euler constant, T is the temperature, $t=k_BT/\Sigma_0$ is the dimensionless temperature, k_B is Boltzmann's constant, $h=\mu_B^*H/\Sigma_0$, $\mu=N_{d0}(0)/N_0(0)$, $N_0(0)=N_{n0}(0)+N_{d0}(0)$, $N_{d0}(0)$ and $N_{n0}(0)$ are the initial (above T_d) electronic densities of states on the d and n FS sections, respectively. The signs + and − indicate a predominant spin polarization of the peaks. Panel (b) shows a decomposition of the total conductance g, displayed in panel (a), into two summands g_s, each comprising contributions of current carriers with the corresponding spin polarization $s=\pm$.

(see a discussion in Appendix C). One can readily see that each square-root singularity from the positive or negative voltage branch is split into two peaks, whereas the steplike peculiarities remain unsplit. Moreover, the conductance in each split peak has a predominant (not unique) polarization indicated by a + or − sign. Figure 2b illustrates a decomposition of the resulting G–V characteristic for $H\neq 0$ into two components with different spin polarization of current carriers. One also sees a novel remarkable feature, namely, the peaks of the ''+'' component move apart in the magnetic field, whereas their ''−'' counterparts converge. Such behav-

ior differs drastically from that appropriate to S–I–N junctions, for which the $g_+(V)$ and $g_-(V)$ peaks move in opposite directions, irrespective of the voltage polarity. As to the tunneling through an S′–I–S junction, the peak-to-peak separation does not depend on H and is the same for either sign of s.[13,14] To explain the distinction between the superconducting and CDW cases, we should consider in detail each current constituent involved (recall that the $cd\pm$ and $dc\pm$ components were excluded from analysis for the symmetrical CDWM–I–CDWM configuration due to their mutual compensation).

First, as stems from the speculations in Appendix A, the tunneling between the gapped FS sections, as well as the transfer of the electron-hole pairs across the barrier, do not induce any peak splitting in the assumed absence of spin flips. This concerns the contributions $dd\pm$, $cc\pm$, $cd\pm$, and $dc\pm$ to both $J(V)$ and $G(V)$, and is similar to what happens in S′–I–S junctions. At the same time, the "normal" $nn\pm$ components should reveal no noticeable magnetoresistance under the action of relatively small magnetic fields $H \leqslant 0.2\Sigma_0/\mu_B^* \approx 2.8H_p/\sqrt{\mu}$, which are, e.g., far below the fields experimentally found necessary for orbital quantization in the organic material α-(BEDT-TTF)$_2$KHg(SCN)$_4$ (Refs. 27, 51). Here relation (8) was taken into account. Had it not been for other components, the G–V characteristics of CDWM–I–CDWM junctions would have possessed only feature points at $eV=\pm 2\Sigma$, as is the case for S–I–S tunneling.[4,8,9]

Now let us pass on to the tunnel processes that connect the n FS section of one electrode and the d FS section of the other (Fig. 3). For the sake of definiteness we start our analysis with the "+"-polarization conductance. The components $dn+$ and $nd+$ are contributions to the G–V characteristics of the type known from the theory of superconducting splitting.[13,14] Using this analogy, it can be shown that the dimensionless conductances $g_{dn+,nd+}=RdJ_{dn+,nd+}/dV$ can be represented as

$$g_{dn+}(eV,H) \propto \int_{-\infty}^{\infty} d\omega K_0(\omega - eV) F'(\omega,H), \tag{17}$$

$$g_{nd+}(eV,H) \propto \int_{-\infty}^{\infty} d\omega K_0'(\omega) F(\omega - eV,H). \tag{18}$$

Here $F^{(\prime)}(\omega,H)=N_{d+}^{(\prime)}(\omega,H)$, i.e., the densities of the gapped "+" states for the relevant electrodes

$$N_{d+}^{(\prime)}(\omega,H)=N_{d0}^{(\prime)}(0)\,\frac{|\omega-\mu_B^*H|\,\theta(|\omega-\mu_B^*H|-\Sigma^{(\prime)})}{2\sqrt{(\omega-\mu_B^*H)^2-\Sigma^{(\prime)2}}} \tag{19}$$

[cf. Eq. (6)], and the kernels $K_0^{(\prime)}$ are the derivatives of the kernel $K(\omega,eV)$ [Eq. (A.5)] in the integrand of Eq. (A3). The quantities $K_0^{(\prime)}$ are δ-like functions with the maxima at the Fermi levels of the unprimed or primed electrodes, respectively, in the degenerate case considered. In the limiting case $T=0$, the V dependence of the conductance $g_{dn+}(eV)$ coincides with that of $N_{d+}'(eV,H)$ [see Eq. (17)], while $g_{nd+}(eV)$ becomes proportional to $N_{d+}(-eV,H)$ [see Eq. (18)].

When $H=0$, the electrode Fermi levels are located at the center of the relevant CDW gaps and coincide in the absence of bias voltage. The bias magnitudes, needed either to shift the Fermi level of the unprimed electrode (see Fig. 3b, K_0) downwards in reference to the lower edge of the CDW gap of the other electrode (Fig. 3a, $1_0'$, dotted) or to step it up with respect to the upper edge of the same gap (Fig. 3a, $2_0'$, dotted) are equal. Hence, the positions of relevant singularities in the term $g_{dn+}(eV)$ are equidistant from $V=0$ (Fig. 3c, component $1_0'$ of the combined peak $1_0'+2_0$ and component $2_0'$ of the combined peak $1_0+2_0'$, dotted). The same is valid for the contribution $g_{nd+}(eV)$ [Eq. (18)] which contains peak 1_0, positioned at the same bias as the $2_0'$ peak, and peak 2_0, disposed at the same bias as the $1_0'$ peak. Their amplitudes are also pairwise equal, since for the symmetrical junction $K_0(\omega)=K_0'(\omega)$ and $N_d(\omega)=N_d'(\omega)$. Evidently, one cannot distinguish between contributions of the pair elements to the corresponding features of the G–V characteristic, the latter therefore being unsplit (Fig. 3c, dotted peaks $1_0'+2_0$ and $1_0+2_0'$).

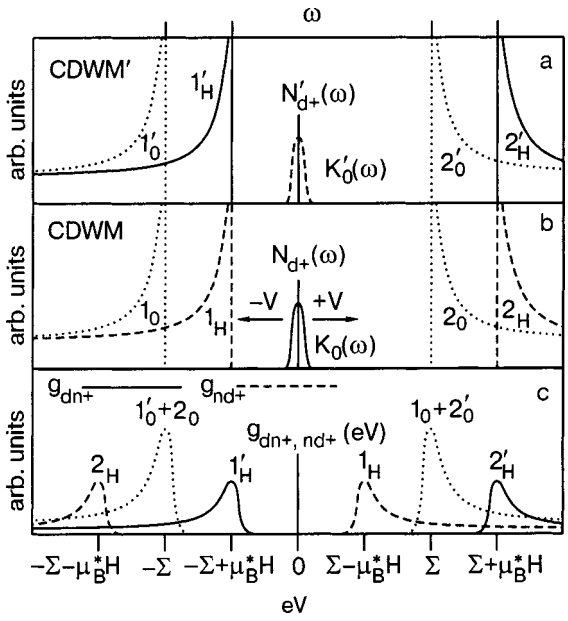

FIG. 3. The scheme of the peak spin-splitting for the conductance components g_{dn+} and g_{nd+} in magnetic field H. (a) The energy dependence of the gapped DOSs $N_{d+}'(\omega)$ for the primed electrode at $H=0$ (dotted curves, subscript 0) and $H\neq 0$ (solid curves, subscript H). The function $K_0'(\omega)$ is a T-dependent kernel [Eq. (18)] originating from the Fermi distribution of the n electrons. (b) The same as in panel (a), with an accuracy up to notation, for the unprimed electrode. All elements of this panel are shifted with respect to those in panel (a) by the value of eV if a bias voltage V is applied. (c) The resulting contributions g_{dn+} and g_{nd+} to the G–V characteristic. Any peak in a certain conductance component appears if a DOS singularity in one panel is overlapped by the kernel function in the other one [those three relevant elements (the peak, the DOS, and the kernel) are drawn using the same style of the curve]. The numbering of the peaks corresponds to the "parent" DOS singularities in panels (a) and (b). See further explanations in the text.

When the magnetic field is switched on but the junction is not biased, the "+" subsystem in each electrode shifts upwards in energy by $+\mu_B^*H$ relative to their common Fermi level, which remains fixed (see Fig. 3a, solid curves, and Fig. 3b, dashed curves). Thus, *different* bias voltages with *different* H-driven offsets should be applied now to obtain peaks in either of the conductance terms. In particular, the singularities in the $g_{dn+}(eV)$ component shift to $\pm\Sigma + \mu_B^*H$ positions (Fig. 3c, solid peaks $1_H'$ and $2_H'$) and the

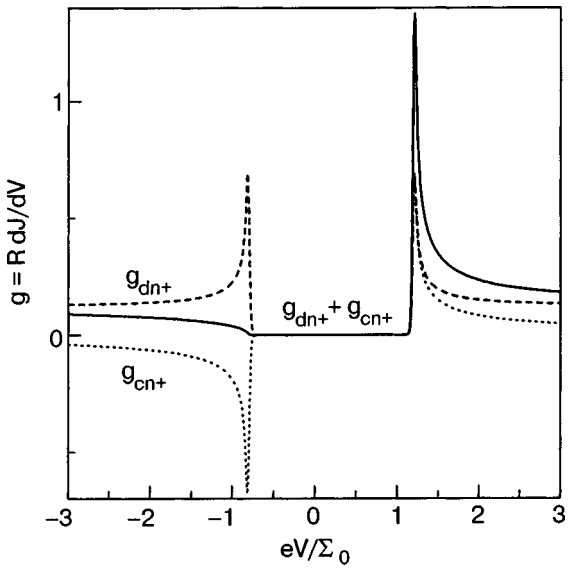

FIG. 4. An illustration of the component compensation: the selected contributions g_{dn+}, g_{cn+} to the overall conductance g and their sum. An almost complete mutual compensation of the logarithmic singularities for negative V and their amplification for positive V is demonstrated. The relevant parameters are the same as in Fig. 2.

singularities in the $g_{nd+}(eV)$ component shift to $\pm\Sigma - \mu_B^* H$ positions (Fig. 3c, dashed peaks 1_H and 2_H). The nomenclature of peaks in Fig. 3c coincides with that in Fig. 3a or 3b, explicitly indicating the gap edge responsible for each feature. Thus, either of the G–V characteristic peaks, being combined in a zero magnetic field, splits into two smaller ones for $H \neq 0$. The peaks belonging to the g_{dn+} or g_{nd+} components shift symmetrically in opposite directions of the V axis, which can be deduced directly from Eqs. (17) and (18). On the other hand, the apparent motion of the peak pairs ($1'_H - 1_H$ and $2'_H - 2_H$), each originating from both g_{dn+} and g_{nd+} terms, is directed inwards and outwards, respectively. But even this rather complicated picture does not signify the end of the story.

The involvement of the $g_{cn+,nc+}$ components, directly descending from the electron-hole pairing, changes the situation radically and makes the resulting G–V characteristics highly unconventional. In particular, the component g_{cn+} is also of the form (17) but with another function $F^{(')}(\omega,H) = N_{d+}^{(')}(\omega,H)$. The term $g_{cn+}(V)$ has the *same functional dependences and amplitude of singularity* at the *same voltage values* as the component g_{dn+} does, but, contrary to the latter and due to the nontrivial properties of the Green's function $G_c(\omega)$, it is antisymmetric with respect to ω. As a consequence, the g_{cn+} singularity enhances its counterpart of g_{dn+} on the positive voltage branch and almost compensates the singularity of g_{dn+} on the negative-V branch, transforming it into a cusp. This is illustrated in Fig. 4. The resulting pattern moves as a whole along the V axis towards larger positive V if an external field H is applied. At the same time, the V dependence of the sum $g_{nd+} + g_{nc+}$ constitutes a mirror reflection of the curve $g_{dn+}(V) + g_{cn+}(V)$ relative to the g axis. Therefore, the overall conductance $g_+(V)$, which is a sum of all the four relevant contributions discussed above, has two peaks symmetrically moving apart and two cusps symmetrically crowding together along the V axis as the magnetic field H grows.

The conductance behavior obtained for the CDWM–I–CDWM sandwich is due to the fact that the FSs have both n and d sections. This means that the whole configuration can be viewed as a combination of two asymmetrical junctions. Hence, there are two *unequal* current components J_{nd+} and J_{dn+} connecting the gapped and non-gapped quasiparticle subsystems. Moreover, the terms J_{cn+} and J_{nc+}, related to the CDW pairing, result in the appearance of antisymmetrical conductance peaks. The interplay of all constituents leads to the effect described above.

An analysis of the sum $g_{dn-} + g_{cn-} + g_{nd-} + g_{nc-}$ is performed in the same way. The resulting two peaks converge symmetrically, whereas the two cusps symmetrically move apart, with increasing H. Since the cusps of one polarization superpose on the singularities of the other polarization and there is no spin filter in the circuit, the cusps may be inconspicuous against the background of the singularities (see Fig. 2b). Taking into account the other components not exhibiting a peak splitting of any nature, we obtain the G-V characteristic shown in Fig. 2, which reveals four H-dependent polarized peaks at $eV = \pm\Sigma \pm \mu_B^* H$ and two fixed jumps at $eV = \pm 2\Sigma$.

The pattern obtained is a consequence of the choice $\varphi = 0$ made above. If one assumes another realistic situation with the order parameter phase averaged out (see the discussion in Sec. 3.2), components (14) and (15) should disappear, so that the G–V characteristics will change substantially. To easily embrace all possible cases with varying φ, it is convenient to analyze all conductance components for $T = 0$. The results are summarized in Appendix C.

3.2. Influence of different factors on the G-V characteristics

Figure 2 distinctly reveals the main peculiarities of the G–V characteristics for a symmetrical CDWM–I–CDWM junction. Namely, there exist discontinuities at H-independent locations $eV = \pm 2\Sigma$, determined merely by a dielectric gap value. Besides, there are H-driven square-root singularities shifted by $\pm\mu_B^* H$ from the basic $eV = \pm\Sigma$ bias values. It is obvious that the larger is the magnetic field H, the stronger are the inward and outward displacements of the singular conductance peaks. As was clearly demonstrated above, the apparent splitting has a dual nature reflecting both the intrinsic configurational asymmetry of the junction concerned and the Zeeman effect.

Nonzero temperatures smear the overall curves $g(V)$ and especially the singular peaks. It is shown in Fig. 5a that these dependences are highly sensitive to the dimensionless parameter t. Therefore, to observe the predicted splitting in the magnetic field one should either heavily reduce T or use CDWMs with large T_d's and hence CDW gaps Σ_0.

The influence of the control gapping parameter μ on the G–V characteristics is demonstrated in Fig. 5b. It is readily seen that the increase of μ reduces the minimal value of $g(V)$, determined by the $g_{nn\pm}$ contributions, and enhances the jump amplitude at $eV = \pm 2\Sigma$. As stems from Fig. 5b and Eqs. (12)–(15), to improve the observability of the predicted splitting effect one should maximize the factor $\mu(1-\mu)$,

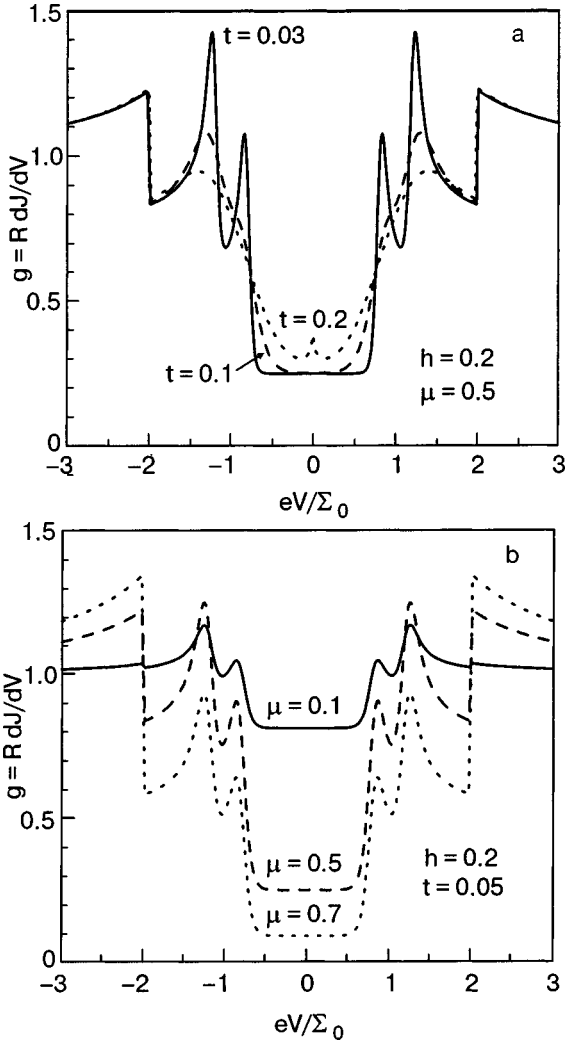

FIG. 5. The dependences $g(eV/\Sigma_0)$ for different t (a) and different μ (b).

i.e., those substances with μ close to 0.5 appear to be more promising.

4. DISCUSSION AND CONCLUSIONS

The predicted splitting of the G–V characteristic induced by the paramagnetic action of the magnetic field H can be observed, in principle, for any CDW *metal*, i.e., the electron spectrum gapping should be incomplete, which is usually the case for a large number of low-dimensional Peierls metals with incommensurate CDWs. The specific requirement is to maintain a balance between d and n portions of the FS ($\mu \approx 0.5$; see Sec. 3.2). This means that external control of the parameter μ (e.g., by an applied pressure) may be crucial for the success of an experiment. The magnitude of the CDW gap Σ defines the natural scale for the field H. Nevertheless, large H and Σ do not mean that the investigations can be carried out at high T. First, the spin splitting will be smeared and not resolved even for moderate T/Σ (see Fig. 5). Second, in a close neighborhood of the paramagnetic limit it is possible to enter the region where, in analogy with the case of superconductors, fluctuations[55] and the influence of the magnetic and spin-orbital scatterings,[56] not covered by the present theory, may become important.

To make the predicted effects observable, it is crucial (at least in the symmetrical setup) for the components J_{dn} and J_{nd}, describing the tunnel current linking d and n FS sections, to survive. In our phenomenological approach, when all matrix elements of the tunnel Hamiltonian[8] are considered equal (tunneling is not considered directional), that is the case. In the other extreme limit of complete tunneling directionality,[57] the components J_{dn} and J_{nd} may not exist, and the spin splitting may disappear. In principle, any degree of directionality is possible. The actual realization of the intermediate situation stems from the analysis carried out for tunnel spectroscopic studies of high-T_c oxides.[58–63] Therefore, one should consider the limit of no directionality and equal probability of all processes connecting different FS sections (a unique quantity R) as an idealized picture, so that for some junctions the feature points at $eV = \pm\Sigma$ might be weakened in comparison to those at $eV = \pm 2\Sigma$. As a consequence, the spin splitting might be also partially suppressed.

The appearance of superconductivity for smaller $T < T_c < T_d$ in any specific CDW substance (see reviews[11,12]) may serve as a clear indication that this material is a metal rather than an insulator, and, therefore, of its ability to demonstrate the Zeeman spin splitting. Hence, the low-dimensional metals exhibiting CDW instabilities, such as $NbSe_3$, Nb_3Te_4, $Li_{0.9}Mo_6O_{17}$, $Tl_2Mo_6Se_6$, layered dichalcogenides, alloys with the A15 and C15 structures, $Lu_5Ir_4Si_{10}$, $P_4W_{14}O_{50}$, tungsten bronzes doped by alkali metals, and solid solutions $BaPb_{1-x}Bi_xO_3$ may serve as good candidates. Other monophosphate bronzes $(PO_2)_4(WO_3)_{2m}$, doped and undoped by alkalis, are also suitable partially gapped CDWMs.[64,65]

An important conjecture should be made concerning the magnitude of the CDW gaps. For superconductors, the ratio $2\Delta(0)/k_BT_c$ is usually of the order or somewhat larger than the BCS value $2\pi/\gamma \approx 3.52$.[4] The only exception is MgB_2. In that case, the very character of the superconductivity is as yet ambiguous and an intrinsic two-gap scenario is often accepted (see the relevant critical discussion of this concept in Refs. 66 and 67). On the other hand, the observed dependence $\Sigma(T)$ in CDWMs and CDW insulators has a generalized BCS-like form. Namely, in the coordinates $\Sigma(T)/\Sigma(T=0)$ versus T/T_d, the data follow the Mühlschlegel curve, whereas the ratio $2\Sigma(0)/k_BT_d$ substantially exceeds the BCS weak-coupling limit (such behavior is described by the phenomenological scheme[68]). For example, this quantity is about 13 in the insulating $La_{1.67}Sr_{0.33}NiO_4$.[69] Layered dichalcogenides $2H-TaSe_2$, $2H-TaS_2$, and $2H-NbSe_2$ are marked by extremely large values $2\Sigma(0)/k_BT_d = 15.2$, 15.4, and 23.9, respectively.[70] In $NbSe_3$, with its two CDW transitions at $T_d^{low} = 59$ K and $T_d^{high} = 145$ K,[11,12] the respective ratios, as was shown by direct tunneling studies,[71] fall into the ranges $2\Sigma^{low}(0)/k_BT_d^{low} \approx 11.8-14.3$ and $2\Sigma^{high}(0)/k_BT_d^{high} \approx 11.4-14.4$. Taking the observed Gaussian spread of the CDW gaps into account gives somewhat lower values $2\Sigma^{low}(0)/k_BT_d^{low} \approx 9.2$ and $2\Sigma^{high}(0)/k_BT_d^{high} \approx 8.2$.[72] Larger gap-to-$T_d$ ratios are favorable for our purposes, since to clearly observe the splitting, one should avoid high temperatures during the experiment, while large gaps are convenient.

Superconducting cuprates can be suggested as another class of substances in which the CDW-triggered spin-

splitting in magnetic field can be observed. Two kinds of features testify that CDWs exist in a number of high-T_c oxides. The first one is a dip-hump structure of $G(V)$ for voltages exceeding the positions of the superconducting gap maxima,[72,73] while the other one is the so-called pseudogap, Σ_*, persisting both above and below T_c.[11,12,74–78] We think that the CDW origin of those peculiarities is quite plausible, whereas the most popular interpretation based on the precursor Cooper pairing (see, e.g., the review[79] and references therein) should be rejected, at least because the applied magnetic field influences true gaps and the Σ_*'s in a different way.[80–82] Moreover, the predominantly paramagnetic character of the magnetic field influence on the Σ_*'s is attested by the existence of Zeeman scaling (proportionality) between the pseudogap-closing field $H_{\rm pg}$ and the characteristic pseudogap temperature T^* determined resistively in $Bi_2Sr_2CaCu_2O_{8-y}$ (Refs. 83, 84). This means that the huge orbital Meissner effect is absent for Σ_*, so that at least in $Bi_2Sr_2CaCu_2O_{8-y}$ it may be identified with Σ. We recommend the recent comprehensive reviews[11,12,74–77,85] to compare the arguments advanced by various analysts in this field.

Low T of measurements may turn out to be a necessary condition for resolving the spin splitting of CDW gaps (pseudogaps). Since one can draw more-definite conclusions for the pure CDW phase above T_c, it is advantageous to carry out investigations in magnetic field for substances with relatively low T_c, much smaller than both T_d and $\Sigma(T)$. That is why we consider the experiments of Ref. 86 very important. Specifically, a well-resolved superconducting gap Δ and a pseudogap Σ were found by the authors of Ref. 86 for $Bi_2(Sr_{2-x}La_x)CuO_{6+\delta}$ mesas with 10 K$\leqslant T_c \leqslant$32 K. In looking for the predicted effect in cuprates, one should search through substances in which the following conditions are satisfied: (i) a clear-cut resolution between Δ and Σ,[73,80–82,86–88] (ii) all four coexistent features, positioned at $\pm\Sigma$ and $\pm 2\Sigma$, should be manifested, and (iii) the temperature of observation must be as low as possible. The last requirement might not be so severe as it seems at first glance, because the same H that drives the Zeeman peak splitting would suppress superconductivity, making the CDW gap itself open for probing.

A.M.G. is grateful to the Japan Society for the Promotion of Science for support of his visit to the Hiroshima University (Grant ID No. S-03204) and to the Mianowski Foundation for support of his visit to Warsaw University. The research has been partly supported by the NATO grant PST-.CLG.979446 and the grants COE (No. 13CE2002) and Scientific Research (No. 15540346) of the Ministry of Education, Culture, Sports, Science and Technology of Japan. The authors are also grateful to Jun Akimitsu (Tokyo), Serguei Brazovskii (Kyoto), Kenji Ishida (Kyoto), Yoshiteru Maeno (Kyoto), and Mai Suan Li (Warsaw) for fruitful discussions.

APPENDIX A: TUNNEL CURRENT COMPONENTS

Let us consider the general case of two different CDWMs with relevant parameters $(\tilde{\Sigma}', \mu')$ and $(\tilde{\Sigma}, \mu)$ on two sides of the potential barrier created by an insulating interlayer. The current-voltage (I–V) characteristics $J(V)$ for the quasiparticle tunnel current in this junction are calculated by the tunnel Hamiltonian method[4,10,40,42] in the first order of the perturbation scheme.[32,89] Under the assumption that there is no spin flipping while tunneling, the overall tunnel current J can be described as consisting of the following 18 terms:

$$J_{ij\pm} \propto \mathrm{Re} \int_{-\infty}^{\infty} d\omega' \times \int_{-\infty}^{\infty} d\omega \frac{\mathrm{Im}\, G'_{is}(\omega' \mp \mu_B^* H) G_{js}(\omega \mp \mu_B^* H)}{\omega' - \omega + eV + i0}, \tag{A1}$$

which correspond to various combinations of Green's functions and spin projections ($s=\pm$) for the two electrodes. Here the quantities related to different electrodes are primed or unprimed, the subscripts i and j of the Green's functions $G(\omega)$ are equal to d, n, or c [see Eqs. (3)–(5)], and the signs in the arguments of the Green's functions are opposite to those of the spin projection. Hereafter, the potential of the primed electrode is taken as zero, so that the bias voltage V comprises the electrostatic potential of the unprimed electrode. After standard calculations following the pattern of Refs. 5, 11, 12, we obtain the expression

$$J = \sum_{\substack{i,j=d,n,c \\ s=+,-}} J_{ijs}, \tag{A2}$$

with each component and the overall current depending on the bias voltage V, temperature T, and H. All current components J_{ijs} have the general form

$$J_{ij\pm} = \frac{1}{4eR} \int_{-\infty}^{\infty} d\omega K Z_i(\omega \mp \mu_B^* H, \tilde{\Sigma}') \times Z_j(\omega \mp \mu_B^* H - eV, \tilde{\Sigma}). \tag{A3}$$

The quantity

$$R^{-1} = 4\pi e^2 N_0'(0) N_0(0) \langle |T_{\mathbf{pq}}|^2 \rangle_{FS} \tag{A4}$$

is the conductance (inverse resistance) of the junction above T_d, where both electrodes are in the non-gapped state. The square of the modulus of the tunnel matrix element $T_{\mathbf{pq}}$ is averaged over the FS, i.e., all matrix elements of the tunnel Hamiltonian are taken equal. Thus we assume a unique tunnel resistance for every current component. From the physical point of view this means, in particular, no tunnel directionality, which is possible, in principle.[58–63] The factor

$$K \equiv K(\omega, V, T) = \tanh \frac{\omega}{2T} - \tanh \frac{\omega - eV}{2T} \tag{A5}$$

stems from the Fermi distribution functions of the two electrodes.

Each Z function in the integrand of Eq. (A3) constitutes a product

$$Z_i(\omega, \tilde{\Sigma}) = z_i(\omega, \tilde{\Sigma}) f_i(\omega, \tilde{\Sigma}) \tag{A6}$$

of one of the characteristic functions

$$z_d(\omega, \tilde{\Sigma}) = \mu |\omega|, \tag{A7}$$

$$z_c(\omega, \tilde{\Sigma}) = \mu\, \mathrm{sgn}(\omega) \tilde{\Sigma}, \tag{A8}$$

$$z_n(\psi, \tilde{\Sigma}) = (1-\mu) |\omega|, \tag{A9}$$

and the factor

$$f_i(\omega,\tilde{\Sigma})=\frac{\theta(|\omega|-\Sigma)}{\sqrt{\omega^2-\Sigma^2}}, \tag{A10}$$

which describes the presence ($\tilde{\Sigma}\neq 0$ for $i=d$ and c) or absence ($\tilde{\Sigma}=0$ for $i=n$) of gapping; $\theta(x)$ is the Heaviside step function. For $i=n$, the Z_n function reduces to

$$Z_n(\omega,\tilde{\Sigma})=1-\mu. \tag{A11}$$

When gapping is absent in both electrodes ($\mu=\mu'=0$), the total current consists of $J_{nn\pm}$ components only and has a conventional Ohm's law form V/R in the whole voltage range, independent of T and H. Of course, in the general case, Ohm's law is restored for large enough voltages substantially exceeding Σ' and Σ.

Tunnel currents between CDWMs across the barriers of different transparencies making allowance for the dependences of J on φ and φ' have been studied in a number of papers.[21,90–93] Contrary to some of them,[91–93] we shall consider the most general setup, when φ and φ' are independent of each other. The situation when $\varphi=\varphi'$ will stem from the general equations as a particular case.

Let us analyze the symmetry properties of different current components. It is convenient to start from the case $H=0$. Such an analysis has been done earlier,[5] but to investigate below a more involved situation with nonzero H, it is necessary to carry out an additional examination. We shall use the notation $J_{ij0}=J_{ijs}(H=0)$, since in this case $\omega_{\pm}=\omega$ in the integrands of (A3), and therefore $J_{ij+}(H=0)=J_{ij-}(H=0)$.

The components can be divided into symmetrical and asymmetrical ones with respect to the voltage V. The symmetrical components, for which an unusual relation[5,54]

$$J_{ij0}(-V)=J_{ij0}(V) \tag{A12}$$

holds, are those that contain the ''anomalous'' Green's function G_c once in the integrand [Eq. (A1)]. These are J_{dc0}, J_{cd0}, J_{nc0}, and J_{cn0}. The other components, namely, J_{dd0}, J_{cc0}, J_{nn0}, J_{dn0}, and J_{nd0}, satisfy the conventional equation[9]

$$J_{ij0}(-V)=-J_{ij0}(V). \tag{A13}$$

It is worth mentioning that the integrand of J_{cc0} includes a product of two Green's functions G_c, the anomalous symmetry properties of which compensate each other.

The differential conductance $G(V)\equiv dJ(V)/dV$ is a quantity of primary interest to experimentalists. The same is true for its symmetry properties. The dependence $G(V)$ and similar V dependences of its components G_{ij} will be henceforth called the conductance-voltage (G–V) characteristics. The symmetry relationships for $G_{ij0}(V)$ are easily deduced from those for $J_{ij0}(V)$. Namely, for the $dd0$, $cc0$, $nn0$, $dn0$, and $nd0$ components, they have the standard form[9]

$$G_{ij0}(-V)=G_{ij0}(V), \tag{A14}$$

whereas for the $dc0$, $cd0$, $nc0$, and $cn0$ terms, the symmetry properties are anomalous:

$$G_{ij0}(-V)=-G_{ij0}(V). \tag{A15}$$

Going to the case $H\neq 0$, we should consider the changes of the CDWM electron spectrum on both sides of the junction under the influence of the external magnetic field (see Fig. 1). As was indicated in Sec. 2.1.2, the Fermi levels (chemical potentials) in both electrodes, differing from each other by eV, remain practically unchanged when H is switched on. Hence, the electron spectrum on the n FS sections is also unchanged. On the other hand, the quasiparticle energy subbands with the spin projection $s=+$ on the d FS sections in both electrodes shift upwards by the value $\mu_B^* H$, while the subbands with the projection $s=-$ shift downwards by the same value.

Since tunneling is assumed to preserve spin values, it is clear that a current component depends on H only in the case where the subbands involved (one from the primed electrode and the other from the unprimed one) change their energy difference with increasing magnetic field. Relevant links are shown in Fig. 1 by dashed lines. Therefore, all 18 components can be divided into three groups. The first one contains those terms which do not depend on H. They are J_{dds}, J_{ccs}, J_{dcs}, J_{cds}, and J_{nns}, and for them

$$J_{ijs}(eV,H)=J_{ijs}(eV,0). \tag{A16}$$

The next group of current components, J_{dn+}, J_{cn+}, J_{nd-}, and J_{nc-}, is shifted towards larger voltages for $H\neq 0$, i.e.,

$$J_{ijs}(eV-\mu_B^* H,H)=J_{ijs}(eV,0). \tag{A17}$$

The remaining terms J_{dn-}, J_{cn-}, J_{nd+}, and J_{nc+} move in the opposite direction of the V axis, i.e.,

$$J_{ijs}(eV+\mu_B^* H,H)=J_{ijs}(eV,0). \tag{A18}$$

Various links describing such H-dependent current components are specified by solid lines in Fig. 1.

Those components play a crucial role, because they lead to a new phenomenon revealed in junctions between CDWMs exposed to a magnetic field. Specifically, the overall tunnel current and peaks in $G(V)$, originating from the CDW gapping, are spin-split even in the symmetrical setup. This is unlike the total absence of splitting when both electrodes are superconducting, whatever the relative magnitudes of the superconducting gaps.[13]

It is worthwhile to discuss one peculiarity, concerning the shifts (A17) and (A18) of the I–V (and, by implication, the G–V) characteristics along the V axis. It happens that $J_{ij+}(eV=0,H\neq 0)\neq 0$ for those current components, although each component in the sum (A2) becomes zero in the absence of H and in the absence of voltage: $J_{ij0}(eV=0)=0$. But this does not signify any violation of the laws of quasi-stationary electrodynamics, since only the total current (A2), for which $J(eV=0,H\neq 0)=0$ irrespective of the magnitude of H, has physical meaning.

APPENDIX B: ANALYTICAL EXPRESSIONS FOR TUNNEL CURRENT COMPONENTS IN ASYMMETRICAL AND SYMMETRICAL JUNCTIONS AT $T=0$ AND $H=0$

Here, the *analytical* expressions for tunnel current components across the insulating barrier between dissimilar CDWM electrodes at $T=0$ and in the absence of the magnetic field are calculated. The derivation of the corresponding expressions is straightforward although cumbersome.

The final results are displayed below. Only the branches $V>0$ of the components of the I–V characteristic are explicitly shown, because their negative V counterparts can be easily obtained using the symmetry properties (A12) and (A13).

$$J_{dd}(V>0)=\frac{\mu'\mu}{eR}\Big\{[N+2\sqrt{\Sigma'\Sigma}]\mathbf{E}(\alpha) - \frac{4\sqrt{\Sigma'\Sigma}[N+\sqrt{\Sigma'\Sigma}]}{[N+2\sqrt{\Sigma'\Sigma}]}\mathbf{K}(\alpha)\theta[eV-(\Sigma'+\Sigma)]; \tag{B1}$$

$$J_{cc}(V>0) = -\frac{4\mu'\mu\Sigma'\Sigma\cos\varphi'\cos\varphi\mathbf{K}(\alpha)\theta[eV-(\Sigma'+\Sigma)]}{eR[N+2\sqrt{\Sigma'\Sigma}]}; \tag{B2}$$

$$J_{dn}(V>0)=\frac{1}{eR}\{\mu'(1-\mu)\theta(eV-\Sigma')\sqrt{(eV)^2-\Sigma'^2}\}; \tag{B3}$$

$$J_{nd}(V>0)=\frac{1}{eR}\{\mu(1-\mu')\theta(eV-\Sigma)\sqrt{(eV)^2-\Sigma^2}\}. \tag{B4}$$

$$J_{cd}(V>0)=\frac{2\mu'\mu\Sigma'\Sigma\theta[eV-(\Sigma'+\Sigma)]}{eRN}\cos\varphi' \times\left\{2\mathbf{\Pi}\left(\frac{\pi}{2},\frac{eV-\Sigma'-\Sigma}{eV-\Sigma'+\Sigma},k\right)-\mathbf{K}(k)\right\}; \tag{B5}$$

$$J_{dc}(V>0)=\frac{2\mu'\mu\Sigma'\Sigma\theta[eV-(\Sigma'+\Sigma)]}{eRN}\cos\varphi \times\left\{-2\mathbf{\Pi}\left(\frac{\pi}{2},\frac{eV-\Sigma'-\Sigma}{eV+\Sigma'-\Sigma},k\right)+\mathbf{K}(k)\right\}; \tag{B6}$$

$$J_{cn}(V>0)=\frac{1}{eR}\mu'\Sigma'\cos\varphi'\theta(eV-\Sigma') \times\ln\left|\frac{eV+\sqrt{(eV)^2-\Sigma'^2}}{\Sigma'}\right|; \tag{B7}$$

$$J_{nc}(V>0)=\frac{1}{eR}\mu\Sigma\cos\varphi\theta(eV-\Sigma) \times\ln\left|\frac{eV+\sqrt{(eV)^2-\Sigma^2}}{\Sigma}\right|. \tag{B8}$$

Expression (11) for the current between n FS sections conserves its form. Here $\mathbf{K}(x)$, $\mathbf{E}(x)$, and $\mathbf{\Pi}(\pi/2,x,y)$ are the complete elliptic integrals of the first, second, and third kind, respectively. Their arguments are

$$k=\frac{\sqrt{(eV)^2-(\Sigma'+\Sigma)^2}}{N} \tag{B9}$$

and

$$\alpha=\frac{N-2\sqrt{\Sigma'\Sigma}}{N+2\sqrt{\Sigma'\Sigma}}, \tag{B10}$$

whereas the quantity N is equal to

$$N=\sqrt{(eV)^2-(\Sigma'-\Sigma)^2}. \tag{B11}$$

One can readily see that the analytical expressions for the tunnel current between dissimilar CDWMs differ substantially from their well-known counterparts in the case of the quasiparticle current between different superconductors.[8] Namely, there is a single term $J_{sc}(V)$ for the superconducting junction, coinciding with our component $J_{dd}(V)$ with an accuracy up to substitution of the superconducting gaps Δ' and Δ for the CDW ones Σ' and Σ, while setting $\mu'=\mu=1$. Extra terms originate from the pairwise combinations of the Green's functions (3), (4), and (5) appropriate to the currently investigated case of the junction involving CDWMs.

The main qualitative distinction between superconductor- and CDWM-based junctions consists in the different form of the feature points. There is one break point in the superconducting junction at $eV=\Delta'+\Delta$, where the current changes steeply from zero to the value

$$\Delta J_{sc}=\frac{\pi\sqrt{\Delta'\Delta}}{2eR}. \tag{B12}$$

At the same time, from Eqs. (B1), (B2), (B5), and (B6) it follows that

$$\Delta J(eV=\Sigma'+\Sigma)=\frac{\pi\mu'\mu\sqrt{\Sigma'\Sigma}}{2eR}(1+\cos\varphi')(1-\cos\varphi). \tag{B13}$$

One should note that there is an intrinsic asymmetry in Eq. (B13), i.e., ΔJ depends on each of the phases φ' and φ separately and in a different way. Both phase factors $\cos\varphi'$ and $\cos\varphi$ will change their signs for the opposite voltage polarity $V<0$. A similar asymmetry takes place in an *asymmetrical* junction between CDW conductors.[5] The jump disappears in the particular case of an excitonic insulator, where each of the phase angles is either 0 or π, contrary to what is appropriate to the superconducting tunneling.

The emergence of square-root singularities in the J_{dn}, J_{nd}, J_{cn}, and J_{nc} components [see Eqs. (B3), (B4), (B7) and (B8)], respectively, is another important phenomenon appropriate to asymmetrical junctions involving CDWMs.

The phase dependences of the current components J_{cd}, J_{dc}, J_{cn} and J_{nc}, represented by Eqs. (B5), (B6), (B7), and (B8), respectively, were obtained assuming definite constant values of the phases φ' and φ for the two electrodes. Actually, an averaging of the currents over the junction cross section, as a consequence of the phase randomness, may wipe out these terms. To preserve them, the use of the break-junction technique, confining the contact area, would be of benefit. Nevertheless, the resulting current $J(V)$ would differ substantially from its superconducting analog even in this case. In particular, the jump $\Delta J(eV=\Sigma'+\Sigma)$, expressed by Eq. (B13), disappears, contrary to what stems from the BCS theory and experiments carried out for S′–I–S junctions.[9] Another very important phenomenon that survives the averaging is the square-root dependence of the components J_{dn} and J_{nd} on the voltage [see Eqs. (B3) and (B4)].

The general results (B1)–(B8) can be substantially simplified in the case of identical CDW parameters in both electrodes ($\tilde{\Sigma}'=\tilde{\Sigma}$ and $\mu'=\mu$). In that case the expression for the tunnel current takes the following form:

$$J(V>0)=\frac{1}{eR}\Big\{(1-\mu)^2eV+2\mu(1-\mu)\theta(eV-\Sigma)\times\sqrt{(eV)^2-\Sigma^2}+\mu^2\theta(eV-2\Sigma)\Big[(eV+2\Sigma)\times\mathbf{E}(\alpha_e)-\frac{4\mathbf{K}(\alpha_e)\Sigma[eV+\Sigma(1+\cos^2\varphi)]}{eV+2\Sigma}\Big]. \quad \text{(B14)}$$

Here

$$\alpha_e=\frac{eV-2\Sigma}{eV+2\Sigma}. \quad \text{(B15)}$$

For the pinned phase of the commensurate excitonic insulator ($\varphi=0$ or π), the results of our previous work[5] are reproduced.

One can imagine a plausible situation wherein a tunnel current is assembled from a large enough contact area, so that the CDW phases vary substantially over the contact plane. Then all φ-dependent terms should be averaged out. This means that all components directly involving CDW pairing amplitude, i.e., possessing at least one c subscript, must vanish in an asymmetrical configuration. For the CDWM–I–CDWM junction, this will result in a substitution of 1/2 for $\cos^2\varphi$.

APPENDIX C: TUNNEL CONDUCTANCE IN A MAGNETIC FIELD AT $T=0$

It follows from the basic equations (9)–(15) that the C–V characteristics for CDWM′–I–CDWM junctions should differ substantially from their counterparts for S′–I–S tunnel structures. Moreover, CDWM′–I–CDWM junctions exhibit peculiar Zeeman splitting (see Sec. 3.1) totally absent for currents between superconducting electrodes. Below, analytical formulas for $G_{\pm}(V)$ components are represented as direct illustrative evidence for the predicted phenomena. Likewise in Appendix B only the branches $V>0$ of the components of the C–V characteristics are explicitly shown.

In particular, the field-independent terms of the total conductance have the form

$$G_{dd+}(V>0)+G_{cc+}(V>0)=G_{dd-}(V>0)+G_{cc-}(V>0)=\frac{\mu^2}{2R}\theta(eV-2\Sigma)\times\Big[\mathbf{E}(\alpha_e)\frac{(eV)^2-2\Sigma^2(1+\cos^2\varphi)}{eV(eV-2\Sigma)}+4\Sigma\mathbf{K}(\alpha_e)\frac{\Sigma(1+\cos^2\varphi)-eV}{(eV)^2-4\Sigma^2}\Big], \quad \text{(C1)}$$

$$G_{nn+}(V>0)=G_{nn-}(V>0)=\frac{(1-\mu)^2}{2R}. \quad \text{(C2)}$$

The notation here coincides with that of Appendix B. The other components split in a magnetic field and appear as

$$G_{dn\pm}(V>0)=\frac{\mu(1-\mu)(eV\pm\mu_B^*H)\,\theta(eV\pm\mu_B^*H-\Sigma)}{2R\sqrt{(eV\pm\mu_B^*H)^2-\Sigma^2}}, \quad \text{(C3)}$$

$$G_{nd\pm}(V>0)=\frac{\mu(1-\mu)(eV\mp\mu_B^*H)\,\theta(eV\mp\mu_B^*H-\Sigma)}{2R\sqrt{(eV\mp\mu_B^*H)^2-\Sigma^2}}, \quad \text{(C4)}$$

$$G_{cn\pm}(V>0)=-\frac{\mu(1-\mu)\Sigma\cos\varphi\,\theta(eV\mp\mu_B^*H-\Sigma)}{2R\sqrt{(eV\mp\mu_B^*H)^2-\Sigma^2}}, \quad \text{(C5)}$$

$$G_{nc\pm}(V>0)=\frac{\mu(1-\mu)\Sigma\cos\varphi\,\theta(eV\pm\mu_B^*H-\Sigma)}{2R\sqrt{(eV\pm\mu_B^*H)^2-\Sigma^2}}. \quad \text{(C6)}$$

A sum of components (C1)–(C6) gives the overall conductance $G(V)$; its shape is shown in Fig. 2.

It follows from Eqs. (C1) and (A14) that

$$\Delta G(eV=\pm2\Sigma)=\frac{\pi\mu^2}{2R}, \quad \text{(C7)}$$

regardless of the order parameter phase φ. It is necessary to underline that the tunneling conductance for the superconducting symmetrical junction is determined by quite a different expression,[8,10]

$$G_{sc}(V>0)=\frac{\theta(eV-2\Delta)}{(eV-2\Delta)R}\Big[\mathbf{E}(\alpha_s)\frac{(eV)^2-2\Delta^2}{eV}+\mathbf{K}(\alpha_s)\frac{4\Delta(eV-\Delta)}{eV+2\Delta}\Big], \quad \text{(C8)}$$

where Δ is the superconducting gap and

$$\alpha_s=\frac{eV-2\Delta}{eV+2\Delta}. \quad \text{(C9)}$$

The conductance $G_{sc}(V)$ diverges when eV tends to 2Δ from above:

$$G_{sc}(V)\ \xrightarrow[eV\to2\Delta+0]{}\ \frac{\pi\Delta}{(eV-2\Delta)R}. \quad \text{(C10)}$$

The distinction between properties (C7) and (C10) is due to the fact that the pertinent tunnel current in superconductors comprises a direct one-term convolution of the Fermi-distribution factor and two gapped DOSs. On the other hand, for CDWMs, the singularities in the terms $G_{dds}(V)$ at $eV=\pm2\Sigma$ are to a certain extent compensated by the contributions from the terms $G_{ccs}(V)$ formed by two ''intersection'' Green's functions G_c (Refs. 5, 11, 12).

As for the spin-split peaks at two times smaller voltages $eV=\pm\Sigma$ in $G(V)$ for CDWM–I–CDWM tunnel junctions, they should be observed only for partially gapped metals. Therefore, such substances, as, e.g., TTF–TCNQ, $(TaSe_4)_2I$,

σ-TaS_3, or $K_{0.33}MoO_3$, which are insulating below T_d,[3] cannot reveal the predicted phenomenon of anomalous magnetic-field-induced splitting.

*E-mail: collphen@iop.kiev.ua

[1] B. I. Halperin and T. M. Rice, Solid State Phys. **21**, 115 (1968).
[2] Yu. V. Kopaev, Trudy Fiz. Inst. Akad. Nauk SSSR **86**, 3 (1975).
[3] G. Grüner, *Density Waves in Solids*, Addison-Wesley, Reading, Massachusetts (1994).
[4] A. A. Abrikosov, *Fundamentals of the Theory of Metals*, North-Holland, Amsterdam (1987).
[5] A. M. Gabovich and A. I. Voitenko, Phys. Rev. B **52**, 7437 (1995).
[6] A. I. Anselm, *Introduction to Semiconductor Theory* [in Russian], Nauka, Moscow (1978).
[7] A. M. Gabovich, A. I. Voitenko, M. S. Li, H. Szymczak, and M. Pekala, in *Physics of Spin in Solids: Materials, Methods and Applications*, S. Halilov (ed.), Kluwer, Dordrecht (2004), p. 25.
[8] D. H. Douglass, Jr. and L. M. Falicov, Prog. Low Temp. Phys. **4**, 97 (1964).
[9] E. L. Wolf, *Principles of Electron Tunneling Spectroscopy*, Oxford University Press, New York (1985).
[10] G. D. Mahan, *Many-Particle Physics*, Kluwer Academic, New York (2000).
[11] A. M. Gabovich and A. I. Voitenko, Fiz. Nizk. Temp. **26**, 419 (2000) [Low Temp. Phys. **26**, 305 (2000)].
[12] A. M. Gabovich, A. I. Voitenko, and M. Ausloos, Phys. Rep. **367**, 583 (2002).
[13] R. Meservey and P. M. Tedrow, Phys. Rep. **238**, 173 (1994).
[14] P. Fulde, Adv. Phys. **22**, 667 (1973).
[15] R. H. McKenzie, cond-mat/9706235.
[16] A. Bjeliš, D. Zanchi, and G. Montambaux, cond-mat/9909303.
[17] N. Harrison, Phys. Rev. Lett. **83**, 1395 (1999).
[18] J. S. Qualls, L. Balicas, J. S. Brooks, N. Harrison, L. K. Montgomery, and M. Tokumoto, Phys. Rev. B **62**, 10008 (2000).
[19] S. J. Williamson, C. S. Ting, and H. K. Fung, Phys. Rev. Lett. **32**, 9 (1974).
[20] M. Matos, G. Bonfait, R. T. Henriques, and M. Almeida, Phys. Rev. B **54**, 15307 (1996).
[21] S. N. Artemenko and A. F. Volkov, Zh. Éksp. Teor. Fiz. **87**, 691 (1984) [Sov. Phys. JETP **60**, 395 (1984)].
[22] I. V. Krive, A. S. Rozhavskii, and I. O. Kulik, Fiz. Nizk. Temp. **12**, 1123 (1986) [Sov. J. Low Temp. Phys. **12**, 635 (1986)].
[23] S. N. Artemenko and A. F. Volkov, in *Charge Density Waves in Solids*, L. P. Gor'kov and G. Grüner (eds.), North-Holland, Amsterdam (1985), p. 365.
[24] N. Harrison, Phys. Rev. B **66**, 121101 (2002).
[25] D. Zanchi, A. Bjeliš, and G. Montambaux, Phys. Rev. B **53**, 1240 (1996).
[26] A. G. Lebed, Phys. Rev. Lett. **88**, 177001 (2002).
[27] D. Andres, M. V. Kartsovnik, P. D. Grigoriev, W. Biberacher, and H. Müller, Phys. Rev. B **68**, 201101 (2003).
[28] T. Ishiguro and K. Yamaji, *Organic Superconductors*, Springer Verlag, Berlin (1990).
[29] G. Bilbro and W. L. McMillan, Phys. Rev. B **14**, 1887 (1976).
[30] R. R. Guseinov and L. V. Keldysh, Zh. Éksp. Teor. Fiz. **63**, 2255 (1972).
[31] A. M. Gabovich, E. A. Pashitskiĭ, and A. S. Shpigel', Fiz. Tverd. Tela (Leningrad) **18**, 3279 (1976) [Sov. Phys. Solid State **18**, 1911 (1976)].
[32] A. M. Gabovich and A. I. Voitenko, J. Phys.: Condens. Matter **9**, 3901 (1997).
[33] A. M. Gabovich and A. I. Voitenko, Phys. Rev. B **56**, 7785 (1997).
[34] V. L. Ginzburg and D. A. Kirzhnitz (eds.), *High Temperature Superconductivity*, Consultants Bureau, New York (1982).
[35] J. Frenkel, Phys. Rev. **36**, 1604 (1930).
[36] J. Frenkel, *Wave Mechanics; Elementary Theory*, Clarendon Press, Oxford (1932), Russ. Vol. 1, State Technical-Theoretical Publishing House, Leningrad-Moscow (1934).
[37] A. Sommerfeld and H. Bethe, *Elektronentheorie der Metalle*, Springer-Verlag, Berlin (1933).
[38] A. I. Khachaturov, E. Hatta, and V. M. Svistunov, J. Phys. Soc. Jpn. **72**, 131 (2003).
[39] J. Bardeen, Phys. Rev. Lett. **6**, 57 (1961).
[40] M. H. Cohen, L. M. Falicov, and J. C. Phillips, Phys. Rev. Lett. **8**, 316 (1962).
[41] L. Solymar, *Superconductive Tunneling and Applications*, Chapman and Hall, London (1972).
[42] I. O. Kulik and I. K. Yanson, *Josephson Effect in Superconducting Tunnel Structures* [in Russian], Nauka, Moscow (1970).
[43] L. D. Landau and E. M. Lifshitz, *Statistical Physics*, Part 1, 3rd ed., Pergamon Press (1980), Nauka, Moscow (1976).
[44] S. V. Vonsovskii, *Magnetism*, Wiley, New York (1974), Nauka, Moscow (1971).
[45] A. M. Gabovich, Fiz. Tverd. Tela (Leningrad) **25**, 3179 (1983) [Sov. Phys. Solid State **25**, 1833 (1983)].
[46] A. M. Gabovich and A. I. Voitenko, Phys. Status Solidi B **133**, 135 (1986).
[47] A. M. Clogston, Phys. Rev. Lett. **9**, 266 (1962).
[48] B. S. Chandrasekhar, Appl. Phys. Lett. **1**, 7 (1962).
[49] A. M. Gabovich, A. S. Gerber, and A. S. Shpigel, Phys. Status Solidi B **141**, 575 (1987).
[50] J. Singleton, Rep. Prog. Phys. **63**, 1111 (2000).
[51] D. Andres, M. V. Kartsovnik, W. Biberacher, H. Weiss, E. Balthes, H. Müller, and N. Kushch, Phys. Rev. B **64**, 161104 (2001).
[52] A. G. Lebed, JETP Lett. **78**, 138 (2003).
[53] J. R. Schrieffer, in *Tunneling Phenomena in Solids*, E. Burstein and S. Lundqvist (eds.), Plenum Press, New York (1969), p. 287.
[54] A. M. Gabovich, Fiz. Nizk. Temp. **19**, 1098 (1993) [Low Temp. Phys. **19**, 779 (1993)].
[55] P. M. Tedrow and R. Meservey, Phys. Rev. B **16**, 4825 (1977).
[56] R. C. Bruno and B. B. Schwartz, Phys. Rev. B **8**, 3161 (1973).
[57] W. A. Harrison, Phys. Rev. **123**, 85 (1961).
[58] M. Ledvij and R. A. Klemm, Phys. Rev. B **51**, 3269 (1995).
[59] Z. Yusof, J. F. Zasadzinski, and L. Coffey, Phys. Rev. B **58**, 514 (1998).
[60] Y.-M. Nie and L. Coffey, Phys. Rev. B **59**, 11982 (1999).
[61] G. B. Arnold and R. A. Klemm, Phys. Rev. B **62**, 661 (2000).
[62] R. A. Klemm, Phys. Rev. B **67**, 174509 (2003).
[63] J. E. Dowman, M. L. A. MacVicar, and J. R. Waldram, Phys. Rev. **186**, 452 (1969).
[64] M. Greenblatt, in *Physics and Chemistry of Low-Dimensional Inorganic Conductors*, C. Schlenker, J. Dumas, M. Greenblatt, and S. van Smaalen (eds.), Plenum Press, New York (1996), p. 15.
[65] V. Bondarenko, J. W. Brill, J. Duma, and C. Schlenker, Solid State Commun. **129**, 211 (2004).
[66] A. M. Gabovich, M. S. Li, M. Pekala, H. Szymczak, and A. I. Voitenko, J. Phys.: Condens. Matter **14**, 9621 (2002).
[67] T. Ekino, T. Takasaki, T. Muranaka, J. Akimitsu, and H. Fujii, Phys. Rev. B **67**, 094504 (2003).
[68] H. Padamsee, J. E. Neighbor, and C. A. Shiffman, J. Low Temp. Phys. **12**, 387 (1973).
[69] T. Katsufuji, T. Tanabe, T. Ishikawa, Y. Fukuda, T. Arima, and Y. Tokura, Phys. Rev. B **54**, 14230 (1996).
[70] C. Wang, B. Giambattista, C. G. Slough, R. V. Coleman, and M. A. Subramanian, Phys. Rev. B **42**, 8890 (1990).
[71] T. Ekino and J. Akimitsu, Jpn. J. Appl. Phys., Suppl. **26**, Suppl. 26-3, 625 (1987).
[72] T. Ekino and J. Akimitsu, Physica B **194–196**, 1221 (1994).
[73] T. Ekino, S. Hashimoto, T. Takasaki, and H. Fujii, Phys. Rev. B **64**, 092510 (2001).
[74] T. Timusk and B. Statt, Rep. Prog. Phys. **62**, 61 (1999).
[75] J. C. Campuzano, M. R. Norman, and M. Randeria, cond-mat/0209476.
[76] T. Timusk, Solid State Commun. **127**, 337 (2003).
[77] J. C. Phillips, A. Saxena, and A. R. Bishop, Rep. Prog. Phys. **66**, 2111 (2003).
[78] A. Damascelli, Z. Hussain, and Z.-X. Shen, Rev. Mod. Phys. **75**, 473 (2003).
[79] V. M. Loktev, R. M. Quick, and S. G. Sharapov, Phys. Rep. **349**, 1 (2001).
[80] A. Yurgens, D. Winkler, T. Claeson, S.-J. Hwang, and J.-H. Choy, Int. J. Mod. Phys. B **13**, 3758 (1999).
[81] M. Suzuki and T. Watanabe, Phys. Rev. Lett. **85**, 4787 (2000).
[82] V. M. Krasnov, A. E. Kovalev, A. Yurgens, and D. Winkler, Phys. Rev. Lett. **86**, 2657 (2001).
[83] T. Shibauchi, L. Krusin-Elbaum, M. Li, M. P. Maley, and P. H. Kes, Phys. Rev. Lett. **86**, 5763 (2001).
[84] L. Krusin-Elbaum, T. Shibauchi, and C. H. Mielke, Phys. Rev. Lett. **92**, 097005 (2004).
[85] Y. Yanase, T. Jujo, T. Nomura, H. Ikeda, T. Hotta, and K. Yamada, Phys. Rep. **387**, 1 (2003).
[86] A. Yurgens, D. Winkler, T. Claeson, S. Ono, and Y. Ando, Phys. Rev. Lett. **90**, 147005 (2003).
[87] T. Ekino, Y. Sezaki, and H. Fujii, Phys. Rev. B **60**, 6916 (1999).

[88] V. M. Krasnov, A. Yurgens, D. Winkler, P. Delsing, and T. Claeson, Phys. Rev. Lett. **84**, 5860 (2000).
[89] A. I. Larkin and Yu. N. Ovchinnikov, Zh. Éksp. Teor. Fiz. **51**, 1535 (1966) [Sov. Phys. JETP **24**, 1035 (1966)].
[90] K. M. Munz and W. Wonneberger, Z. Phys. B: Condens. Matter **79**, 15 (1990).
[91] M. I. Visscher and G. E. W. Bauer, Phys. Rev. B **54**, 2798 (1996).
[92] K. Sano, Prog. Theor. Phys. **109**, 11 (2003).
[93] K. Sano, Physica E **18**, 245 (2003).

This article was published in English in the original Russian journal. Reproduced here with stylistic changes by AIP.

Temperature anomalies of the resistivity and thermopower of polycrystalline copper subjected to plastic deformation

V. M. Dmitriev

B. Verkin Institute for Low Temperature Physics and Engineering, National Academy of Sciences of Ukraine, pr. Lenina 47, Kharkov 61103, Ukraine; International Laboratory of High Magnetic Fields and Low Temperatures, 53-421 Wroclaw, Poland

N. N. Prentslau, V. N. Svetlov, and V. B. Stepanov

B. Verkin Institute for Low Temperature Physics and Engineering, National Academy of Sciences of Ukraine, pr. Lenina 47, Kharkov 61103, Ukraine

(Submitted June 4, 2004)
Fiz. Nizk. Temp. **31**, 94–98 (January 2005)

The results of an experimental study of the resistivity ρ and thermopower in the temperature range 4.2–300 K are presented for commercial-grade copper subjected to plastic deformation at room temperature. A number of inter-correlated anomalies, due to dislocations, are observed in the temperature dependence of the resistivity and thermopower. The probable cause of these anomalies is the resonance scattering of free electrons and thermal phonons by electrons localized near the dislocations. © *2005 American Institute of Physics.* [DOI: 10.1063/1.1820371]

INTRODUCTION

Measurement of the resistivity ρ is known to be an efficient macroscopic means of studying the structural state of a metal. It has been noted[1–4] that the change in resistivity resulting from the introduction of dislocations into a metal displays a number of features as the temperature is lowered which are due to the scattering of electrons by the dislocations themselves. For example, these features can be manifested in the form of a step on the curve of the additional resistivity in a certain temperature interval (30–150 K); as was noted in Ref. 4, they do not depend very much on the degree and means of deformation.

However, besides this step, which has been observed by many authors,[1,2,4] there are also features in the resistivity at lower temperatures ($T \sim 10$ K),[3] which are also sensitive to the deformation state of the metal. Thus the temperature dependence $\rho(T)$ of deformed copper exhibits features of the resistivity both at comparatively high temperatures (30–150 K) and at low temperatures (<30 K). None of the theoretical models currently known to us predicts anomalies caused by plastic deformation in the temperature dependence of the resistivity.

Many papers have been published on the behavior of the thermopower in pure metals[5–8] and the effect of various impurities[9] and plastic deformation[10,11] on its temperature dependence. As a rule, those studies examined the features of ρ and of the thermopower in narrow temperature intervals, and from those sources it is difficult to assess the behavior of ρ and of the thermopower of deformed copper over the temperature interval from helium to room temperatures and to discern the temperature correlation between the features of the resistivity and thermopower.

The present study was devoted to investigating the temperature dependence of ρ and of the thermopower of deformed copper in the temperature interval 4.2–300 K. A comparative analysis of the two temperature dependences is carried out to establish the temperature correlation between the features of ρ of the thermopower.

EXPERIMENTAL TECHNIQUE

In our experiment, part of a commercial-grade copper wire 0.47 mm in diameter was rolled at room temperature to a strip 0.05 mm thick. Figure 1 shows a diagram of the sample, where part A of the wire was rolled and part B was not.

To distinguish the contribution due to dislocations, the samples were annealed after rolling, since it is well known that the resistivity of a metal increases as a result of plastic deformation because of the introduction of defects in it—vacancies, dislocations, etc. It is also known that processes of recovery and recrystallization occur in deformed metals during a controlled heat treatment. For example, a partial annealing of defects, vacancies in particular, takes place in copper even at close to room temperatures. Therefore to remove the vacancies formed we annealed our samples at 100 °C for one hour.

It follows from Fig. 1 that the copper sample comprises a differential thermocouple, one of its metals being the rolled wire (A) and the other the unrolled wire (B). The transition from the deformed to the undeformed part of the copper is essentially equivalent to a junction between different metals in an ordinary thermocouple. The resistivity measurements were done by the four-probe method (sensitivity $\sim 10^{-7}$ V, measurement current ~ 0.1 A) simultaneously on the deformed and undeformed parts of the wire. In addition, for temperatures in the range 4.2–60 K measurements were made using a bridge circuit.

In the thermopower measurements the wire leads were held at one temperature, e.g., room temperature, while the junctions between the deformed and undeformed parts were held at temperatures T_1 and T_2, one of which was constant and the other varied from room temperature to helium tem-

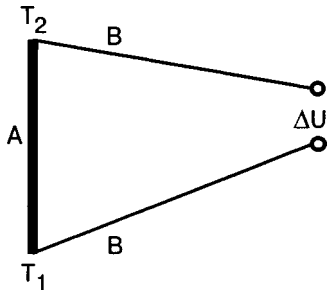

FIG. 1. Diagram of the sample for measurement of the thermopower: segment A is the deformed part of the wire, part B is undeformed.

perature. The voltage $\Delta U=\int_{T_1}^{T_2}(S_B-S_A)dT$ is the thermopower, and the differential difference thermopower is determined as $S_{AB}=\lim_{\Delta T\to 0}\Delta U/\Delta T$. It is easily shown that $S_{AB}=S_B-S_A$, where S_B and S_A are the absolute or specific thermopowers of metals B and A. It is usually assumed[9] that the absolute thermopower consists of two terms, $S=S_d+S_g$, where S_d is the diffusion thermopower and S_g is due to phonon drag. For certain metals, copper in particular, at $T\geqslant 0.05Q_D$ the term $S_g\gg S_d$, and a maximum is observed on the temperature curve of S at temperatures $\sim 0.2Q_D$ (here Q_D is the Debye temperature). Such nonmonotonic behavior, as has been confirmed by numerous studies,[7–10] is a result of phonon drag and is very sensitive to various forms of impurities and deformations.

EXPERIMENTAL RESULTS AND DISCUSSION

Curve *1* in Fig. 2a shows the temperature dependence of the ratio of the resistivities of the undeformed and deformed parts of the wire.

It is clearly seen in the figure that the deformation contribution is manifested as nonmonotonic temperature dependence of the ratio of the resistivities of the undeformed (ρ) and deformed (ρ_d) wires. Figures 2b and 2c show an enlarged view of the given fragments of the $\rho/\rho_d(T)$ curve (curve *1* in Fig. 2a) in temperature intervals where the dislocation contribution is manifested.

In the determination of the temperature dependence of the thermopower, metal B (Fig. 1) was the same undeformed wire of commercial-grade copper that was used in the resistivity measurements, while metal A was the same deformed wire; temperature T_1 was held constant (0 °C) and T_2 was varied from room to helium temperature.

Curve *1* in Fig. 3 shows the temperature dependence of the thermopower of the given pair of metals. Curve *2* describes the behavior of the differential difference thermopower S_{AB} in this same temperature region. Naturally this curve, as the derivative, reflects the behavior of the integral thermopower (curve *1*).

Thus in the measurements of the temperature dependences of the thermopower and resistivity our main objective was to distinguish the dislocation contribution after the vacancies were annealed out, and in addition to note the correspondence between the features on these curves, since these quantities are related by the Wiedemann–Franz law.

For a comparative analysis of $\rho/\rho_d(T)$ and $S_{AB}(T)$ see Fig. 2. Curve *1* describes the deformation contribution to the

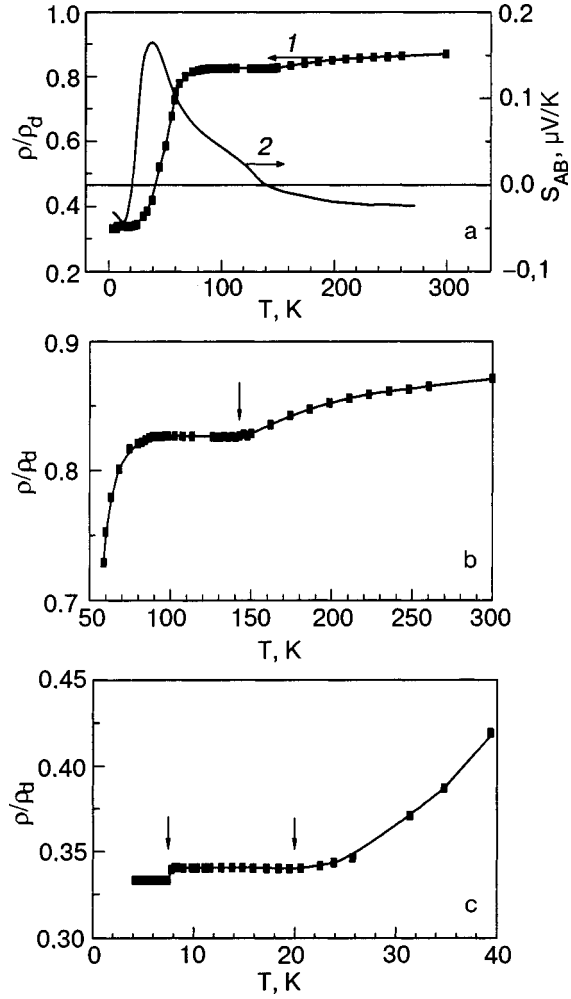

FIG. 2. Temperature dependence of the ratio of the resistivities of the undeformed (ρ) and deformed (ρ_d) parts of the sample (*1*) and of the differential difference thermopower S_{AB} (*2*). The temperature dependence of ρ/ρ_d is shown on an expanded scale in the interval 50–300 K (b) and 4.2–40 K (c).

temperature dependence of the ratio of the resistivity ρ_d of the undeformed part of the sample to that of these undeformed part. Curve *2* demonstrates the deformation contribution to the temperature dependence of the differential difference thermopower $S_{AB}=S_B-S_A$.

One notices the influence of the correlation of the characteristic features on the curves. For clarity the features of

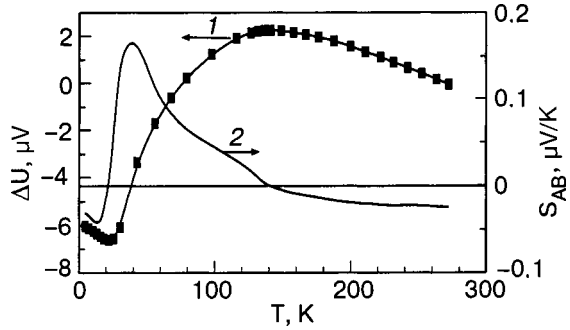

FIG. 3. Temperature dependence of the thermopower ΔU of the sample (*1*) and the differential difference thermopower S_{AB} (*2*).

the dependence $\rho/\rho_d(T)$ are shown on an enlarged scale and are indicated by arrows in Figs. 2b and 2c.

For example, at a temperature of $\sim$140 K the $S_{AB}(T)$ curve has a feature in the form a passage through zero. This corresponds to a plateauing of the $\rho/\rho_d(T)$ curve as the temperature is lowered (see Fig. 2b). The next feature is at a temperature of $\sim$40 K: a maximum is observed on the $S_{AB}(T)$ curve and an inflection point on the $\rho/\rho_d(T)$ curve.

It should be noted that these two features correspond to a step on the temperature dependence of the difference of the resistivities of the deformed and undeformed parts of the sample and are analogous to those observed in Refs. 1 2, and 4.

As the temperature is decreased further we again see a passage through zero on curve *2* at a temperature of $\sim$20 K, which corresponds to plateauing of curve *1* (see Fig. 2c). The next feature on curve *2* takes the form of a minimum at $\sim$12 K, which corresponds to a sharp drop on curve *1* at $\sim$8 K. It should be noted that in Ref. 3 this feature was manifested either as nonmonotonic behavior of $\rho(T)$ in the $\sim$10 K region for samples of pure copper deformed by bending or as a plateau in a certain temperature interval. The slight disagreement of the temperatures at which the features appear on curves *1* and *2* (Fig. 2) can be explained by the circumstance that the Wiedemann–Franz law is no longer obeyed at low temperatures.

Thus it can be assumed that such nonmonotonic behavior of the two curves characterizes a change of mechanisms for the scattering of electrons on dislocations. One possible explanation of this behavior is the presence of quasilocal vibrational modes of the dislocations.[2] Indeed, such an hypothesis is justified if it is assumed that a mechanism analogous to that considered in Ref. 12 is operating in our system (in that paper the influence of impurity-related quasilocal modes on the resistivity in the Cu–Be system was investigated theoretically and experimentally). At least the low-temperature intervals in which the anomalies were observed in the impurity resistivity in Ref. 12 and in the present paper are practically the same. We note, however, that this hypothesis has not yet found rigorous experimental confirmation, and the influence of quasilocal modes on the resistivity of polycrystalline samples subjected to plastic deformation remains a topic for further study.

Another explanation is based on the fact that dislocations in a metal are known to influence various thermodynamic and kinetic characteristics of the electron gas. For example, the thermopower is due not only to the onset of electron diffusion in the bulk of the conductor as a result of a temperature gradient between the two contacts but also to potential jumps resulting from a difference of the chemical potentials of electrons in the contact materials. In our case we are talking about a contact between deformed and undeformed parts of the wire (see Fig. 1).

As was noted in Ref. 13, the influence of dislocations leads to a dislocation shift of the chemical potential. In particular, localized electronic states arise on a rectilinear edge dislocation,[14] and a shift of the chemical potential is caused by electrons leaving the conduction band for dislocation levels. In a bulk metal this leads to a lowering of the chemical potential of the electrons. In our case part A in Fig. 1 is such a metal.

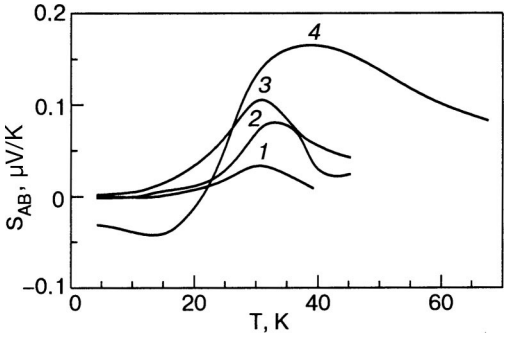

FIG. 4. Temperature dependence of the differential difference thermopower of a sample under tensile loads of 10 (*1*), 15 (*2*), 20 (*3*) kg/mm^2; the temperature dependence of S_{AB} from Fig. 3 (*4*).

Unfortunately, the presence of characteristic resonance energies or temperatures corresponding to the features on our experimental temperature curves of the resistivity and thermopower was not dicussed in the papers cited, although it was mentioned in Ref. 15 that it remains possible that interesting features appear in connection with the possibility of resonance scattering of free electrons and thermal phonons on electrons localized near dislocations.

To estimate the dislocation density ρ_N we use the fact that in polycrystalline copper the resistivity increment $\Delta\rho$ due to dislocations increases in proportion to the dislocation density. Therefore, using the coefficients of proportionality given for various metals in Refs. 16 and 17, we obtain in our case $\rho_N \leqslant 10^{14}$ m^2. Such a dislocation density is also characteristic for the samples in Ref. 3, indicating that in both cases the densities are rather high.

It should be noted that the features on the S_{AB} curve below 40 K are more sensitive to the degree of deformation in comparison to the higher-temperature parts. This effect was mentioned back in Ref. 10, where the rolling of copper had a substantial influence on the phonon drag effect. It is therefore of interest to compare the influence of various forms of deformation on the behavior of the differential difference thermopower in this temperature interval.

Figure 4 shows a comparison of the behavior of the differential thermopower S_{AB} in the region of large "elastic," linear strains and during plastic deformation by rolling. The experiment was done according to the same scheme (Fig. 1), only part A was subjected to linear extension rather than plastic deformation. As a criterion of the region of elasticity we used the absence of thermopower when the load was removed. Curves *1–3* in Fig. 4 show the variation of the differential thermopower $S_{AB}(T)$ for different degrees of tensile loading. For comparison, curve *4* reflects the $S_{AB}(T)$ dependence for the same sample under plastic deformation (see curve *2* in Fig. 3).

The maxima on curves *1–3*, in the 30–35 K, region differ slightly in position from the maximum on curve *4*, at $\sim$40 K; this is evidence that mechanisms of electron scattering on dislocations are turned on at these temperatures, and that circumstance is reflected on the $\rho(T)$ curves. Unlike curves *1–3*, curve *4* passes through zero at $T\sim$20 K and has a minimum at $T\sim$12 K, thus indicating a different scattering

mechanism resulting from the different kind of deformation (plastic) and which is confirmed by the features of the resistivity.

CONCLUSIONS

Summarizing what we have said, we have for the first time carried out a comparative analysis of the temperature dependence of the resistivity and thermopower on the same sample with the same plastic deformation over a wide range of temperatures, 4.2–300 K. Besides the known features of the resistivity above 40 K, we have observed new anomalies in the region $\sim 8-12$ K and ~ 20 K, which also correlate with features of the thermopower. These features are probably due to the existence of resonance scattering of free electrons and thermal phonons on electrons localized near dislocations. Further studies will presumably make it possible to distinguish and investigate the mechanisms by which the electrons are scattered by different dislocations and also to study the deviations from the Wiedemann–Franz law.

In closing the authors thank K. A. Chishko, S. N. Smirnov, and A. I. Kopeliovich for helpful discussions and also E. S. Syrkin for calling our attention to Ref. 12.

[1] Z. S. Basinski, J. S. Dugdale, and A. Howie, Philos. Mag. **8**, 1989 (1963).
[2] V. F. Gantmakher and G. I. Kulesko, Zh. Éksp. Teor. Fiz. **67**, 2335 (1974) [Sov. Phys. JETP **40**, 1158 (1975)].
[3] V. M. Dmitriev, I. L. Lebedeva, and N. N. Prentslau, Fiz. Nizk. Temp. **27**, 657 (2001) [Low Temp. Phys. **27**, 484 (2001)].
[4] G. N. Kulesko, Zh. Éksp. Teor. Fiz. **72**, 2167 (1977) [Sov. Phys. JETP **45**, 1138 (1977)].
[5] N. Cusack and P. Kendall, Proc. Phys. Soc. London **72**, 898 (1958).
[6] V. A. Rowe and P. A. Schroeder, J. Phys. Chem. Solids **31**, 1 (1970).
[7] R. J. Gripshover, J. B. Van Zytveld, and J. Bass, Phys. Rev. **163**, 163 (1967).
[8] E. R. Rumbo, J. Phys. F: Metal Phys. **6**, 85 (1976).
[9] R. P. Huebener, Phys. Rev. **171**, 634 (1968).
[10] R. H. Kropschot and F. J. Blatt, Phys. Rev. **116**, 617 (1959).
[11] M. J. Druyvesteyn and D. J. Van Ooijen, Appl. Sci. Res. **5**, 437 (1956).
[12] V. N. Morgun, E. S. Syrkin, and S. B. Feodos'ev, Fiz. Nizk. Temp. **7**, 244 (1981) [Sov. J. Low Temp. Phys. **7**, 119 (1981)].
[13] V. D. Natsik, S. N. Smirnov, and N. É. Tikhonenkov, Fiz. Nizk. Temp. **19**, 931 (1993) [Low Temp. Phys. **19**, 662 (1993)].
[14] V. A. Slyusarev and K. A. Chishko, Fiz. Met. Metalloved. **58**, 877 (1984).
[15] V. D. Natsik and L. D. Potemina, Zh. Éksp. Teor. Fiz. **79**, 2398 (1980) [Sov. Phys. JETP **52**, 1215 (1980)].
[16] L. M. Clarebrough, M. E. Hargreaves, and M. H. Loretto, Philos. Mag. **6**, 807 (1961).
[17] L. M. Clarebrough, M. E. Hargreaves, and M. H. Loretto, Philos. Mag. **7**, 115 (1962).
[18] J. Friedel, *Dislocations*, Pergamon Press, Oxford (1964), Mir, Moscow (1967).

Translated by Steve Torstveit

High-frequency polariton waves on a metal–vacuum interface

S. N. Smirnov*

B. Verkin Institute for Low Temperature Physics and Engineering, National Academy of Sciences of Ukraine, pr. Lenina 47, Kharkov 61103, Ukraine

V. D. Natsik

B. Verkin Institute for Low Temperature Physics and Engineering, National Academy of Sciences of Ukraine, pr. Lenina 47, Kharkov 61103, Ukraine; V. N. Karazin Kharkov National University, pl. Svobody 4, Kharkov 61077, Ukraine

L. D. Natsik

B. Verkin Institute for Low Temperature Physics and Engineering, National Academy of Sciences of Ukraine, pr. Lenina 47, Kharkov 61103, Ukraine; Kharkov Military University, pl. Svobody 6, Kharkov 61043, Ukraine

(Submitted June 7, 2004)
Fiz. Nizk. Temp. **31**, 99–108 (January 2005)

Some novel aspects of the problem of linear electromagnetic–plasma waves on a plane metal–vacuum interface are investigated. The analysis is based on Maxwell's equations for the electric and magnetic fields, supplemented by the hydrodynamic equation for the electron plasma of the metal. This system of equations admits the existence of specific long-wavelength inhomogeneous eigenmodes of the polariton type (E waves) having frequencies ω of the order of the plasma frequency ω_p of the conduction electrons and a polarization direction of the magnetic field oscillations that lies in the plane of the interface and perpendicular to the direction of propagation along the boundary. These waves, which have not been discussed before, are the result of hybridization of longitudinal electron-density waves (plasmons) of the metal with the transverse modes (photons) of the metal and vacuum. In particular, it is shown that the excitation of plasmons in the bulk of the metal is accompanied by the appearance of an electromagnetic wave localized near the surface, consisting of a mixture of metallic and vacuum photons. This inhomogeneous wave has the dispersion relation of of bulk plasmons and exists in the frequency band that is characteristic for such plasmons, $\omega_p < \omega < \sqrt{2}\omega_p$; here the characteristic values of the localization parameter are of the order of c/ω_p (c is the speed of light in vacuum). For standard metals this parameter has values of 10–50 nm, and these modes can therefore play an important role in the description of electromagnetic resonances and radiation effects in metallic nanostructures. © *2005 American Institute of Physics.* [DOI: 10.1063/1.1820374]

INTRODUCTION

The interaction of electromagnetic radiation with metal surfaces has been studied for many decades, and the experimental and theoretical results have been described in many review articles and monographs (see, e.g., Refs. 1–5). The overwhelming majority of the theoretical papers addressing this problem have been devoted to the study of the diverse linear and nonlinear effects due to the specific and extremely significant frequency dispersion of the dielectric function $\hat{\varepsilon}(\omega)$ of metals: the vanishing of $\hat{\varepsilon}(\omega)$ in the vicinity of the characteristic plasma frequency ω_p of the conduction electrons; the large negative values of $\hat{\varepsilon}(\omega)$ for $\omega \ll \omega_p$, and the presence of an imaginary component of $\hat{\varepsilon}(\omega)$ due to the dissipative properties of the electrons.

The propagation of electromagnetic waves in the bulk of a metal is ordinarily analyzed with allowance for the spatial dispersion of the dielectric function, i.e., the dependence of $\hat{\varepsilon}(\omega, \mathbf{k})$ on the wave vector $\mathbf{k}$.[6] In the long-wavelength limit $|\mathbf{k}|a \ll 1$ (a is the characteristic interatomic distance) this dependence is due to the finite value of the compressibility of a degenerate electron plasma,[3–7] and taking it into account leads to the well-known dispersion relation $\omega_l(\mathbf{k})$ for longitudinal charge-density waves (plasmons) in a homogeneous and isotropic metal:

$$\omega_l^2(\mathbf{k}) = \omega_p^2 + v_p^2 k^2, \tag{1}$$

where the dispersion relation parameter v_p has a value of the order of the electron velocity v_F on the Fermi surface (the quantity v_p^2 is proportional to the derivative of the quantum pressure $p(n)$ in the electron plasma with respect to its density n). The finite compressibility of the electron plasma is also taken into account in constructing the general theory of charge-density waves localized near the free surface of a metal (surface plasmons),[4,5] for which the dispersion relation $\omega_s(k)$ is described by the expression

$$\omega_s^2(k) = \frac{1}{2}[\omega_p^2 + v_p^2 k^2 + v_p |k| (2\omega_p^2 + v_p^2 k^2)^{1/2}], \tag{2}$$

where k is the wave number of the surface mode.

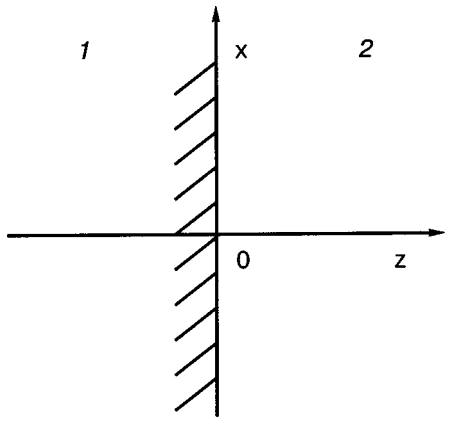

FIG. 1. Geometry of the problem: *1*—metal, *2*—vacuum.

In the theoretical description of the many specific phenomena of linear and nonlinear interaction of electromagnetic waves with atomically smooth metal surfaces, particular attention is paid to frequencies $\omega \ll \omega_p$, and the effects of spatial dispersion are usually neglected against the background of more significant effects due to frequency dispersion and damping. The high-frequency region $\omega \gtrsim \omega_p$ in this problem has remained little studied, apparently because of the difficulties of conducting experiments at such frequencies. We have not found a systematic description and classification of electromagnetic waves on the metal–vacuum interface at frequencies $\omega \gtrsim \omega_p$ in the literature that is available to us, although the features of the dispersion of the dielectric function of an infinite metal at high frequencies have been studied in some detail.[2,6] At such frequencies the dissipation in real metals is small, and one therefore expects a clearer manifestation of not only spatial dispersion effects but also of some other dynamical features of the modes of oscillation of a spatially inhomogeneous system, which at low frequencies are masked by dissipation.

In the analysis of the changes introduced in the electromagnetic–plasma modes by a plane metal surface (Fig. 1) it is convenient to employ a diagram in the (ω^2, k^2) plane (Fig. 2). Shown schematically on this diagram are the dispersion relations of photons in vacuum, $\omega_{\rm ph}^2(\mathbf{k}) = c^2k^2$, and of photons $\omega_t^2(\mathbf{k}) = \omega_p^2 + c^2k^2$ and plasmons $\omega_l^2(\mathbf{k}) = \omega_p^2 + v_p^2k^2$ in an unbounded metal (c is the speed of light in vacuum). In a homogeneous physical system (metal or vacuum) all of these modes are uniform plane waves of the electric field $\mathbf{E}(\mathbf{r},t)$ and magnetic field $\mathbf{H}(\mathbf{r},t)$, which have a constant amplitude $\mathbf{A}$ and are classified according to the values of the wave vector $\mathbf{k}$:

$$\{\mathbf{E}(\mathbf{r},t);\mathbf{H}(\mathbf{r},t)\} = \mathbf{A}\exp[i(\mathbf{kr} - \omega(\mathbf{k})t]. \qquad (3)$$

Analogous formulas describe the oscillations of the electron charge density and current in an unbounded metal. The values of $\mathbf{k}$ occupy continuously all the points of reciprocal space (in a metal with a boundary $|k|a < 1$), but for any chosen direction of propagation $\mathbf{k}$, free oscillations exist only on the lines in the (ω^2, k^2) plane shown in Fig. 2.

In a spatially inhomogeneous metal–vacuum system a hybridization of the waves listed above occurs, and the free oscillations take the form of mixed waves, which in the case of a plane boundary remain uniform along the boundary but

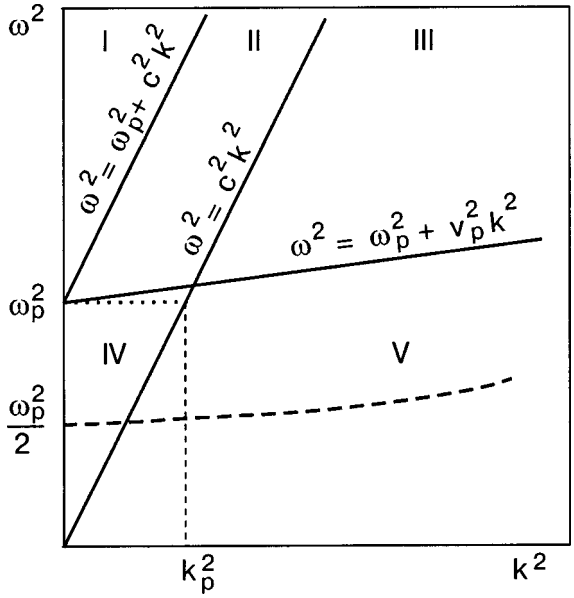

FIG. 2. Schematic illustration of the dispersion relations for electromagnetic and plasma waves in systems of infinite extent (vacuum and metal) and also the existence regions I–V of inhomogeneous electromagnetic–plasma modes in a metal–vacuum system with a plane interface.

acquire substantial inhomogeneity in the transverse direction, i.e., the complex amplitudes become dependent on the transverse coordinate z:

$$\{\mathbf{E}(\mathbf{r},t);\mathbf{H}(\mathbf{r},t)\} = \{\boldsymbol{\mathcal{E}}(z);\boldsymbol{\mathcal{H}}(z)\}\exp[i(kx - \omega t)]. \qquad (4)$$

The dispersion relations for the waves and their existence regions on the (ω^2, k^2) plane are thereby altered significantly: new existence lines appear, e.g., the plot of dispersion relation (2), $\omega^2 = \omega_s^2(k)$, shown by the dashed curve in Fig. 2;[1)] in addition to the lines there are several existence sectors I–V with dispersion relations specific for each of them and a specific character of the spatial distribution of the fields.

A detailed description and classification of such oscillations will be the subject of a separate paper; in the present article we analyze two particular examples of inhomogeneous waves existing in sectors III and IV in Fig. 2. These waves are hybrid modes that arise as a result of surface mixing of transverse electromagnetic (photon) modes having the dispersion relations $\omega_{\rm ph}^2(\mathbf{k}) = c^2k^2$ and $\omega_t^2(\mathbf{k}) = \omega_p^2 + c^2k^2$ with plasmons having the dispersion relation $\omega_l^2(\mathbf{k}) = \omega_p^2 + v_p^2k^2$: they propagate along the interface, remaining delocalized on one side (in the vacuum or the metal) and exponentially localized on the other (in the metal or the vacuum, respectively). In the terminology of the electrodynamics of continuous media they can be classified as waves of the polariton type.[2,3] A specific feature of these waves is the substantially different character of the spatial distribution of the electric and magnetic fields. In particular, at frequencies $\omega > \omega_p$ there exist inhomogeneous waves with a magnetic field that is localized on both sides of the surface and with electric-field, electron-charge, and current oscillations that are delocalized inside the metal.

It is important to note that for the waves under discussion the characteristic spatial scale of the inhomogeneity (localization) in the distribution of the wave fields in the vicinity of the metal interface is determined by the parameter

$k_p^{-1}=c/\omega_p$, which for typical metals has a value of the order of 10–50 nm. This means that the field inhomogeneities and resonances associated with these modes can be important in the analysis of the high-frequency electromagnetic and radiation properties of metallic nanostructure systems, the study of which has in recent years has again become a topical problem in solid-state physics.

1. BASE SYSTEM OF EQUATIONS AND BOUNDARY CONDITIONS

The analysis of the problem under discussion is based on well-developed concepts wherein the low-energy excitations of the system of conduction electrons in a metal can be divided into two branches.[7,10] The first of these is the Fermi branch of one-electron excitations with a certain dispersion relation $\varepsilon(\mathbf{p})$ and a corresponding Fermi energy ε_F, which is determined by the average density of collectivized electrons, n_0. The second branch, of the Bose type, comprises collective oscillations of the electron density $\tilde{n}=n-n_0$ and current which are coupled to the oscillations of the electric and magnetic fields $\mathbf{E}$ and $\mathbf{H}$. It is also known[3–5,8] that in metals the dynamics of collective motions of the electron plasma with characteristic spatial scales greater than the interatomic distance is described rather well in the hydrodynamic approximation. In that approximation the ion core of the metal is treated as a continuously distribution positively charged ''jelly'' that compensates the equilibrium distribution of the electron charge, and the electron plasma is identified as a liquid whose motion is characterized by fields of density $n(\mathbf{r},t)$, velocity $\mathbf{v}(\mathbf{r},t)$, and interelectron stress $P_{ik}(\mathbf{r},t)$ which are interrelated by the hydrodynamic equation

$$m^*n\left[\frac{\partial \mathbf{v}}{\partial t}+(\mathbf{v}\cdot\nabla)\mathbf{v}\right]=-\nabla\cdot\hat{P}-en\mathbf{E}-\frac{e}{c}n(\mathbf{v}\times\mathbf{H}) \tag{5}$$

Here e and m^* are the modulus of the charge and the effective mass of a one-electron excitation, $\hat{P}$ is the stress tensor introduced above, and $\mathbf{E}(\mathbf{r},t)$ and $\mathbf{H}(\mathbf{r},t)$ are the local values of the macroscopic (averaged over a volume with linear dimensions of the order of a) electric and magnetic fields, which satisfy Maxwell's equations:

$$\text{curl}\ \mathbf{H}-\frac{1}{c}\frac{\partial \mathbf{E}}{\partial t}=-\frac{4\pi e}{c}n\mathbf{v},\quad \text{curl}\ \mathbf{E}+\frac{1}{c}\frac{\partial \mathbf{H}}{\partial t}=0,$$

$$\text{div}\,\mathbf{E}=-4\pi e(n-n_0),\ \ \text{div}\,\mathbf{H}=0. \tag{6}$$

Equations (5) and (6) turn into a closed system of equations describing the self-consistent evolution of the electron plasma and and electromagnetic field if they are supplemented with an expression for the stress tensor P_{ik} that specifies explicitly its relation to the variations of the density $\tilde{n}$ and velocity $\mathbf{v}$. Strictly speaking, such a relation has been obtained in a consistent approach only by solving the quantum kinetic equation for the conduction electrons.[6] However, in the solution of the problem we are interested in, that of short-wavelength oscillations of the electron plasma, one can use a phenomenological linear expansion of P_{ik} in powers of $\tilde{n}$ and $\mathbf{v}$.[3–5] If, moreover, one is considering an isotropic model of the metal and neglects dissipation, then this expansion has the form

$$P_{ik}=p(\mathbf{r},t)\,\delta_{ik}=[p_0+v_p^2m^*\tilde{n}(\mathbf{r},t)]\,\delta_{ik}. \tag{7}$$

Here $p(\mathbf{r},t)$ and p_0 are the total and equilibrium values of the pressure in the electron plasma, and v_p^2 is a coefficient characterizing its compressibility. In a simple model of the conduction electrons the parameter v_p^2 is given by the expression $v_p^2=3/5v_F^2$, where v_F is the electron velocity on the Fermi surface.[3,4]

A quantum statistical analysis shows that expansion (7) describes the main features of the dynamic behavior of the electron plasma in a metal rather well at frequencies ω and wave numbers k satisfying the inequalities $\tau^{-1}\ll\omega\sim\omega_p$ and $|k|<k_c$, where $k_c=\omega_p/v_p\sim 1/a$, and τ is a relaxation time characterizing the dissipative properties of the electrons. At frequencies considerably greater than ω_p relation (7) breaks down on account of the complicating influences of interband transitions and excitation of the electron shells of the ions.

In a description of the joint free oscillations of the electron plasma together with the electromagnetic field it is assumed that the density $n(\mathbf{r},t)$ is nonzero only in the metal (including the boundary S), that the condition of global electrical neutrality of the metal holds, and that on the surface the component of the electron plasma velocity along the surface normal $\mathbf{s}$ is zero:

$$\int\ [n(\mathbf{r},t)-n_0]d^3\mathbf{r}=0, \tag{8}$$

$$\mathbf{s}\cdot\mathbf{v}(\mathbf{r},t)=0\ \ \text{for}\ \ \mathbf{r}\in S. \tag{9}$$

In Eq. (8) the integration is over the volume of the metal. The natural conditions that all physical fields related by the system of equations (5)–(7) be finite and the conditions of continuity of all components of the vectors $\mathbf{E}(\mathbf{r},t)$ and $\mathbf{H}(\mathbf{r},t)$ on the surface S between the metal and vacuum should also hold: we note that boundary conditions (9) ensure the continuity of the normal component of the vector $\mathbf{E}$ at the interface.[11]

We shall consider small free oscillations, with angular frequency ω, of the electromagnetic field and plasma in a structurally homogeneous and isotropic metal ($n_0=\text{const}$). Assuming that the time dependence of all the dynamic fields is given by the factor $\exp(-i\omega t)$, linearizing equations (5)–(7), and eliminating the plasma dynamical variables from these equations, we obtain a closed system of equations determining the spatial distribution of the electric field $\mathbf{E}(\mathbf{r},t)$ and magnetic field $\mathbf{H}(\mathbf{r},t)$:

$$v_p^2\nabla\,\text{div}\,\mathbf{E}+(\omega^2-\omega_p^2)\mathbf{E}-i\omega c\ \ \text{curl}\ \ \mathbf{H}=0, \tag{10a}$$

$$c\ \text{curl}\ \ \mathbf{E}-i\omega\mathbf{H}=0. \tag{10b}$$

Here ω_p is the plasma frequency, which is related to the mean density n_0, effective mass m^*, and electron charge e by the expression

$$\omega_p^2=\frac{4\pi n_0e^2}{m^*}. \tag{11}$$

We note that the equation $\text{div}\,\mathbf{H}=0$ is satisfied identically by virtue of Eq. (10b).

Equations (10) are valid in a metal; these same equations describe the fields in the vacuum if one sets $\omega_p=0$ and $v_p=0$ in them. The solutions of the system of equations (10)

permit one to find the spatial distribution of the electron charge $n(\mathbf{r})$ and the current density $\mathbf{j}(\mathbf{r})$ in the metal, according to the formulas

$$n = n_0 - \frac{1}{4\pi e}\operatorname{div}\mathbf{E}, \tag{12}$$

$$\mathbf{j} = -en_0\mathbf{v} = \frac{i}{4\pi\omega}(\omega_p^2\mathbf{E} - v_p^2\nabla\operatorname{div}\mathbf{E}). \tag{13}$$

The equations given above are valid for any shape of the metal–vacuum interface, but in this paper we restrict consideration to the simplest geometry of the problem: we shall assume that the surface S is a plane and use a rectangular Cartesian coordinate system (x,y,z) with the z axis perpendicular to the surface and the x and y axes in the plane (Fig. 1). By virtue of the homogeneity and isotropicity of the metal we can without loss of generality seek the modes in the form (4). The amplitudes of $\boldsymbol{\mathcal{E}}(z)$ and $\boldsymbol{\mathcal{H}}(z)$ must satisfy the conditions of finiteness and continuity at all values of z, including the point $z=0$. Formula (13) and the boundary condition (9) imply an auxiliary condition on the components of the vector $\boldsymbol{\mathcal{E}}(z)$:

$$v_p^2[\mathcal{E}_z''(z) + ik\mathcal{E}_x'(z)] = \omega_p^2\mathcal{E}_z(z) \text{ at } z = -0; \tag{14}$$

here and below we use the notation $df/dz \equiv f'$. According to Ref. 11, condition (14) is equivalent to the condition of continuity of $\mathcal{E}_z(z)$ at $z=0$.

If the vector equations (10) are written for the components in the coordinate system chosen above, a remarkable thing happens. First, the six equations (10) decompose into two independent subsystems giving two sets of unknown functions, $\{\mathcal{E}_x,\mathcal{E}_z,\mathcal{H}_y\}$ and $\{\mathcal{H}_x,\mathcal{H}_z,\mathcal{E}_y\}$; second, since the auxiliary condition (14) pertains only to the solutions of the first of these subsystems of equations, the independence of the solutions is not destroyed by the boundary conditions either. This means that the vibrational states of our physical metal–vacuum system with a plane interface consists of two sets of mutually independent waves of the form (4):

—in waves described by the set of functions $\{\mathcal{E}_x,\mathcal{E}_z,\mathcal{H}_y\}$ the magnetic field $\mathbf{H}$ is polarized in the plane of the interface and perpendicular to the direction of propagation of the wave along the surface. These waves are usually called modes of the electric (E) type or, alternatively, transverse magnetic (TM) modes;

—the second set of functions, $\{\mathcal{H}_x,\mathcal{H}_z,\mathcal{E}_y\}$, describes waves with an analogous type of polarization for the electric field $\mathbf{E}$. They are called modes of the magnetic (H) type or, alternatively, transverse electric (TE) modes.

We note that the possibility of separating the electromagnetic waves into modes of the electric and magnetic types has been discussed previously in several problems of macroscopic electrodynamics (see, e.g., §88 and §91 of Ref. 2).[2)] To the best of our knowledge, however, the possibility of a strict separation of electromagnetic–plasma modes into two independent sets of modes has not been discussed before. Meanwhile, this possibility permits one relatively simply to obtain in explicit form a complete set of eigenfunctions and the dispersion relations for the free oscillations of the given physical system and to propose an exhaustive classification of them. The results of such an analysis will be given later in a separate paper; here we shall only describe two particular E modes. We shall therefore not write out and discuss the equations for the functions $\{\mathcal{H}_x,\mathcal{H}_z,\mathcal{E}_y\}$; the system of equations that determines the E modes has the form

$$v_p^2(\mathcal{E}_z'' + ik\mathcal{E}_x') + (\omega^2 - \omega_p^2)\mathcal{E}_z + \omega ck\mathcal{H}_y = 0, \tag{15a}$$

$$ikv_p^2\mathcal{E}_z' + (\omega^2 - \omega_p^2 - v_p^2k^2)\mathcal{E}_x + i\omega c\mathcal{H}_y' = 0, \tag{15b}$$

$$ic\mathcal{E}_x' + ck\mathcal{E}_z + \omega\mathcal{H}_y = 0. \tag{15B}$$

We recall that on going from the metal ($z<0$) to the vacuum ($z>0$) one should set $\omega_p=0$ and $v_p=0$ in equations (15) and the unknown functions $\{\mathcal{E}_x,\mathcal{E}_z,\mathcal{H}_y\}$ must remain bounded at all values of z and must satisfy the conditions of continuity and the auxiliary condition (14) at $z=-0$.

The propagation of an inhomogeneous E wave of the form (4) is accompanied by analogous oscillations of the electron density $\tilde{n}(\mathbf{r},t)$ and current density $\mathbf{j}(\mathbf{r},t)$ in the metal. The complex amplitudes of these oscillations $N(z)$ and $\mathbf{J}(z)$ are easily calculated if the solutions of the system of equations (15) have been found. According to formulas (12) and (13) we have

$$N(z) = -\frac{1}{4\pi e}[\mathcal{E}_z'(z) + ik\mathcal{E}_x], \tag{16}$$

$$J_x(z) = \frac{i}{4\pi\omega}[\omega_p^2\mathcal{E}_x + i4\pi ekv_p^2N(z)], \tag{17a}$$

$$J_z(z) = \frac{i}{4\pi\omega}[\omega_p^2\mathcal{E}_z + 4\pi ev_p^2N'(z)]. \tag{17b}$$

2. INHOMOGENEOUS POLARITON MODES WITH FREQUENCY $\omega = \omega_p$

In the description of electromagnetic modes on the metal–vacuum interface in the framework of the electrodynamics of continuous media, when the plasma properties of the metal are characterized by a dielectric function $\hat{\varepsilon}$, certain anomalies appear at the frequency $\omega=\omega_p$ if damping and spatial dispersion effects are ignored. These features are due to the vanishing of $\hat{\varepsilon}$ at $\omega=\omega_p$; strictly speaking, they are of a nonphysical nature and vanish when a more accurate description of the modes is used. Since at frequencies $\omega\approx\omega_p$ in simple metals dissipation effects are actually extremely small, it can be important to take into account the dispersion due to the parameter $v_p^2\neq 0$. In this Section we examine the question of the existence and character of E modes with frequencies ω and wave numbers k lying in sector IV in Fig. 2; in particular, we shall consider E modes with $\omega=\omega_p$ and $|k|\leqslant k_p=\omega_p/c$. The existence region of these waves is a straight line segment represented by the dotted line in Fig. 2. For $\omega=\omega_p$ the expressions describing inhomogeneous waves have a comparatively simple form and can be used to illustrate the main features characteristic of polariton modes in sector IV.

We note yet another circumstance that determines the influence of the parameter v_p on the character of the modes for $\omega=\omega_p$. From a comparison of (10) or (15) it is seen that the relations $\omega=\omega_p$ and $v_p=0$ define a singular point in the space (ω,ω_p,v_p) of admissible values of the parameters of

these equations, and it is therefore important to pay attention to the procedure for obtaining physically correct solutions corresponding to that point.

Let us first consider the space $z<0$ occupied by the metal. For $\omega=\omega_p$ equations (15a) and (15b) imply a closed second-order equation (the Helmholtz equation) for the amplitude of the magnetic field $\mathcal{H}_y(z)$:

$$\mathcal{H}_y''-k^2\mathcal{H}_y=0. \tag{18}$$

If the solution of equation (18) has been found, the calculation of the amplitudes of the electric field components $\mathcal{E}_x(z)$ and $\mathcal{E}_z(z)$ reduces to the solution of a system of two inhomogeneous first-order differential equations:

$$\mathcal{E}_x'-ik\mathcal{E}_z=ik_p\mathcal{H}_y, \tag{19a}$$

$$\mathcal{E}_z'+ik\mathcal{E}_x=-\frac{c^2k_p}{v_p^2k}\mathcal{H}_y'. \tag{19b}$$

In the vacuum region $z>0$ one must set $\omega_p=0$ and $v_p=0$ and then $\omega=\omega_p$ in Eqs. (15). In this case the amplitude of the magnetic component of the E mode with frequency $\omega=\omega_p$ should satisfy the equation

$$\mathcal{H}_y''+(k_p^2-k^2)\mathcal{H}_y=0, \tag{20}$$

and the amplitudes of the electric field components are determined by the relations

$$k_p\mathcal{E}_x=-i\mathcal{H}_y', \tag{21a}$$

$$k_p\mathcal{E}_z=-k\mathcal{H}_y. \tag{21b}$$

The bounded solutions of equations (18) and (20) in their domains of definition have the form

$$\mathcal{H}_y(z)=A_1e^{|k|z}, \quad z<0; \tag{22a}$$

$$\mathcal{H}_y(z)=A_2\sin qz+A_3\cos qz, \quad z>0. \tag{22b}$$

Here and below the symbol A_α ($\alpha=1,2,\ldots$) denotes an arbitrary constant, and the parameter q can without loss of generality be assumed nonnegative:

$$q=(k_p^2-k^2)^{1/2}. \tag{23}$$

After substituting (22a) into (19) one can without particular difficulty find those solutions of the system of the inhomogeneous equations (19) which are bounded at $z<0$. Let us seek those solutions in the form

$$\mathcal{E}_x(z)=(A_4+A_5z)e^{|k|z}, \tag{24a}$$

$$\mathcal{E}_z(z)=(A_6+A_7z)e^{|k|z}. \tag{24b}$$

The solutions giving the components of the electric field for $z>0$ are analogous to (22b) and can be obtained by substituting (22b) into (21).

Thus the solutions (22) and (24) contain seven arbitrary constants A_α ($\alpha=1,2,\ldots7$). The conditions that the system of equations (19) be solvable and the continuity conditions for the amplitudes $\mathcal{H}_y$, $\mathcal{E}_x$, and $\mathcal{E}_x$ leave only one arbitrary constant in this set, which we denote as A (the auxiliary condition (14) holds automatically if the amplitudes are continuous). In addition, since for real metals the ratio v_p^2/c^2 has a very small value (of the order of 10^{-4}), in writing the coefficients in the final expressions for the amplitudes of the E-mode states investigated here we shall limit consideration to the linear approximation in that parameter. As a result we obtain:

—in the vacuum for $z>0$

$$\mathcal{H}_y(z)=A\left(\sin qz-\frac{2v_p^2q|k|}{c^2k_p^2}\cos qz\right), \tag{25a}$$

$$\mathcal{E}_x(z)=-iA\frac{q}{k_p}\left(\frac{2v_p^2q|k|}{c^2k_p^2}\sin qz+\cos qz\right), \tag{25b}$$

$$\mathcal{E}_z(z)=-A\frac{k}{k_p}\left(\sin qz-\frac{2v_p^2q|k|}{c^2k_p^2}\cos qz\right); \tag{25c}$$

—in the metal for $z<0$

$$\mathcal{H}_y(z)=-A\frac{2v_p^2q|k|}{c^2k_p^2}\exp(|k|z); \tag{26a}$$

$$\mathcal{E}_x(z)=iA\frac{q}{k_p}(|k|z-1)\exp(|k|z); \tag{26b}$$

$$\mathcal{E}_z(z)=A\frac{qk}{k_p^2}\left(k_pz+\frac{2v_p^2|k|}{c^2k_p}\right)\exp(|k|z). \tag{26c}$$

We note several key features of these solutions (25), (26). They describe waves traveling along the interface and which are inhomogeneous in the transverse direction. These waves are conveniently classified according to the values of their wave number k, which varies in the interval $|k|\leqslant k_p$. In the vacuum ($z>0$) these waves can be regarded as a superposition of photons with frequency ω_p incident on the surface $[\exp i(kx-\sqrt{k_p^2-k^2}z-\omega_pt)]$ and reflected from it $[\exp i(kx+\sqrt{k_p^2-k^2}z-\omega_pt)]$. In the metal ($z<0$) the propagation of an E mode of the electromagnetic field is accompanied by oscillations of the electron charge density and current density [see formulas (16) and (17)]; those modes are localized near the interface at distances of the order of $|k|^{-1}$ and are qualitatively similar to the modes accompanying the propagation of surface polaritons with a frequency $\omega_p/\sqrt{2}$ (Ref. 4). However, unlike the surface polaritons, the localization near the surface of the inhomogeneous E-polariton modes considered here is not purely exponential because of the presence of the power-law functions in the preexponential factors in formulas (26).

In formulas (25) and (26) we have kept the corrections linear in the small parameter v_p^2/c^2 to permit illustration of the degree to which the structure of the E mode is influenced by the finite compressibility of the electron plasma ($v_p\neq0$) and the finite propagation velocity of the electromagnetic field ($c\neq\infty$). It is easy to see that the electric field distribution in the E mode under discussion is practically insensitive to the value of the parameter v_p^2/c^2, but the magnetic field penetrates into the metal only insofar as that parameter is nonzero. Formulas (25) and (26) admit a physically correct transition to the limit $v_p^2/c^2\to0$. When one neglects the spatial dispersion ($v_p=0$) or retardation ($c=\infty$) the component of this mode that penetrates into the metal goes over to purely longitudinal plasma waves (curl $\mathbf{E}=0$) localized near the surface to depth of the order of $|k|^{-1}$.

3. INHOMOGENEOUS *E* MODES WITH MAGNETIC FIELD LOCALIZED NEAR THE SURFACE OF THE METAL

Let us now consider E modes with frequencies and wave vectors lying in sector III on the (ω^2,k^2) plane (Fig. 2). In this case the construction of the solutions of the system of equations (15) conveniently reduces to the solution of two independent equations for the amplitudes of the magnetic field $\mathcal{H}_y(z)$ and the amplitude $N(z)$ of the electron-density wave. Straightforward transformations of equations (15) with (16) taken into account lead to two Helmholtz equations:

$$\mathcal{H}_y''-\eta^2(\omega,k)\mathcal{H}_y=0, \tag{27}$$

$$N''+q^2(\omega,k)N=0. \tag{28}$$

Equation (27), which determines $\mathcal{H}_y(z)$, is valid both in the metal $(z<0)$ and in the vacuum $(z>0)$, but the value of the parameter η^2 makes a jump on passage through the interface:

$$\eta^2=\begin{cases}\eta_t^2=c^{-2}(\omega_p^2+c^2k^2-\omega^2) & \text{for } z<0,\\ \eta_{\rm ph}^2=c^{-2}(c^2k^2-\omega^2) & \text{for } z>0.\end{cases} \tag{29}$$

Equation (28) and the function $N(z)$ have physical meaning only in the metal, for $z\leqslant 0$, and there

$$q^2=v_p^{-2}(\omega_2-\omega_p^2-v_p^2k^2). \tag{30}$$

If the solution of equations (27) and (28) has been found, then the amplitudes of the electric field components can be calculated using the formulas

$$\mathcal{E}_x(z)=\frac{i}{\omega_2-\omega_p^2}[4\pi e v_p^2 kN(z)-c\omega\mathcal{H}_y'(z)], \tag{31a}$$

$$\mathcal{E}_z(z)=\frac{1}{\omega_2-\omega_p^2}[4\pi e v_p^2 N'(z)-c\omega k\mathcal{H}_y(z)]. \tag{31b}$$

It is seen that in the region under consideration, sector III on the (ω^2,k^2) plane, the coefficients in front of the unknown functions in both Eqs. (27) and (28) have positive values: η_t^2, $\eta_{\rm ph}^2$, $q^2>0$. In the case of Eq. (27) this circumstance leads to exponential localization of the magnetic field on both sides of the interface. The solution of equation (27) that is bounded at all z and continuous at the point $z=0$ is a piecewise-continuous function with one arbitrary constsant A_1:

$$H_y(z)=A_1e^{\eta_t z}, \quad z\leqslant 0; \tag{32a}$$

$$\mathcal{H}_y(z)=A_1e^{-\eta_{\rm ph}z}, \quad z>0. \tag{32b}$$

The solution of equation (28) that is bounded inside the metal for $q^2\geqslant 0$ is the sum of two trigonometric functions with arbitrary coefficients A_2 and A_3:

$$N(z)=A_2\sin qz+A_3\cos qz, \quad z\leqslant 0. \tag{33}$$

In this solution the parameter q can, without loss of generality, be assumed nonnegative.

Substituting (32) and (33) into (31) and taking into account the continuity conditions for the electric field components at $z=0$, we are left with only one arbitrary constant in expressions (32) and (33), which we shall denote by the symbol A [we note that the continuity of $\mathcal{E}_x$ and $\mathcal{E}_z$ also ensures satisfaction of the auxiliary condition (14)].

The inhomogeneous E modes of the type (4) with amplitudes (31)–(33) obtained here are the result of mixing of plasmons with two transverse photon modes. Unlike the modes considered in the previous Section, in this case the electromagnetic field in the vacuum is exponentially localized near the interface, and the modes in the metal are delocalized and can be regarded as a superposition of charge-density waves (plasmons) incident on the surface $[\exp i(kx+qz-\omega t)]$ and reflected from it $[(\exp i(kx-qz-\omega t)]$. These waves are conveniently classified according to a two-dimensional continuum of values of the wave numbers (k,q), with Eq. (30) considered to be the dispersion relation:

$$\omega=\omega_l(k,q)=[\omega_p^2+v_p^2(k^2+q^2)]^{1/2}. \tag{34}$$

For such a classification, the parameters $\eta_{\rm ph}$ and η_t characterizing the inhomogeneity of the fields near the interface will be determined by the expressions

$$\eta_t=\eta_t(k,q)=\left[\left(1-\frac{v_p^2}{c^2}\right)k^2-\frac{v_p^2}{c^2}q^2\right]^{1/2}, \tag{35a}$$

$$\eta_{\rm ph}=\eta_{\rm ph}(k,q)=\left[\left(1-\frac{v_p^2}{c^2}\right)k^2-\frac{v_p^2}{c^2}q^2-k_p^2\right]^{1/2}. \tag{35b}$$

One must of course remember that the domain of variation of the wave numbers k and q is determined by several conditions:

$$\left(1-\frac{v_p^2}{c^2}\right)^{-1/2}k_p\leqslant|k|<k_c, \quad k_c=\frac{\omega_p}{v_p}\sim a^{-1}; \tag{36a}$$

$$0\leqslant q\leqslant\frac{c}{v_p}\left[\left(1-\frac{v_p^2}{c^2}\right)k^2-k_p^2\right]^{1/2}, \quad q<k_c. \tag{36b}$$

Inequality (36) ensures both the applicability of the hydrodynamic approximation and that the values of k under consideration lie in sector III in Fig. 2. In particular, inequalities (36b) restrict the region of admissible values of q for which $\eta_t^2,\eta_{\rm ph}^2\geqslant 0$ [see formula (31)]. In accordance with these inequalities the frequency of the inhomogeneous E modes considered here is restricted to the interval

$$\left(1-\frac{v_p^2}{c^2}\right)^{-1}\omega_p^2\leqslant\omega^2<\omega_p^2+v_p^2k_c^2\approx 2\omega_p^2, \tag{37}$$

which approximately coincides with the interval in which plasmons exist in an unbounded metal.

The final expressions for the functions $\mathcal{E}_x(z)$, $\mathcal{E}_z(z)$, and $\mathcal{H}_y(z)$ take the following form:

—in the metal (for $z\leqslant 0$)

$$\mathcal{E}_x(z)=Ak\{[\omega_l^2\eta_t+v_p^2(k^2+q^2)\eta_{\rm ph}]q\cos qz + \omega_p^2k^2\sin qz-\omega_l^2q\eta_te^{\eta_t z}\}, \tag{38a}$$

$$\mathcal{E}_z(z)=iAq\{[\omega_l^2\eta_t+v_p^2(k^2+q^2)\eta_{\rm ph}]q\sin qz - \omega_p^2k^2\cos qz+\omega_l^2k^2e^{\eta_t z}\}, \tag{38b}$$

$$\mathcal{H}_y(z)=-\frac{iA}{c}v_p^2(k^2+q^2)\omega_l qke^{\eta_t z}; \tag{38c}$$

—in the vacuum (for $z\geqslant 0$)

$$\mathcal{E}_x(z)=Av_p^2(k^2+q^2)qk\eta_{\rm ph}e^{-\eta_{\rm ph}z}, \tag{39a}$$

$$\mathcal{E}_z(z)=iAv_p^2(k^2+q^2)qk^2\mathrm{e}^{-\eta_{\mathrm{ph}}z}, \tag{39b}$$

$$\mathcal{H}_y(z)=-\frac{iA}{c}v_p^2(k^2+q^2)\omega_l qk\mathrm{e}^{-\eta_{\mathrm{ph}}z}. \tag{39c}$$

The most interesting feature of the metal–vacuum system modes considered in this Section is the essentially different character of the spatial distribution of the electric and magnetic fields. In the propagation of inhomogeneous E modes of this type the magnetic field remains exponentially localized near the interface: to a depth η_t^{-1} in the metal and η_{ph}^{-1} in the vacuum. Here, according to formulas (35), $\eta_t=(k_p^2+\eta_{\mathrm{ph}}^2)^{1/2}>n_{\mathrm{ph}}$, and therefore $\eta_{\mathrm{ph}}^{-1}>\eta_t^{-1}$. The characteristic values of the wave numbers $|k|$ and q for these waves, of the order of k_p, correspond to values of the penetration depths of the order of $k_p^{-1}=c/\omega_p$.

The electric field in the E mode of this type also has an exponential inhomogeneity near the interface, but its distribution in the interior of the metal corresponds to a superposition of the fields of two homogeneous electron-density waves (plasmons). Thus the excitation of longitudinal waves of the electron density and electric field (plasmons) in the bulk of the metal is accompanied by the appearance of a wave localized near its surface, consisting of a ''mixture'' of metallic and vacuum photons. We note that in the localized component of the E wave the magnetic and electric fields are of the same order of magnitude when $|k|$ is of the order of k_p:

$$|\mathcal{H}_y|\sim\frac{\omega_p}{c|k|}|\mathcal{E}|\sim\frac{k_p}{|k|}|\mathcal{E}|.$$

There are two other noteworthy features of the E modes under discussion. First, at the lower boundary of sector III (Fig. 2), which is specified by the equation $\omega^2=\omega_p^2+v_p^2k^2$ and on which the parameter q goes to zero if $v_p^2\neq 0$ [see formula (30)], these waves vanish: $\mathcal{E}_x,\mathcal{E}_z,\mathcal{H}_y\equiv 0$ for all values of z. Second, their existence for $\omega>\omega_p$ is possible only because of the finite compressibility of the electron plasma ($v_p^2\neq 0$). It is seen from formulas (38) and (39) that for $v_p^2\to 0$ the magnetic component vanishes ($\mathbf{H}=0$), and waves of this type degenerate into modes with a single frequency $\omega=\omega_p$: these are longitudinal modes of the electron density and electric field ($\mathrm{curl}\,\mathbf{E}\equiv 0$) which are concentrated entirely in the metal. Thus solutions (38) and (39), like solutions (25) and (26) obtained in the previous Section, admit transition to the limits $\omega\to\omega_p$ and $v_p^2\to 0$ and give a physically correct description of the modes corresponding to the ''singular point'' of the base system of equations (10).

CONCLUSION

We have investigated some novel aspects of the problem of linear electromagnetic–plasma waves on a plane metal–vacuum interface. Our analysis was based on Maxwell's equations for the electric field $\mathbf{E}(\mathbf{r},t)$ and magnetic field $\mathbf{H}(\mathbf{r},t)$, supplemented by the hydrodynamic equation for the density field $n(\mathbf{r},t)$ and velocity field $\mathbf{v}(\mathbf{r},t)$ of the constituents of the electron plasma of the metal.

We have shown that this system of equations admits the existence of specific long-wavelength spatially inhomogeneous modes of the polariton type (E modes) with frequencies $\omega\lesssim\omega_p$, in which the magnetic field oscillations are polarized in the plane of the interface and perpendicular to the direction of propagation of the waves along the surface of the metal. Such modes are the result of mixing of longitudinal electron-density waves (plasmons) of the metal with transverse modes (photons) of the metal and vacuum on the metal–vacuum interface. It was assumed that in the high-frequency region considered, the effects of dissipation in the system of conduction electrons and the resulting frequency dispersion are negligible, and attention was focused mainly on an analysis how the structure of the modes is influenced by the spatial dispersion due to the finite compressibility of the electron plasma. The compressibility was characterized by the parameter v_p^2, the value of which is proportional to the derivative of the quantum pressure in the electron plasma with respect to its density ($v_p\cong v_F$).

We have considered in detail the structure of the inhomogeneous modes of the polariton type at the singular point of the mode spectrum $\omega=\omega_p$. We showed that an inhomogeneous E mode with frequency $\omega=\omega_p$ and propagation parameter (wave number) k taking on arbitrary values in the interval $|k|\leqslant k_p=\omega_p/c$ can propagate along the surface of the metal. The amplitude of such a wave is substantially nonuniform in the direction perpendicular to the interface: the vacuum wing of the wave is delocalized and consists of a superposition of photons with wave vectors $q=\pm\sqrt{k_p^2-k^2}$, incident on the boundary and reflected from it; in the metal the propagation of this mode is accompanied by almost longitudinal electron-density and electric-field oscillations, localized to a depth of the order of $|k|^{-1}$, with a small (of the order of v_p^2/c^2) admixture of magnetic field.

We have also described inhomogeneous E modes with frequencies $\omega>\omega_p$ and wave numbers $|k|>k_p$. Such waves are specified by values of the propagation parameters k along the surface and q in the perpendicular direction, which are related to the mode frequency by the plasmon dispersion relation $\omega^2=\omega_p^2+v_p^2(k^2+q^2)$. In the bulk of the metal these waves are delocalized and consist of a superposition of plasmons with wave vectors (k,q), incident on the interface and reflected from it. There are also electric and magnetic components in the wave which are exponentially localized on both sides of the interface: to a depth $\eta_t^{-1}=c(\omega_p^2+c^2k^2-\omega^2)^{-1/2}$ in the metal and $\eta_{\mathrm{ph}}^{-1}=c(c^2k^2-\omega^2)^{-1/2}$ in the vacuum. In the limit where the compressibility parameter goes to zero ($v_p^2\to 0$) the magnetic component in this wave vanishes, and the wave degenerates into a purely longitudinal wave of electron density and electric field which is concentrated entirely in the metal.

The inhomogeneous polariton modes considered in this paper, with frequencies $\omega\cong\omega_p$, have a characteristic inhomogeneity parameter of the order of $k_p^{-1}=c/\omega_p$, which for standard metals has a value of 10–50 nm. Therefore, these modes or others like them can play a substantial role in the description of electromagnetic resonances and radiation effects in metallic nanostructures.

The authors are sincerely grateful to A. M. Kosevich for his interest in this study and helpful advice.

This study was supported in part by the Comprehensive Program of Basic Research of the National Academy of Sciences of Ukraine, ''Nanostructure Systems, Nanomaterials,

and Nanotechnology,'' Projects Nos. 3-025/2004 and 3-026/2004.

*E-mail: smirnov@ilt.kharkov.ua

[1)]The dispersion relation (2) for surface plasmons is obtained in the limit $c \to \infty$ (in neglect of retardation). Taking retardation into account[8,9] leads to an acoustic type of dispersion relation $\omega_s(k) \sim c|k|$ at rather small values of the wave number, i.e., in Fig. 2 the line $\omega^2 = \omega_s^2(k)$ goes to the origin of coordinates, while remaining in sector V.

[2)]It should be noted that the use of the terms *E* mode and *H* mode is contradicted by §88 and §91 of the monograph.[2]

[1] A. V. Sokolov, *Optical Properties of Metals*, American Elsevier, New York (1967), Fizmatgiz, Moscow (1961).

[2] L. D. Landau and E. M. Lifshitz, L. D. Landau and E. M. Lifshitz, *Electrodynamics of Continuous Media*, 2nd ed., rev. and enl., by E. M. Lifshitz and L. P. Pitaevskii, Pergamon Press, Oxford (1984), Nauka, Moscow (1982).

[3] V. M. Agranovich and D. L. Mills (eds.), *Surface Polaritons*, North-Holland, Amsterdam (1982), Nauka, Moscow (1985).

[4] H. March and M. Parrinello, *Collective Effects in Solids and Liquids*, Adam Hilger, Bristol (1982), Mir, Moscow (1986).

[5] G. Barton, Rep. Prog. Phys. **42**, 963 (1979).

[6] E. M. Lifshitz and L. P. Pitaevskiĭ, *Physical Kinetics*, Pergamon Press, Oxford (1981), Nauka, Moscow (1979).

[7] D. Pines, *Elementary Excitations in Solids*, Benjamin, New York–Amsterdam (1963), Mir, Moscow (1965).

[8] K. Sturm, Z. Phys. B **209**, 329 (1968).

[9] V. M. Gokhfel'd, Fiz. Nizk. Temp. **28**, 304 (2002) [Low Temp. Phys. **28**, 215 (2002)].

[10] V. L. Bonch-Bruevich and S. V. Tyablikov, *The Green Function Method in Statistical Mechanics*, North-Holland, Amsterdam (1962), Fizmatgiz, Moscow (1961).

[11] N. S. Koshlyakov, É. B. Gliner, and M. M. Smirnov, *Partial Differential Equations of Mathematical Physics* [in Russian], Vysshaya Shkola, Moscow (1970).

Translated by Steve Torstveit

Manifestation of the band structure in the tunneling characteristics of materials with low Fermi energies

A. I. Khachaturov*

A. A. Galkin Donetsk Physicotechnical Institute, ul. R. Lyuksemburg 72, Donetsk 83114, Ukraine
(Submitted July 12, 2004)
Fiz. Nizk. Temp. **31**, 109–114 (January 2005)

The ideal behavior of the tunneling characteristics is investigated for metal–insulator–metal junctions in which the Fermi energies of the electrodes do not exceed 1.5–2.0 eV. It is shown that in this case the band structure of the electrodes has a substantial influence on the tunneling characteristics, contrary to the accepted ideas in tunneling spectroscopy. For example, the dependence of the differential tunneling conductance $\sigma(V)$, calculated for a symmetric rectangular barrier, is asymmetric. In addition, at a bias voltage eV equal to the difference of the Fermi energies of the electrodes one observes a jump of the conductance that is not susceptible to temperature smearing. It is shown that curve of the second derivative of the current with respect to voltage can display the feature corresponding to this jump even in the case of conventional metal electrodes with Fermi energies of the order of several electron-volts. [DOI: 10.1063/1.1820377]

1. INTRODUCTION

The problem of determining the ideal behavior of the intrinsic characteristics is of fundamental importance in electron tunneling spectroscopy, as for any other spectroscopic method. For the case when the ''banks'' of the tunnel junction are Fermi metals found in the normal state, this problem was solved back in the early 1970s.[1–4] Detailed studies have established that the dependence of the differential tunneling conductance $\sigma(V)=dI/dV$ on the bias voltage V across the junction in the intermediate voltage region, when eV is no longer small but is not yet greater than the height of the tunnel barrier, is in the form of a parabola shifted with respect to zero voltage by an amount V_{shift} that is determined exclusively by the asymmetry of the potential barrier $\Delta\varphi=\varphi_1-\varphi_2$, where φ_1 and φ_2 are the barrier heights on the two sides of the tunnel junction. The electronic properties of the electrodes, in particular the values of their Fermi energies, do not have a material effect on the shape of the $\sigma(V)$ curves. Their behavior is entirely determined by the barrier parameters. It is for this reason that they have come to be called the barrier characteristics in the literature. The validity of the conclusions drawn in Refs. 1–4 has since been confirmed in practice in tunneling research.[5–7] Suffice it to say that a parabolic rise of the differential tunneling conductance $\sigma(V)$ in the intermediate voltage region serves as a criterion of proof that the main mechanism responsible for the charge transfer between electrodes in the normal state is tunneling.

However, the notions discussed above as to the behavior of the ideal characteristics were developed for conventional metals with Fermi energies of the order of several electron-volts. It is therefore incorrect to apply them in the study of novel materials such as metal-oxide superconductors. This circumstance was first pointed out in Refs. 8 and 9, where it was shown that if the Fermi energies of both electrodes are low, then $\sigma(V)$ is no longer a monotonically increasing function, and a conductance peak should be observed in the zero-bias region. In the present paper it is shown that for a certain combination of barrier parameters the electronic characteristics can not only have a substantial influence on the behavior of the $\sigma(V)$ curve as a whole but can also lead to a sharp local feature on it.

2. ZERO TEMPERATURE

Let us begin by considering the zero-temperature case $T=0$. We shall assume that the tunneling is of a specular character, i.e., in going from the initial electrode to the final electrode the electron conserves its total energy E and transverse quasimomentum component $k_{\parallel}$. Figure 1a shows the reciprocal space of the initial electrode, the Fermi energy E_{F_1} of which is less than the Fermi energy E_{F_2} of the final electrode. In such a case at a voltage V all of the electrons moving toward the boundary ($k_z>0$) which lie in a spherical shell $E_{F_1}-eV<E<E_{F_1}$ (the shaded region in the figure) can take part in tunneling. Since their momentum k_z varies from 0 to k_{F_1}, the integration over energy E_z in the expression for the tunneling current is done from 0 to E_{F_1} (Refs. 8 and 9):

$$I(V)=K\left\{\int_{E_{F_1}-eV}^{E_{F_1}}(E_{F_1}-E_z)P(E_z,V)dE_z + eV\int_0^{E_{F_1}-eV}P(E_z,V)dE_z\right\}, \tag{1}$$

where $K=4\pi me/h^3$, $P(E_z,V)$ is the transparency of the tunnel barrier, and m is the effective mass of an electron, which for simplicity is assumed to be equal to the free electron mass in all three components of the tunnel junction.

If the Fermi energy E_{F_1} of the initial electrode is greater than the Fermi energy E_{F_2} of the final electrode, then at bias voltages $eV<E_{F_1}-E_{F_2}$ only those electrons lying in a spherical shell $E_{F_1}-eV<E<E_{F_1}$ and having momentum greater than $k_{\min}=2m\sqrt{E_{F_1}-E_{F_2}-eV}/\hbar$ participate in the

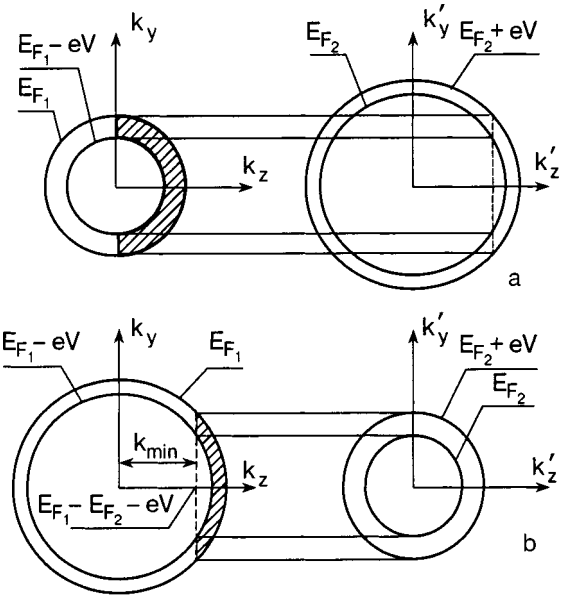

FIG. 1. Reciprocal space of the initial and final electrodes at a bias voltage V across the contact: a) The Fermi radius k_{F_1} of the initial electrode is less than or equal to the Fermi radius k_{F_2} of the second, and therefore all of those electrons from a spherical shell $E_{F_1}-eV<E<E_{F_1}$ that are moving toward the boundary, $k_z>0$ (the shaded region), can take part in tunneling; b) $k_{F_1}<k_{F_2}$, and only electrons with $E_z \geqslant E_{F_1}-E_{F_2}-eV$ take part in the tunneling.

tunneling (i.e., their momentum satisfies the inequality $k_{\min}<k_z<k_{F_1}$; the shaded region in Fig. 1b). In this case the integration is done from $E_{F_1}-E_{F_2}-eV$ to E_{F_1}:

$$I(V)=K\left\{\int_{E_{F_1}-eV}^{E_{F_1}}(E_{F_1}-E_z)P(E_z,V)dE_z + eV\int_{E_{F_1}-E_{F_2}-eV}^{E_{F_1}-eV}P(E_z,V)dE_z\right\},\quad eV<E_{F_1}-E_{F_2}. \tag{2}$$

For $eV>E_{F_1}-E_{F_2}$ the expression for the tunneling current agrees with formula (1).

Differentiating (1) and (2) with respect to voltage V, we obtain an analytical expression for the differential conductance which in the case $E_{F_1}\leqslant E_{F_2}$ consists of two terms:

$$\sigma(V)=K[\sigma_1(V)+\sigma_2(V)], \tag{3}$$

where

$$\sigma_1(V)=e\int_0^{E_{F_1}-eV}\left(P(E_z,V)+V\frac{\partial P}{\partial V}\right)dE_z,$$

$$\sigma_2(V)=\int_{E_{F_1}-eV}^{E_{F_1}}(E_{F_1}-E_z)\frac{\partial P}{\partial V}dE_z,$$

and in the case $E_{F_1}>E_{F_2}$ has three terms:

$$\sigma(V)=K[\sigma_1(V)+\sigma_2(V)+\sigma_3(V)], \tag{4}$$

where

$$\sigma_3(V)=e^2VP(E_{F_1}-E_{F_2}-eV,V)\Theta(E_{F_1}-E_{F_2}-eV),$$

and $\Theta(E_{F_1}-E_{F_2}-eV)$ is the Heaviside step function.

Analyzing formula (4), we see that for bias voltages $V_{\text{jump}}=(E_{F_1}-E_{F_2})/e$ a jump is expected to appear which is directly proportional to the product of the difference of the Fermi energies $\Delta E_F=E_{F_1}-E_{F_2}$ of the electrodes multiplied by $P(0,V_{\text{jump}})$, the barrier transparency for electrons lying at the bottom of the conduction band:

$$\Delta\sigma_1=Ke\Delta E_F P(0,V_{\text{jump}}). \tag{5}$$

The barrier height for electrons at the bottom of the conduction band is made up of two terms:

$$\phi_1=\varphi_1+E_{F_1}, \tag{6}$$

where φ_1 is the barrier height measured from the Fermi level. Therefore the absolute value of the jump falls off rapidly with increasing Fermi energy E_{F_1}. To estimate the relative value of the effect, we use the approximate formula (7) from Ref. 4, according to which the quadratic rise of the conductance for a rectangular barrier $\varphi=\varphi_1=\varphi_2$ can be written as

$$\Delta\sigma_2\approx\frac{3}{32}\frac{A_d}{\sqrt{\varphi}}Ke\Delta E_F^2\exp\left(-\frac{3}{2}A_d\sqrt{\varphi}\right), \tag{7}$$

where $A_d=4d\sqrt{2m}/3\hbar$. The relative value η of the effect is inversely proportional to the difference ΔE_F:

$$\eta=\frac{\Delta\sigma_1}{\Delta\sigma_1+\Delta\sigma_2} \approx\frac{3}{32}\frac{\sqrt{\varphi}}{A_d\Delta E_F}\frac{P\left(0,\dfrac{\Delta E_F}{e}\right)}{\exp\left(\dfrac{3}{2}A_d\sqrt{\varphi}\right)+P\left(0,\dfrac{\Delta E_F}{e}\right)}, \tag{8}$$

and therefore, in order for the effect to be noticeable against the overall background of the voltage dependence of the differential conductance, it is necessary that ΔE_F be small. Assuming $\Delta E_F\ll 4\varphi$, we have

$$P\left(0,\frac{\Delta E_F}{e}\right)\approx\exp\left(-\frac{3}{2}A_d\sqrt{\varphi+E_{F_1}}\right)$$

and

$$\eta\approx\frac{3}{32}\frac{\sqrt{\varphi}}{A_d\Delta E_F}\frac{\exp\left(-\dfrac{3}{2}A_d\sqrt{\varphi+E_{F_1}}\right)}{\exp\left(-\dfrac{3}{2}A_d\sqrt{\varphi}\right)+\exp\left(-\dfrac{3}{2}A_d\sqrt{\varphi+E_{F_1}}\right)}. \tag{9}$$

For tunnel junctions made from ordinary metals, in which the Fermi energies of the electrodes exceed the height of the tunnel barrier by several electron-volts, the value of η is negligibly small. However, if the electrodes have Fermi energies of the order of one or two electron-volts, being, say, metal-oxide superconductors, the jump in question can be quite noticeable. For example, in order for the relative value of the jump to be greater than η, it is necessary that the Fermi energies of the electrodes not exceed the values

$$E_F<\left[\sqrt{\varphi}-\frac{2}{3A_d}\ln\left(\frac{3}{32}\frac{\eta}{1-\eta}\frac{A_d\Delta E_F}{\sqrt{\varphi}}\right)\right]^2-\varphi. \tag{10}$$

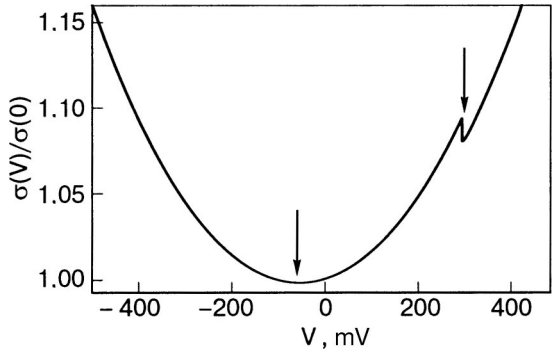

FIG. 2. Differential conductance of a tunnel junction with electrodes having low Fermi energies $E_{F_2}=1.8$ eV and $E_{F_2}=1.5$ eV, calculated for a symmetric rectangular barrier $\varphi_1=\varphi_2=4$ eV of thickness $d=10$ Å. The curve is asymmetric: the left arrow shows the position of the minimum, $V_{\text{shift}}\approx 55$ mV; the right arrow indicates the position of the local band feature at $V_{\text{jump}}=(E_{F_1}-E_{F_2})/e$.

Inequality (10) can be used to determine what values of the Fermi energies can be considered small. For example, for a tunnel junction of thickness $d=10$ Å and height $\varphi_1=\varphi_2=4$ eV the jump should exceed ten percent ($\eta>0.1$) under the condition that $E_F<1.75$ eV.

Figure 2 shows the results of a calculation of the differential conductance $\sigma(V)$ in the framework of the WKB model, according to which the expression for the transparency of the tunnel barrier is given by the formula

$$P(E_z,V)=\exp\left\{-\frac{2e}{\hbar}\int_0^d 2m\sqrt{\phi(z,V)-E_z}\,dz\right\},$$

where d is the thickness of the tunnel barrier, $\phi(z,V)=\phi_1+(\phi_1-eV-\phi_2)z/d$, and $\phi_2=\varphi_2+E_{F_1}$ (remember that all energy values in formulas (1)–(4) are measured from the bottom of the conduction band of the initial electrode). The following values of the barrier parameters were assumed: $E_{F_1}=1.8$ eV, $E_{F_2}=1.5$ eV, $d=10$ Å, $\varphi_1=\varphi_2=4$ eV. Notice that the curve in Fig. 2 is asymmetric—its minimum is shifted with respect to zero voltage by an amount $V_{\text{shift}}\approx 55$ mV. Since it was calculated using a symmetric rectangular barrier, its asymmetry can only be due to differences in the electron density of states in the materials. As expected, the jump on the $\sigma(V)$ curve at V_{jump} can be large enough to influence the behavior of the differential tunneling conductance $\sigma(V)$ as a whole.

3. FINITE TEMPERATURES

We now consider the case of finite temperatures $T\neq 0$. It can be shown that if as a result of temperature excitation an electron occupies a state with $k_z>k_{\min}=2m\sqrt{E_{F_1}-E_{F_2}-eV}/\hbar$, then it will be able to take part in tunneling, while if $k_z<k_{\min}$ it cannot. That is, the plane $k_z=2m\sqrt{E_{F_1}-E_{F_2}-eV}/\hbar=\text{const}$ as before divides the reciprocal space into two regions. To the right of that plane lie states from which tunneling is possible, and to the left of it states from which tunneling cannot occur. Therefore, unlike the corresponding expression given in Ref. 5, in the present case the lower limit of the integration over $E_\parallel$ in the formula for the tunneling current is equal to zero only if $eV>E_{F_1}-E_{F_2}$:

$$I(V,T)=\frac{2e}{h}\int_{L(V)}^{\infty}dE_zP(E_z,V)\int_0^{\infty}dE_\parallel[f(E_\parallel+E_z,T)-f(E_\parallel+E_z+eV,T)],\qquad(11)$$

where $L(V)=(E_{F_1}-E_{F_2}-eV)\Theta(E_{F_1}-E_{F_2}-eV)$, and $f(E,T)$ is the Fermi–Dirac distribution function. After integration over $E_\parallel$ we have

$$I(V,T)=KkT\int_{L(V)}^{\infty}dE_zP(E_z,V)\times\ln\left\{\frac{1+\exp[-(E_z-E_{F_1})/kT]}{1+\exp[-(E_z-E_{F_1}+eV)/kT]}\right\}.\qquad(12)$$

Without loss of accuracy the upper limit in this formula can be replaced by the finite value $E_{F_1}+\eta(T)$, where $\eta(T)\gg kT$. We differentiate (12) with respect to V and write the resulting differential conductance $\sigma(V,T)$ in a form analogous to formula (4):

$$\sigma(V,T)=K[\sigma_1(V,T)+\sigma_2(V,T)+\sigma_3(V,T)],\qquad(13)$$

where

$$\sigma_1(V)=\left[eV\int_{E_{F_1}-E_{F_2}-eV}^{E_{F_1}-\eta(T)-eV}\frac{\partial P}{\partial V}dE_z+\int_{E_{F_1}-\eta(T)-eV}^{E_{F_1}-\eta(T)}(E_{F_1}-E_z)\frac{\partial P}{\partial V}dE_z\right]+kT\left\{\int_{E_{F_1}-\eta(T)}^{E_{F_1}+\eta(T)}\frac{\partial P}{\partial V}\ln\left[1+\exp\left(\frac{E_{F_1}-E_z}{kT}\right)\right]\times dE_z-\int_{E_{F_1}-\eta(T)-eV}^{E_{F_1}+\eta(T)-eV}\frac{\partial P}{\partial V}\times\ln\left[1+\exp\left(\frac{E_{F_1}-E_z-eV}{kT}\right)\right]dE_z\right\},$$

$$\sigma_2(V,T)=ekT\left\{\int_{E_{F_1}-eV-\eta(T)}^{E_{F_1}-eV+\eta(T)}P(E_z,V)\times\frac{\exp[-(E_z-E_{F_1}+eV)/kT]}{1+\exp[-(E_z-E_{F_1}+eV)/kT]}dE_z+\int_{L(V)}^{E_{F_1}-eV-\eta(T)}P(E_z,V)dE_z\right\},$$

$$\sigma_3(V,T)=ekTP(E_{F_1}-E_{F_2}-eV,V)\times\ln\left\{\frac{1+\exp[(E_{F_2}+eV)/kT]}{1+\exp[E_{F_2}/kT]}\times\Theta(E_{F_1}-E_{F_2}-eV)\right\}.$$

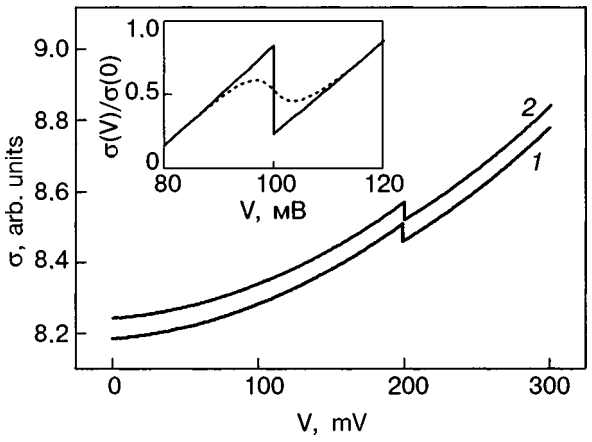

FIG. 3. The $\sigma(V)$ curves calculated for temperatures of 4.2 K (curve *1*) and 295 K (curve *2*), demonstrating the stability of the local band feature against temperature smearing. The fixed parameters of the calculation were assumed to have the values $E_{F_1}=2.0$ eV, $E_{F_2}=1.8$ eV, $\varphi_1=\varphi_2=4$ eV, $d=10$ Å. The inset shows the influence of the finite lifetime of an electron near the Fermi surface on the sharpness of the band feature: $\Gamma=0$ (——) and $\Gamma=5$ meV (· · · ·). The fixed parameters were assumed to have the values $E_{F_1}=1.6$ eV, $E_{F_2}=1.5$ eV, $\varphi_1=\varphi_2=4$ eV, $d=10$ Å.

We note that if E_{F_2} is not very small, say, $E_{F_2}>50$ meV, then the condition $\exp(E_{F_2}/kT)\gg 1$ holds even at room temperatures, and, as a result, the $\sigma_3(V,T)$ term in formula (13), which is responsible for the jump on the differential conductance curve, is practically the same as the analogous term in formula (4). This means that the $\sigma(V)$ feature under discussion is insensitive to temperature smearing. Indeed, curves *1* and *2* in Fig. 3, calculated for helium temperature and room temperature, $T=4.2$ K and 295 K, differ only by a slight shift relative to each other along the vertical axis. The presence of local features insensitive to temperature was noted back in Ref. 10. We emphasize that such behavior is extremely nontrivial, since the effects ordinarily considered in tunneling spectroscopy are due to the interaction of the tunneling electron with different types of excitations that are observed both in the electrodes and inside the barrier. Since in those processes the electron starts from the Fermi level of one metal and finishes at the Fermi level of another, the presence of low temperatures is a necessary condition for their observation. In our case, however, the sharpness of the feature in question is determined by the smearing of the plane $k_{\min}=2m\sqrt{E_{F_1}-E_{F_2}-eV}/\hbar=\text{const}$, which does not depend directly on temperature.

4. ALLOWANCE FOR THE FINITE LIFETIME IN THE ELECTRONIC STATES

The boundary between tunneling and nontunneling electrons can be smeared on account of the finite lifetimes of the particles in the initial and final states. This smearing is taken into account according to the formula

$$\sigma_{\text{smear}}(V)=\frac{1}{\pi}\int\frac{\Gamma}{[E^2+\Gamma^2]}\sigma(V,E)dE, \tag{14}$$

$$\sigma(V,E)=K[\sigma_1(V)+\sigma_2(V)+eVP(E_{F_1}-E_{F_2}-eV+E,V)\Theta(E_{F_1}-E_{F_2}-eV+E)],$$

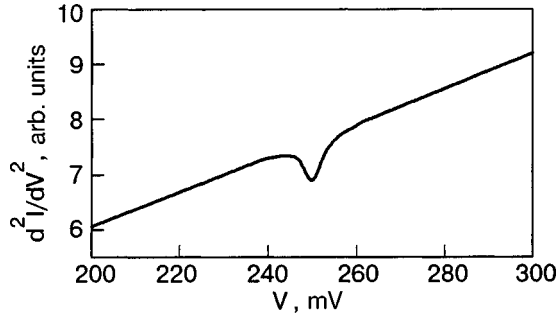

FIG. 4. Dependence of the second derivative d^2I/dV^2 on the bias voltage V across the function, calculated for values of the barrier parameters $\varphi_1=\varphi_2=4$ eV, $d=10$ Å, and $\Gamma=2$ meV. The local band feature is well resolved against the background of the characteristic shown, even though the Fermi energies of the electrodes are not small: $E_{F_1}=3.75$ eV, $E_{F_2}=3.5$ eV.

where Γ is an energy parameter related to the lifetime τ of the particle in the electronic state by the relation $\Gamma=\hbar/\tau$ and is assumed to be constant in our calculations.

It is shown in the inset to Fig. 3 that the effect is extremely sensitive to the parameter Γ, i.e., pure materials are required for observation of a clear jump in the tunneling conductance. However, if the purity condition is met, then as is shown in Fig. 4, the feature in question remains noticeable against the overall background of the V dependence of d^2I/dV^2 even when the "banks" of the tunnel junction are made of materials with Fermi energies of the order of several electron-volts.

5. CONCLUSION

It is generally known that the electron density of states is reflected in the tunneling characteristics of superconductors. It is owing to to this circumstance that tunneling has played a key role in understanding the mechanism of superconductivity. However, for normal metal electrodes the question of the influence of their band structure on the tunneling characteristics is not so obvious. In the classic paper by Harrison[1] it was shown in the framework of an independent-electron model that the electron density of states in the WKB approximation should not be manifested in the tunneling curves, since the one-dimensional density of states $N(E_z)\propto(\partial E/\partial k_z)^{-1}$ is completely canceled out by the preexponential factor from the expression for the transparency of the tunnel barrier. In the present paper we have shown that Harrison's conclusion is valid only for electrons with large Fermi energies, for which inequality (10) is clearly cannot hold. For tunnel junctions in which the electrodes are conductors with low Fermi energies (less than 2 eV) inequality (10) may or may not hold, depending on the barrier parameters: it can hold for high and thin barriers but not for wide and low barriers. Satisfaction of condition (10) means that a substantial role in the formation of the tunneling current is played by electrons with a nonzero transverse momentum component $k_\parallel$, as a result of which the tunneling characteristics can reflect the associated two-dimensional density of states $N(E_\parallel)\propto(\partial E/\partial k_\parallel)^{-1}$. In that case the tunneling conductance of symmetric junctions $E_{F_1}=E_{F_2}$ can exhibit an anomalous zero peak,[8] while asymmetric junctions $E_{F_1}\neq E_{F_2}$ have a local feature at a bias voltage across the junc-

tion equal to $V_{\text{jump}}=(E_{F_1}-E_{F_2})/e$. In our view, this circumstance can partially account for the diversity of experimental data observed in tunneling studies of metalorganic compounds.

The author thanks M. A. Belogolovskiĭ, Yu. V. Medvedev, and V. M. Svistunov for helpful remarks and discussions of the results.

*E-mail: khach@hsts.fti.ac.donetsk.ua

[1] W. A. Harrison, Phys. Rev. **123**, 85 (1961).
[2] R. Stratton, J. Phys. Chem. Solids **23**, 1177 (1962).
[3] J. G. Simmons, J. Appl. Phys. **34**, 2581 (1963).
[4] W. F. Brinkman, R. C. Dynes, and J. M. Rowell, J. Appl. Phys. **41**, 1915 (1970).
[5] C. B. Duke, in *Tunneling Phenomena in Solids*, E. Burstein and S. Lundqvist (eds.), Plenum Press, New York (1969), p. 31; Mir, Moscow (1973), p. 36.
[6] V. M. Svistunov and M. A. Belogolovskiĭ, *Tunneling Spectroscopy of Quasiparticles Excited in Metals* [in Russian], Naukova Dumka, Kiev (1986).
[7] E. L. Wolf, *Principles of Electron Tunneling Spectroscopy*, Oxford, New York (1985), Naukova Dumka, Kiev (1990).
[8] V. M. Svistunov, A. I. Khachaturov, M. A. Belogolovskiĭ, and O. I. Chernyak, Fiz. Nizk. Temp. **22**, 605 (1996) [Low Temp. Phys. **22**, 461 (1996)].
[9] A. I. Khachaturov, M. A. Belogolovskii, and V. M. Svistunov, in *Proceedings of the 21st International Conference on Low Temperature Physics*, Prague 1996, Czech. J. Phys. **46**, Suppl. S2, 1031 (1996).
[10] A. I. Khachaturov, Zh. Éksp. Teor. Fiz. **118**, 622 (2000) [JETP **91**, 541 (2000)].

Translated by Steve Torstveit

SHORT NOTES

Resonance spin modes in layered conductors

D. I. Stepanenko*

B. Verkin Institute for Low Temperature Physics and Engineering, National Academy of Sciences of Ukraine, pr. Lenina 47, Kharkov 61103, Ukraine

(Submitted May 6, 2004)
Fiz. Nizk. Temp. **31**, 115–119 (January 2005)

The propagation of spin waves in layered conductors in the presence of an external magnetic field is studied theoretically. It is it is shown that for certain orientations of the magnetic field with respect to the layers of the conductor there is no collisionless absorption, and weakly damped collective modes can propagate even under conditions of strong spatial dispersion. © *2005 American Institute of Physics.* [DOI: 10.1063/1.1820379]

In recent years there has been a significant increase in interest in layered structures with a metallic type of conductivity and a quasi-two-dimensional electron energy spectrum. These include organic conductors of the family of tetrathiafulvalene salts, transition metal dichalcogenides, graphite, etc. In the absence of external magnetic field the conductivity of these substances along the layers, $\sigma_\parallel$, is several orders of magnitude greater than the conductivity across the layers, $\sigma_\perp$. The marked anisotropy of the kinetic coefficients of layered conductors is a consequence of the quasi-two-dimensionality of their electron energy spectrum. The maximum velocity of electrons with the Fermi energy ε_F along the normal $\mathbf{n}$ to the layers, $v_z=\mathbf{v}\cdot\mathbf{n}$, is much less than the characteristic velocity of electrons in the plane of the layers, v_F, and their energy can be written in the form of a rapidly converging series:

$$\varepsilon(\mathbf{p})=\varepsilon_0(p_x,p_y)+\sum_{n=1}^{\infty}\varepsilon_n(p_x,p_y,\eta)\cos\frac{np_z}{p_0}. \tag{1}$$

The functions $\varepsilon_n(p_x,p_y,\eta)$ fall off substantially with increasing index:

$$\varepsilon_{n+1}(p_x,p_y,\eta)\ll\varepsilon_n(p_x,p_y,\eta),\varepsilon_1(p_x,p_y,\eta)\sim\eta\varepsilon_F.$$

Here $\eta=(\sigma_\perp/\sigma_\parallel)^{1/2}$ is the quasi-two-dimensionality parameter, $p_0=\hbar/a$, $\hbar$ is Planck's constant, and a is the distance between layers. Formula (1) corresponds to the tight binding approximation, when the overlap of the electron shells of atoms belonging to different layers is small and the distance between layers is much greater than the interatomic distance within a layer. The Fermi surface $\varepsilon(\mathbf{p})=\varepsilon_F$ corresponding to dispersion relation (1) is open, with a slight corrugation along the p_z axis; it can be multisheet and consist of topologically different elements, e.g., cylinders and planes. It will be assumed from here on that the Fermi surface of the layered conductor is a slightly corrugated cylinder, all sections of which by the plane $p_B=(\mathbf{p}\cdot\mathbf{B}_0)/B_0=p_z\cos\vartheta+p_x\sin\vartheta=$const are closed for $\pi/2-\vartheta>\eta$; here $\mathbf{B}_0=(B_0\sin\vartheta,0,B_0\cos\vartheta)$ is the external magnetic induction. Numerous experimental studies of magnetic oscillations have shown that such a Fermi surface is possessed by a considerable number of organic conductors based on tetrathiafulvalene salts.[1]

In normal metals at low temperatures in a magnetic field, various weakly damped collective modes of the Bose type can exist: electromagnetic, sound, and spin waves. In layered conductors the propagation of collective modes differs in a number of features due to the topology of the Fermi surface. For certain orientations of the magnetic field relative to the layers of the conductor the projection of the electron velocity on the direction of $\mathbf{B}_0$, averaged over the period of motion of an electron along the cyclotron orbit, is negligible. For those directions of $\mathbf{B}_0$ collisionless absorption is absent, and the propagation of weakly damped waves is possible even under conditions of strong spatial dispersion. In this communication we report an investigation of spin waves in layered conductors with a quasi-two-dimensional electron energy spectrum. Collective modes involving oscillations of the spin density of the conduction electrons in quasi-isotropic conductors lacking magnetic order were predicted by Silin[2] and observed experimentally in alkali metals by Schultz and Dunifer.[3]

In the case when the condition $\hbar\omega_B\lesssim T\ll\eta\varepsilon_F$ is met (where T is the temperature and ω_B is the cyclotron frequency of a conduction electron), the density matrix $\hat{\rho}$ is an operator in the space of spin variables and a quasiclassical function of the coordinates and momenta, while the additional energy of the quasiparticle due to electron–electron interaction effects can be written in the framework of the Landau–Silin theory of the Fermi liquid:

$$\delta\hat{\varepsilon}(\mathbf{p},\mathbf{r},t)=\mathrm{Tr}_{\sigma'}\int\frac{d^3p'}{(2\pi\hbar)^3}L(\mathbf{p},\hat{\sigma},\mathbf{p}',\hat{\sigma}')\delta\rho'(\mathbf{p}',\mathbf{r},\hat{\sigma}',t), \tag{2}$$

where $L(\mathbf{p},\hat{\sigma},\mathbf{p}',\hat{\sigma}')=N(\mathbf{p},\mathbf{p}')+S(\mathbf{p},\mathbf{p}')\hat{\sigma}\hat{\sigma}'$ is the Landau correlation function, $\delta\hat{\rho}$ is the nonequilibrium admixture to the density matrix, and $\hat{\sigma}$ are the Pauli matrices.

For angles ϑ between vectors $\mathbf{B}_0$ and $\mathbf{n}$ not too close to $\pi/2$, the closed electron orbits in momentum space are almost the same for different values of the momentum projec-

tion on the magnetic field direction, and the area $S(\varepsilon,p_B)$ of the section of the Fermi surface by the plane $p_B=\text{const}$ and the components v_x and v_y of the velocity $\mathbf{v}=\partial\varepsilon(\mathbf{p})/\partial\mathbf{p}$ of the conduction electrons in the plane of the layers depends weakly on p_B, with an order of smallness $\eta\tan\vartheta$. This means that the energy of the quasiparticles in the one-electron approximation and the Landau correlation function can be expanded in an asymptotic series, the leading term of which is independent of p_B. In the zeroth approximation in the small parameter η the functions $N(\mathbf{p},\mathbf{p}')$ and $S(\mathbf{p},\mathbf{p}')$ can be represented as Fourier series:

$$N(\mathbf{p},\mathbf{p}')=\sum_{n=-\infty}^{\infty}N_n(\varepsilon_F)e^{in(\varphi-\varphi')},$$

$$S(\mathbf{p},\mathbf{p}')=\sum_{n=-\infty}^{\infty}S_n(\varepsilon_F)e^{in(\varphi-\varphi')} \tag{3}$$

with coefficients coupled by the relations $N_{-n}=N_n$, $S_{-n}=S_n$. As variables in $\mathbf{p}$ space we chose the integrals of motion ε and p_B of the charge carriers in the magnetic field and also the phase of the electron velocity, $\varphi=\omega_B t_1$, where t_1 is the time of motion along the trajectory $\varepsilon=\varepsilon_F$, $p_B=\text{const}$. Taking the next terms of the expansion of the correlation function in powers of η into account leads only to negligibly small corrections to the spectrum of the collective modes.

The paramagnetic spin modes are space–time perturbations of the spin density $\mathbf{g}(\mathbf{r},\mathbf{p},t)=\mathrm{Tr}_\sigma(\hat{\sigma}\rho)$. For small deviations from the equilibrium state the spin density can be written as the sum of the equilibrium part $\mathbf{g}_0=-\mu\mathbf{B}_0(\partial f_0/\partial\varepsilon)$ and a small nonequilibrium admixture $-(\partial f_0/\partial\varepsilon)\boldsymbol{\xi}(\mathbf{r},\mathbf{p},t)$, where $f_0(\varepsilon)$ is the Fermi function, $\mu=\mu_0/(1+S_0^{\sim})$, μ_0 is the magnetic moment of a conduction electron, $S_0^{\sim}=\nu(\varepsilon_F)S_0$, and $\nu(\varepsilon_F)$ is the density of states at the Fermi level. The integral of $\mu_0\mathbf{g}_0(\varepsilon)$ over the unit cell in $\mathbf{p}$ space gives the magnetization $\mathbf{M}_0=\chi_0\mathbf{B}_0$ in a uniform static magnetic field with induction $\mathbf{B}_0$, and $\chi_0=\mu_0\mu\nu(\varepsilon_F)$ is the static paramagnetic susceptibility.

According to Ref. 2, the linearized kinetic equation in the case when the perturbation of the spin density $\boldsymbol{\xi}$ is perpendicular to $\mathbf{B}_0$ has the form

$$\frac{\partial\boldsymbol{\xi}}{\partial t}+\left(\mathbf{v}\frac{\partial}{\partial\mathbf{r}}+\frac{e}{c}(\mathbf{v}\times\mathbf{B}_0)\frac{\partial}{\partial\mathbf{p}}\right)\boldsymbol{\Phi}-\frac{2\mu}{\hbar}[\mathbf{B}_0\times\boldsymbol{\Phi}]$$
$$-\mu_0\mathbf{v}\frac{\partial\mathbf{B}^{\sim}}{\partial\mathbf{r}}+\frac{2\mu\mu_0}{\hbar}[\mathbf{B}_0\times\mathbf{B}^{\sim}]=I_{\text{coll}}. \tag{4}$$

Here $\boldsymbol{\Phi}=\boldsymbol{\xi}+\langle S\boldsymbol{\xi}\rangle$, the angle bracket denotes averaging over the Fermi surface,

$$\langle S\boldsymbol{\xi}\rangle=\int\frac{2d^3p'}{(2\pi\hbar)^3}\left(-\frac{\partial f_0(\varepsilon')}{\partial\varepsilon'}\right)S(\mathbf{p},\mathbf{p}')\boldsymbol{\xi}(\mathbf{p}',\mathbf{r},t)$$

$$\frac{\partial f_0}{\partial\varepsilon}=-\delta(\varepsilon-\varepsilon_F),$$

$\mathbf{B}^{\sim}(r,t)$ is the rf field, e is the electron charge, and c is the speed of light. The collision integral I_{coll} determines two relaxation times: τ_1 and τ_2, the momentum and spin-density relaxation times; $\tau_2\gg\tau_1$. For processes corresponding to the frequency region $kc\gg\omega\gg\tau^{-1}=\tau_1^{-1}+\tau_2^{-1}$ [the wave vector $\mathbf{k}=(k_x,0,k_z)$], the asymptotic behavior of the spectrum of collective modes is completely independent of the specific form of the collision integral.

Expanding the functions $\boldsymbol{\Phi}=\boldsymbol{\xi}+\langle S\boldsymbol{\xi}\rangle$ and $\boldsymbol{\xi}$ in Fourier series in the variable φ and substituting the results into Eq. (4), we find that the circular components of the renormalized spin density $\Phi^{(\pm)}=\Phi_{x1}\pm i\Phi_y\sim\exp(-i\omega t+i\mathbf{k}\cdot\mathbf{r})$ of the conduction electrons satisfy the integral equations[4]

$$\Phi^{(\pm)}=\int_{-\infty}^{\varphi}d\varphi'\exp\left(\frac{i}{\omega_B}\int_{\varphi'}^{\varphi}d\varphi''(\tilde{\omega}\pm\Omega\right.$$
$$\left.-\mathbf{k}\cdot\mathbf{V}(\varphi'',p_B))\right)\left(i\frac{\mu_0}{\omega_B}(\mathbf{k}\cdot\mathbf{v}(\varphi',p_B)\pm\Omega)B_{\pm}^{\sim}\right.$$
$$\left.-i\frac{\omega}{\omega_B}\sum_{p=-\infty}^{\infty}\lambda_p\overline{\Phi}_p^{(\pm)}e^{ip\varphi'}\right), \tag{5}$$

$\Phi_{x_1}=\Phi_x\cos\vartheta-\Phi_z\sin\vartheta$, the x_1 axis is directed perpendicular to the y axis and to the vector $\mathbf{B}_0$, where $\lambda_p=S_p^{\sim}/(1+S_p^{\sim})$, $\tilde{\omega}=\omega+i0$, $\overline{\boldsymbol{\Phi}}_p=\langle e^{-ip\varphi}\boldsymbol{\Phi}\rangle/\langle 1\rangle$, $B_{\pm}^{\sim}=B_{x_1}^{\sim}\pm iB_y^{\sim}$, $\Omega=\omega_s/(1+S_0^{\sim})$, and $\omega_s=-2\mu_0B_0/\hbar$ is the spin paramagnetic resonance frequency.

Multiplying Eq. (5) by $\exp(-in\varphi)$ and integrating with respect to the variables $\beta=p_B/p_0\cos\vartheta$ and φ, we obtain an infinite system of linear equations for the coefficients $\overline{\boldsymbol{\Phi}}_n^{(\pm)}$ of the Fourier series of the function

$$\langle\Phi^{(\pm)}\rangle_\beta\equiv\frac{1}{2\pi}\int_{-\pi}^{\pi}d\beta\Phi^{(\pm)}(\varepsilon_F,\beta,\varphi)$$

$$\sum_{p=-\infty}^{\infty}\left(\delta_{np}-\lambda_p\frac{\omega}{\omega_B}\langle f_{np}(\beta)\rangle_\beta\right)\overline{\Phi}_p^{(\pm)}$$
$$=-\mu_0B_{\pm}^{\sim}\left\langle\frac{1}{2\pi i}\frac{\int_0^{2\pi}\int_0^{2\pi}d\varphi d\varphi_1[\mathbf{kv}(\beta,\varphi-\varphi_1)\mp\Omega]\exp[i(p-n)\varphi-ip\varphi_1+iR(\varphi,\varphi_1)]}{1-\exp[2\pi iR(2\pi,2\pi)]}\right\rangle_\beta, \tag{6}$$

$$f_{np}(\beta)=\frac{1}{2\pi i}\frac{\int_0^{2\pi}\int_0^{2\pi}d\varphi d\varphi_1\exp[i(p-n)\varphi-ip\varphi_1+iR(\varphi,\varphi_1)]}{1-\exp[2\pi iR(2\pi,2\pi)]}. \tag{7}$$

Here $R(\varphi,\varphi_1)\equiv 1/\omega_B\int_{\varphi-\varphi_1}^{\varphi}d\varphi'[\tilde{\omega}\mp\Omega-\mathbf{k}\cdot\mathbf{v}(\beta,\varphi')]$, and δ_{np} is the Kronecker delta. The dependence of the cyclotron frequency on p_B should be taken into account only in the expression $k_x v_x/\omega_B$ in the argument of the exponential function, under the condition that $\eta k_x v_F\sim\omega_B$.

The coefficients of the Fourier series of the smooth function $\nu(\varepsilon_F)S(\mathbf{p},\mathbf{p}')$ fall off rapidly with increasing summation index, and it is therefore sufficient to keep a finite number of terms of the series in Eqs. (5) and (6). The system of equations (6), together with Maxwell's equation, relates the variable magnetic field and the magnetization and describes the natural oscillations of the spin density in layered conductors with an arbitrary energy spectrum and correlation function. It is easy to see that for finding the spin-wave spectrum it is sufficient to use the homogeneous version of the system of equations (6). We shall neglect in (6) the small inhomogeneous term proportional to $\mu_0 B_{\pm}^{\sim}$, which takes into account the influence of the self-consistent field $B_{\pm}^{\sim}$. The dispersion relation for the ''free'' oscillations of the spin density has the form

$$D(\omega^{(0)},\mathbf{k})\equiv\det\left[\delta_{np}-\lambda_p\frac{\omega^{(0)}}{\omega_B}\langle f_{np}(\beta)\rangle_\beta\right]=0. \tag{8}$$

Up to terms proportional to $\chi_0\sim\mu_0^2\nu(\varepsilon_F)$ the frequency ω of the natural oscillations of the magnetization is equal to the frequency $\omega^{(0)}$ of the ''free'' oscillations of the spin density. At that frequency the magnetic susceptibility has a sharp maximum, and the determinant $D(\omega,\mathbf{k})$ is equal in order of magnitude to χ_0.

The condition that there be no collisionless damping of spin waves reduces to satisfaction of the inequality

$$|\omega-n\omega_B\mp\Omega|>\max|\langle\mathbf{k}\cdot\mathbf{v}\rangle_\varphi|. \tag{9}$$

Outside the region of ω, $\mathbf{k}$ values corresponding to condition (9) the functions $f_{np}(\beta)$ have a pole, and after integration over p_B the dispersion relation acquires a imaginary part responsible for strong absorption of the wave. In layered conductors the electron drift velocity along the magnetic field, $\mathbf{v}_B=\langle\mathbf{v}\rangle_\varphi$, oscillates as a function of the angle ϑ between the magnetic field and the normal to the layers. For certain directions of $\mathbf{B}_0$ with respect to the layers of the conductor $\mathbf{v}_B$ is close to zero, and the damping of the wave is governed by collision processes. Here the existence of collective modes is possible even under the condition $\eta k v_F\gtrsim\omega_B$. In the region of ω and $\mathbf{k}$ values such that $\mathbf{k}\cdot\mathbf{v}_m\gg\omega_B$, $\omega\mp\Omega\ll\mathbf{k}\cdot\mathbf{v}_m$, where $\mathbf{v}_m$ is the maximum value of the velocity in the $\mathbf{k}$ direction, there exist solutions of the dispersion relation (8) in the neighborhood of the resonance

$$\omega=n\omega_B\pm\Omega+\Delta\omega,\Delta\omega\ll\omega_B,n=0,1,2\ldots. \tag{10}$$

Keeping only the first two terms in formula (1) and neglecting anisotropy in the plane of the layers, we write the energy of a quasiparticle in the one-electron approximation as

$$\varepsilon(\mathbf{p})=\frac{p_x^2+p_y^2}{2m}-\eta v_F p_0\cos\frac{p_z}{p_0}, \tag{11}$$

where $v_F=\sqrt{2\varepsilon_F/m}$. The asymptotic solutions accurate to terms of order η for the system of equations of motion corresponding to the dispersion relation (11) are easily found using the standard methods of nonlinear mechanics[5]

$$\begin{aligned}
&v_x(t_1)=v_x^{(0)}(t_1)+v_x^{(1)}(t_1),v_x^{(0)}(t_1)=v_\perp\cos\omega_B(\beta)t_1,\\
&v_x^{(1)}(t_1)=\eta v_F\tan\vartheta J_0(\alpha)\sin\beta\\
&\qquad-\eta v_F\tan\vartheta\sum_{n=2}^{\infty}\frac{J_n(\alpha)\sin(\beta-n\pi/2)}{n^2-1}\\
&\qquad\times\cos n\omega_B(\beta)t_1,\\
&v_z(t_1)=\eta v_F\sin(\beta-\alpha\cos\omega_B(\beta)t_1).
\end{aligned} \tag{12}$$

Here $\omega_B(\beta)=\omega_B[1+(\eta\tan\vartheta J_1(\alpha)\cos\beta)/2]$ is the cyclotron frequency of quasiparticles with energy (11) in a field

$$\mathbf{B}_0=(B_0\sin\vartheta,0,B_0\cos\vartheta),\ \omega_B=(|e|B_0/mc)\cos\vartheta,$$

$$\alpha=(mv_F/p_0)\tan\vartheta,$$

$J_n(\alpha)$ is the Bessel function,

$$v_\perp=v_F\left(1-\frac{v_x^{(1)}(0)}{v_F}+\frac{\eta p_0}{mv_F}\cos(\beta-\alpha)\right)$$

is the amplitude of the first harmonic of $v_x(t)$, and the initial phase is chosen such that $v_y(0)=0$.

It follows from relations (12) that

$$\langle\mathbf{kv}\rangle_\varphi=\mathbf{kv}_B=\eta v_F J_0(\alpha)(k_x\tan\vartheta+k_z)\sin\beta. \tag{13}$$

For those directions of $\mathbf{B}_0$ for which α is equal to one of the zeros $\alpha_i=(mv_F/p_0)\tan\vartheta_i$ of the Bessel function $J_0(\alpha)$ the average $\langle\mathbf{k}\cdot\mathbf{v}\rangle_\varphi\sim\eta^2$, and the asymptotic expression for the coefficients $f_{np}(\beta)$ takes the form

$$f_{np}(\beta)=\frac{1}{k_x r_0}\left(\cot\frac{\pi(\omega\mp\Omega)}{\omega_B}\cos\frac{\pi}{2}(n-p)+\frac{\sin\left(R_1(\vartheta_1)+\frac{\pi}{2}(n+p)\right)}{\sin\frac{\pi(\omega\mp\Omega)}{\omega_B}}\right), \tag{14}$$

where

$$\begin{aligned}
R_1(\vartheta_i)&=\int_{-\pi/2}^{\pi/2}\frac{\mathbf{k}\cdot\mathbf{v}(\varphi)}{\omega_B(\beta_i)}d\varphi=2\frac{k_x v_\perp}{\omega_B(\beta_i)}\\
&\quad-\pi\eta\frac{k_z v_F}{\omega_B}H_0(\alpha_i)\cos\beta_i\\
&\quad+\eta\frac{k_x v_F}{2\omega_B}\tan\vartheta_i\cos\beta_i\sum_{n=1}^{\infty}\frac{J_{2n+1}(\alpha_i)}{n(n+1)(2n+1)},
\end{aligned}$$

is the Struve function, $r_0=v_F/\omega_B$, and $\beta_i=p_B/p_0\cos\vartheta_i$. In the case when the correlation function is determined by the zeroth and first Fourier harmonics

$$S(\mathbf{p},\mathbf{p}')=S_0+2S_1\cos(\varphi-\varphi'),$$

the solution of dispersion relation (8) is determined by formula (10) with

$$\Delta\omega = \frac{n\omega_B \pm \Omega}{\pi k_x r_0}\,\gamma_{1,2}.$$

It is easy to obtain from (8) a quadratic equation for $\gamma_{1,2}$, the roots of which are

$$\gamma_{1,2} = \frac{1}{2}[\lambda_0 + 2\lambda_1 + (-1)^n(\lambda_0 - 2\lambda_1)g \pm ((\lambda_0 + 2\lambda_1 + (-1)^n(\lambda_0 - 2\lambda_1)g)^2 + 8\lambda_0\lambda_1(-1 + g^2 + h^2))^{1/2}],$$

where $g = \langle \sin R_1(\vartheta_i)\rangle_\beta$, and $h = \langle \cos R_1(\vartheta_i)\rangle_\beta$.

In the short-wavelength limit for the selected directions of the external magnetic field there exist spin waves with frequencies (10) close to the resonance frequencies $\omega_r = n\omega_B \pm \Omega$. The correction (15) to the resonance frequency is a rapidly oscillating function of wave number. An analogous type of excitations exists in quasi-isotropic metals only when the direction of wave propagation is strictly perpendicular to $\mathbf{B}_0$.

*E-mail: stepanenko@ilt.kharkov.ua

[1] J. Singelton, Rep. Prog. Phys. **63**, 1111 (2000).
[2] V. P. Silin, Zh. Eksp. Teor. Fiz. **35**, 1243 (1958) [Sov. Phys. JETP **8**, 870 (1959)].
[3] S. Schultz and G. Dunifer, Phys. Rev. Lett. **18**, 283 (1967).
[4] V. G. Peschansky and D. I. Stepanenko, JETP Lett. **78**, 322 (2003).
[5] N. N. Bogolyubov and Yu. A. Mitropol'skiĭ, *Asymptotic Methods in the Theory of Nonlinear Oscillations*, translation of 2nd Russ. ed., Gordon and Breach, New York (1962), cited 4th Russ. ed., Nauka, Moscow (1974).

Translated by Steve Torstveit

LETTER TO THE EDITOR

On the nature of the reentrant effect in susceptibility of mesoscopic cylindrical samples

G. A. Gogadze*

B. Verkin Institute for Low Temperature Physics and Engineering of the National Academy of Sciences of Ukraine, 47 Lenin Ave., Kharkov 61103, Ukraine
(Submitted October 12, 2004; revised October 22, 2004)
Fiz. Nizk. Temp. **31**, 120–123 (January 2005)

A theory of the reentrant effect in the susceptibility of mesoscopic cylindrical NS samples is proposed which is essentially based on the properties of the Andreev levels. The specific feature of the quantum levels of the structure is that in a varying magnetic field (or temperature) each level periodically comes into coincidence with the chemical potential of the metal. As a result, the state of the system becomes strongly degenerate and the amplitude of the paramagnetic contribution to the susceptibility increases sharply. © *2005 American Institute of Physics.*
[DOI: 10.1063/1.1820383]

In 1990 Mota and co-workers[1] detected a surprising behavior of the magnetic susceptibility of a cylindrical NS structure (N and S are for the normal metal and superconductor, respectively) at very low temperature ($T<100$ mK) when the external magnetic field was applied parallel to the NS boundary. Most intriguingly, a decrease in the sample temperature below a certain point T_r (at a fixed field) produced a reentrant effect: the decreasing magnetic susceptibility of the structure unexpectedly started growing. A similar behavior was observed with the isothermal reentrant effect in a field decreasing to a certain value H_r below which the susceptibility started to grow sharply. The samples were superconducting Nb wires with a radius R of tens of μm coated with a thin layer d of very pure Ag. It is emphasized in Ref. 2 that the detected magnetic response of the NS structure is similar to the properties of the persistent currents in mesoscopic normal rings. It is assumed[1–5] that the reentrant effect reflects the behavior of the total susceptibility χ of the NS structure: the paramagnetic contribution is superimposed on the Meissner effect-related diamagnetic contribution and nearly compensates it. Anomalous behavior of the susceptibility has also been observed in AgTa, CuNb, and AuNb structures.[2,4]

The origin of paramagnetic currents in NS structures has been discussed in a number of theoretical studies. Bruder and Imry[6] analyzed the paramagnetic contribution to susceptibility taking into account the paths of the quasiparticles that do not collide with the superconducting boundary. The authors note an appreciable paramagnetic effect in the physical situation under discussion. However, the ratio derived by them for the paramagnetic and diamagnetic contributions is rather small, and cannot account for the experimental results.[1–5]

Fauchere, Belzig, and Blatter[7] explain the high paramagnetic effect assuming the pure repulsive electron–electron interaction in noble metals. The proximity effect in the normal metal induces an order parameter whose phase is π-shifted against the Δ_s phase of the superconductor. This leads to paramagnetic instability of the Andreev states, and the density of states of the NS structure exhibits a peak near zero energy. The theory[7] is largely based on the assumption of the repulsive electron interaction in the normal metal. The question of whether the reentrant effect is due to specific properties of the noble metals or is shared by any normal metal experiencing the proximity effect can only be answered experimentally. We can just note that the theories in Refs. 6 and 7 do not describe the temperature and field dependences of the paramagnetic susceptibility of the NS structure and do not explain the origin of the anomalously large amplitude of the reentrant effect.

It is worth mentioning the assumption made by Maki and Haas[8] that below the transition temperature ($\sim$10 mK) some noble metals (Cu, Ag, Au) can exhibit p-wave superconducting ordering, which may be responsible for the reentrant effect. This theory does not explain the high paramagnetic reentrant effect either.

In this Letter a theory of the reentrant effect is proposed which is essentially based on the properties of the quantized levels of the NS structure. Levels with energies no more than Δ_0 ($2\Delta_0$ is the gap of the superconductor) appear inside the normal metal bounded by the dielectric (vacuum) on one side and contacting the superconductor on the other side. The number of levels n_0 in the well is finite. Because of the Aharonov-Bohm effect,[9] the spectrum of the NS structure is a function of the magnetic flux in a weak field. The specific feature of the quantum levels of the structure is that in a varying field H (or temperature) each level in the well periodically comes into coincidence with the chemical potential of the metal. As a result, the state of the system suffers strong degeneracy and the density of states of the NS sample experiences resonance spikes. We attribute the reentrant effect to this resonance.

Resonance spikes of the density of states as a function of the magnetic field were predicted earlier in our study of a structure consisting of a normal metal cylinder coated with a thin superconducting layer.[10]

Let us consider a superconducting cylinder of radius R

coated with a thin layer d of a pure normal metal. The structure is placed in a weak magnetic field $\mathbf{H}(0,0,H)$ applied along its symmetry axis. We proceed from a simplified NS model assuming that the order parameter modulus of the superconductor changes in a jump at the NS boundary. We introduce the angle of incidence of a quasiparticle α on the dielectric boundary, measured from the cylinder radius. It is evident that there are two classes of quasiparticle paths inside the normal metal. One class includes those in which α varies within $0 \leqslant \alpha \leqslant \alpha_{\rm cr}$ ($\alpha_{\rm cr}$ is the angle at which the path touches the NS boundary). In this case the quasiparticle collides successively with the dielectric and the NS boundary. The other class with $\alpha > \alpha_{\rm cr}$ consists of the paths whose spectra are formed only by the quasiparticle–dielectric collisions. The spectra of the two classes of paths differ considerably.

First we consider the paths with $\alpha \leqslant \alpha_{\rm cr}$. The spectrum of quasiparticles of the NS structure is readily obtainable by the method of multidimensional quasiclassics[10,11] generalized for the presence of the Andreev scattering in the system.[12] We have

$$\varepsilon_n(q,\alpha) = \frac{\pi\hbar V_{\mathcal{L}}(q)\cos\alpha}{2d}\left(n + \frac{1}{\pi}\arccos\frac{\varepsilon}{\Delta_0} - \frac{\Phi(\alpha)}{\Phi_0}\right). \tag{1}$$

Here $V_L(q) = \sqrt{p_F^2 - q^2}/m^*$, p_F is the Fermi momentum, q is the momentum component along the cylinder axis, m^* is the effective mass of the quasiparticle, and Φ_0 is the superconducting flux quantum. The magnetic flux through the area bounded by a part of the NS boundary and by the quasiparticle path at an angle α is given by

$$\Phi(\alpha) = 2\tan\alpha \int_0^d A(x)dx.$$

The integral of $A(x)$ can be calculated if we know the distribution of the vector potential field inside the normal metal. The problem of the Meissner effect in superconductor-normal metal (proximity) sandwiches was solved by Zaikin.[13] The screening current in the NS structure was calculated in terms of the microscopic theory, and the expression $A(x) = Hx + (4\pi/c)j(a)x(d - x/2)$ can be obtained from the Maxwell equation $\operatorname{curl}\mathbf{H} = (4\pi/c)\mathbf{j}$ with the boundary conditions $A(x=0) = 0$ and $\partial_x A(x=d) = H$. The screening current is a function of

$$a = \int_0^d A(x)dx, \quad j(a) = -j_s\varphi(a/\Phi_0),$$

where j_s is the superfluid current and $\varphi(x)$ is an oscillating function of flux (at $a/\Phi_0 \ll 1$ we have $j(a) = -j_s a/\Phi_0$). Thus, we can write down the self-consistent equation for a:[13–15]

$$a = H\frac{d^2}{2} + \frac{4\pi}{3c}j(a)d^3, \tag{2}$$

$j(a)$ becomes zero recurrently when $a/\Phi_0 = 1/2, 1, 3/2, 2, \ldots$. The spectrum of Eq. (1) is similar to Kulik's spectrum[16] for the current state of an SNS contact. However, Eq. (1) includes an angle-dependent magnetic flux instead of the phase difference of the contacting superconductors.

We proceed from the expression for the thermodynamic potential

$$\Omega = -T\sum_S \ln[1 + \exp(-\varepsilon_S/T)],$$

where the summation is over all quantum states of the spectrum, Eq. (1), and the spin (Boltzmann's constant $k_B = 1$). We use the approximation of equidistant levels in which the second term in Eq. (1) can be replaced with 1/2. The contribution to susceptibility (per unit volume V of the normal metal) can be found as $\chi = -(1/V)(\partial^2\Omega/\partial H^2)$. Taking into account two orientations of the spin and two possible signs of α and q, as well as the finite number of levels n_0, we have the starting expression for the susceptibility (L is the cylinder height, ζ is the chemical potential of the metal):

$$\chi \sim \sum_{n=-n_0}^{+n_0} \int_{-\zeta}^{+\infty} \frac{d\varepsilon}{\operatorname{ch}^2\dfrac{\varepsilon}{2T}} \int_0^{\alpha_{\rm cr}} d\alpha \sin^2 a \int_0^{p_F} dq V_{\mathcal{L}}^2(q) \times \delta(\varepsilon - \varepsilon_n(q,\alpha)). \tag{3}$$

We take an integral over q using the δ function and introduce the dimensionless energy

$$\boldsymbol{\epsilon} = \varepsilon/\delta\varepsilon \quad (\delta\varepsilon = \pi\hbar V_F/2d).$$

Since $\zeta/\delta\varepsilon \gg 1$, the lower limit of the energy integral can be replaced with $-\infty$. By introducing the variable $x \equiv \tan\alpha$ and the notation $a_n = n + 1/2$, $b = b(H,T) = a/\Phi_0$, $x_0 = \tan\alpha_{\rm cr} \simeq \sqrt{2R/d}$ and taking into account the parity of the integrand we obtain, instead of Eq. (3):

$$\chi = A\sum_{n=0,1,\ldots}^{n_0} \int_0^{+\infty} \frac{d\boldsymbol{\epsilon}|\boldsymbol{\epsilon}|^3}{\cosh^2[\eta\boldsymbol{\epsilon}/2]} \times \int_0^{x_0} \frac{dx x^2 \theta(|a_n - bx| - |\boldsymbol{\epsilon}|\sqrt{1+x^2})}{|a_n - bx|^3\sqrt{|a_n - bx|^2 - \boldsymbol{\epsilon}^2(1+x^2)}}. \tag{4}$$

Here $A = 2\zeta d^2\eta/(\pi R\Phi_0^2)$, $\eta = \delta\varepsilon/T$, and θ is the Heaviside step function. It is seen in Eq. (4) that for a given "subzone" n the amplitude of the paramagnetic susceptibility increases sharply whenever the Andreev level coincides with the chemical potential of the metal. The resonant spike of susceptibility occurs when $a_n - bx$ tends to zero on a change in the magnetic field (or temperature). Because of the finite number of Andreev levels, the existence region of the isothermal reentrant effect is within $0 < H \leqslant H_{n_0}$.

The indefinite integral over x can be calculated exactly. The roots of the square trinomial under the radical to within the first-order terms in $\boldsymbol{\epsilon}$ are $x_{1,2} \simeq \alpha_0 \pm |\boldsymbol{\epsilon}|\sqrt{1+\alpha_0^2}/b$ ($\alpha_0 = a_n/b; 0 < x_1 < \alpha_0 < x_2 < x_0$). The θ function bars the region $x_1 < x < x_2$ from consideration. On substituting the limits of integration, the expressions obtained have different powers of the parameter $|\boldsymbol{\epsilon}|^{-1}$. We retain only the most important terms of order $|\boldsymbol{\epsilon}|^{-3}$. The integral over energy is taken easily when these terms are substituted in it. Finally, the susceptibility of the NS structure becomes

$$\chi \cong \frac{\zeta d^2}{\pi R \Phi_0^2} \sum_{n=0,1,\ldots}^{n_0} \frac{\left(n+\frac{1}{2}\right)^2 \mathrm{th}\left[\frac{\pi\hbar V_F}{4dT}\left(n+\frac{1}{2}\right)\right]}{\left[\left(n+\frac{1}{2}\right)^2 + b^2(H,T)\right]^{3/2}}. \qquad (5)$$

The flux $b = a/\Phi_0$ (Eq. (2)) depends on both the magnetic field and temperature. The screening current of the NS structure is $j = -j_s \varphi(a/\Phi_0)$, where $j_s \sim T^{-1}\exp(-4\pi T d/\hbar V_F)$ for $T \gg \hbar V_F/d$.[13,15] It is seen from Eq. (5) that $b(H,T)$ increases with rising temperature (at fixed H). At the same time the argument of the hyperbolic tangent becomes smaller than unity starting with a certain temperature. As a result, the amplitude of paramagnetic susceptibility decreases rapidly as the temperature rises. The isothermal reentrant effect occurs when a decreasing magnetic field causes an increase in the amplitude of paramagnetic susceptibility. Choosing the characteristic parameters of the problem $d = 3.3\times10^{-4}$ cm, $R = 8.2\times10^{-4}$ cm, $\zeta \sim 10^{-12}$ erg, $\Phi_0 = 2\times10^{-7}$ G/cm^2, we can estimate the coefficient in front of the sum in Eq. (5) to be $\simeq 10^{-2}$. The sum itself has the logarithmic scale $\simeq \ln n_0$. The effect is caused by the paths of the quasiparticles with $\alpha \lesssim \alpha_{\mathrm{cr}}$.

The paths of the quasiparticles with $\alpha > \alpha_{\mathrm{cr}}$ do not collide with the NS boundary and their quantum states are essentially similar to the states of the "whispering gallery" type that appear in the cross section of a normal solid cylinder in a weak magnetic field.[17,18] The caustic of these paths is approximately equal to the cylinder radius, and the spectrum of the states carries no information about the parameters of the superconductor. The energy levels cannot be made coincident with the chemical potential of the metal by varying the magnetic field or temperature. As a result, the paramagnetic contribution to the thermodynamics of the paths with $\alpha > \alpha_{\mathrm{cr}}$ has a much smaller amplitude.

The author is indebted to A. N. Omelyanchouk and A. A. Slutskin for helpful discussions.

*E-mail: gogadze@ilt.kharkov.ua

[1] P. Visani, A. C. Mota, and A. Pollini, Phys. Rev. Lett. **65**, 1514 (1990).
[2] A. C. Mota, P. Visani, A. Pollini, and K. Aupke, Physica B **197**, 95 (1994).
[3] F. B. Müller-Allinger and A. C. Mota, Phys. Rev. Lett. **84**, 3161 (2000).
[4] F. B. Müller-Allinger and A. C. Mota, cond-mat/0007331 (2000).
[5] R. Frassanito, P. Visani, M. Nideröst, A. C. Mota, P. Smeibidl, K. Swieca, W. Wendler, and F. Pobell, *Proceedings LT-21, Part S4-LT: Properties of Solids I*, Prague (1996), p. 2317.
[6] C. Bruder and Y. Imry, Phys. Rev. Lett. **80**, 5782 (1998).
[7] A. L. Fauchere, W. Belzig, and G. Blatter, Phys. Rev. Lett. **82**, 3336 (1999).
[8] K. Maki and S. Haas, cond-mat/0003413 (2000).
[9] Y. Aharonov and D. Bohm, Phys. Rev. **115**, 485 (1959).
[10] G. A. Gogadze, R. I. Shekhter, and M. Jonson, Fiz. Nizk. Temp. **27**, 1237 (2001) [Low Temp. Phys. **27**, 913 (2001)].
[11] J. B. Keller and S. I. Rubinow, Ann. Phys. (N.Y.) **9**, 24 (1960).
[12] A. F. Andreev, Zh. Éksp. Teor. Fiz. **46**, 1823 (1964) [Sov. Phys. JETP **19**, 1228 (1964)].
[13] A. D. Zaikin, Solid State Commun. **41**, 533 (1982).
[14] W. Belzig, G. Bruder, and G. Schön, Phys. Rev. B **53**, 5727 (1996).
[15] A. L. Fauchere and G. Blatter, Phys. Rev. B **56**, 14102 (1997).
[16] I. O. Kulik, Zh. Éksp. Teor. Fiz. **57**, 1745 (1969) [Sov. Phys. JETP **30**, 944 (1969)].
[17] E. N. Bogachek and G. A. Gogadze, Zh. Éksp. Teor. Fiz. **63**, 1839 (1972) [Sov. Phys. JETP **36**, 973 (1973)].
[18] G. A. Gogadze, Fiz. Nizk. Temp. **9**, 1051 (1983) [Sov. J. Low Temp. Phys. **9**, 543 (1983)].

This article was published in English in the original Russian journal. Reproduced here with stylistic changes by AIP.